

c.1

**ARCHIVE COPY
DO NOT LOAN**



Influence of Wind Tunnel Noise on the
Location of Boundary-Layer
Transition on a Slender Cone at
Mach Numbers from 0.2 to 5.5

Volume II
Tabulated and Plotted Data

N. Sam Dougherty, Jr.
ARO, Inc.

March 1980

Final Report for Period January 26, 1970 — April 28, 1977

Approved for public release; distribution unlimited.

AEDC TECHNICAL LIBRARY



5 0720 00034 2149

**ARNOLD ENGINEERING DEVELOPMENT CENTER
ARNOLD AIR FORCE STATION, TENNESSEE
AIR FORCE SYSTEMS COMMAND
UNITED STATES AIR FORCE**

NOTICES

When U. S. Government drawings, specifications, or other data are used for any purpose other than a definitely related Government procurement operation, the Government thereby incurs no responsibility nor any obligation whatsoever, and the fact that the Government may have formulated, furnished, or in any way supplied the said drawings, specifications, or other data, is not to be regarded by implication or otherwise, or in any manner licensing the holder or any other person or corporation, or conveying any rights or permission to manufacture, use, or sell any patented invention that may in any way be related thereto.

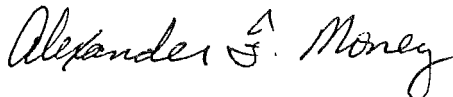
Qualified users may obtain copies of this report from the Defense Technical Information Center.

References to named commercial products in this report are not to be considered in any sense as an indorsement of the product by the United States Air Force or the Government.

This report has been reviewed by the Office of Public Affairs (PA) and is releasable to the National Technical Information Service (NTIS). At NTIS, it will be available to the general public, including foreign nations.

APPROVAL STATEMENT

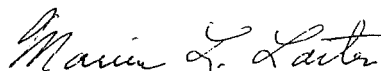
This report has been reviewed and approved.



ALEXANDER F. MONEY
Project Manager
Directorate of Technology

Approved for publication:

FOR THE COMMANDER



MARION L. LASTER
Director of Technology
Deputy for Operations

UNCLASSIFIED

REPORT DOCUMENTATION PAGE		READ INSTRUCTIONS BEFORE COMPLETING FORM
1. REPORT NUMBER AEDC-TR-78-44	2. GOVT ACCESSION NO.	3. RECIPIENT'S CATALOG NUMBER
4. TITLE (and Subtitle) INFLUENCE OF WIND TUNNEL NOISE ON LOCATION OF BOUNDARY-LAYER TRANSITION ON A SEENDER CONE AT MACH NUMBERS FROM 0.2 TO 5.5, Volume II: Tabulated and Plotted Data		5. TYPE OF REPORT & PERIOD COVERED Final Report, January 26, 1970 - April 28, 1977
		6. PERFORMING ORG. REPORT NUMBER
7. AUTHOR(s) N. Sam Dougherty, Jr., ARO, Inc., a Sverdrup Corporation Company		8. CONTRACT OR GRANT NUMBER(s)
9. PERFORMING ORGANIZATION NAME AND ADDRESS Arnold Engineering Development Center Air Force Systems Command Arnold Air Force Station, Tennessee 37389		10. PROGRAM ELEMENT, PROJECT, TASK AREA & WORK UNIT NUMBERS Program Element 65807F
11. CONTROLLING OFFICE NAME AND ADDRESS Arnold Engineering Development Center/DOS Air Force Systems Command Arnold Air Force Station, Tennessee 37389		12. REPORT DATE March 1980
		13. NUMBER OF PAGES 246
14. MONITORING AGENCY NAME & ADDRESS (if different from Controlling Office)		15. SECURITY CLASS. (of this report) UNCLASSIFIED
		15a. DECLASSIFICATION DOWNGRADING SCHEDULE N/A
16. DISTRIBUTION STATEMENT (of this Report) Approved for public release; distribution unlimited.		
17. DISTRIBUTION STATEMENT (of the abstract entered in Block 20, if different from Report)		
18. SUPPLEMENTARY NOTES Available in Defense Technical Information Center (DTIC).		
19. KEY WORDS (Continue on reverse side if necessary and identify by block number)		
<div style="display: flex; justify-content: space-between;"> <div> wind tunnels noise boundary-layer transition conical bodies </div> <div> slender bodies Mach numbers Reynolds numbers subsonic flow </div> <div> transonic flow supersonic flow </div> </div>		
20. ABSTRACT (Continue on reverse side if necessary and identify by block number)		
<p>A study was conducted to investigate the effects of wind tunnel test section noise on the location of boundary-layer transition. The study was carried out by conducting experiments on a slender, highly polished cone with an included angle of 10 deg. Wind tunnel test section noise was measured by microphones flush-mounted on the cone surface. In most of the experiments, boundary-layer transition was measured with a surface-mounted, traversing pitot pressure probe. The experiments were conducted</p>		

UNCLASSIFIED

UNCLASSIFIED

20. ABSTRACT, Concluded.

in 23 different subsonic, transonic, and supersonic wind tunnels over a Mach number range from 0.2 to 5.5 and a unit Reynolds number range from 1.0×10^6 to 7.0×10^6 per foot, the bulk of the data being obtained between 2.0×10^6 and 4.0×10^6 per foot. The results show an influence of wind tunnel noise on boundary-layer transition for most of the wind tunnels.

AFSC
Arnold AFS Tenn

UNCLASSIFIED

PREFACE

The research reported herein was conducted by the Arnold Engineering Development Center (AEDC), Air Force Systems Command (AFSC). The results were obtained by ARO, Inc., AEDC Division (a Sverdrup Corporation Company), operating contractor for the AEDC, AFSC, Arnold Air Force Station, Tennessee, under ARO Project Numbers PW5201, PW5301, PF206, PF406, P32A-B0A, and P32A-G2A. Data presented in this report were acquired in cooperation with the NASA/Langley Aeronautical Research Center and Ames Research Center, the Naval Ship Research and Development Center, the Calspan Corporation, and three Western European governments: the United Kingdom, France, and the Netherlands. The Air Force project manager was Mr. A. F. Money, AEDC/DOTR. The manuscript was submitted for publication on February 9, 1979.

The author wishes to acknowledge contributions to this work from several persons within Sverdrup/ARO, Inc.: Dr. M. D. High, O. P. Credle, H. T. Jones, R. G. Butler, R. E. Rieben, J. A. Benek, and J. S. Hahn. The author also wishes to acknowledge the special contributions of Capt. Carlos Tirres, USAF, project manager for AEDC during most of this work. Furthermore, the author wishes to acknowledge efforts of several persons outside AEDC in the acquisition of data from many facilities, in particular: F. W. Steinle, Jr., NASA/Ames Research Center; R. L. Stallings, Jr. and J. T. Foughner, NASA/Langley Research Center; D. G. Mabey, U. K. Royal Aircraft Establishment; X. Vaucheret, Office National D'Etudes et de Recherches Aerospatiales; Dr. R. Ross, National Luchten Ruimtevaartlaboratorium (NLR); R. Jordan, Aeronautical Research Association, Ltd., U.K.; D. Davidson, Naval Ship Research and Development Center; R. de Kuyper, Calspan Corporation; and Col. D. H. Daley, USAF, while at the USAF European Office of Aerospace Research.

CONTENTS

	<u>Page</u>
1.0 INTRODUCTION	11
2.0 EXPERIMENTAL APPARATUS	
2.1 AEDC Transition Cone Model	11
2.2 Pitot Pressure Probe	12
2.3 Fluctuating Static Pressure Instrumentation	12
3.0 PRESENTATION OF DATA	12
3.1 Transition Reynolds Number	13
3.2 Test Section Noise Level	20
3.3 Wind Tunnel Group Data	20
3.3.1 Group 1 Tunnels: Subsonic and Transonic, Slotted	
NASA/Langley 8 TPT	20
NASA/Langley 16 TT	26
NASA/Langley 16 TDT	31
Naval Ship R&DC 7 x 10 T	50
NLR 6.55 x 5.28 HST	62
NASA/Ames 12 PT	65
RAE Farnborough 8 x 6	74
3.3.2 Group 2 Tunnels: Transonic, Porous	
AEDC/PWT Tunnel 4T	81
ONERA 6 x 6 S-2 Modane	101
ONERA 2.56 x 1.83 S-3 Modane	110
AEDC/PWT Tunnel 16T	116
NASA/Ames 11 TWT	128
NASA/Ames 14 TWT	157
Calspan 8 TWT	162
ARA, Ltd. Bedford 9 x 8	168
3.3.3 Group 3 Tunnels: Supersonic, Two-Dimensional Nozzle	
RAE Bedford 8 x 8 SWT	175
NASA/Langley 4 SPT	181
AEDC/PWT Tunnel 16S	187
AEDC/VKF Tunnel A	189
RAE Bedford 3 x 4 HSST	203
3.3.4 Group 4 Tunnels: Supersonic, Sliding Block Nozzle	
NASA/Ames 9 x 7 SWT	209
NASA/Langley 4 SUPWT (TS No. 1)	226
NASA/Langley 4 SUPWT (TS No. 2)	235

	<u>Page</u>
4.0 CONCLUDING REMARKS	243
REFERENCES	243

ILLUSTRATIONS

Figure

1. AEDC 10-deg Transition Cone Model	14
2. Pitot Pressure Probe Assembly	16
3. Details of Microphone Transducer Installation in Cone	17
4. Definition of Transition Locations	18
5. Photograph of the Cone Installed in the NASA/Langley 8 TPT	22
6. End-of-Transition Reynolds Numbers in the NASA/Langley 8TPT	23
7. Noise Levels in the NASA/Langley 8 TPT	24
8. Photograph of the Cone Installed in the NASA/Langley 16 TT	27
9. End-of-Transition Reynolds Numbers in the NASA/Langley 16 TT	28
10. Noise Levels in the NASA/Langley 16 TT	29
11. Photograph of the Cone Installed in the NASA/Langley 16 TDT	33
12. End-of-Transition Reynolds Numbers in the NASA/Langley 16 TDT	34
13. Onset-of-Transition Reynolds Numbers in the NASA/Langley 16 TDT	35
14. Noise Levels in the NASA/Langley 16 TDT	36
15. Comparison of Transition Locations in Air and in Freon	37
16. Comparison of Noise Levels in Air and in Freon	39
17. Power Spectral Density Measurements in the NASA/Langley 16 TDT at $M_\infty = 0.85$ (0 to 10 kHz)	40
18. Power Spectral Density Measurements in the NASA/Langley 16 TDT at $M_\infty = 1.00$ (0 to 10 kHz)	42
19. Power Spectral Density Measurements in the NASA/Langley 16 TDT at $M_\infty = 0.85$ (0 to 200 Hz)	44
20. Power Spectral Density Measurements in the NASA/Langley 16 TDT at $M_\infty = 1.00$ (0 to 200 Hz)	46
21. Photograph of the Cone Installed in the NSR&DC 7 x 10 T	51
22. End-of-Transition Reynolds Numbers in the NSR&DC 7 x 10 T	52
23. Onset-of-Transition Reynolds Numbers in the NSR&DC 7 x 10 T	53
24. Noise Levels in the NSR&DC 7 x 10 T	54
25. Power Spectral Density Measurements in the NSR&DC 7 x 10 T	55
26. Noise Levels in the NLR 6.55 x 5.28 HST	63
27. Typical Power Spectral Densities of Cone Microphone Data in the NLR 6.55 x 5.28 HST	64

<u>Figure</u>	<u>Page</u>
28. End-of-Transition Reynolds Numbers in the NASA/Ames 12 PT	66
29. Onset-of-Transition Reynolds Numbers in the NASA/Ames 12 PT	67
30. Noise Levels in the NASA/Ames 12 PT	68
31. Power Spectral Density Measurements in the NASA/Ames 12 PT	69
32. Photograph of the Cone Installed in the RAE Farnborough 8 x 6	75
33. Photograph of the Sublimation Pattern Behind the Fixed Pitot Probe Attached to the Cone Surface	76
34. Comparison of the Cone Microphone and the Fixed Pitot Probe Data in the RAE Farnborough 8 x 6	77
35. End-of-Transition Reynolds Numbers in the RAE Farnborough 8 x 6	79
36. Noise Levels in the RAE Farnborough 8 x 6	80
37. Photographs of the Cone Installed in AEDC/PWT Tunnel 4T with Tape and Wire Screen on the Tunnel Walls	83
38. End-of-Transition Reynolds Numbers in AEDC/PWT 4T	85
39. Onset-of-Transition Reynolds Numbers in AEDC/PWT 4T	88
40. Noise Levels in AEDC/PWT 4T	89
41. Fourier Spectrum Measurements in AEDC/PWT 4T	92
42. Transition Reynolds Numbers in the ONERA 6 x 6 S-2 Modane	103
43. Noise Levels in the ONERA 6 x 6 S-2 Modane Measured by the Cone Microphones	104
44. Noise Levels in the ONERA 6 x 6 S-2 Modane Measured by the Wall Microphones	105
45. Noise Levels in the ONERA 6 x 6 S-2 Modane Measured at $M_\infty = 0.80$ and 0.95 at Varied Wall Porosity	106
46. Variation in Noise Levels with U_∞/ν_∞ in the ONERA 6 x 6 S-2 Modane Measured by the Cone Microphones at $M_\infty = 0.80$ and 0.95	107
47. Fourier Spectrum Measurements in the ONERA 6 x 6 S-2 Modane	108
48. Effect of Wall Porosity Variation on the Power Spectral Density in the ONERA 6 x 6 S-2 Modane at $M_\infty = 0.80$	109
49. Noise Levels in the ONERA 2.56 x 1.83 S-3 Modane	111
50. Variation in Noise Levels with U_∞/ν_∞ in the ONERA 2.56 x 1.83 S-3 Modane at $M_\infty = 0.80$ and 0.95	112
51. Fourier Spectrum Measurements in the ONERA 2.56 x 1.83 S-3 Modane	113
52. Effects of Changing Perforated to Solid Walls on the Noise Levels in the ONERA 2.56 x 1.83 S-3 Modane	114

<u>Figure</u>	<u>Page</u>
53. Fourier Spectrum Measurement Comparisons for Closed versus Open Walls at $M_\infty = 0.70$ and 0.80 in the ONERA 2.56×1.83 S-3 Modane	115
54. End-of-Transition Reynolds Numbers in AEDC/PWT Tunnel 16T	118
55. Onset-of-Transition Reynolds Numbers in AEDC/PWT Tunnel 16T	119
56. Noise Levels in AEDC/PWT Tunnel 16T (Sting-Support Cart)	120
57. Noise Levels in AEDC/PWT Tunnel 16T (Strut-Support Cart)	121
58. Fourier Spectrum Measurements in AEDC/PWT 16T (Sting-Support Cart)	122
59. Photographs of the Cone Installation in the NASA/Ames 11 TWT	129
60. End-of-Transition Reynolds Numbers in the NASA/Ames 11 TWT at Sta. 110 in.	131
61. Onset-of-Transition Reynolds Numbers in the NASA/Ames 11 TWT at Sta. 110 in.	132
62. Noise Levels in the NASA/Ames 11 TWT at Sta. 110 in.	133
63. Typical Power Spectral Density Measurements in the NASA/Ames 11 TWT	134
64. End-of-Transition Reynolds Numbers in the NASA/Ames 11 TWT at Sta. 122 in.	141
65. Onset-of-Transition Reynolds Numbers in the NASA/Ames 11 TWT at Sta. 122 in.	142
66. Noise Levels in the NASA/Ames 11 TWT at Sta. 122 in.	143
67. End-of-Transition Reynolds Numbers in the NASA/Ames 11 TWT at Sta. 133 in.	144
68. Onset-of-Transition Reynolds Numbers in the NASA/Ames 11 TWT at Sta. 133 in.	145
69. Noise Levels in the NASA/Ames 11 TWT at Sta. 133 in.	146
70. End-of-Transition Reynolds Numbers in the NASA/Ames 11 TWT at Sta. 150 in.	147
71. Onset-of-Transition Reynolds Numbers in the NASA/Ames 11 TWT at Sta. 150 in.	148
72. Noise Levels in the NASA/Ames 11 TWT at Sta. 150 in.	149
73. End-of-Transition Reynolds Numbers in the NASA/Ames 14 TWT	158
74. Onset-of-Transition Reynolds Numbers in the NASA/Ames 14 TWT	159
75. Noise Levels in the NASA/Ames 14 TWT	160
76. End-of-Transition Reynolds Numbers in the Calspan 8 TWT	163
77. Onset-of-Transition Reynolds Numbers in the Calspan 8 TWT	163

<u>Figure</u>	<u>Page</u>
78. Noise Levels in the Calspan 8 TWT	164
79. Fourier Spectrum Measurements in the Calspan 8 TWT	165
80. Transition Locations on the Cone in the ARA, Ltd. Bedford 9 x 8	169
81. Transition Reynolds Numbers in the ARA, Ltd. Bedford 9 x 8	170
82. Noise Levels in the ARA, Ltd. Bedford 9 x 8	171
83. Fan Tone Identifications in the ARA, Ltd. Bedford 9 x 8	172
84. Fourier Spectrum Measurements in the ARA, Ltd. Bedford 9 x 8	173
85. Photograph of the Cone Installation in the RAE Bedford 8 x 8 SWT	176
86. Noise Level as a Function of U_∞/ν_∞ at $M_\infty = 0.19$ and 0.6 in the RAE Bedford 8 x 8 SWT	177
87. Noise Level as a Function of U_∞/ν_∞ at $M_\infty = 1.4$ and 2.4 in the RAE Bedford 8 x 8 SWT	179
88. End-of-Transition Reynolds Numbers in the NASA/Langley 4 SPT at $M_\infty = 1.6$	182
89. Onset-of-Transition Reynolds Numbers in the NASA/Langley 4 SPT at $M_\infty = 1.6$	182
90. Noise Levels in the NASA/Langley 4 SPT at $M_\infty = 1.6$	183
91. End-of-Transition Reynolds Numbers in the NASA/Langley 4 SPT at $M_\infty = 2.0$	184
92. Onset-of-Transition Reynolds Numbers in the NASA/Langley 4 SPT at $M_\infty = 2.0$	184
93. Noise Levels in the NASA/Langley 4 SPT at $M_\infty = 2.0$	185
94. Noise Levels in AEDC/PWT Tunnel 16S Measured on the Cone	188
95. Photograph of the Cone Installation in AEDC/VKF Tunnel A	190
96. Transition Reynolds Numbers in AEDC/VKF Tunnel A at $M_\infty \cong 1.5$	191
97. Transition Reynolds Numbers in AEDC/VKF Tunnel A at $M_\infty \cong 1.7$	192
98. Transition Reynolds Numbers in AEDC/VKF Tunnel A at $M_\infty \cong 1.96$	193
99. Transition Reynolds Numbers in AEDC/VKF Tunnel A at $M_\infty \cong 2.47$	194
100. Transition Reynolds Numbers in AEDC/VKF Tunnel A at $M_\infty \cong 2.98$	195
101. Transition Reynolds Numbers in AEDC/VKF Tunnel A at $M_\infty \cong 3.22$	196

<u>Figure</u>	<u>Page</u>
102. Transition Reynolds Numbers in AEDC/VKF Tunnel A at $M_\infty \cong 3.45$	197
103. Transition Reynolds Numbers in AEDC/VKF Tunnel A at $M_\infty \cong 4.05$	198
104. Transition Reynolds Numbers in AEDC/VKF Tunnel A at $M_\infty \cong 4.48$	199
105. Transition Reynolds Numbers in AEDC/VKF Tunnel A at $M_\infty \cong 5.05$	200
106. Noise Levels as a Function of U_∞/ν_∞ at $M_\infty = 2.5$ in the RAE Bedford 3 x 4 HSST	204
107. Noise Levels as a Function of U_∞/ν_∞ at $M_\infty = 3.0$ in the RAE Bedford 3 x 4 HSST	205
108. Noise Levels as a Function of U_∞/ν_∞ at $M_\infty = 3.5$ in the RAE Bedford 3 x 4 HSST	206
109. Noise Levels as a Function of U_∞/ν_∞ at $M_\infty = 4.0$ in the RAE Bedford 3 x 4 HSST	207
110. Noise Levels as a Function of U_∞/ν_∞ at $M_\infty = 4.5$ in the RAE Bedford 3 x 4 HSST	208
111. Photograph of the Cone Installation in the NASA/Ames 9 x 7 SWT	210
112. Transition Reynolds Numbers at $M_\infty = 1.5$ in the NASA/Ames 9 x 7 SWT	211
113. Transition Reynolds Numbers at $M_\infty = 1.6$ in the NASA/Ames 9 x 7 SWT	212
114. Transition Reynolds Numbers at $M_\infty = 1.7$ in the NASA/Ames 9 x 7 SWT	213
115. Transition Reynolds Numbers at $M_\infty = 1.8$ in the NASA/Ames 9 x 7 SWT	214
116. Transition Reynolds Numbers at $M_\infty = 2.0$ in the NASA/Ames 9 x 7 SWT	215
117. Transition Reynolds Numbers at $M_\infty = 2.2$ in the NASA/Ames 9 x 7 SWT	216
118. Transition Reynolds Numbers at $M_\infty = 2.5$ in the NASA/Ames 9 x 7 SWT	217
119. Composite Envelope of End-of-Transition Reynolds Numbers in the NASA/Ames 9 x 7 SWT	218
120. Noise Levels in the NASA/Ames 9 x 7 SWT	219
121. Photograph of the Cone Installation in the NASA/Langley 4 SUPWT (TS No. 1)	227

<u>Figure</u>	<u>Page</u>
122. Transition Reynolds Numbers at $M_\infty = 1.6$ in the NASA/Langley 4 SUPWT (TS No. 1)	228
123. Transition Reynolds Numbers at $M_\infty = 2.0$ in the NASA/Langley 4 SUPWT (TS No. 1)	229
124. Transition Reynolds Numbers at $M_\infty = 2.86$ in the NASA/Langley 4 SUPWT (TS No. 1)	230
125. Noise Levels at $M_\infty = 1.6$ in the NASA/Langley 4 SUPWT (TS No. 1)	231
126. Noise Levels at $M_\infty = 2.0$ in the NASA/Langley 4 SUPWT (TS No. 1)	232
127. Noise Levels at $M_\infty = 2.86$ in the NASA/Langley 4 SUPWT (TS No. 1)	233
128. Transition Reynolds Numbers at $M_\infty = 2.86$ in the NASA/Langley 4 SUPWT (TS No. 2)	236
129. Transition Reynolds Numbers at $M_\infty = 3.5$ in the NASA/Langley 4 SUPWT (TS No. 2)	237
130. Transition Reynolds Numbers at $M_\infty = 4.6$ in the NASA/Langley 4 SUPWT (TS No. 2))	238
131. Noise Levels at $M_\infty = 2.86$ in the NASA/Langley 4 SUPWT (TS No. 2) . . .	239
132. Noise Levels at $M_\infty = 3.5$ in the NASA/Langley 4 SUPWT (TS No. 2)	240
133. Noise Levels at $M_\infty = 4.6$ in the NASA/Langley 4 SUPWT (TS No. 2)	241

TABLES

1. Summary of Wind Tunnel Characteristics	19
2. NASA/Langley 8 TPT Data	25
3. NASA/Langley 16 TT Data	30
4. NASA/Langley 16 TDT Data	48
5. Naval Ship R&DC 7 x 10 T Data	60
6. NASA/Ames 12 PT Data	73
7. AEDC/PWT Tunnel 4T Data	93
8. AEDC/PWT Tunnel 16T Data	123
9. NASA/Ames 11 TWT Data	150
10. NASA/Ames 14 TWT Data	161
11. Calspan 8 TWT Data	167
12. NASA/Langley 4 SPT Data	186
13. AEDC/VKF Tunnel A Data	201
14. NASA/Ames 9 x 7 SWT Data	224

<u>Table</u>	<u>Page</u>
15. NASA/Langley 4 SUPWT (TS No. 1) Data	234
16. NASA/Langley 4 SUPWT (TS No. 2) Data	242
NOMENCLATURE	245

1.0 INTRODUCTION

Research on the behavior of laminar boundary-layer transition under varying flow conditions and differing model geometric configurations has been conducted at the Arnold Engineering Development Center (AEDC) for many years (Ref. 1). For the most part, the research has been experimental and has focused on the macroscopic behavior of boundary-layer transition at supersonic and hypersonic speeds in a search for the effects of model roughness, geometry (such as bluntness), and facility environment. One of the problems that came to the forefront during this research was that of a single test model's having different measured transition locations depending upon the wind tunnel in which the model was tested. Pate and Schueler (Ref. 2) were able to shed considerable light on this anomaly by demonstrating that each facility test section flow environment had a definite effect on transition location and that this effect manifested itself through the acoustic disturbances (noise) that are radiated from the turbulent boundary layer on the test section walls. This effect was demonstrated on both planar and conical models over a Mach number range from about 3.0 to 8.0.

Because it was evident that flow environment influenced transition, and since it was known that some subsonic and transonic wind tunnels were "noisier" than supersonic wind tunnels, a natural extension of the research was to investigate the effects of flow environment and noise level on a standard geometry model at lower Mach numbers. This report presents the results obtained from an investigation of transition location and test section noise levels covering a Mach number range from 0.2 to 5.5 on a conical model tested in 23 different wind tunnels. The report consists of two volumes: Volume I, "Experimental Methods and Summary of Results"; and Volume II, "Tabulated and Plotted Data."

2.0 EXPERIMENTAL APPARATUS

A complete discussion of the experimental apparatus and calibration procedures is given in Volume I of this report; however, for the sake of completeness a brief description of the experimental apparatus is given in this section.

2.1 AEDC TRANSITION CONE MODEL

All the measured boundary-layer transition locations and test section noise levels were obtained on a 10-deg included angle, sharp, slender cone with a highly polished surface. Details of the cone model and its associated hardware including the traversing pitot pressure probe used to detect transition are shown in Fig. 1. Flush mounted in the cone surface were two sensors sensitive to static pressure fluctuations. During the majority of the experiments these sensors were Bruel and Kjaer[®] microphones, but on a few occasions Kulite[®] pressure transducers were used.

2.2 PITOT PRESSURE PROBE

A schematic and photograph of the pitot pressure probe that was used to detect the location of boundary-layer transition are shown in Fig. 2. One important feature that should be noted concerning the probe is that extreme care was taken during all of the experiments 1) to maintain the small and precise tube opening and 2) to ensure that the probe tip maintained very good and smooth contact with the cone surface at all times.

2.3 FLUCTUATING STATIC PRESSURE INSTRUMENTATION

A schematic giving details of the microphone installation is shown in Fig. 3. It was assumed that acoustic radiation generated within the wind tunnel test section reached the cone microphones and was unattenuated, provided that a laminar boundary layer existed over the microphones. This surface-measuring technique followed the techniques employed in the investigations reported in Ref. 2.

3.0 PRESENTATION OF DATA

This section is devoted to presenting the detailed data acquired during experiments conducted in the wind tunnels listed in Table 1. The presentation of the data is grouped according to Table 1 and contains the following information for each wind tunnel:

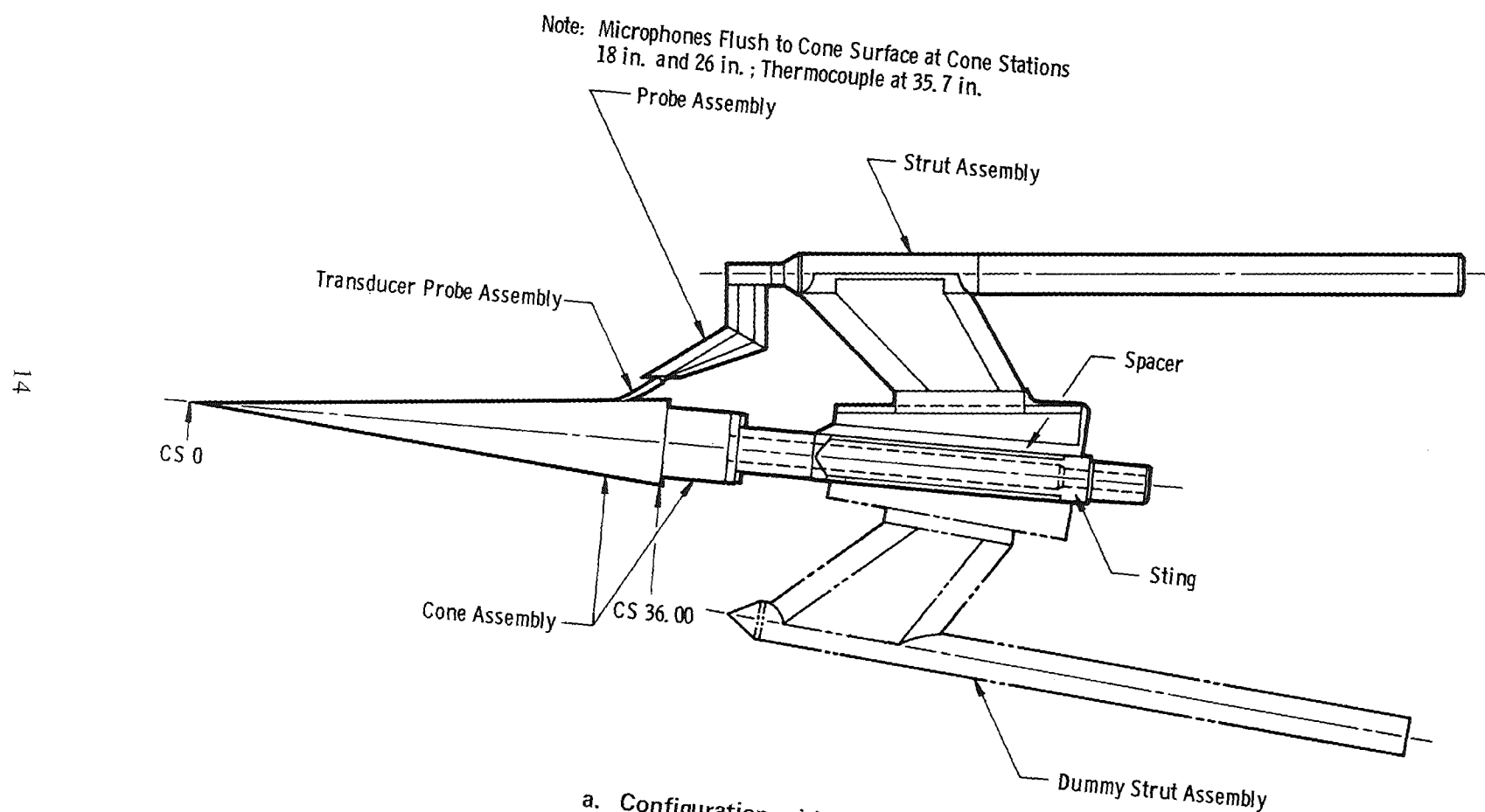
1. Range of experimental conditions covered
2. Description of any peculiar problems that rendered the data acquired questionable
3. Brief discussion of data trends
4. Plotted data
5. Tabulation of data (where possible)

Transition Reynolds numbers were computed from the measured values of x_t and X_T at each test condition using U_∞/ν_∞ and M_∞ rather than the less certain local boundary-layer edge conditions. The resulting values of Re_t and Re_T , along with the measured ΔC_p and test conditions, are presented in tabular form. However, in order to have a more consistent basis of comparison and to reduce random scatter in the comparison data, the transition and ΔC_p data from each tunnel were manually smoothed (when sufficient data existed) as a function of either U_∞/ν_∞ or M_∞ . The values of Re_t , Re_T , X_t , X_T , and ΔC_p shown in the data figures of this report were obtained from the smoothed data fairings. Where ΔC_p data are given and no reference is made as to whether

the data are from the forward or aft microphone, the values from the lower of the two are presented.

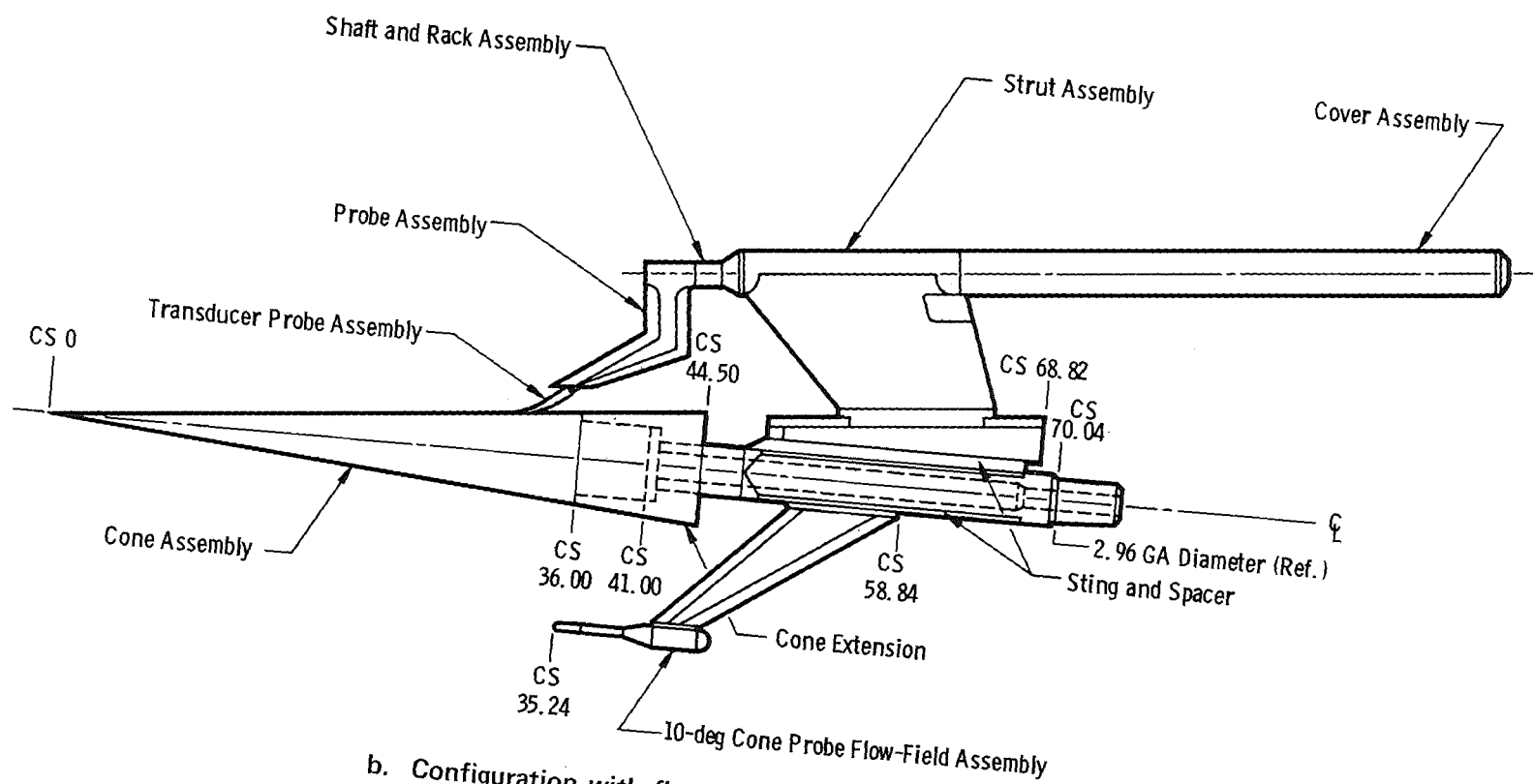
3.1 TRANSITION REYNOLDS NUMBER

One of the two principal results obtained was the measurement of the location of transition. Detailed definitions of the points of transition are given in Volume I; however, Fig. 4 is shown to illustrate the points as defined from a typical pitot pressure probe traverse through transition. No argument is given as to which point actually represents what part of the transition process, but the point X_T is defined as the end of transition in terms of a transition Reynolds number, Re_T , and is used as the primary variable in this report. The point X_t is defined as the onset of transition in terms of a transition Reynolds number, Re_t . In general, Re_t could not be defined with as good a fidelity as Re_T using the pitot probe because of the relatively smaller laminar thickness.

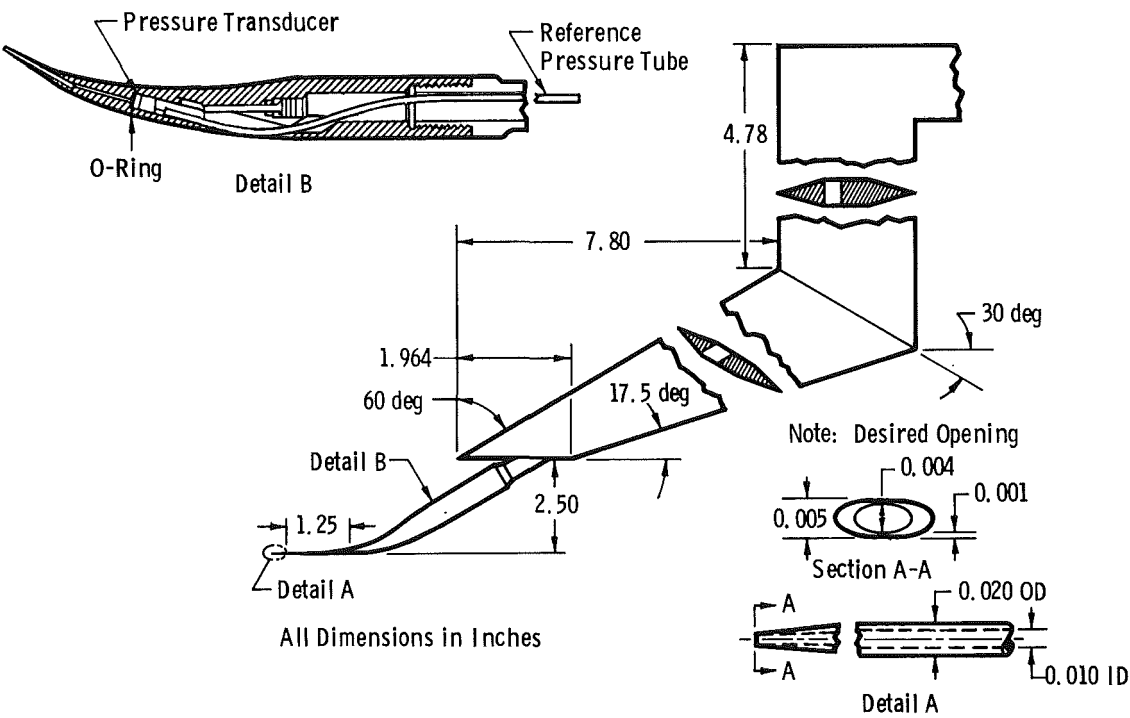


a. Configuration with dummy strut
Figure 1. AEDC 10-deg transition cone model.

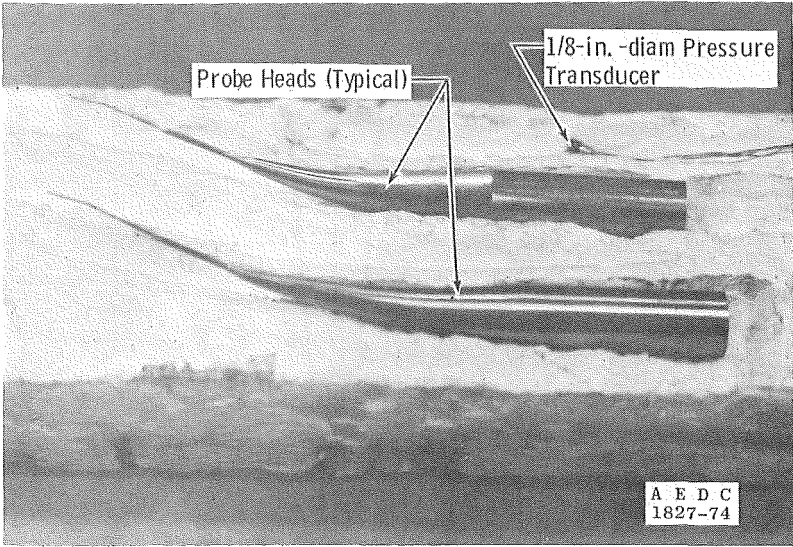
15



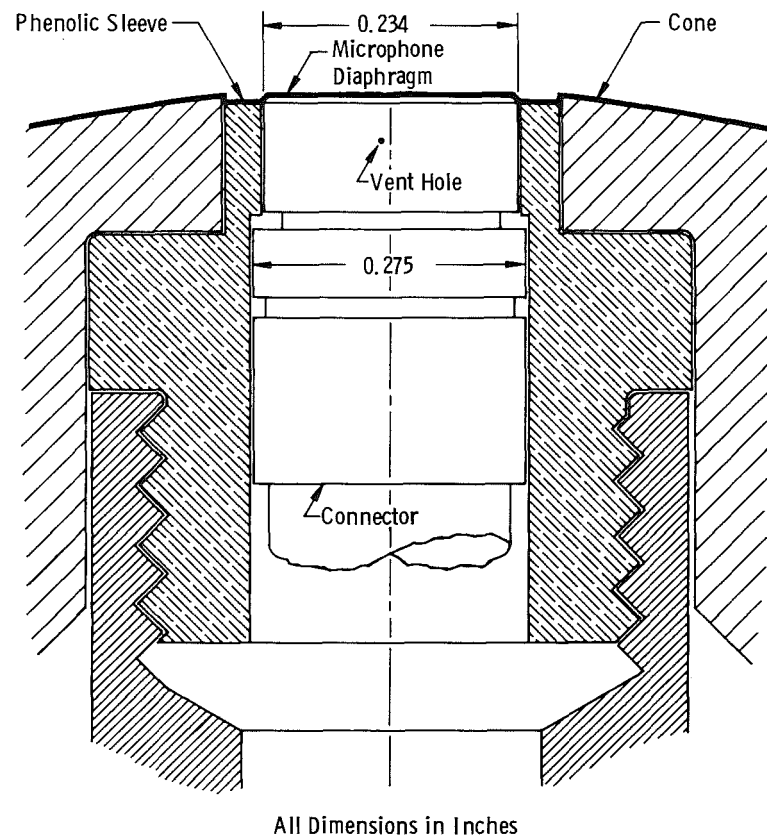
b. Configuration with flow angle probe and cone extension
Figure 1. Concluded.



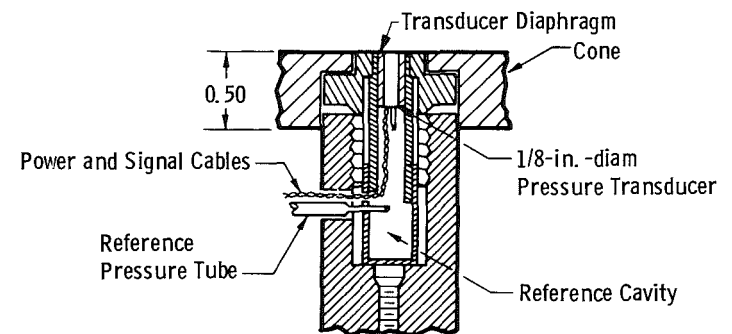
a. Schematic diagram



b. Photograph of probes and transducer
Figure 2. Pitot pressure probe assembly.



a. Microphone installation details at $x_1 = 18$ in.



b. Transducer installation details at $x_1 = 18$ in.

Figure 3. Details of microphone transducer installation in cone.

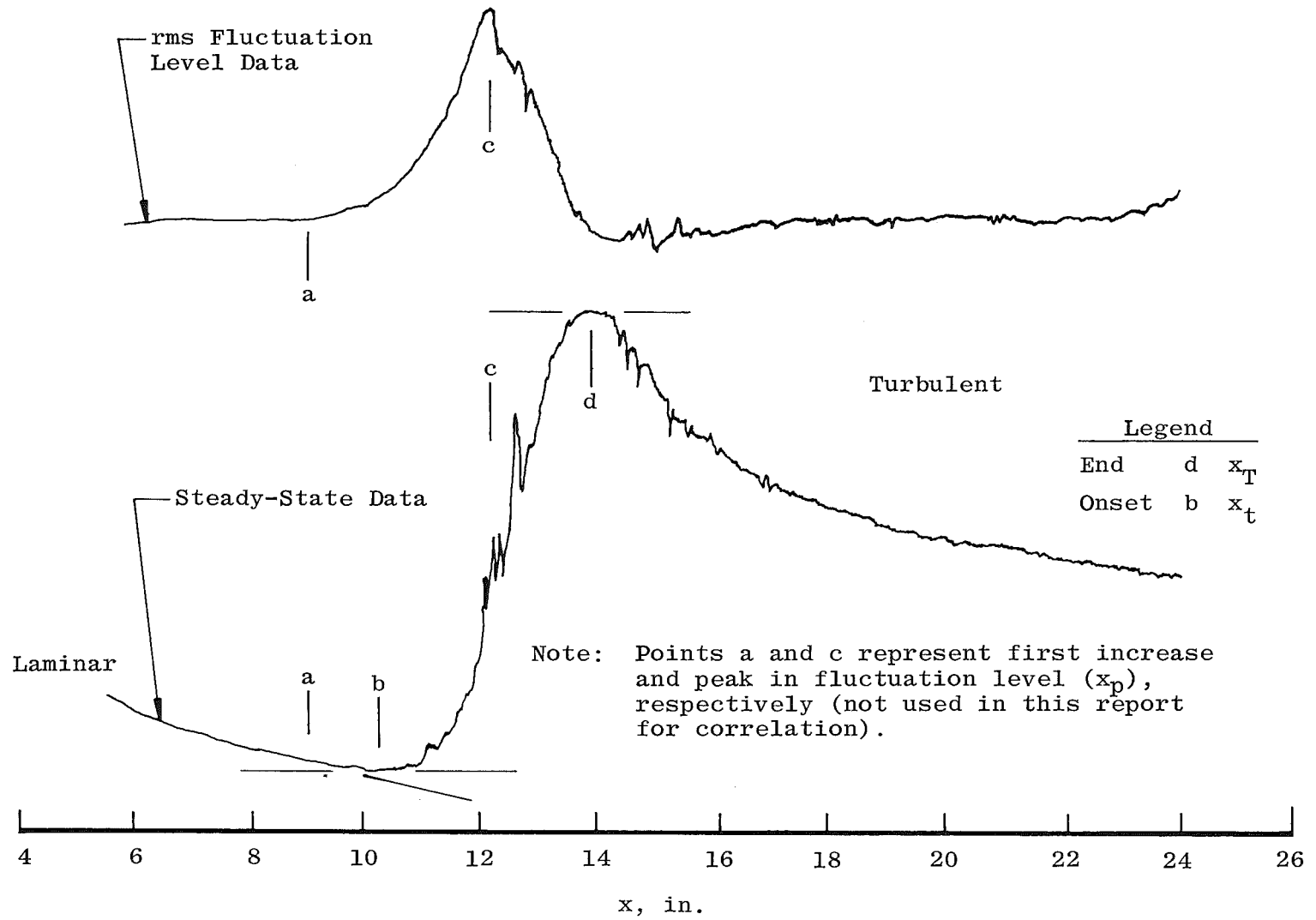


Figure 4. Definition of transition locations.

Table 1. Summary of Wind Tunnel Characteristics

Group	Tunnel	Distinguishing Geometry	Mach Number Range	Unit Reynolds Number Range x 10 ⁻⁶	Predominant Disturbances	Resonant Mach Number	ΔC_{pmax} , percent	On-Line Recording Bandwidth of ΔC_p ⁷	Method of ΔC_p Correction for Microphone Resonance ⁸
1	NASA/Langley 8 TPT	Slotted Wall	0.25 - 1.20	2.0 - 3.0	Low Frequency	0.80	2.20	0 - 60 kHz	No Corrections
	NASA/Langley 16 TT	Slotted Wall	0.20 - 1.30	1.3 - 3.9	Low Frequency	0.82	3.60	0 - 60 kHz	No Corrections
	NASA/Langley 16 TDT (Freon) ¹	Slotted Wall	0.30 - 1.15	1.5 - 3.7	Low Frequency	0.85	1.40	50 Hz - 60 kHz	No Corrections
	NSR&DC 7 x 10 T	Slotted Wall	0.20 - 1.13	1.5 - 4.0	Low Frequency	0.75	1.26	50 Hz - 60 kHz	No Corrections
	NLR 6.55 x 5.28 HST ²	Slotted Wall	0.15 - 1.30	1.5 - 1.4	Compressor	0.80	1.01	50 Hz - 60 kHz	No Corrections
	RAE Farnborough 8 x 6 ^{3,6}	Slotted Wall	0.20 - 1.19	0.4 - 2.5	Compressor	0.60	1.90	200 Hz - 60 kHz	No Corrections
	NASA/Ames 12 PT	Solid Wall	0.20 - 0.90	2.0 - 3.0	Test Section	0.65	1.65	50 Hz - 60 kHz	No Corrections
	RAE Bedford 8 x 8 SWT (Subsonic Mode)	Solid Wall	0.20 - 0.80	0.25 - 3.0	---	None	0.80	50 Hz - 60 kHz	No Corrections
2	AEDC/PWT Tunnel 4T	Perforated Wall	0.40 - 1.30	1.5 - 5.0	Edgetones	0.80/1.30	3.75	50 Hz - 60 kHz	No Corrections
	ONERA 6 x 6 S-2 Modane	Perforated Wall	0.25 - 1.30	2.0 - 7.2	Edgetones	0.80	2.77	50 Hz - 60 kHz	No Corrections
	ONERA 2.56 x 1.83 S-3 Modane ^{2,6}	Perforated Wall	0.25 - 1.00	2.0 - 12.5	Stilling Chamber	0.25	12.7	50 Hz - 60 kHz	No Corrections
	AEDC/PWT Tunnel 16T	Perforated Wall	0.20 - 1.60	1.0 - 5.6	Edgetones	0.71	2.68	50 Hz - 60 kHz	See Footnote 8
	NASA/Ames 11 TWT	Corrugated-Slot Wall	0.40 - 1.20	1.5 - 6.0	Slot Organ Pipe	0.75	2.00	50 Hz - 60 kHz	No Corrections
	NASA/Ames 14 TWT	Corrugated-Slot Wall	0.40 - 1.05	2.6 - 4.0	Slot Organ Pipe	0.95	2.05	50 Hz - 60 kHz	No Corrections
	Calspan 8 TWT	Perforated Wall	0.60 - 0.95	2.0 - 3.0	Wall Tones	0.85	2.10	50 Hz - 60 kHz	No Corrections
	ARA, Ltd. Bedford 9 x 8 ⁴	Perforated Wall	0.21 - 1.40	1.5 - 4.4	Wall Tones	0.68	2.65	50 Hz - 60 kHz	No Corrections
3	RAE Bedford 8 x 8 SWT ⁵	Converg/Diverg Nozzle	1.40 - 2.40	0.6 - 4.0	Wall Boundary Layer	None	0.45	50 Hz - 60 kHz	See Footnote 8
	NASA/Langley 4 SPT	Converg/Diverg Nozzle	1.61 - 2.01	1.0 - 5.0	Wall Boundary Layer	None	0.12	50 Hz - 60 kHz	See Footnote 8
	AEDC/PWT Tunnel 16S ⁶	Converg/Diverg Nozzle	1.67 - 2.20	0.9 - 2.2	Wall Boundary Layer	None	0.50	0 - 60 kHz	No Corrections
	AEDC/VKF Tunnel A	Converg/Diverg Nozzle	1.51 - 5.50	2.3 - 6.8	Wall Boundary Layer	None	---	---	---
	RAE Bedford 3 x 4 HSST	Converg/Diverg Nozzle	2.50 - 4.50	0.7 - 9.2	Wall Boundary Layer	None	0.20	50 Hz - 60 kHz	See Footnote 8
4	NASA/Ames 9 x 7 SWT	Sliding-Block Nozzle	1.50 - 2.50	2.0 - 4.5	Wall Boundary Layer	None	0.18	50 Hz - 30 kHz	Cutoff Filter at 30 kHz
	NASA/Langley 4 SUPWT (TS No. 1)	Sliding-Block Nozzle	1.60 - 2.86	1.5 - 5.0	Wall Boundary Layer	None	0.14	50 Hz - 60 kHz	See Footnote 8
	NASA/Langley 4 SUPWT (TS No. 2)	Sliding-Block Nozzle	2.86 - 4.60	1.5 - 6.5	Wall Boundary Layer	None	0.24	50 Hz - 60 kHz	Cutoff Filter at 30 kHz

¹Tests performed using both Freon and air as tunnel working fluid.

²Only noise data, no transition data.

³Results affected by model surface imperfections during this test.

⁴Transition data at Mach numbers from 0.2 to 0.6 only.

⁵Data acquired in Mach number range from 0.2 to 0.8 also.

⁶Data not included in Volume I but presented in Volume II.

⁷Effective bandwidth varies with sensor type, use of filters, and corrections for sensor diaphragm resonance when appropriate.

⁸Corrected per Table 1, AEDC-TR-78-44, Vol. I.

3.2 TEST SECTION NOISE LEVEL

The second principal result obtained was the recording of test section noise level as measured by the cone surface microphones. The fluctuations were reduced to an rms level (called herein "noise level") and normalized by the dynamic pressure. The normalized rms pressure is given by the notation ΔC_p and is shown in percent except where otherwise noted ($\Delta C_p = \sqrt{\overline{p'^2}}/q_\infty \times 100$). In some cases the spectral composition of the data recorded by the microphones is also given.

The effective online bandwidths over which ΔC_p was recorded varied with choice of either Bruel and Kjaer or Kulite sensors, use of filters, or corrections applied for sensor diaphragm resonance. The effective bandwidth is given together with maximum ΔC_p ($\Delta C_{p_{max}}$) in Table 1, together with the applicable method of handling sensor resonance. When the resonant frequency was below approximately 60 kHz, dependent upon tunnel free-stream static pressure, p_∞ , corrections were applied to remove the resonance. These corrections are described in Volume I of this report.

3.3 WIND TUNNEL GROUP DATA

This section contains the data presentation as described in the preceding discussion.

3.3.1 Group 1 Tunnels: Subsonic and Transonic, Slotted

NASA/Langley 8 TPT

Data were acquired in this tunnel at two values of U_∞/ν_∞ , 2.0×10^6 and 3.0×10^6 per foot. The total temperature, T_t , was held at a near-constant 580°R , and the total pressure, p_t , was varied as M_∞ was varied. Difficulties were experienced during the test in maintaining good contact of the pitot probe with the cone surface. Consequently, although some of the onset-of-transition data were lost, the end-of-transition measurements all appeared to be valid and are the only data presented.

The installation of the cone in this tunnel is shown in Fig. 5. The variation of Re_T with M_∞ at constant U_∞/ν_∞ is shown in Fig. 6. At $M_\infty \geq 0.9$, Re_T was slightly higher at $U_\infty/\nu_\infty = 3.0 \times 10^6$. The variation in ΔC_p with M_∞ is shown in Fig. 7. The data are listed in Table 2. The ΔC_p measurements were made with Kulite pressure transducers in place of the Bruel and Kjaer microphones.

The ΔC_p data in Fig. 7 indicate a localized peak in normalized overall noise level occurring at $M_\infty = 0.80$ and highest level at $M_\infty = 0.25$. Spectral analysis of noise data indicated that the peak in noise amplitude near $M_\infty = 0.8$ was associated with an increase in amplitude of spectral components in the 200 to 300-Hz range. There was also a

concentration of narrow-band energy near 4.8 and 10.2 kHz. Below approximately $M_\infty = 0.7$, the spectra were dominated by a discrete tone (narrow-band energy concentration) which increased from about 3.0 to about 6.5 kHz as M_∞ was increased from 0.25 to 0.5. For $M_\infty \geq 0.7$, the tone diminished in relative amplitude to the broadband background level.



Figure 5. Photograph of the cone installed in the NASA/Langley 8 TPT.

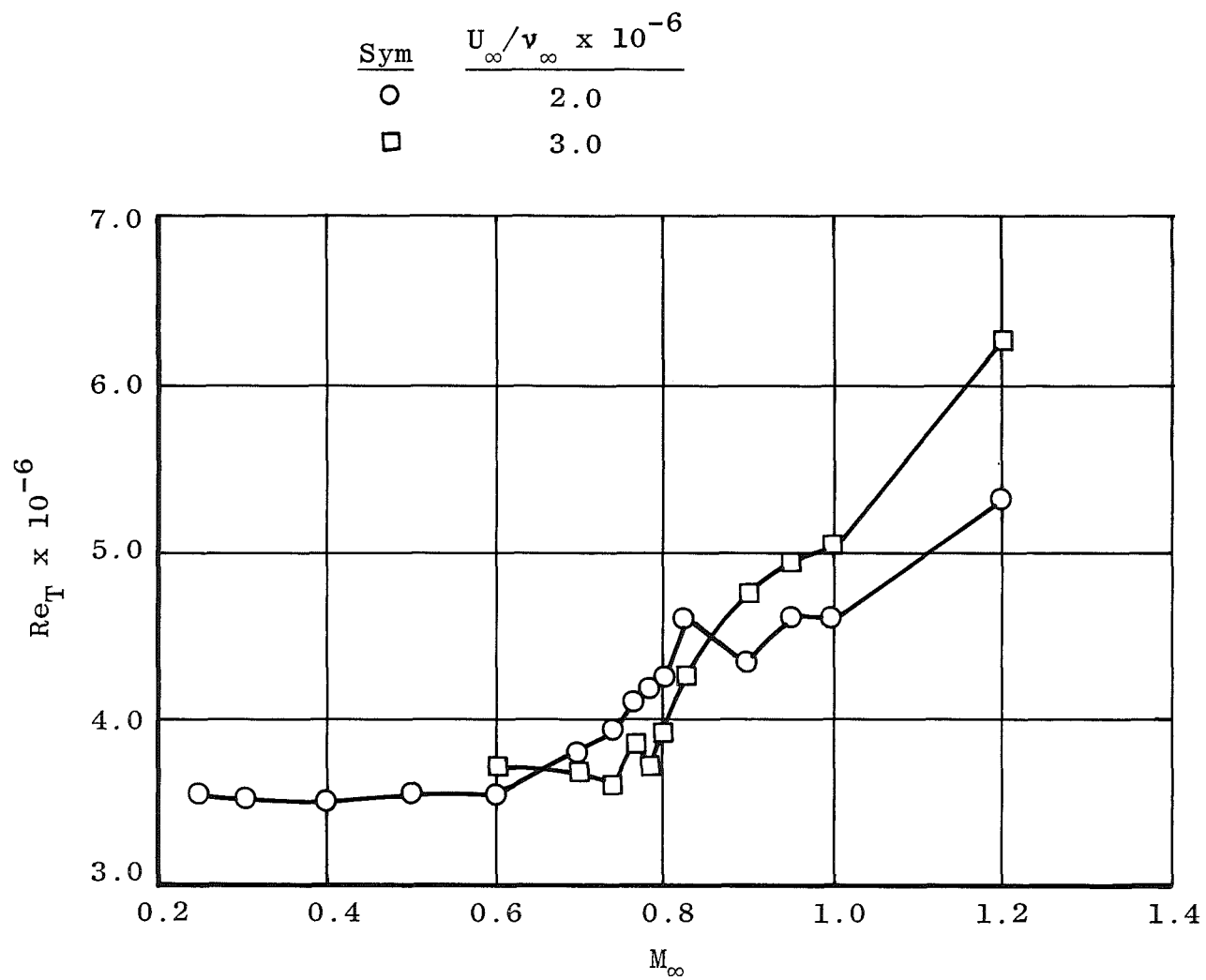


Figure 6. End-of-transition Reynolds numbers in the NASA/Langley 8 TPT.

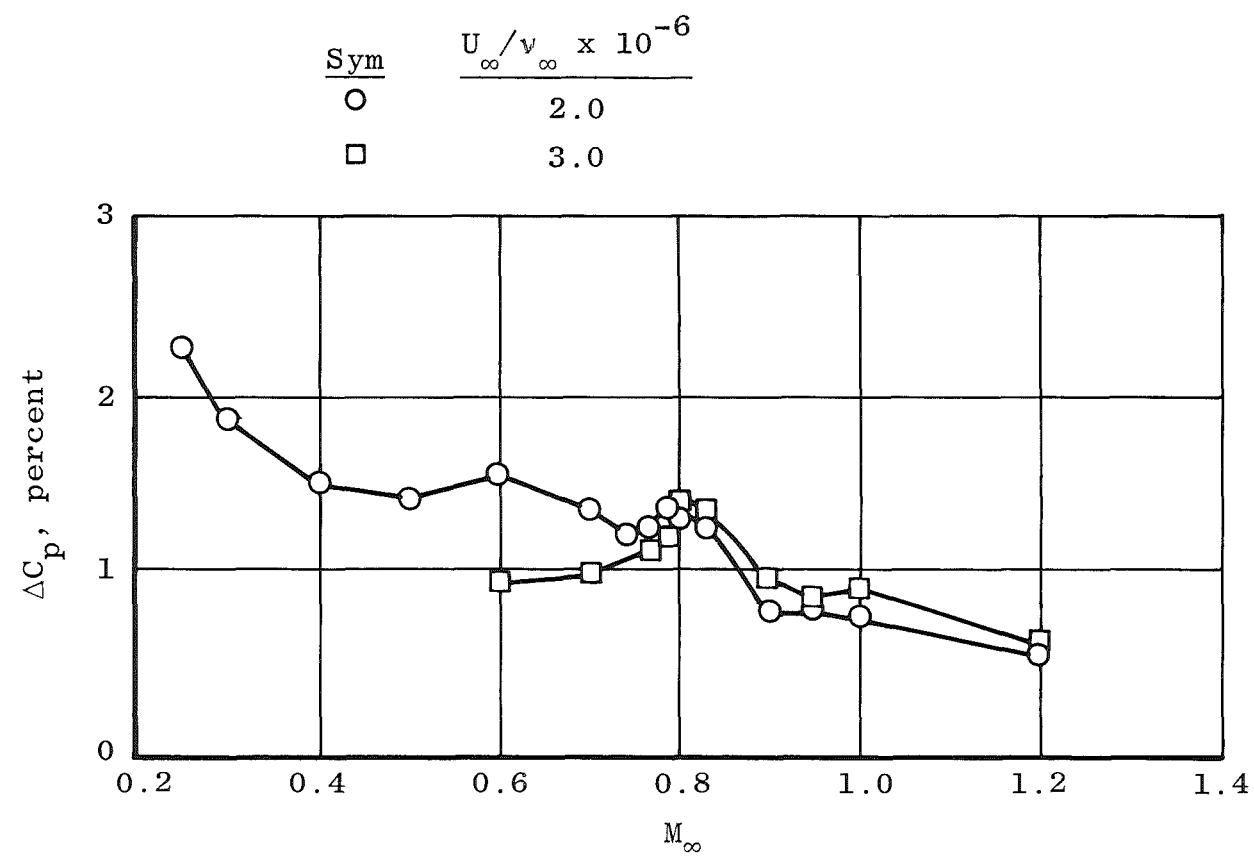


Figure 7. Noise levels in the NASA/Langley 8 TPT.

Table 2. NASA/Langley 8 TPT Data

M_∞	U_∞/v_∞ $\times 10^{-6}$	ΔC_p , percent	$Re_T \times$ 10^{-6}
0.25	2.02	2.27	3.53
0.30	2.01	1.88	3.52
0.40	2.01	1.51	3.50
0.50	2.01	1.43	3.55
0.60	2.00	1.57	3.53
0.70	2.00	1.38	3.77
0.74	2.00	1.26	3.92
0.77	2.00	1.29	4.10
0.79	2.00	1.37	4.18
0.80	2.00	1.32	4.24
0.83	2.00	1.29	4.60
0.90	2.00	0.81	4.33
0.95	2.00	0.81	4.61
1.00	2.00	0.79	4.60
1.20	2.00	0.56	5.30
0.60	3.00	0.98	3.73
0.70	3.00	1.02	3.67
0.74	3.00	—	3.65
0.77	3.00	1.16	3.84
0.79	3.00	1.19	3.72
0.80	3.00	1.41	3.90
0.83	3.00	1.37	4.25
0.90	3.00	1.00	4.75
0.95	3.01	0.90	4.84
1.00	3.00	0.95	5.02
1.20	3.00	0.65	6.25

NASA/Langley 16 TT

Total pressure, p_t , was held essentially constant at 2,120 psfa, and the total temperature, T_t , varied from 545 to 620°R as M_∞ increased from 0.2 to 1.3. The respective variation in U_∞/ν_∞ was from 1.3×10^6 to 3.9×10^6 per foot. The same problem that occurred in the NASA/Langley 8 TPT, that of poor pitot probe contact with the cone surface, occurred in this tunnel, invalidating the onset-of-transition measurements. Accordingly, only end-of-transition Reynolds numbers, Re_T , are presented.

The installation of the cone in the tunnel is shown in Fig. 8. Transition Reynolds numbers, Re_T , are shown as a function of M_∞ in Fig. 9. The variation in ΔC_p with M_∞ is shown in Fig. 10. The tabulated data are included in Table 3.

Maximum ΔC_p occurs in this tunnel at the lowest M_∞ , 0.2. There is a localized peak at $M_\infty = 0.85$. The measurements of ΔC_p were made using Kulite pressure transducers instead of Bruel and Kjaer microphones. The noise spectra had greatest amplitudes at low frequencies, 200 Hz and below. There was a narrow-band concentration of noise at 6 kHz at $M_\infty = 0.3$, which increased to approximately 8 kHz at $M_\infty = 0.4$. This particular tone may be associated with the variable-speed, two-stage, counter-rotating fan since its relative amplitude diminishes to the background level as M_∞ increases. There was another narrow-band concentration of spectral energy near 10 kHz at $M_\infty = 0.85$.

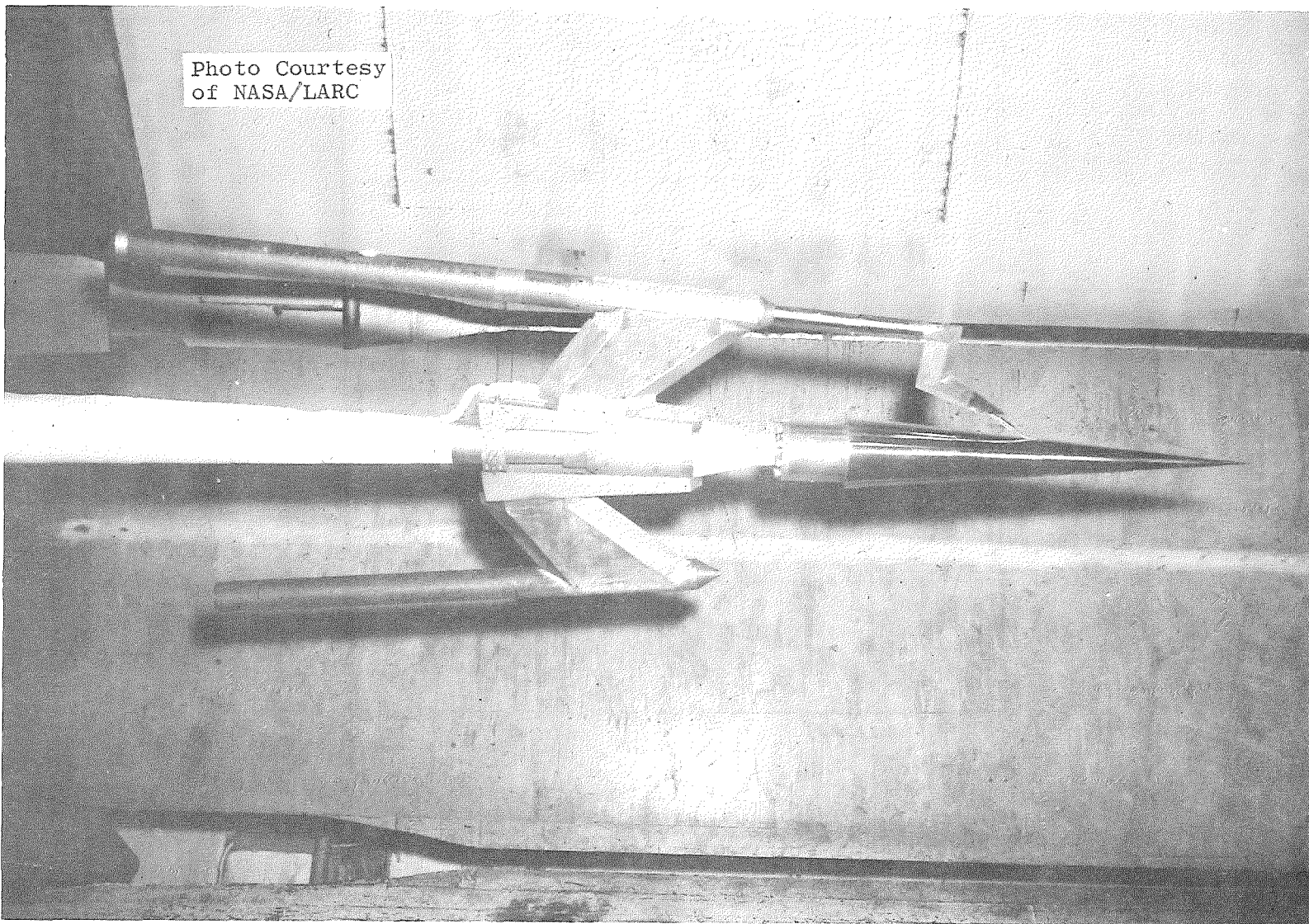


Figure 8. Photograph of the cone installed in the NASA/Langley 16 TT.

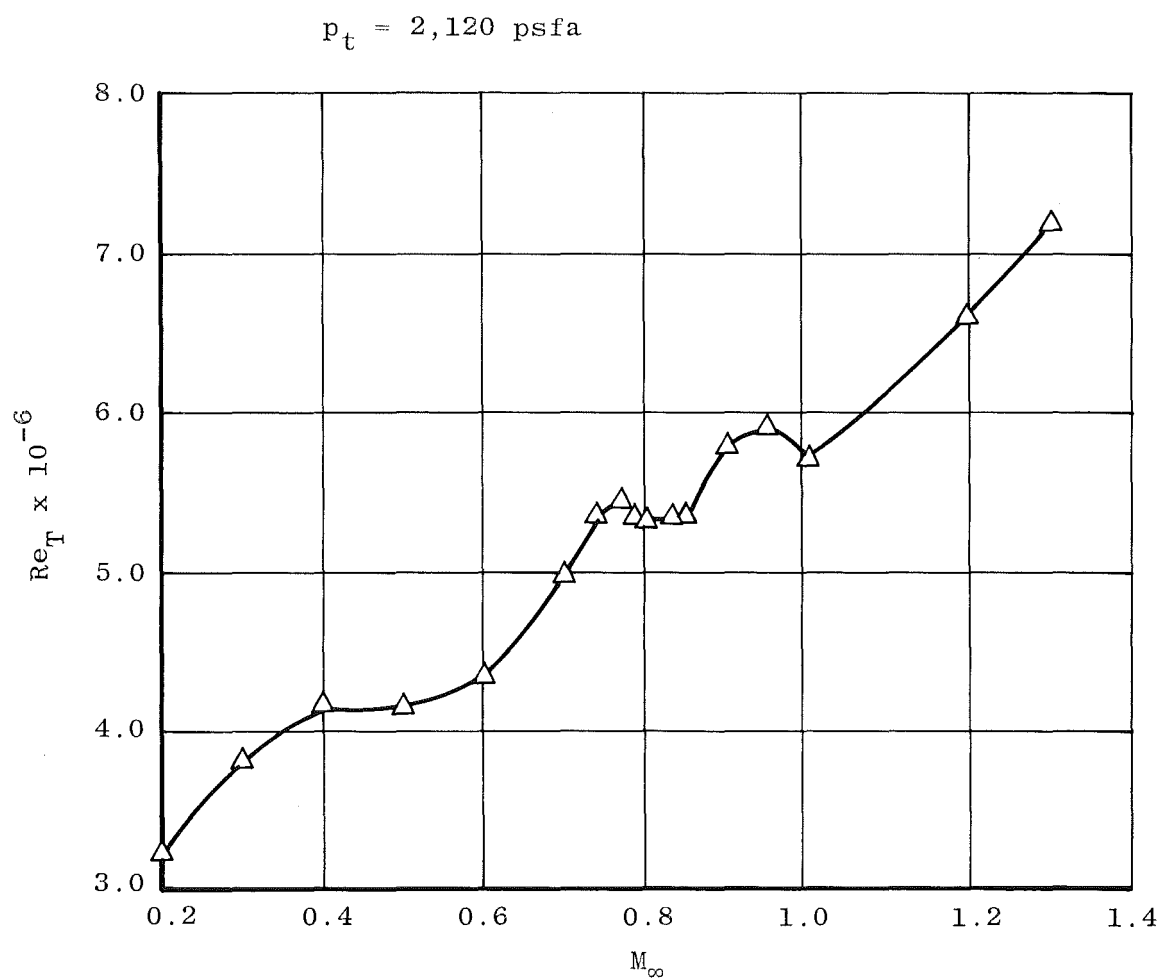


Figure 9. End-of-transition Reynolds numbers in the NASA/Langley 16 TT.

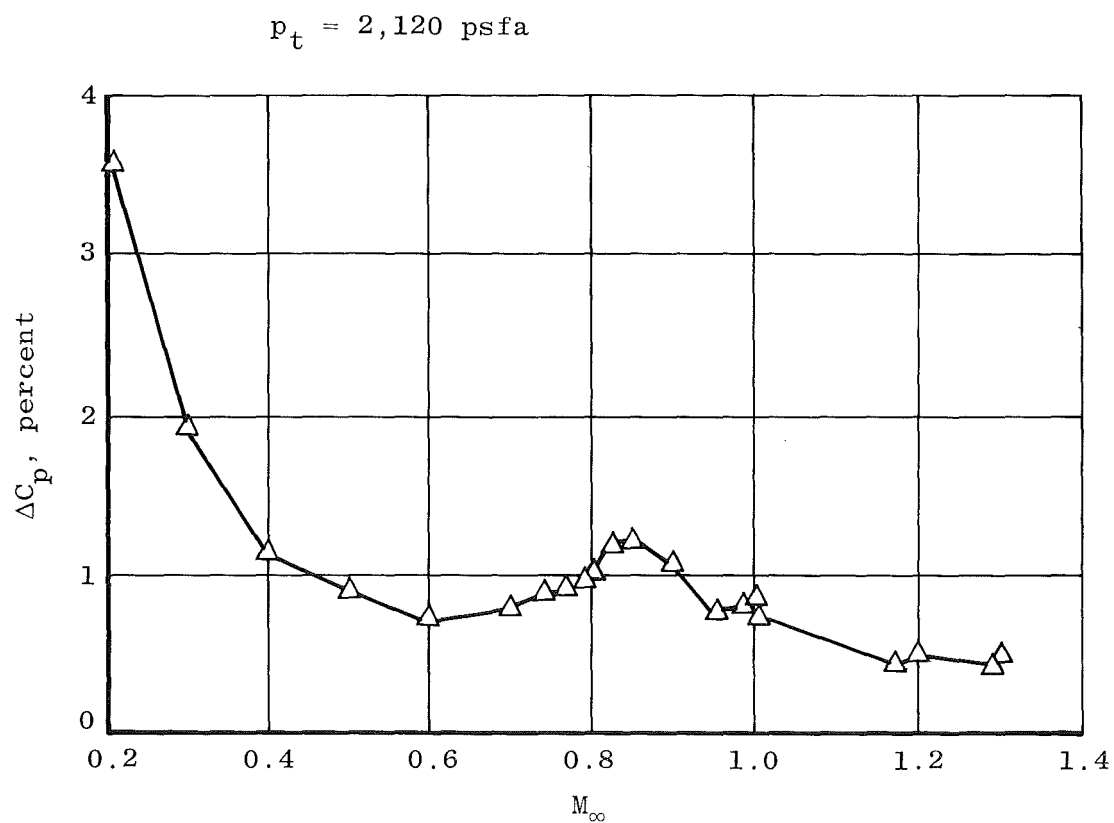


Figure 10. Noise levels in the NASA/Langley 16 TT.

Table 3. NASA/Langley 16 TT Data

M_∞	U_∞/v_∞ $\times 10^{-6}$	ΔC_p , percent	$Re_T \times$ 10^{-6}
0.20	1.283	3.57	3.21
0.30	1.906	1.95	3.81
0.40	2.456	1.16	4.13
0.50	2.921	0.93	4.14
0.60	3.276	0.74	4.34
0.70	3.526	0.81	4.97
0.74	3.597	0.91	5.34
0.77	3.634	0.94	5.45
0.79	3.654	0.99	5.33
0.80	3.667	1.04	5.32
0.83	3.687	1.21	5.34
0.85	3.711	1.24	5.35
0.90	3.757	1.10	5.79
0.95	3.779	0.81	5.92
1.02	3.733	0.88	5.72
1.20	3.808	0.51	6.75
1.30	3.850	0.48	7.16

NASA/Langley 16 TDT

Data were acquired in the NASA/Langley 16 TDT using both air and Freon as the working medium. An overlapping range of U_∞/ν_∞ using the two fluid media was obtained in the range of M_∞ from 0.3 to 0.5, permitting a unique opportunity to compare transition Reynolds numbers in two fluids at matched flow conditions. The overlapping in U_∞/ν_∞ was accomplished by appropriate p_t adjustments, holding T_t essentially constant. Because of the limitations on compressor drive power with air, there was insufficient Reynolds number capability to cause complete transition to occur on the cone for $M_\infty \geq 0.6$. However, transition data could be acquired in Freon over the full operating range up to $M_\infty = 1.15$.

The data acquired in the NASA/Langley 16 TDT are shown in Table 4. The installation of the cone in the tunnel is shown in Fig. 11. End-of-transition Reynolds numbers are shown as a function of M_∞ for selected values of U_∞/ν_∞ in Fig. 12. Onset-of-transition Reynolds numbers are shown for the same conditions in Fig. 13. The data in Figs. 12 and 13 were taken using Freon as the working fluid. Presented in Fig. 14 are values of ΔC_p as a function of M_∞ for three values of p_t which gave U_∞/ν_∞ values within the range for which the transition data are presented. The ΔC_p data, Re_T and Re_t , all appear to have been invariant with U_∞/ν_∞ (p_t) in this tunnel over the full range of M_∞ . There was a sharply defined peak in ΔC_p at $M_\infty = 0.85$.

A comparison of transition data obtained in air and Freon is shown in Fig. 15 for M_∞ from 0.3 to 0.5, including locations of the onset, X_t , and end of transition, X_T . These data indicate that for low-speed flow, transition Reynolds numbers were essentially the same for air and Freon. A comparison of the ΔC_p data for M_∞ from 0.3 to 0.6 in air and Freon is shown in Fig. 16 where ΔC_p is shown as a function of M_∞ for constant p_t , and the results are seen to be essentially the same for air and Freon.

The noise spectra in this tunnel using Freon were dominated by disturbances very low in frequency. Selected power density spectra for $M_\infty = 0.85$ and 1.00 are shown in Figs. 17 and 18 for cases which happened to have been transitional over the forward microphone and turbulent over the aft microphone. In the case of transitional flow at $M_\infty = 0.85$ (Fig. 17a), there is the indication of a concentration of energy near 7.6 kHz, which is more than three orders of magnitude lower in power than the predominant spectral peak. For turbulent flow at this same test condition (Fig. 17b), the power spectrum is similar to the transitional only for frequencies greater than about 1 kHz, the level of power being considerably less over the lower portion of the frequency band. Shapes of power density spectra similar to those of Fig. 17a are seen in Fig. 18a with a slightly broader concentration of energy at high frequencies around 7.6 and 8.7 kHz. The smoothness of the high frequency level of power seen for $M_\infty = 1.0$ in Fig. 18b is similar to that for the high frequency level of power for the turbulent case in Fig. 17b.

Expanded spectra to 200 Hz maximum frequency are shown for these same data in Figs. 19 and 20. For both cases of transitional flow, Figs. 19a and 20a, there were many spectral peaks of energy below 200 Hz. The turbulent spectra, Fig. 20b in particular, show a component in the neighborhood of 10 Hz. The near-10-Hz component appeared in virtually all of the data obtained at higher Mach numbers in this tunnel. It should be noted that Bruel and Kjaer microphones were used for these measurements and that their frequency response was such that the 10-Hz component was significantly attenuated, by perhaps as much as 10 dB in amplitude or more than a factor of 3. Therefore, at higher Mach numbers the ΔC_p values given in Fig. 14 have an inherent error caused by the low frequency roll-off of the microphone response.

The values of ΔC_p in the NASA/Langley 16 TDT shown in Fig. 14 exhibit more than a factor of 3 variation over the range in M_∞ . The transition Reynolds number data in Figs. 12 and 13 exhibit no apparent correlation with the ΔC_p data, however. The reason may be that the major contributions to the free-stream disturbances in this tunnel occurred at frequencies too low to have influenced transition.

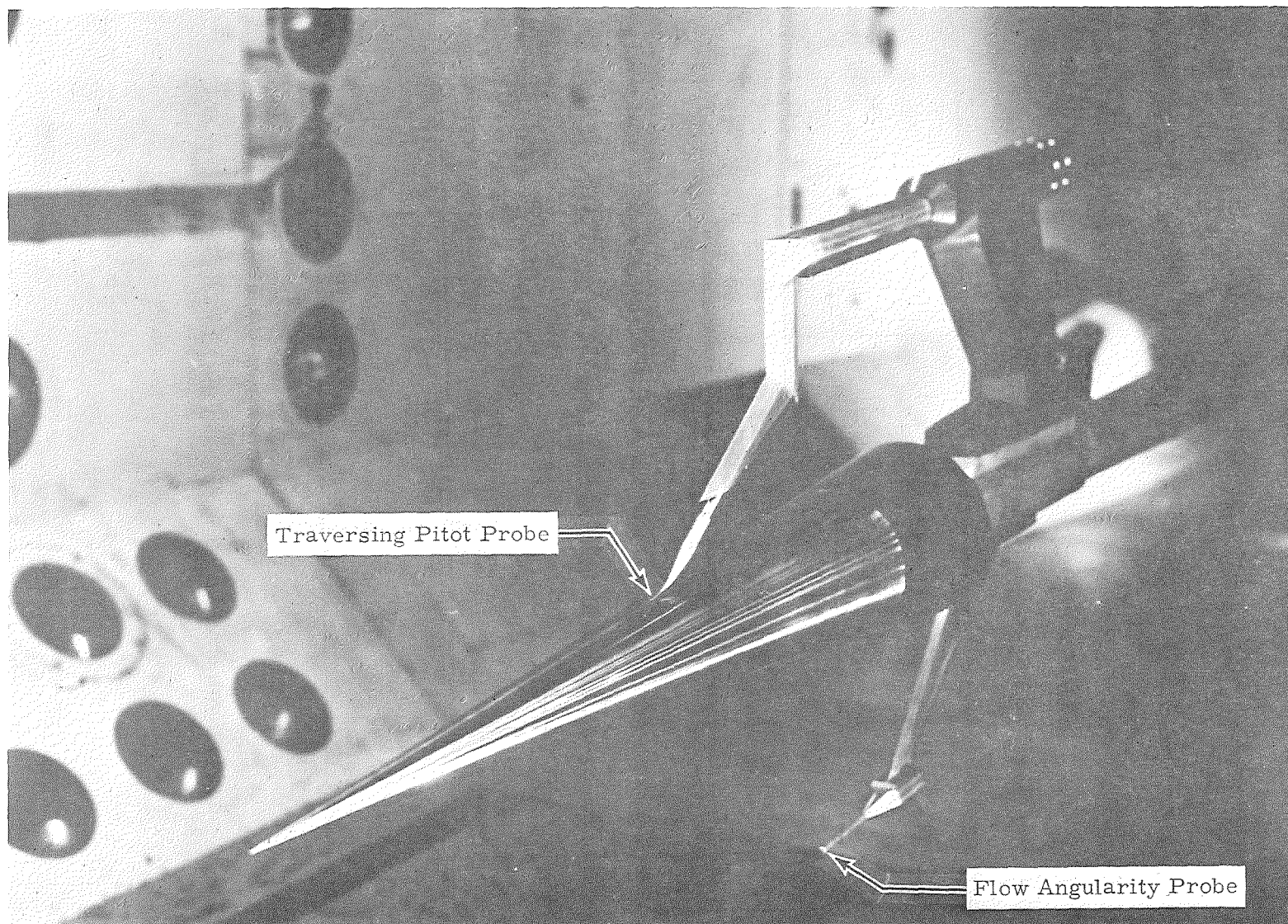


Figure 11. Photograph of the cone installed in the NASA/Langley 16 TDT.

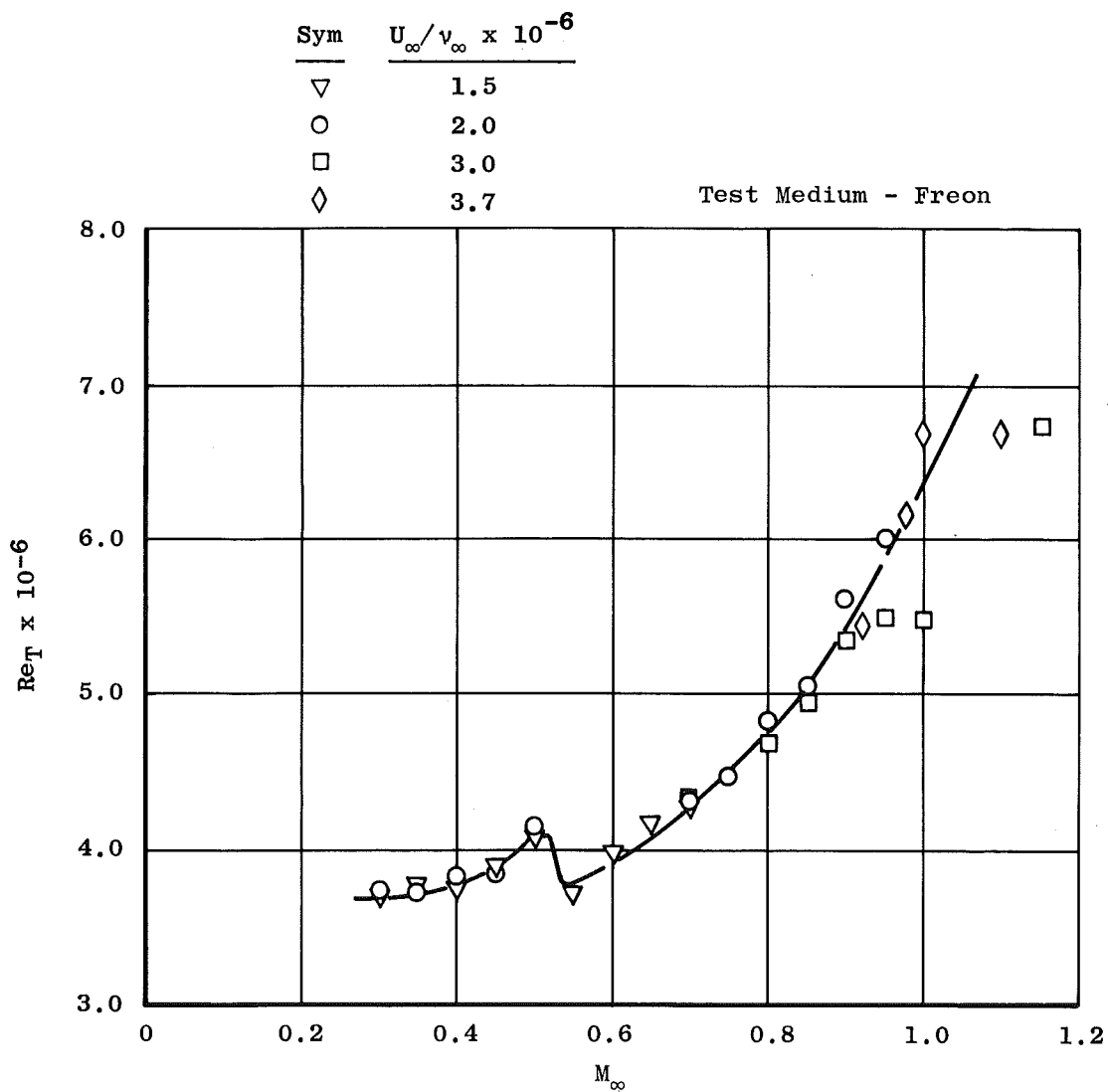


Figure 12. End-of-transition Reynolds numbers in the NASA/Langley 16 TDT.

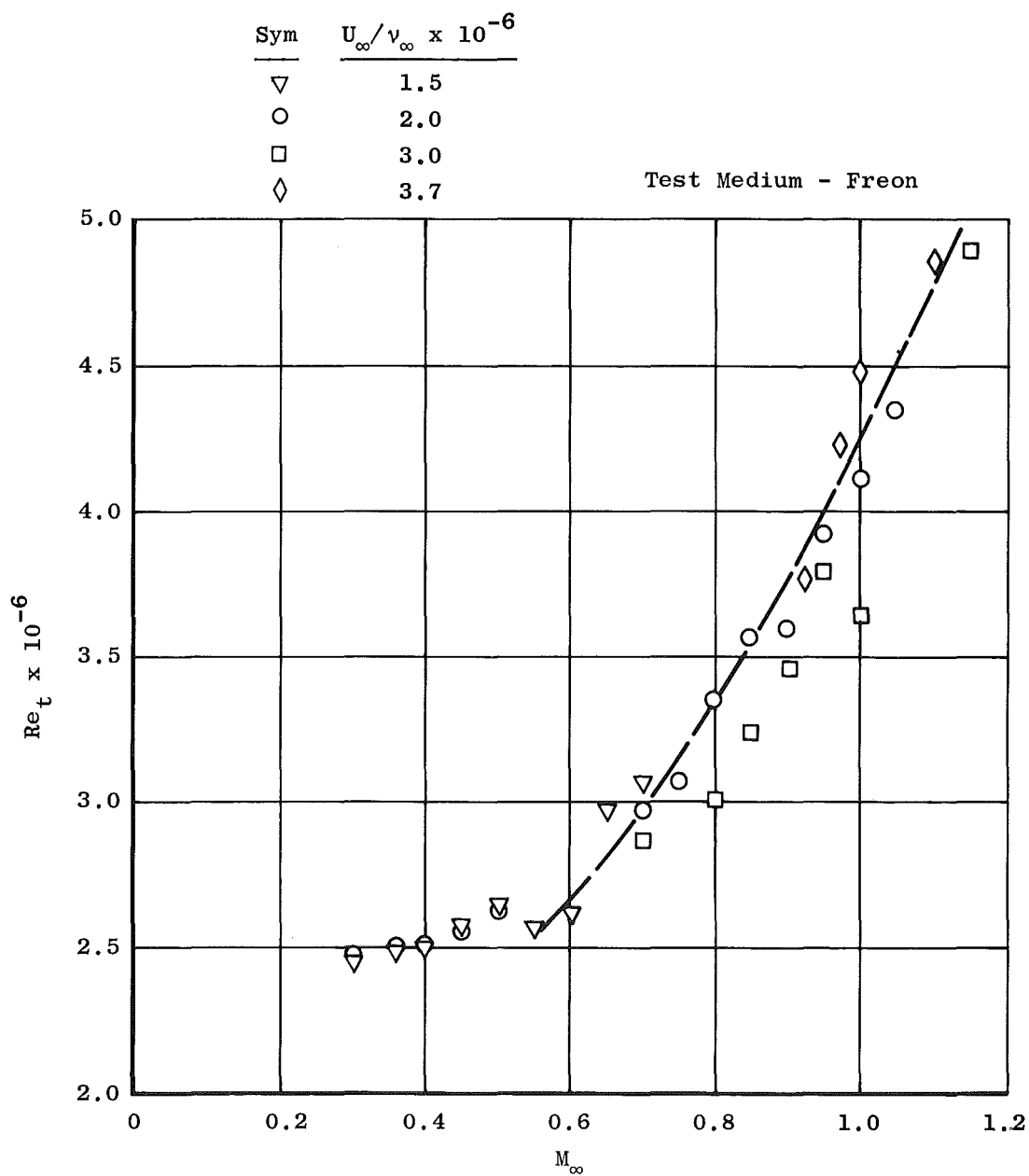


Figure 13. Onset-of-transition Reynolds numbers in the NASA/Langley 16 TDT.

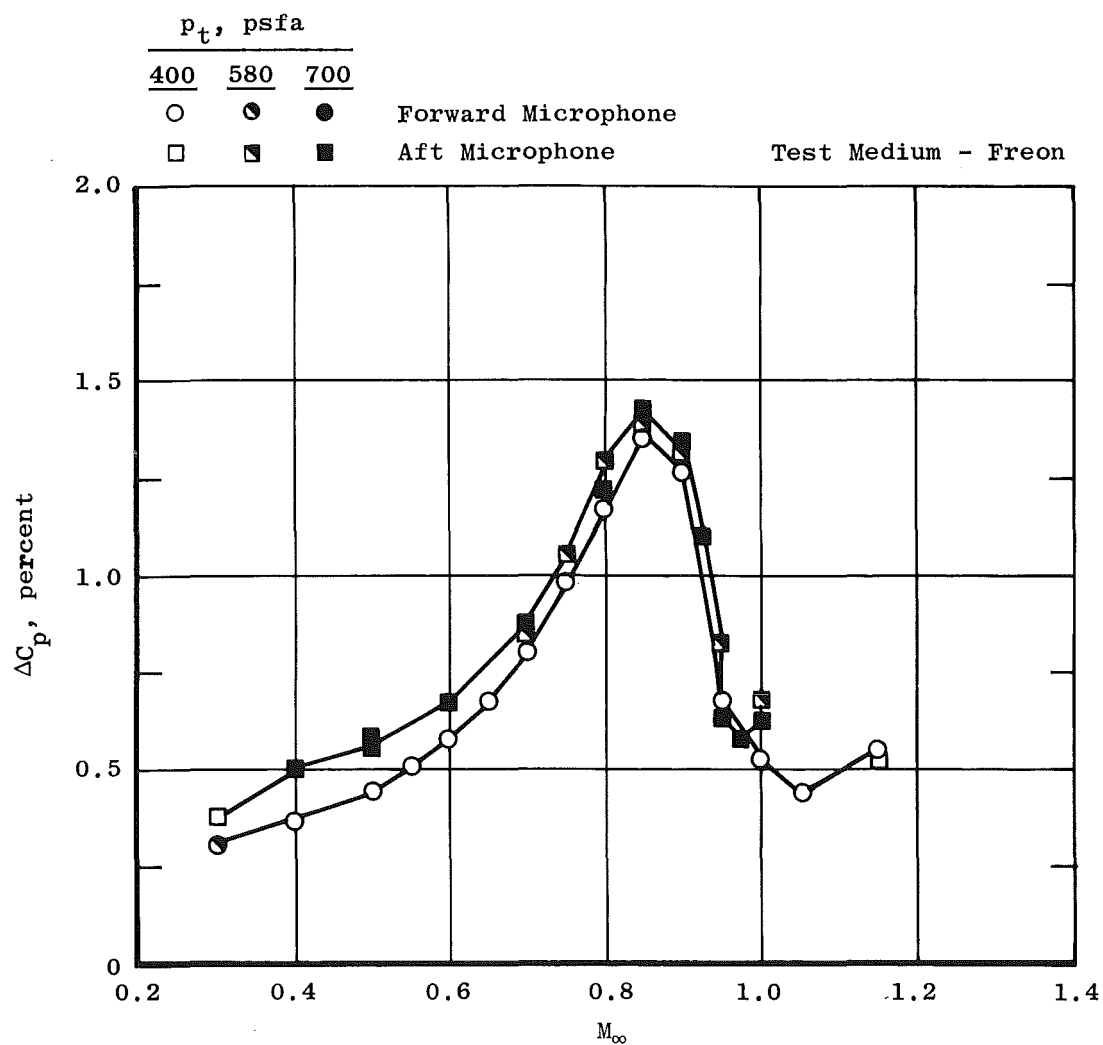


Figure 14. Noise levels in the NASA/Langley 16 TDT.

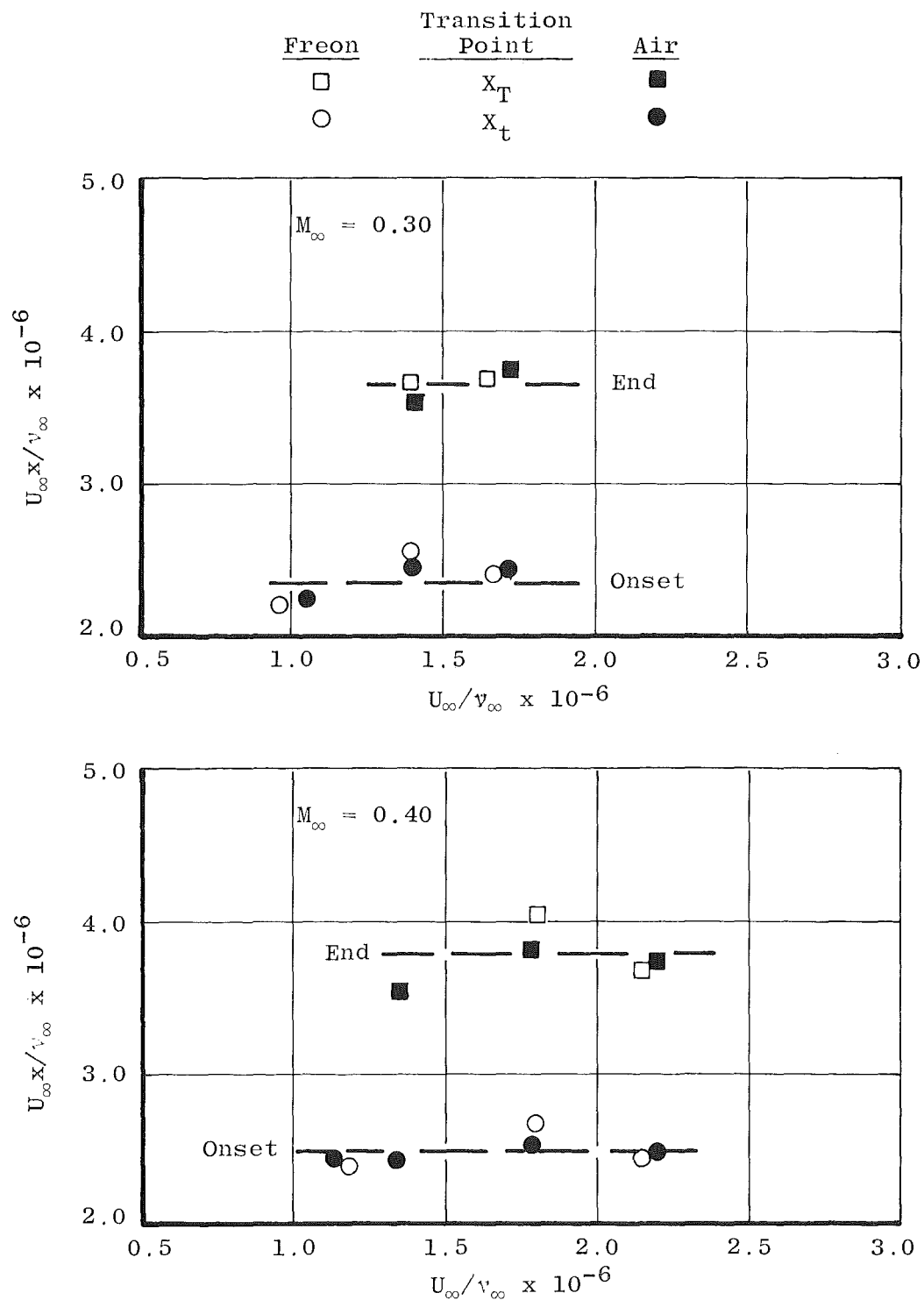


Figure 15. Comparison of transition locations in air and in freon.

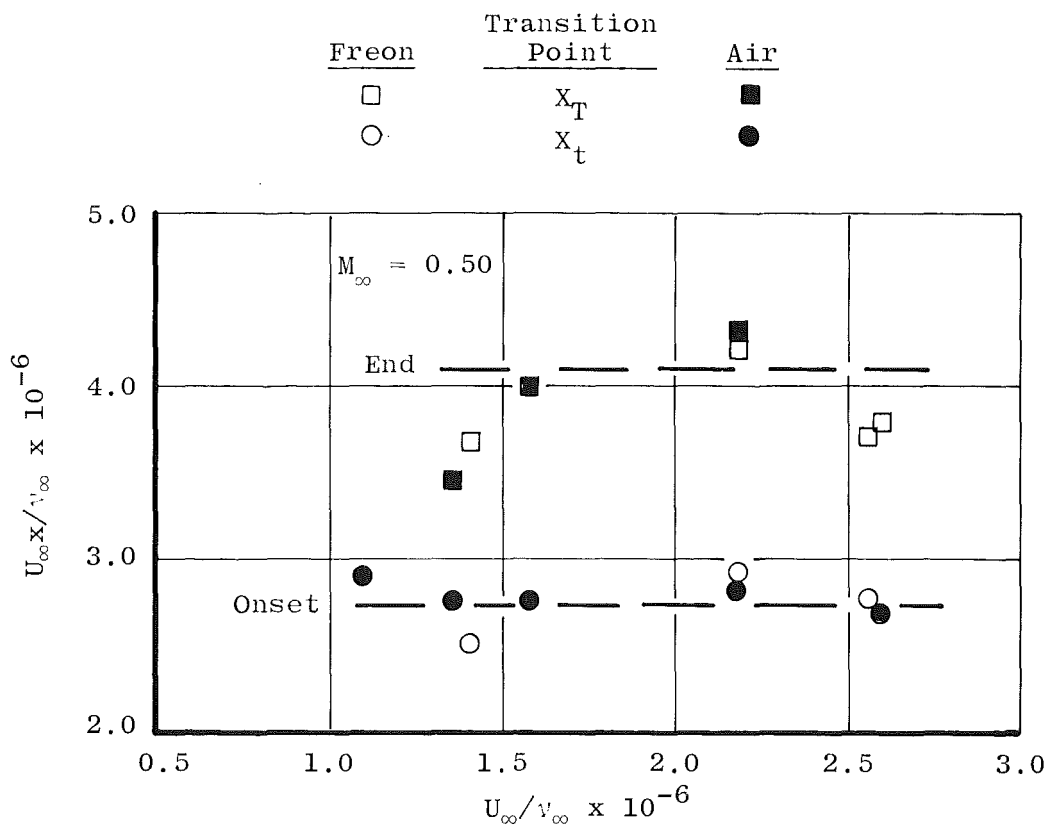


Figure 15. Concluded.

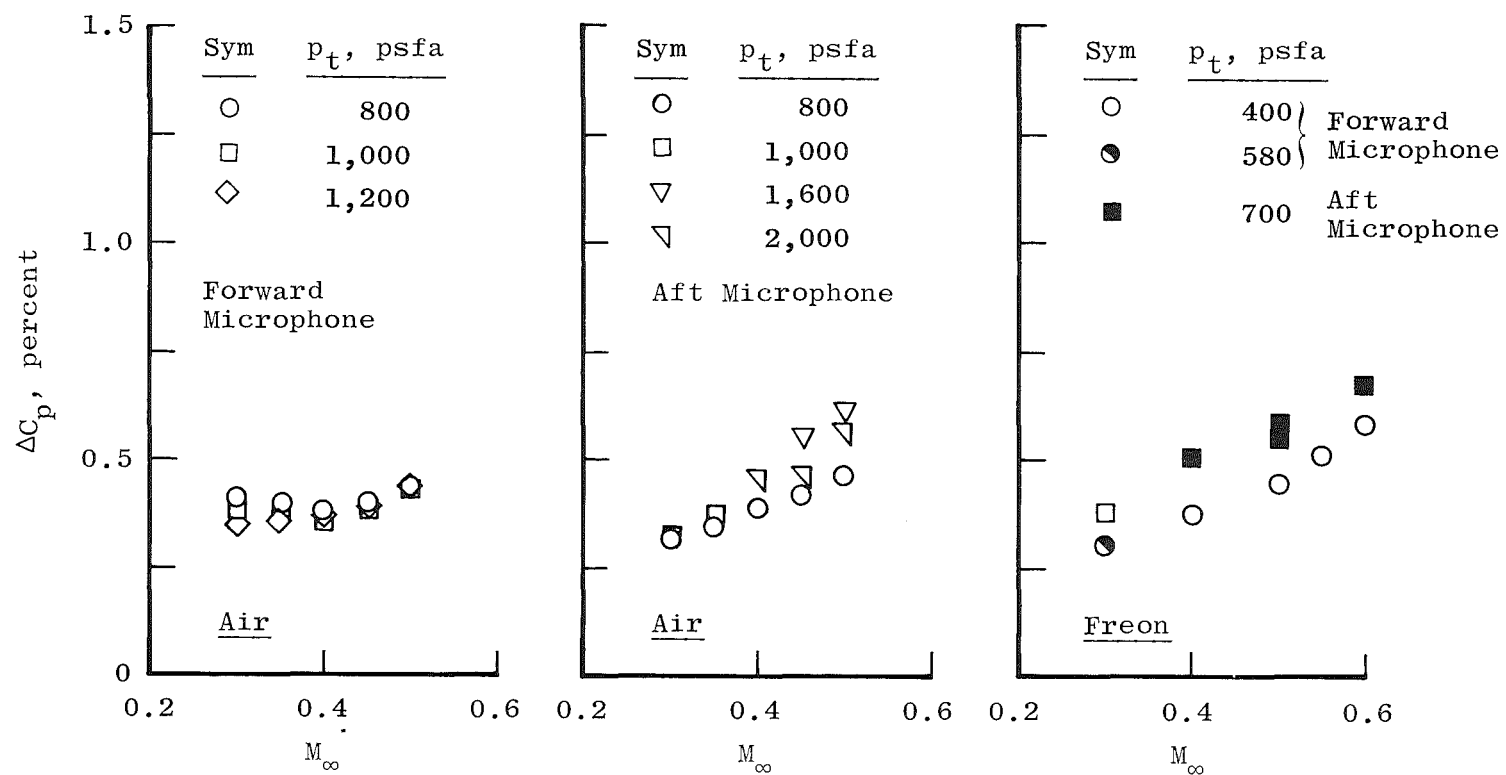
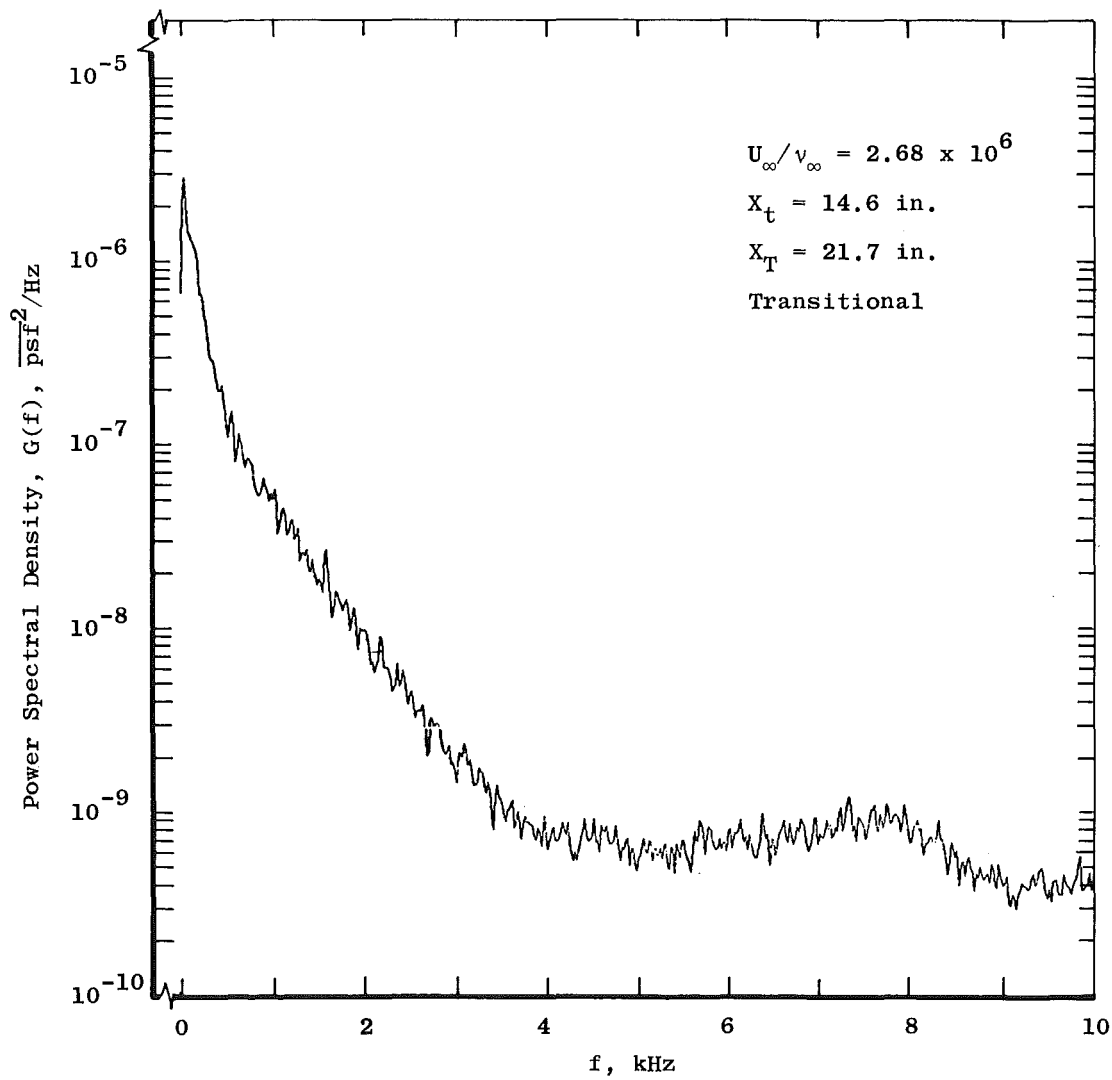
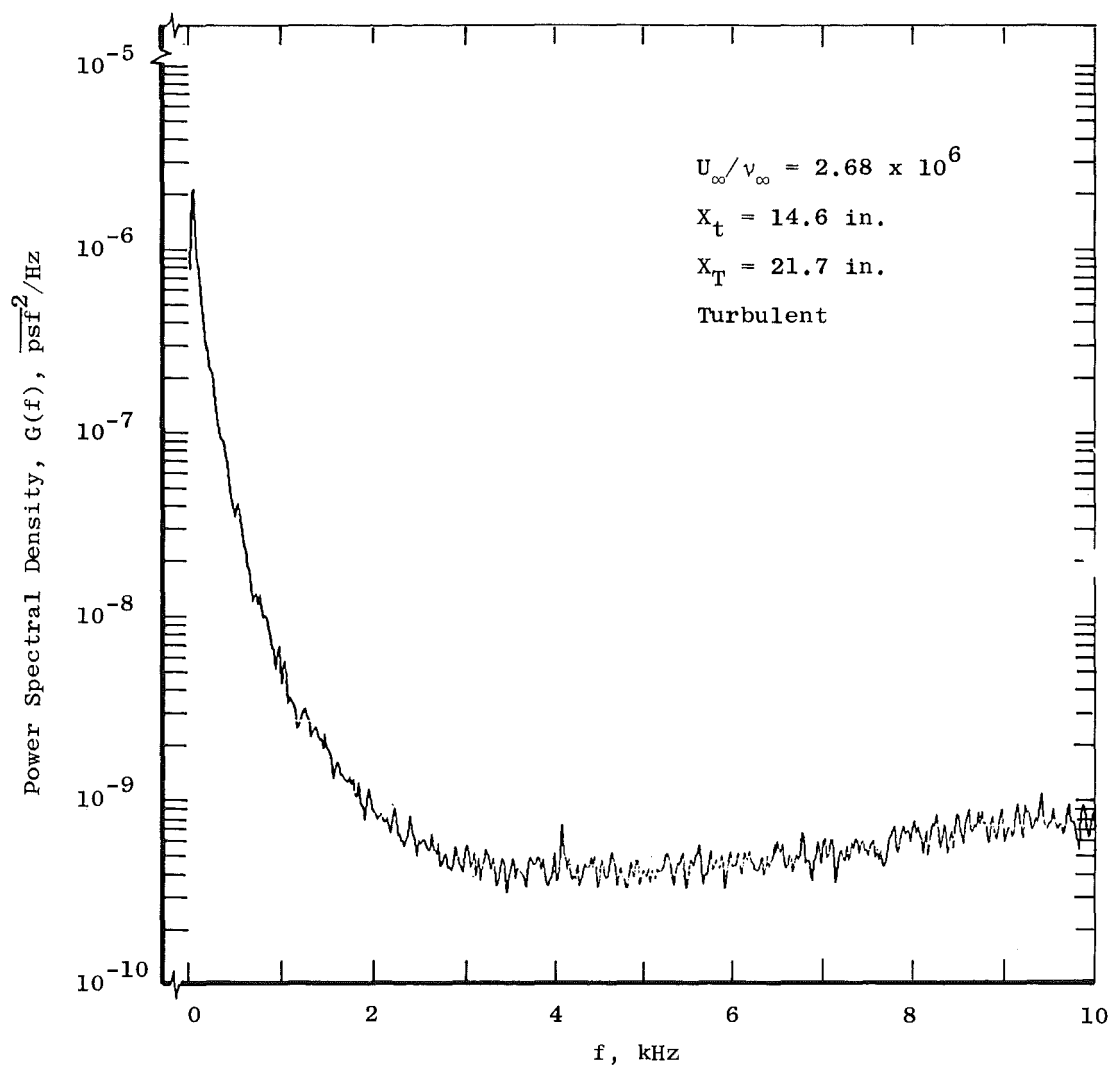


Figure 16. Comparison of noise levels in air and in freon.

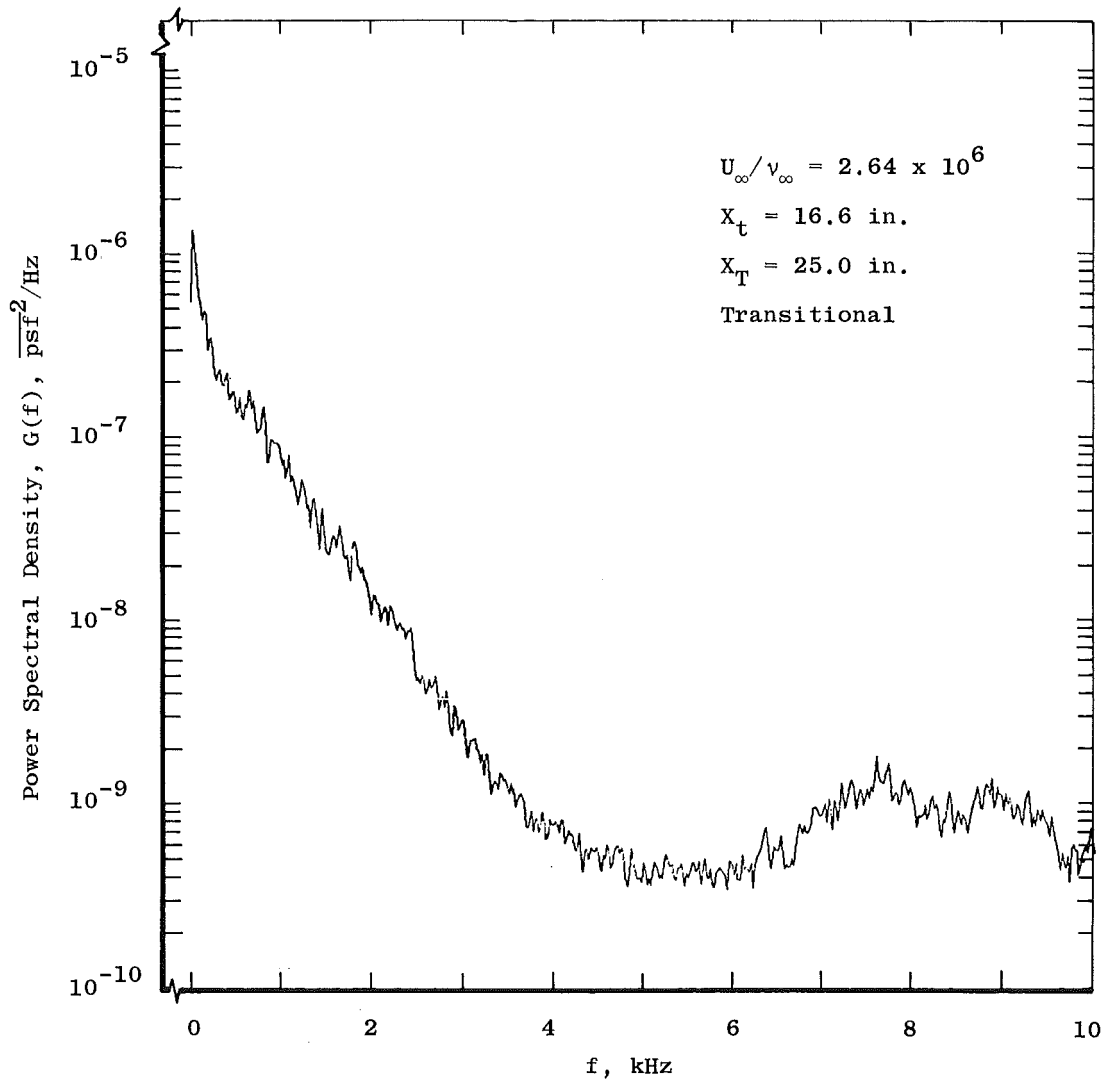


a. Forward microphone

Figure 17. Power spectral density measurements in the NASA/Langley 16 TDT at $M_{\infty} = 0.85$ (0 to 10 kHz).

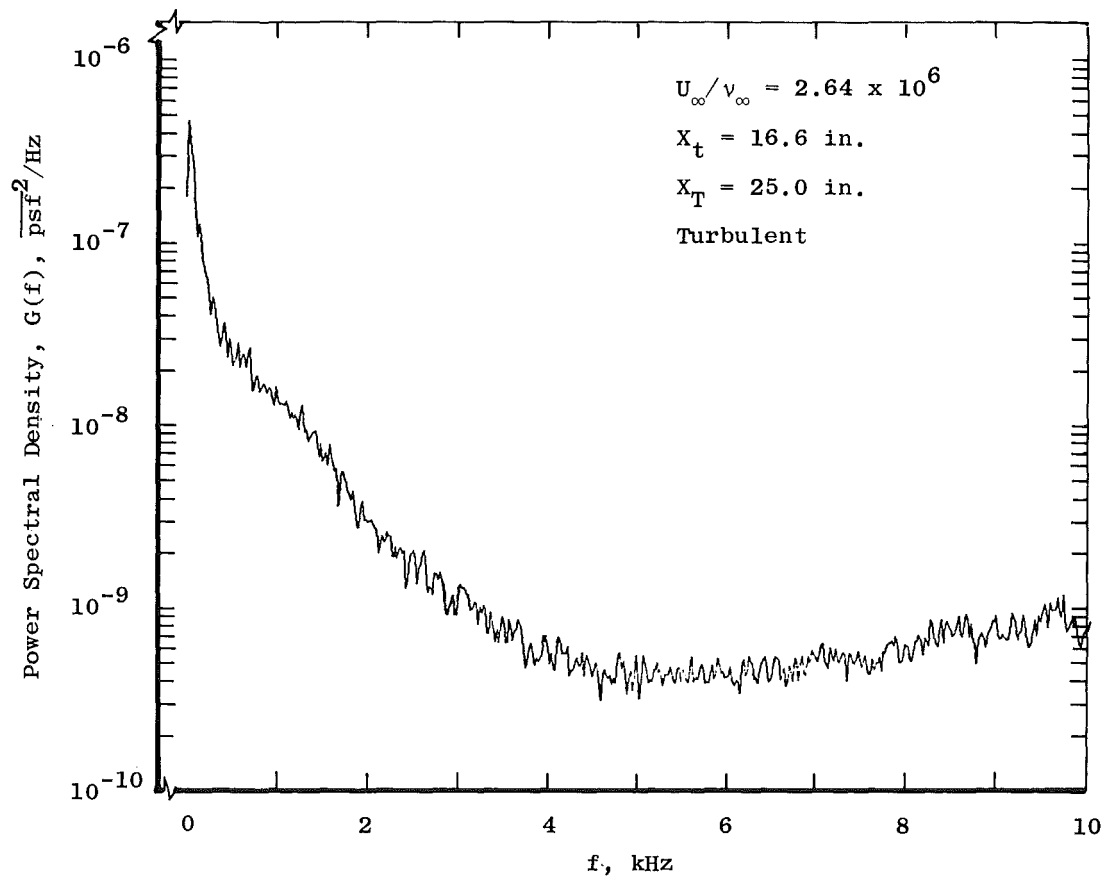


b. Aft microphone
Figure 17. Concluded.

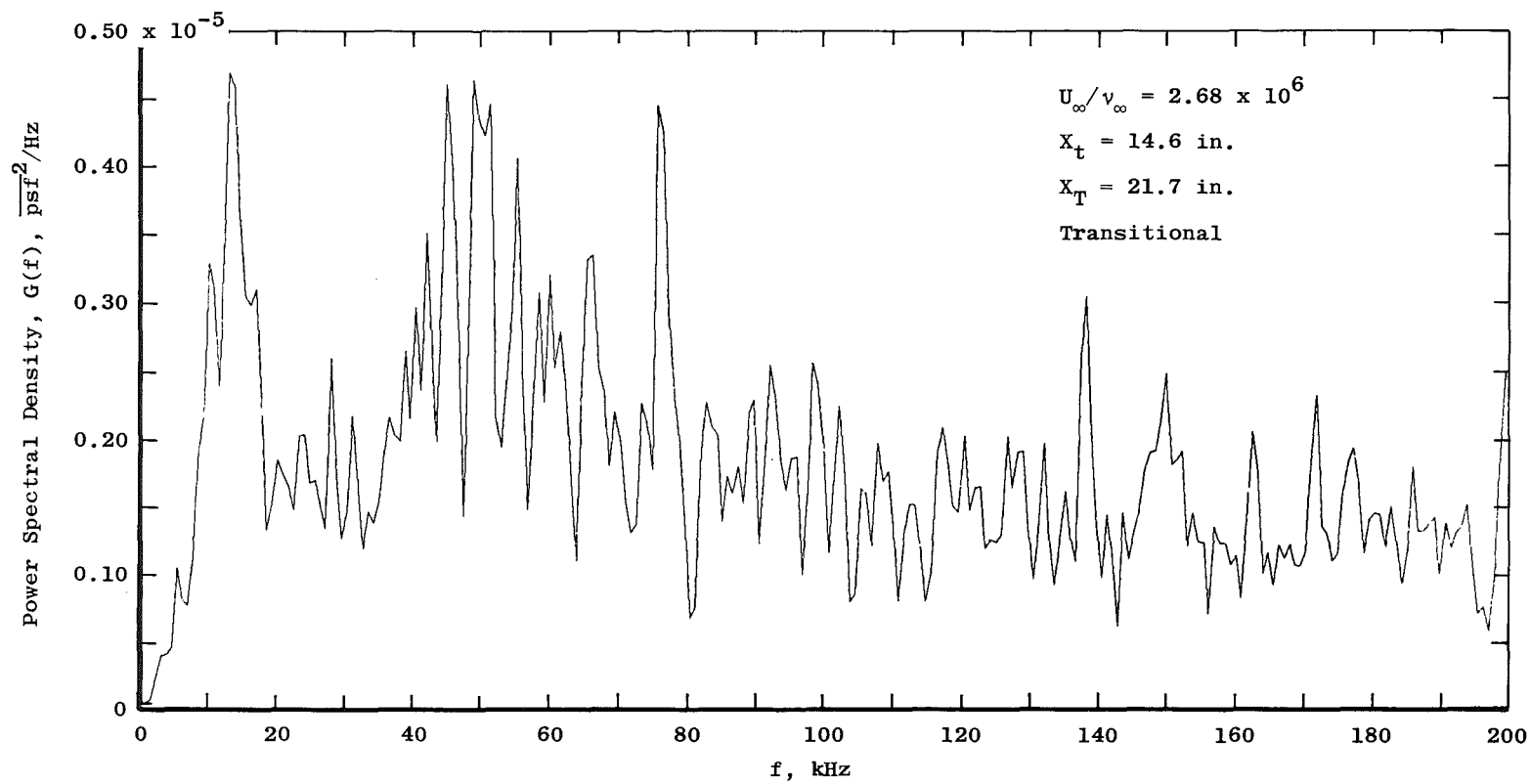


a. Forward microphone

Figure 18. Power spectral density measurements in the NASA/Langley 16 TDT at $M_{\infty} = 1.00$ (0 to 10 kHz).

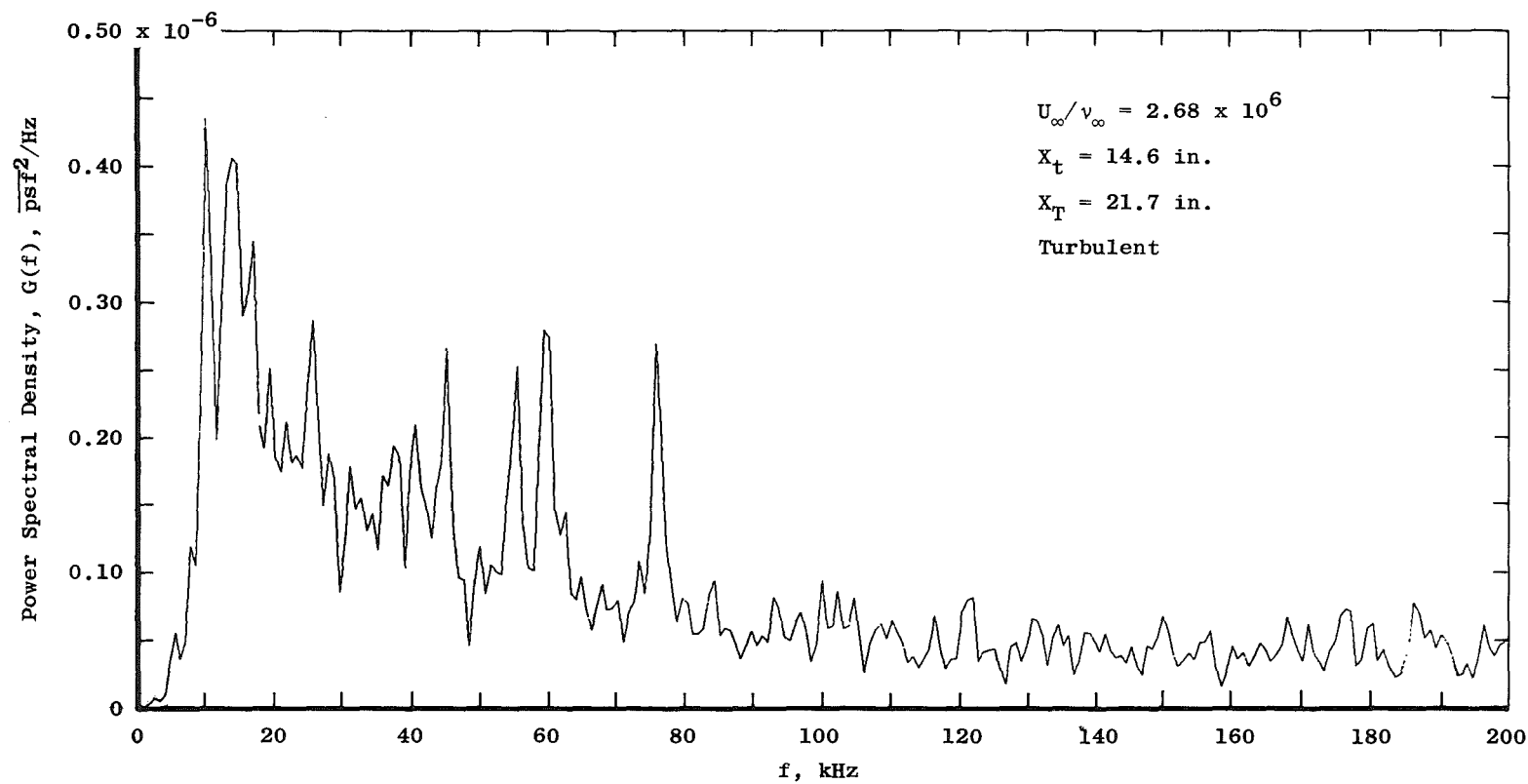


b. Aft microphone
Figure 18. Concluded.

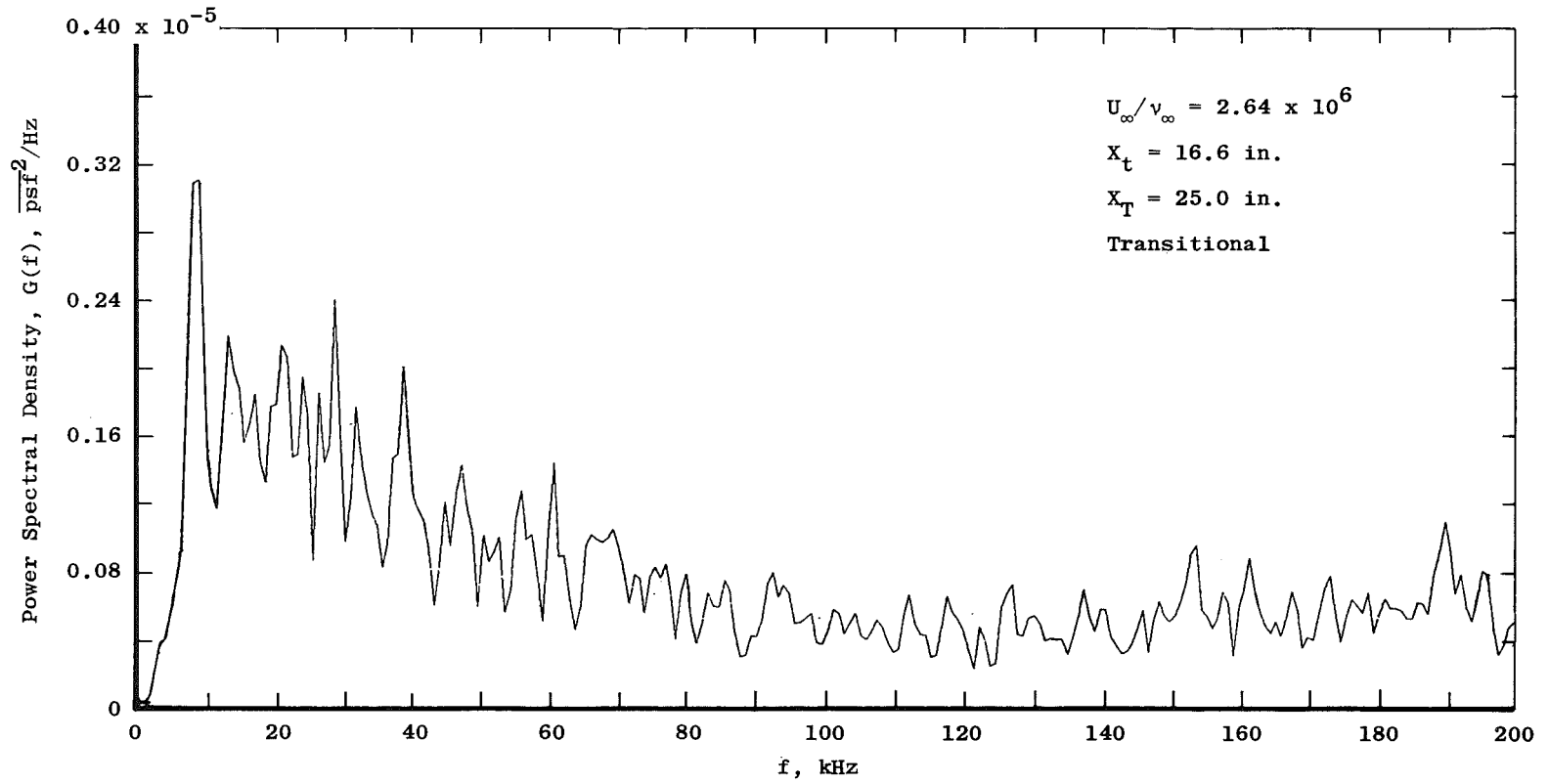


a. Forward microphone

Figure 19. Power spectral density measurements in the NASA/Langley 16 TDT at $M_\infty = 0.85$ (0 to 200 Hz).

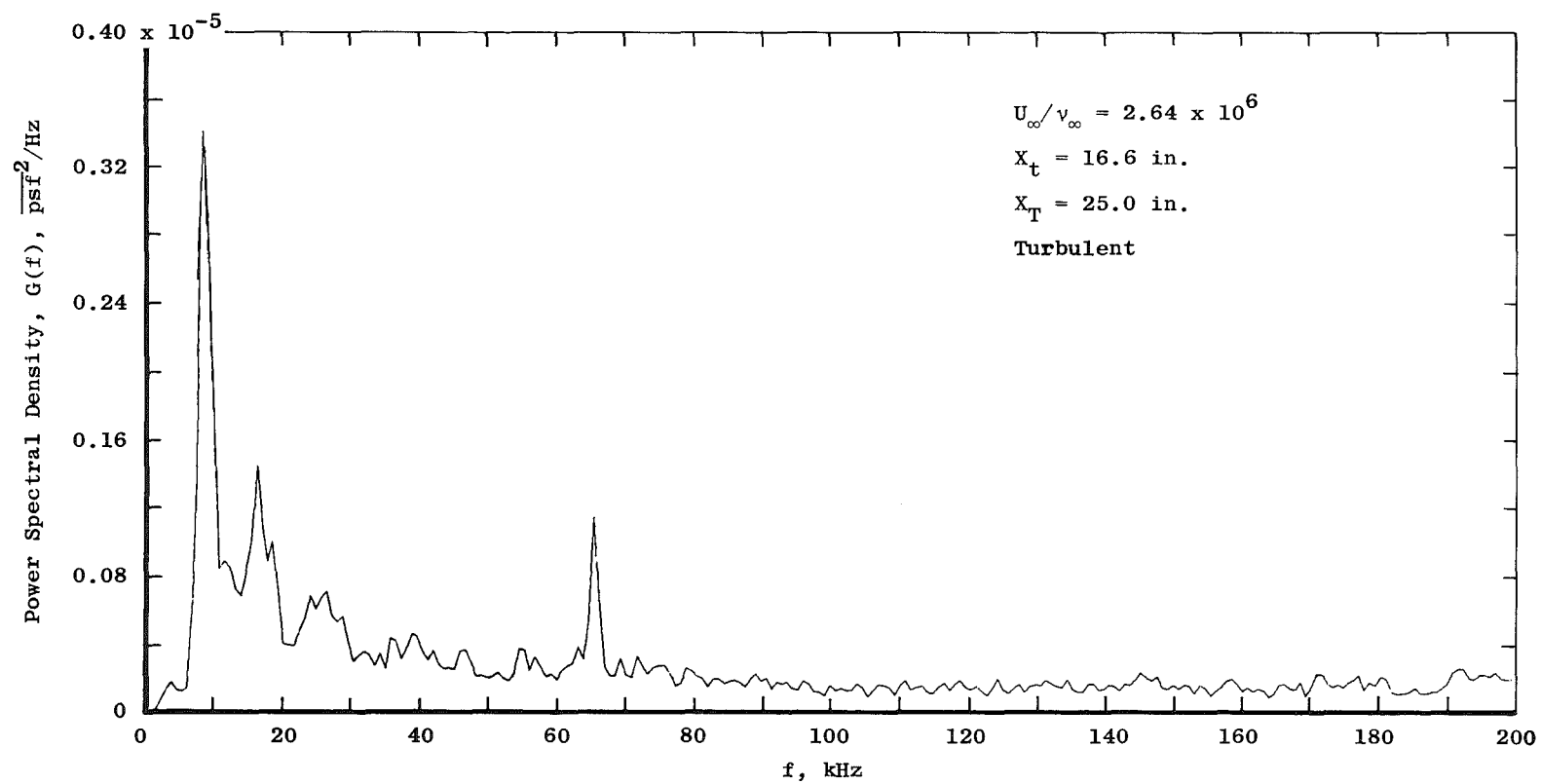


b. Aft microphone
Figure 19. Concluded.



a. Forward microphone

Figure 20. Power spectral density measurements in the NASA/Langley
 16 TDT at $M_\infty = 1.00$ (0 to 200 Hz).



b. Aft microphone
Figure 20. Concluded.

Table 4. NASA/Langley 16 TDT Data

Test Medium: Air

M_∞	U_∞ / v_∞ $\times 10^{-6}$	ΔC_p , percent	$Re_t \times$ 10^{-6}	$Re_T \times$ 10^{-6}	p_t , psfa
0.50	1.093	0.431	2.912	-	800
0.45	1.001	0.405	-	-	↓
0.40	0.909	0.379	-	-	
0.35	0.812	0.344	-	-	
0.30	0.706	0.314	-	-	
0.50	1.355	0.428	2.772	3.463	1,000
0.45	1.238	0.394	2.630	-	↓
0.40	1.126	0.376	2.405	-	
0.35	1.003	0.365	2.455	-	
0.30	0.882	0.311	-	-	
0.50	1.581	0.438	2.760	4.032	1,200
0.45	1.472	0.393	2.614	3.701	↓
0.40	1.345	0.368	2.413	3.519	
0.35	1.209	0.355	2.314	-	
0.30	1.061	0.343	2.241	-	
0.50	2.178	-	2.829	4.339	1,600
0.45	1.976	-	2.561	4.043	↓
0.40	1.784	-	2.521	3.821	
0.35	1.599	0.402	2.456	3.722	
0.30	1.404	0.328	2.437	3.522	
0.50	2.598	0.547	2.681	3.796	2,000
0.45	2.417	0.450	2.639	3.640	↓
0.40	2.204	0.442	2.466	3.703	
0.35	1.985	-	2.453	3.728	
0.30	1.747	-	2.427	3.742	

Table 4. Concluded

Test Medium: Freon

M_∞	U_∞ / ν_∞ $\times 10^{-6}$	ΔC_p , percent	$Re_t \times$ 10^{-6}	$Re_T \times$ 10^{-6}	p_t , psfa
0.30	0.927	0.301	2.203	—	400 ↓
0.40	1.185	0.363	2.371	—	
0.50	1.412	0.438	2.508	3.681	
0.55	1.518	0.499	2.655	3.757	
0.60	1.586	0.575	2.722	3.963	
0.65	1.665	0.674	2.942	4.149	
0.70	1.745	0.798	3.036	4.251	
0.75	1.820	0.979	3.210	4.521	
0.80	1.874	1.172	3.463	4.869	
0.85	1.922	1.350	3.633	5.189	
0.90	1.942	1.261	3.694	—	
0.95	1.960	0.665	4.057	—	
1.00	1.958	0.527	4.206	—	
1.05	1.986	0.436	4.373	—	580 ↓
1.15	2.007	0.517	—	—	
0.30	1.396	0.302	2.555	3.660	
0.40	1.794	0.618	2.659	4.047	
0.50	2.176	0.557	2.938	4.217	
0.70	2.400	0.877	2.851	4.262	
0.75	2.503	1.053	3.004	4.355	
0.80	2.602	1.290	3.976	4.637	
0.85	2.683	1.372	3.252	4.862	
0.90	2.747	1.323	3.395	5.390	
0.95	2.794	0.818	3.638	5.448	
1.00	2.740	0.671	3.715	5.605	
1.00	2.640	0.746	3.674	5.742	
1.10	2.700	—	5.090	—	700 ↓
1.15	2.725	0.822	5.141	—	
0.30	1.670	—	2.405	3.687	
0.40	2.150	0.502	2.425	3.664	
0.50	2.563	0.577	2.776	3.721	
0.60	2.934	0.671	—	—	
0.70	3.044	0.852	2.712	4.219	
0.80	3.304	1.208	2.924	4.698	
0.85	3.410	1.420	3.192	4.992	
0.90	3.487	1.341	3.504	5.231	
0.923	3.526	1.098	3.790	5.407	
0.95	3.551	0.628	3.936	5.327	
0.975	3.585	0.569	4.216	6.152	
1.00	3.634	0.671	—	—	
1.10	3.706	0.569	4.818	6.486	

Naval Ship R&DC 7 x 10 T

The NSR&DC 7 x 10 T has three basic modes of operation: stilling chamber vented to atmosphere, test section vented to atmosphere, and the circuit evacuated below atmosphere. As M_∞ is varied, these three modes essentially provide for testing at constant p_t with varying p_∞ , constant p_∞ near sea level with varying p_t , or at reduced p_t (which is about 900 psfa and corresponds to pressure altitude variation approximately from 30,000 to 40,000 ft as M_∞ is increased from 0.7 to 1.17). The upper limit of capability in M_∞ is about 1.17 for the tunnel. The cone was tested in all three modes with the addition of two partial-evacuation levels of p_t , 1,900 and 1,600 psfa, while the stilling chamber was vented. The resulting range in U_∞/ν_∞ was from 1.5×10^6 to 4.0×10^6 . Visible fogging, indicating a high humidity level, occurred at some of the M_∞ settings above 0.95.

The data acquired in the NSR&DC 7 x 10 T are presented in Table 5. A photograph of the model in the tunnel is shown in Fig. 21. End-of-transition Reynolds numbers, Re_T , are shown as a function of M_∞ for $U_\infty/\nu_\infty = 2.0 \times 10^6$, 3.0×10^6 , and 4.0×10^6 in Fig. 22. Onset-of-transition Reynolds numbers, Re_t , are shown in Fig. 23. Complete transition did not occur on the cone for M_∞ between 0.85 and 1.10. Representative microphone data (ΔC_p versus M_∞) are shown in Fig. 24 for p_t varied from 900 psfa to 2,700 psfa. Virtually no influence of U_∞/ν_∞ was found in either the ΔC_p data or the transition Reynolds number data in this tunnel. Values of ΔC_p selected for presentation in Fig. 24 were selected simply on the basis of avoiding transitional boundary-layer conditions over the microphones. No differences could be found for different modes of tunnel operation.

There was a sharply defined peak in ΔC_p at $M_\infty = 0.75$. Selected power density spectra from the cone microphones are presented in Fig. 25. Some unidentified narrow-band peaks occurred in the spectrum at $M_\infty = 0.25$ (Fig. 25a) at frequencies between 2 and 5 kHz. Under these conditions the boundary-layer flow was laminar. At $M_\infty = 0.4$ (Fig. 25b), the boundary layer happened to be transitional. The spectra in Figs. 25 c through e were all under laminar conditions. At $M_\infty = 0.77$, there was a concentration of spectral energy near 100 Hz (Fig. 25c). Other than this, the spectra exhibited only a general roll-off character with nothing definitive to explain the variation in ΔC_p with M_∞ observed in this tunnel.

As in the NASA/Langley 16 TDT there is little or no apparent correlation between the trends in Re_T , Re_t , and ΔC_p with M_∞ in this tunnel. This could be due to the dominance of the spectra where ΔC_p was greatest by low-frequency disturbances (i.e., 100 Hz), these disturbances being too low in frequency to influence transition.

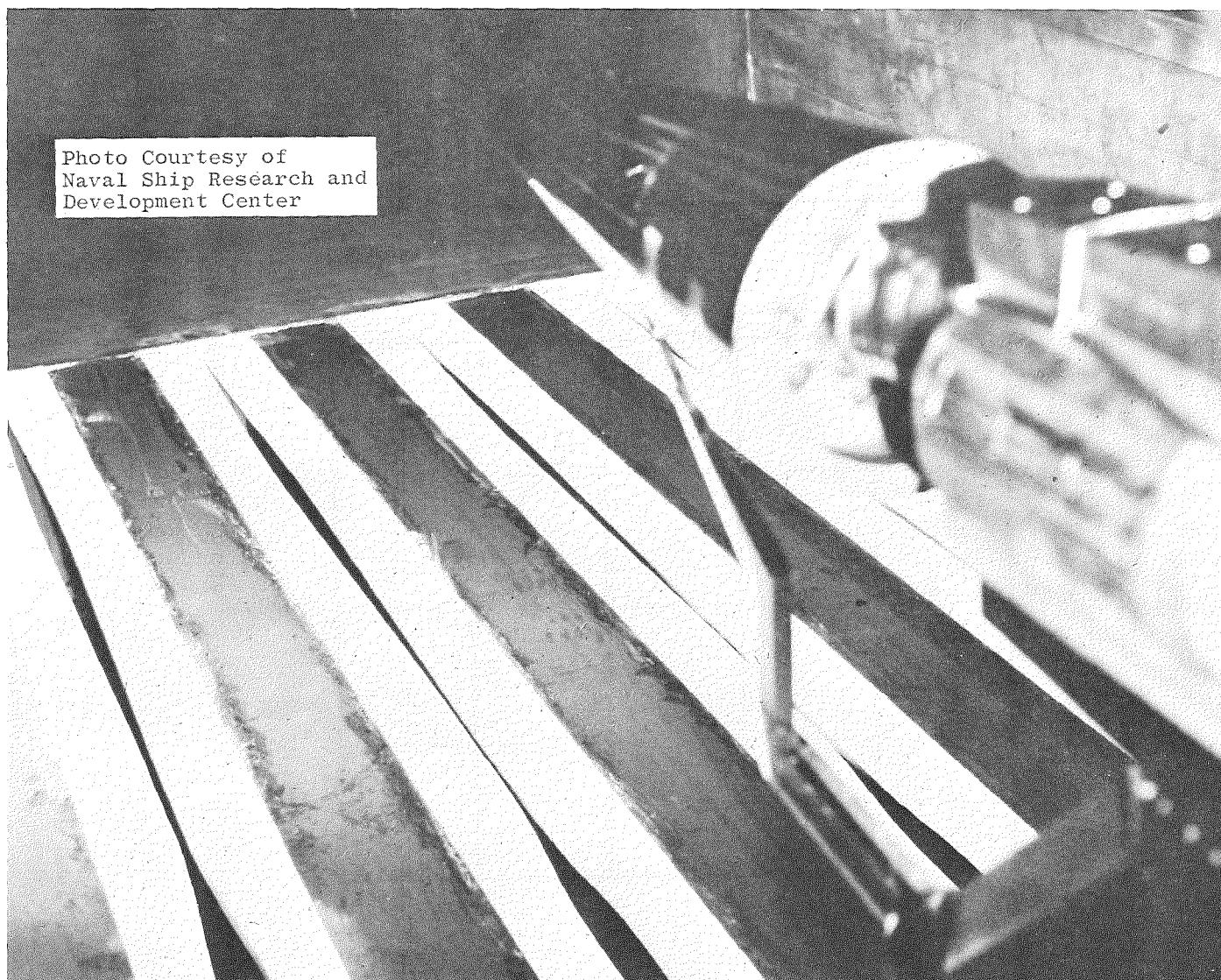


Figure 21. Photograph of the cone installed in NSR&DC 7 x 10 T.

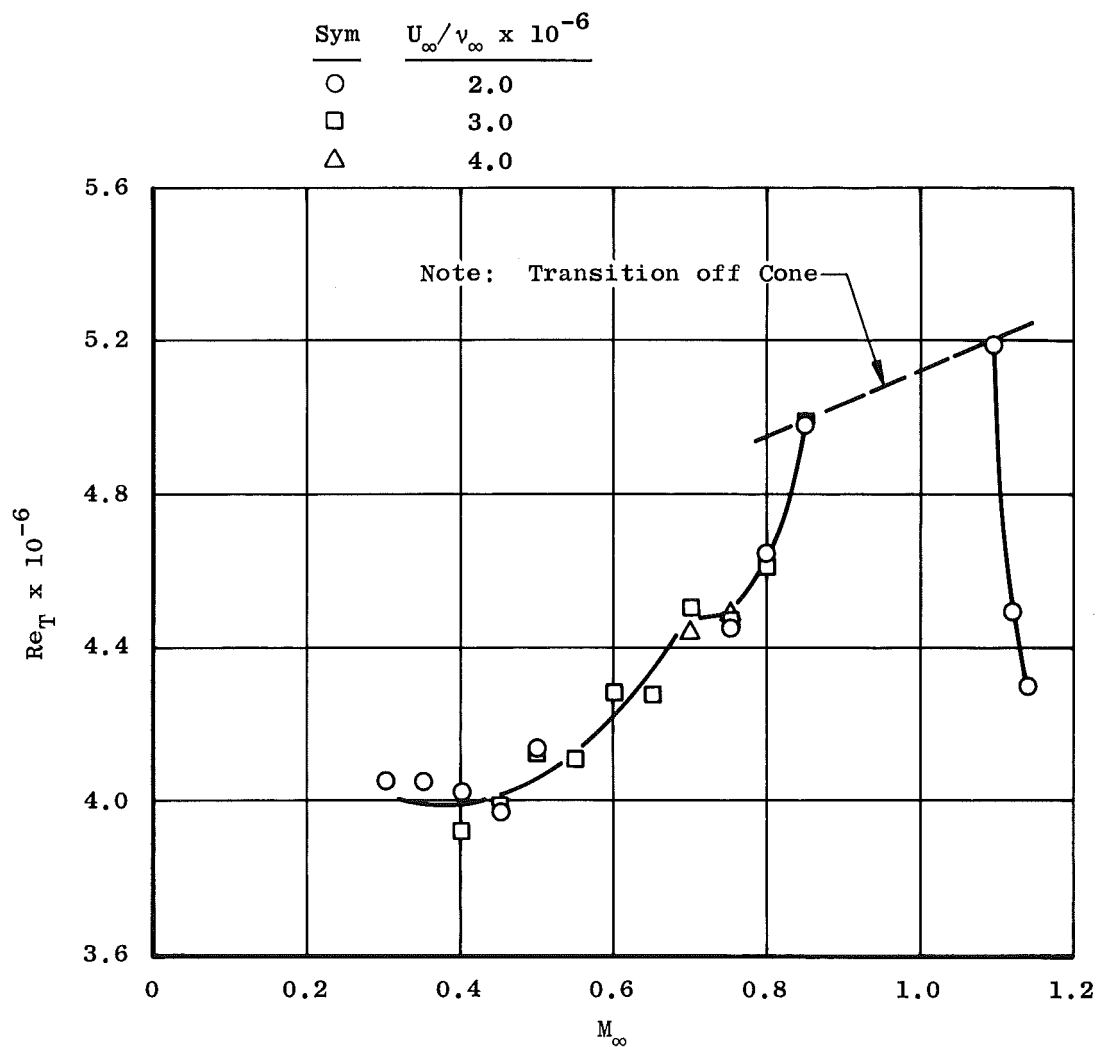


Figure 22. End-of-transition Reynolds numbers in the NSR&DC 7 x 10 T.

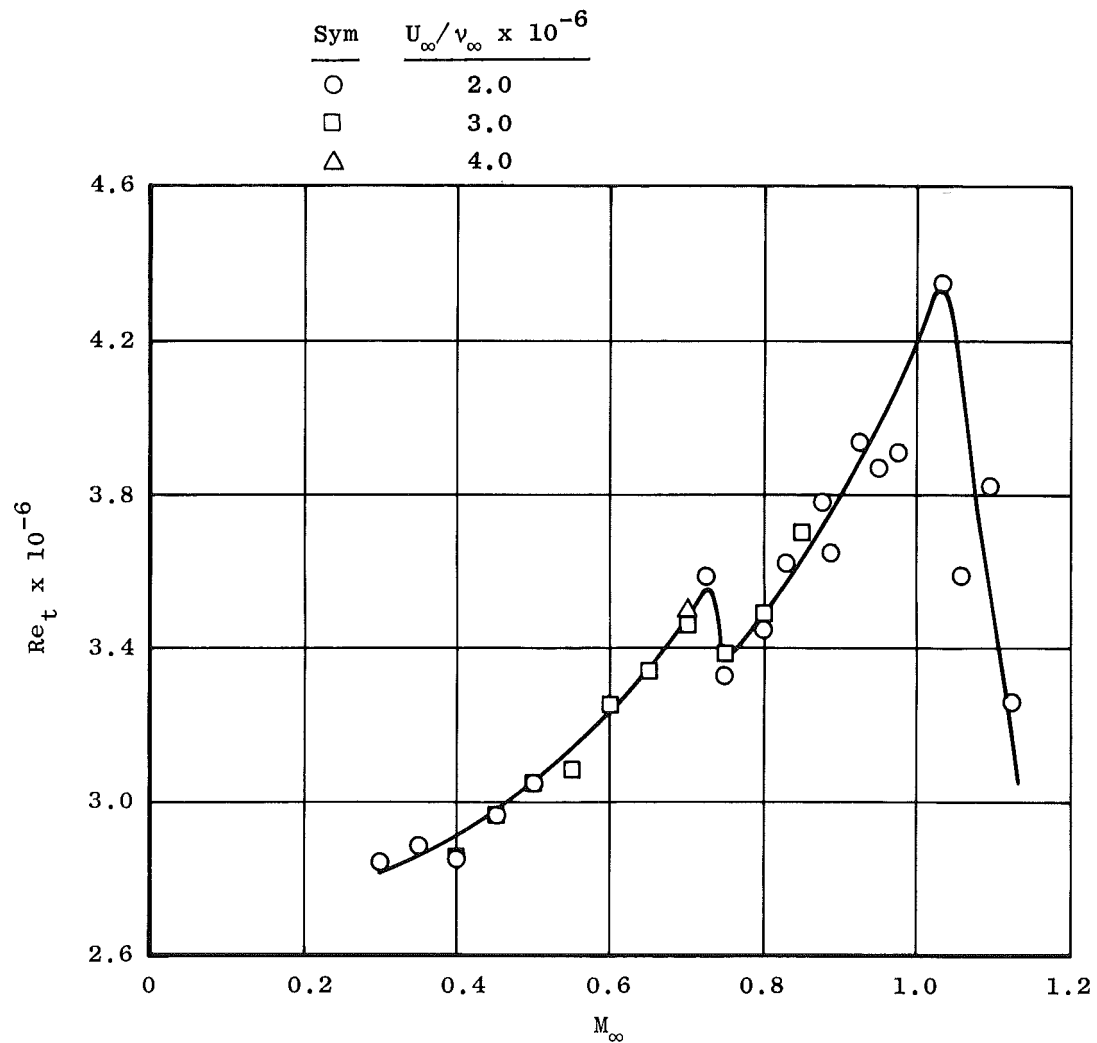


Figure 23. Onset-of-transition Reynolds numbers in the NSR&DC 7 x 10 T.

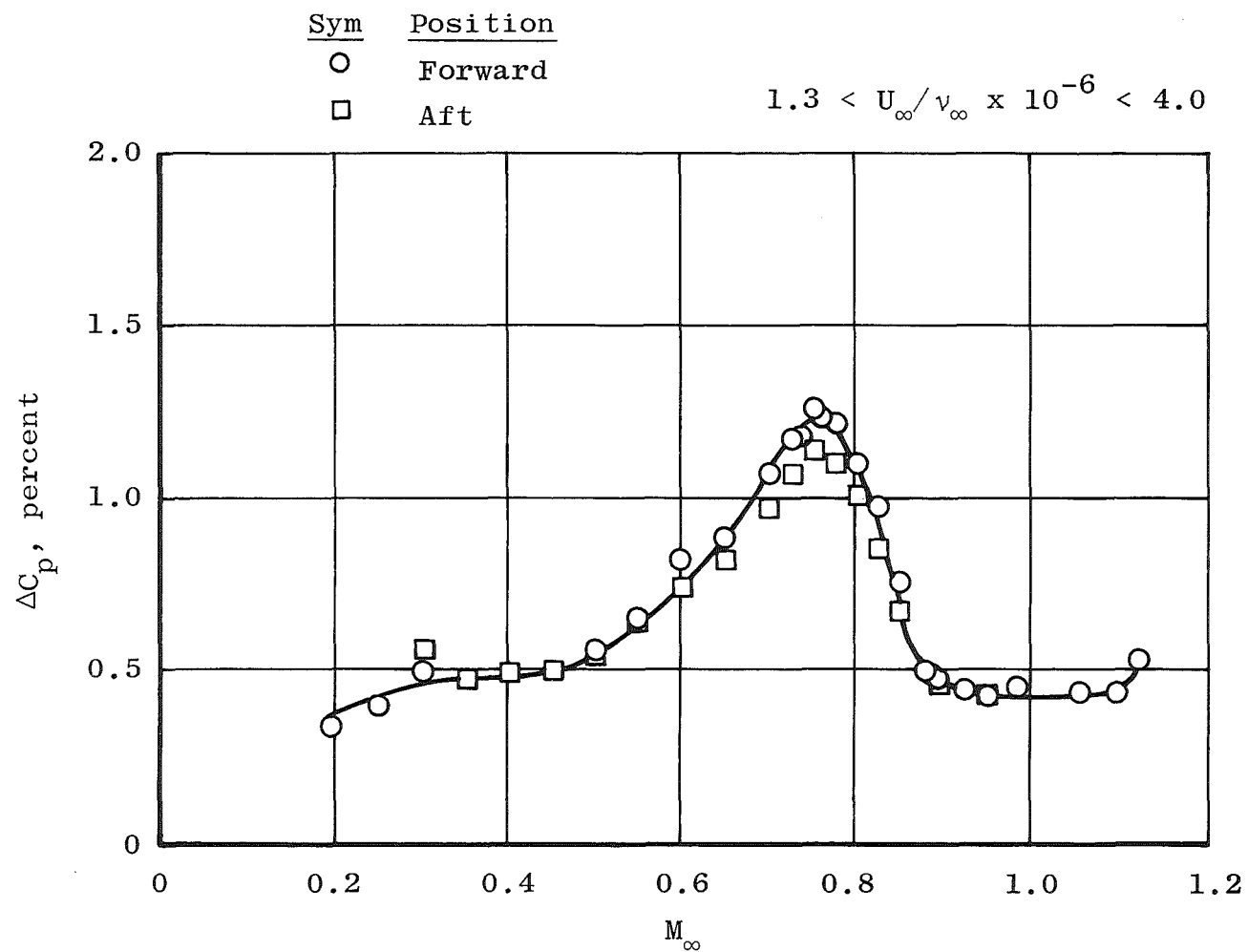
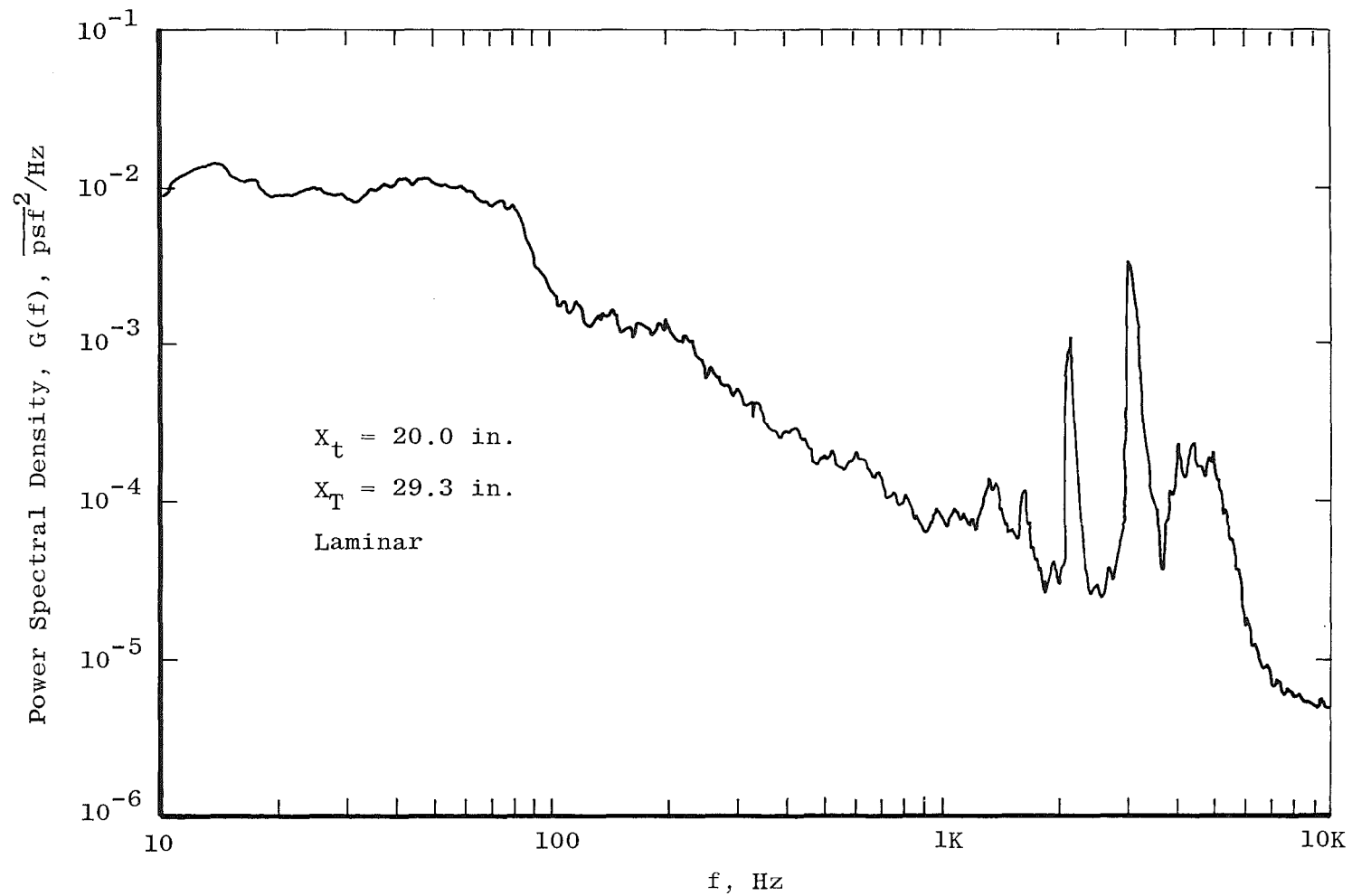
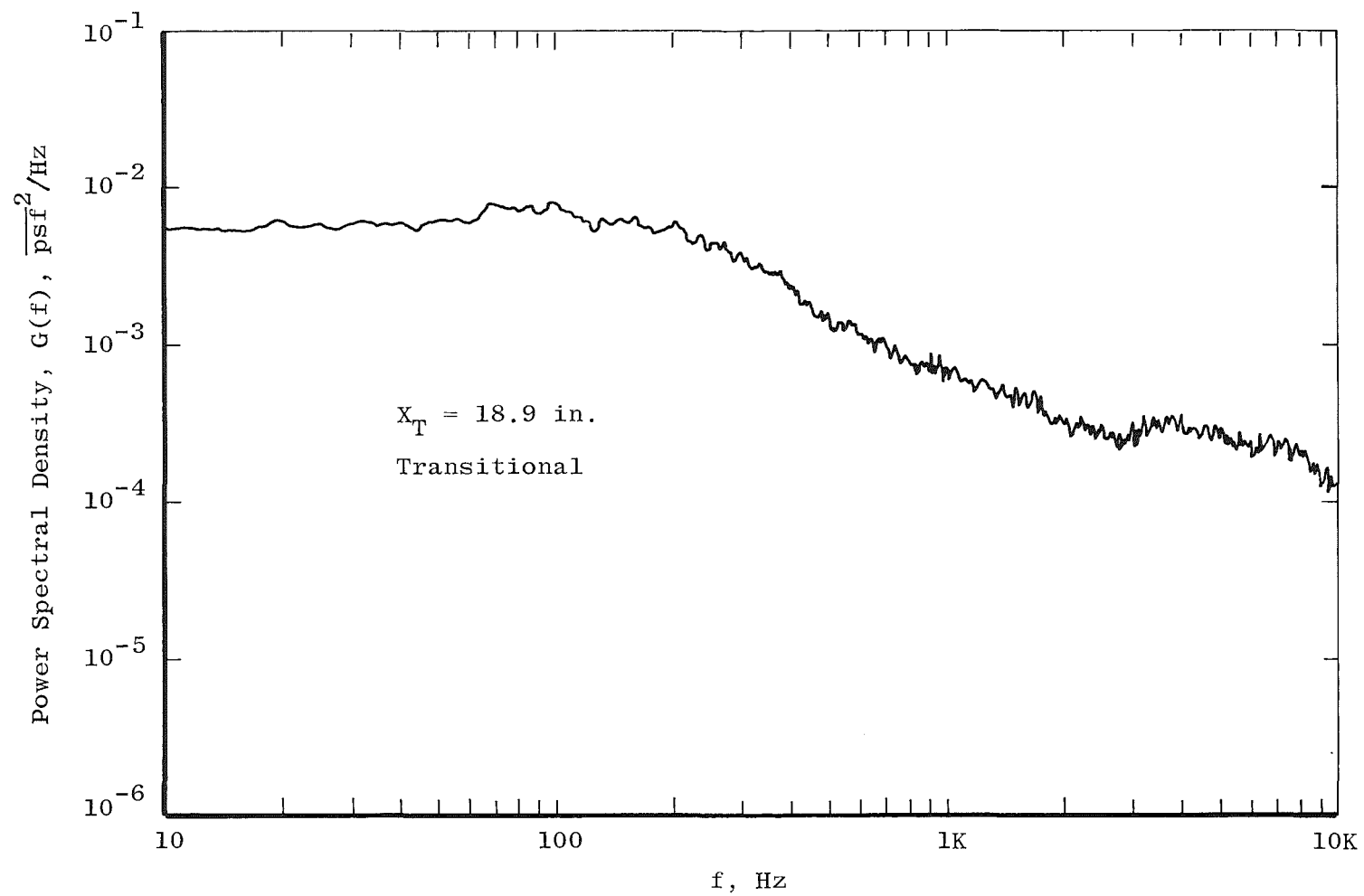


Figure 24. Noise levels in the NSR&DC 7 x 10 T.

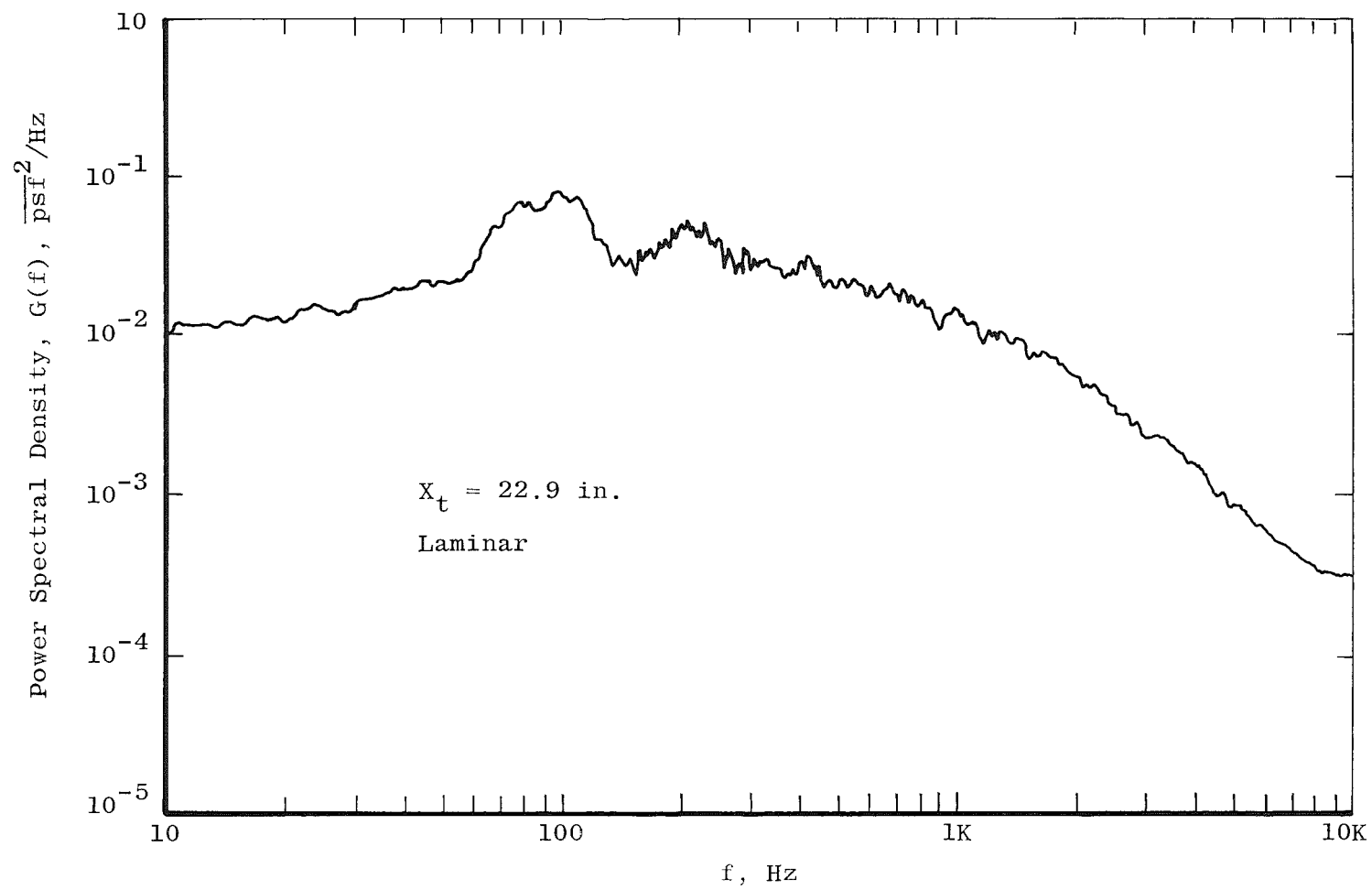


a. $M_\infty = 0.25$

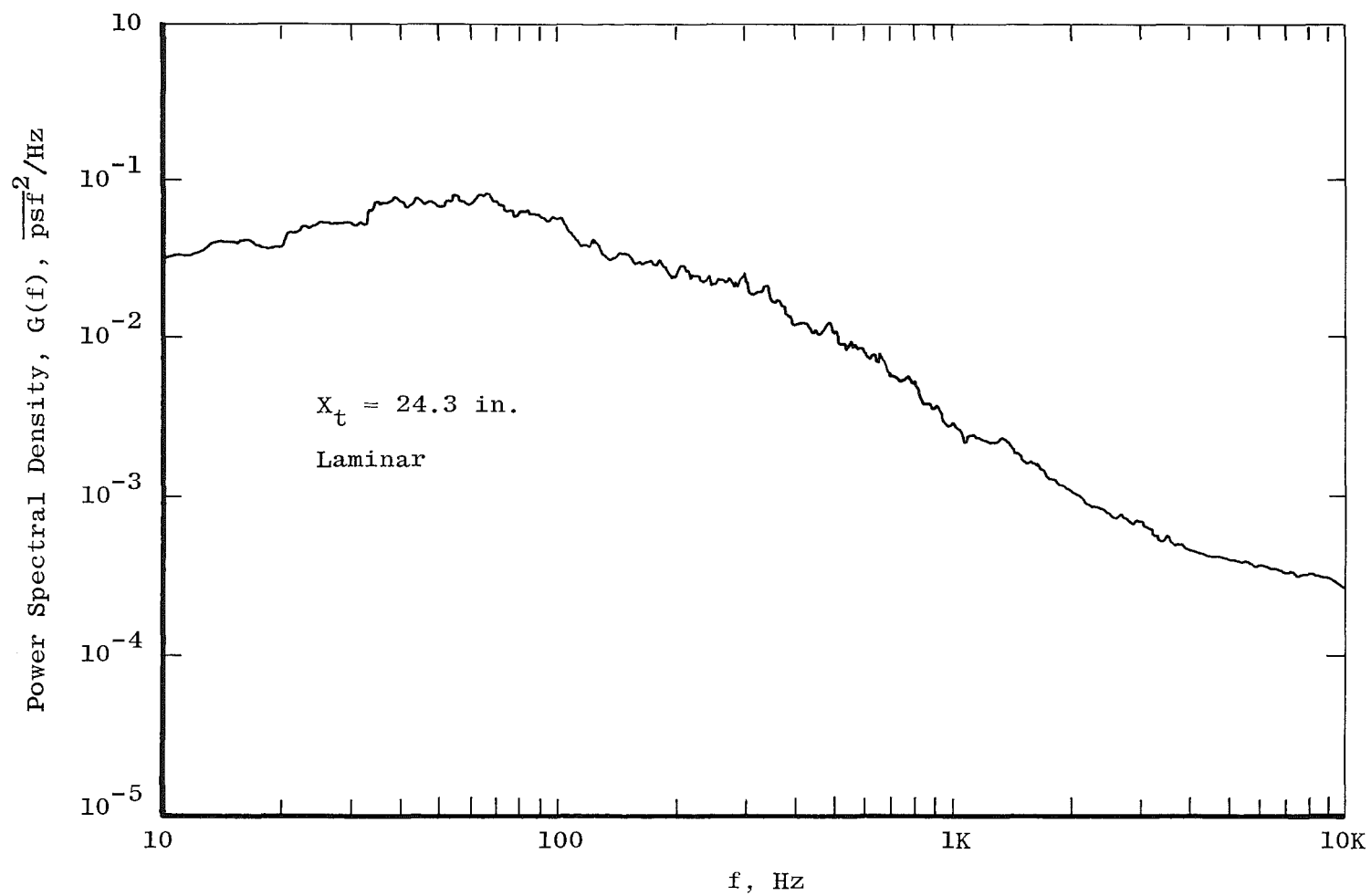
Figure 25. Power spectral density measurements in the NSR&DC 7 x 10 T.



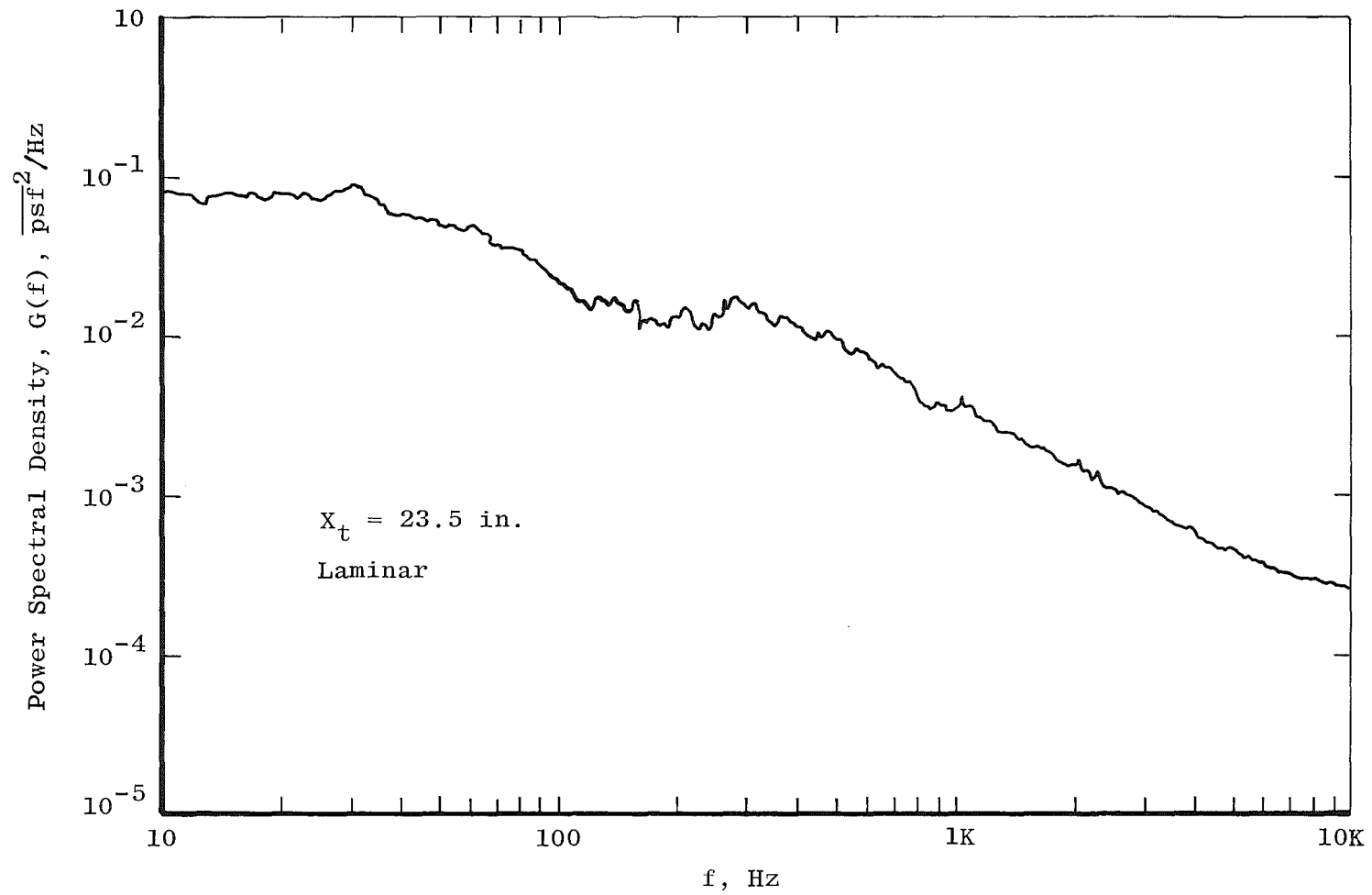
b. $M_\infty = 0.40$
Figure 25. Continued.



c. $M_\infty = 0.77$
Figure 25. Continued.



d. $M_\infty = 0.985$
Figure 25. Continued.



e. $M_\infty = 1.10$
Figure 25. Concluded.

Table 5. Naval Ship R&DC 7 x 10 T Data

M_∞	$U_\infty / \nu_\infty \times 10^{-6}$	ΔC_p , percent	$Re_t \times 10^{-6}$	$Re_T \times 10^{-6}$
0.599	3.270	0.73	3.58	4.333
0.896	3.918	0.46	-	-
0.949	3.986	0.42	-	-
0.801	3.800	1.01	2.69	3.483
0.850	3.835	0.67	3.13	4.315
0.752	3.652	1.13	3.56	4.352
0.700	3.674	0.97	3.15	3.858
0.800	3.800	1.02	2.72	3.167
0.601	3.292	0.71	3.29	4.005
0.652	3.468	0.82	3.37	4.190
0.700	3.596	0.97	3.55	4.301
0.750	3.703	1.10	3.74	4.459
0.777	3.797	1.10	3.27	3.892
0.801	3.810	1.03	2.54	3.175
0.825	3.862	0.85	2.57	3.315
0.726	3.659	1.07	3.20	4.451
0.196	1.301	1.01	2.58	-
0.301	1.950	0.49	2.88	4.047
0.349	2.227	0.47	2.86	4.046
0.401	2.511	0.49	2.86	3.955
0.450	2.755	0.50	3.03	3.903
0.500	3.001	0.54	2.80	3.701
0.552	3.231	0.64	2.83	3.635
0.253	1.673	0.39	2.79	4.087
0.736	1.696	1.17	3.14	4.311
0.755	1.718	1.21	3.24	4.366
0.777	1.739	1.28	3.32	4.493
0.801	1.766	1.15	3.44	4.638
0.828	1.787	0.97	3.62	4.770
0.852	1.804	0.73	3.62	-
0.878	1.819	0.93	3.79	-
0.886	1.869	1.00	3.74	-
0.923	1.879	0.44	3.95	-
0.950	1.896	0.47	3.87	-
0.985	1.932	0.45	3.91	-
1.032	1.951	0.98	4.35	-
1.057	2.007	0.43	3.60	-
1.098	2.015	0.43	3.07	5.210
1.122	2.037	0.55	3.26	4.500
1.140	2.055	-	2.48	4.281
0.301	2.192	0.52	2.83	4.056
0.349	2.546	0.49	2.99	3.926
0.398	2.911	0.50	3.08	3.911
0.449	3.280	0.53	3.28	4.018
0.498	3.623	0.60	3.38	4.151
0.549	3.998	0.56	-	4.198

Table 5. Concluded

M_∞	$U_\infty / v_\infty \times 10^{-6}$	ΔC_p , percent	$Re_t \times 10^{-6}$	$Re_T \times 10^{-6}$
0.503	3.215	0.61	3.27	4.153
0.301	1.766	-	2.87	4.120
0.353	2.035	-	2.85	4.240
0.399	2.260	0.56	2.78	4.030
0.451	2.490	0.38	2.97	3.964
0.501	2.692	0.42	3.03	4.060
0.551	2.867	0.65	3.14	4.086
0.600	3.027	0.74	3.32	4.238
0.651	3.170	0.90	3.46	4.360
0.701	3.283	1.02	3.55	4.514
0.749	3.368	1.13	3.65	4.716
0.800	3.438	1.07	3.84	4.871
0.848	3.468	0.72	3.90	5.144
0.304	1.475	-	2.75	3.811
0.352	1.694	-	2.91	4.094
0.400	1.890	-	2.88	4.254
0.451	2.076	0.59	2.77	4.240
0.499	2.252	0.61	2.89	4.054
0.551	2.416	0.67	3.06	4.127
0.600	2.545	0.74	3.17	4.200
0.649	2.664	0.89	3.20	4.351
0.700	2.768	1.04	3.40	4.441
0.750	2.876	1.16	3.45	4.422
0.803	2.976	1.07	3.60	4.588
0.849	3.052	0.73	3.74	4.959

NLR 6.55 x 5.28 HST

No transition data were acquired on the cone in the Dutch HST at Amsterdam. However, a very useful set of noise measurements was obtained over a broad range of M_∞ and U_∞/ν_∞ using the cone microphones. During this test additional measurements were made using a sidewall-mounted Kulite pressure transducer and a hot-film anemometer, placed just outside the tunnel wall boundary-layer edge, and a Kulite pressure transducer located in the plenum chamber.

Results of the test were published by Ross and Rohne in Ref. 3. Some of these results are given in this report as they have bearing on the definition of free-stream disturbances in this type of slotted-wall transonic tunnel.

Data were obtained over a Mach number range from 0.15 to 1.3 at levels of p_t from 1,460 to 8,350 psfa. The noise levels recorded by the cone and sidewall microphones are presented in Fig. 26. Even though p_t (and U_∞/ν_∞) in this tunnel at Mach numbers 0.15 to 0.3 covered a very broad range, ΔC_p remained essentially invariant with p_t .

As seen in Fig. 26, agreement between the two cone microphones was good except at $M_\infty = 1.1$ and 1.3, where the impingement of extraneous shock waves on the aft microphone was suspected to have raised ΔC_p . In Ref. 3, slight differences in overall ΔC_p were noted between $M_\infty = 0.6$ and 1.1 between the sidewall transducer and the cone microphones.

Ross and Rohne (Ref. 3) attribute the major source of disturbance in the HST to the variable speed main compressor. Blade-passing tones were registered on both microphone and hot-film anemometer instrumentation. Typical frequency spectra to 4 kHz are shown in Fig. 27. Cone microphone power density spectra are shown for $p_t = 2,090$ psfa at $M_\infty = 0.3, 0.8$, and 1.1.

Space-time correlations performed by Ross and Rohne between the two cone microphones and between the wall transducer and the hot-film anemometer showed the predominant spectral components to be traveling in the upstream direction with propagation velocities corresponding to $(1 - M_\infty)$. No correlations were found at velocities corresponding to M_∞ or $(1 + M_\infty)$, which would have indicated downstream-traveling waves.

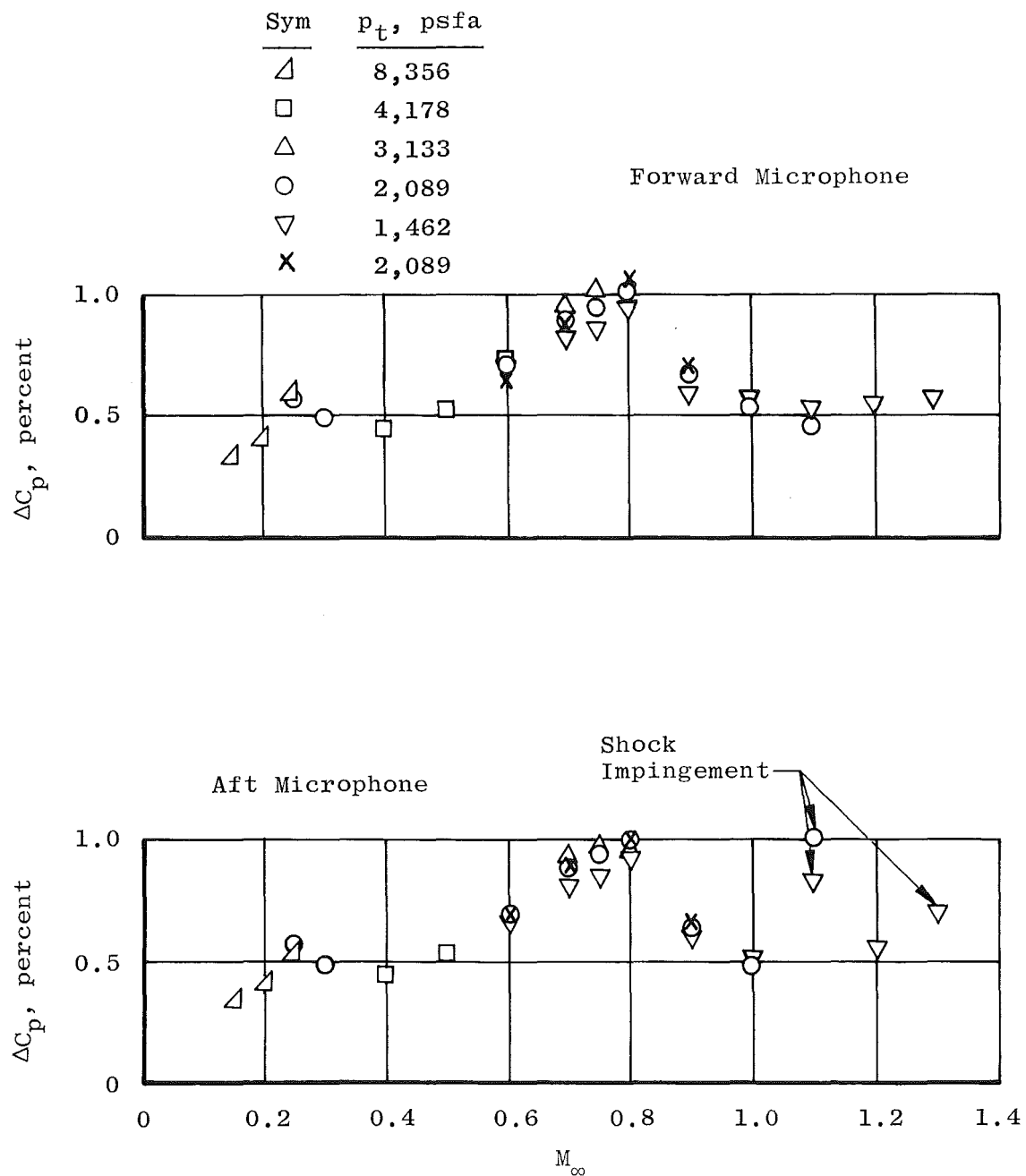


Figure 26. Noise levels in the NLR 6.55 x 5.28 HST.

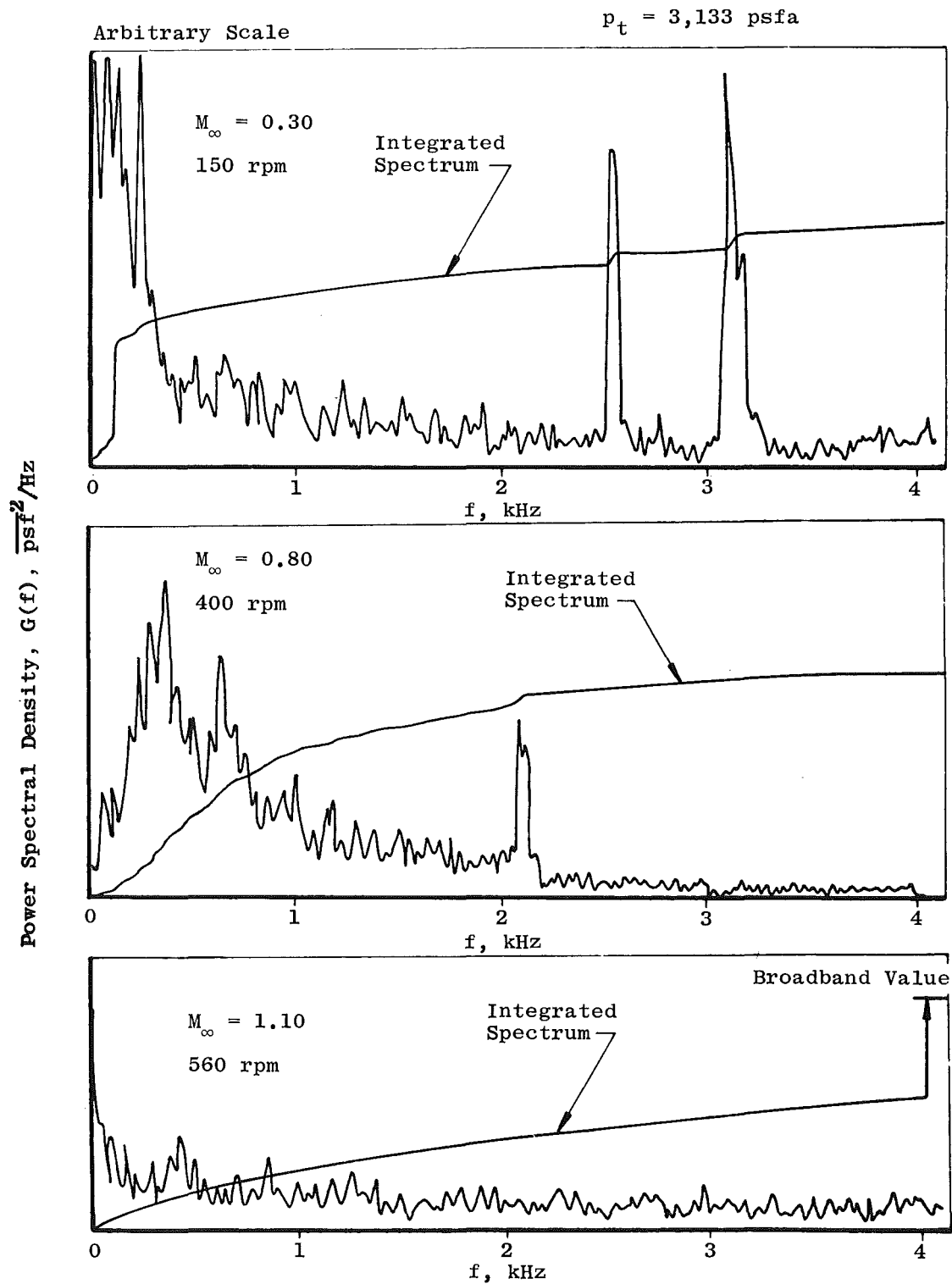


Figure 27. Typical power spectral densities of cone microphone data in the NLR 6.55 x 5.28 HST.

NASA/Ames 12 PT

Data were acquired on the cone in the NASA/Ames 12 PT at $M_\infty = 0.2, 0.5, 0.7,$ and 0.9 at U_∞/ν_∞ levels between 1.4×10^6 and 3.5×10^6 . End-of-transition Reynolds numbers, Re_T , at $U_\infty/\nu_\infty = 2.0 \times 10^6$ and 3.0×10^6 are shown in Fig. 28; onset-of-transition Reynolds numbers are shown in Fig. 29.

Measured values of ΔC_p are shown in Fig. 30 for M_∞ varied from 0.2 to 0.9 . These data are compared with prior measurements by Dods and Hanly (Ref. 4) which were taken at higher levels of p_t than the present measurements. Neither set of measurements shown is sufficiently complete to define what ΔC_p variation with p_t (U_∞/ν_∞) exists in this tunnel; however, the present data and Ref. 4 data appear to be in reasonably good agreement, the maximum in ΔC_p occurring near $M_\infty = 0.65$. The measured data are presented in Table 6.

Power spectral density measurements are presented in Fig. 31 and show that strong discrete disturbances dominate the spectra at $M_\infty = 0.50, 0.70,$ and 0.90 . However, it was not determined from what sources these disturbances were generated.

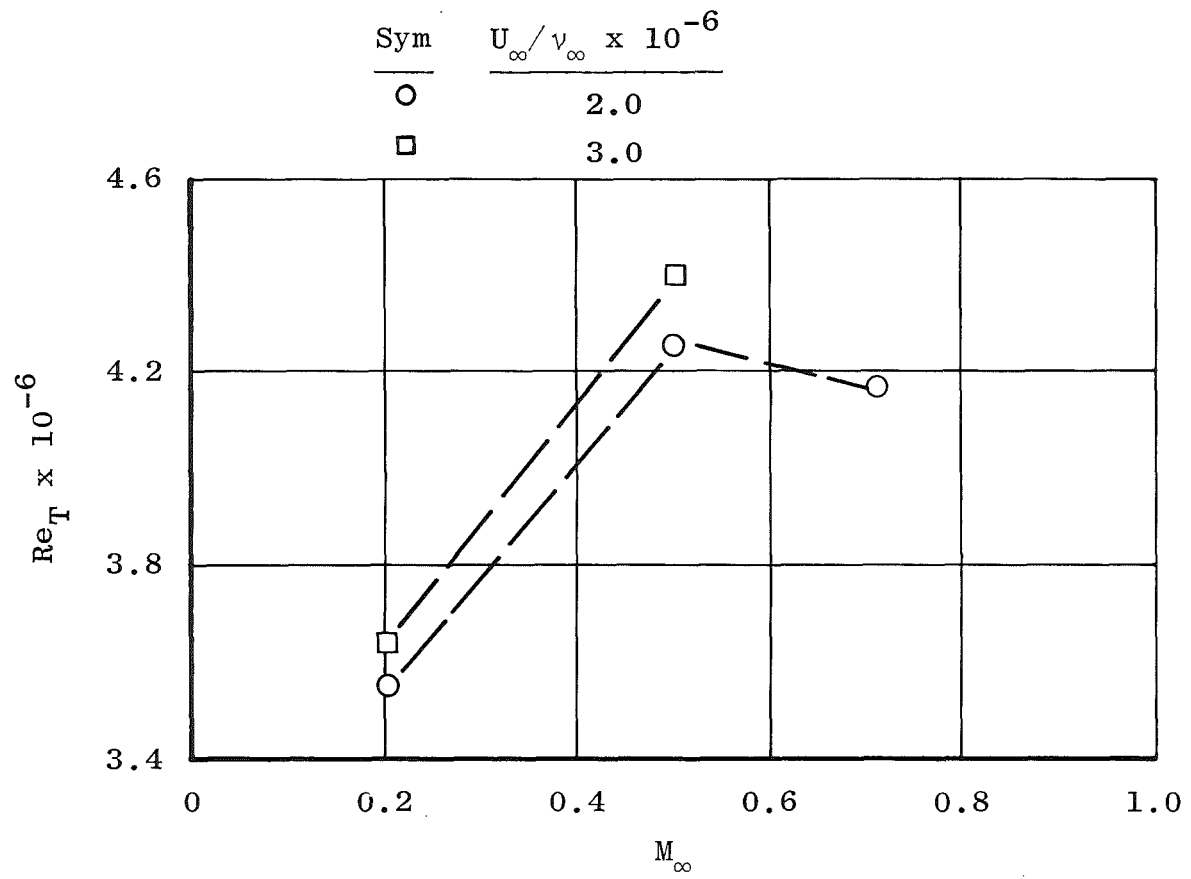


Figure 28. End-of-transition Reynolds numbers in the NASA/Ames 12 PT.

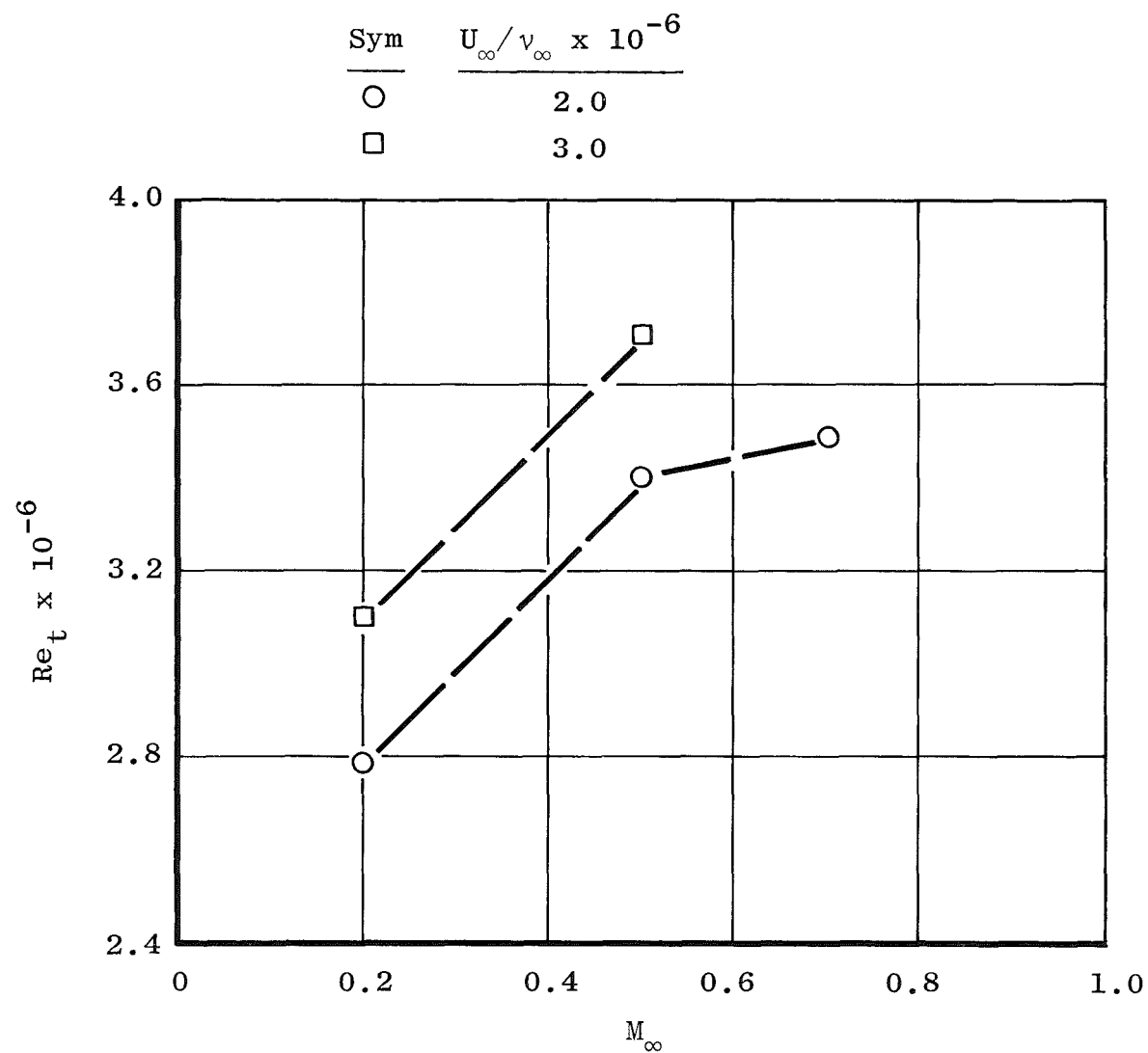


Figure 29. Onset-of-transition Reynolds numbers in the NASA/Ames 12 PT.

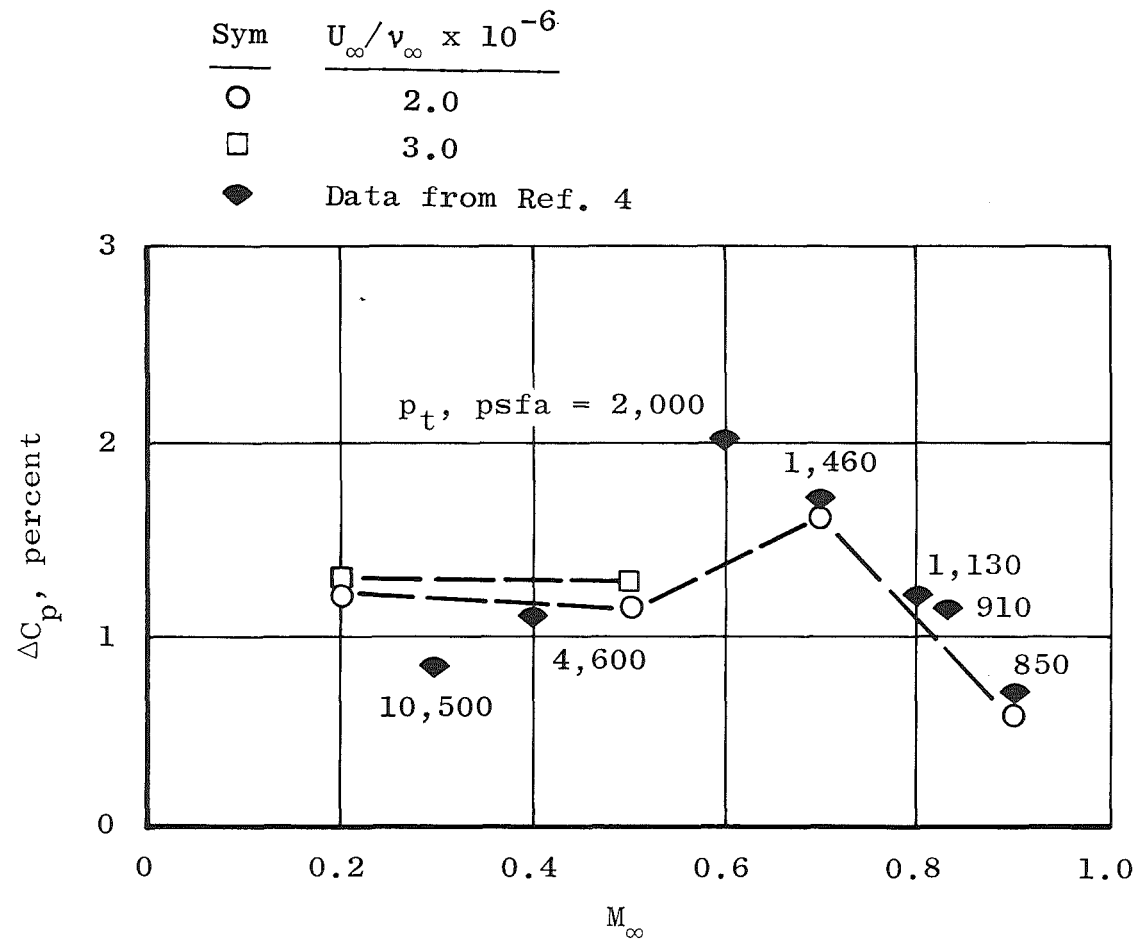
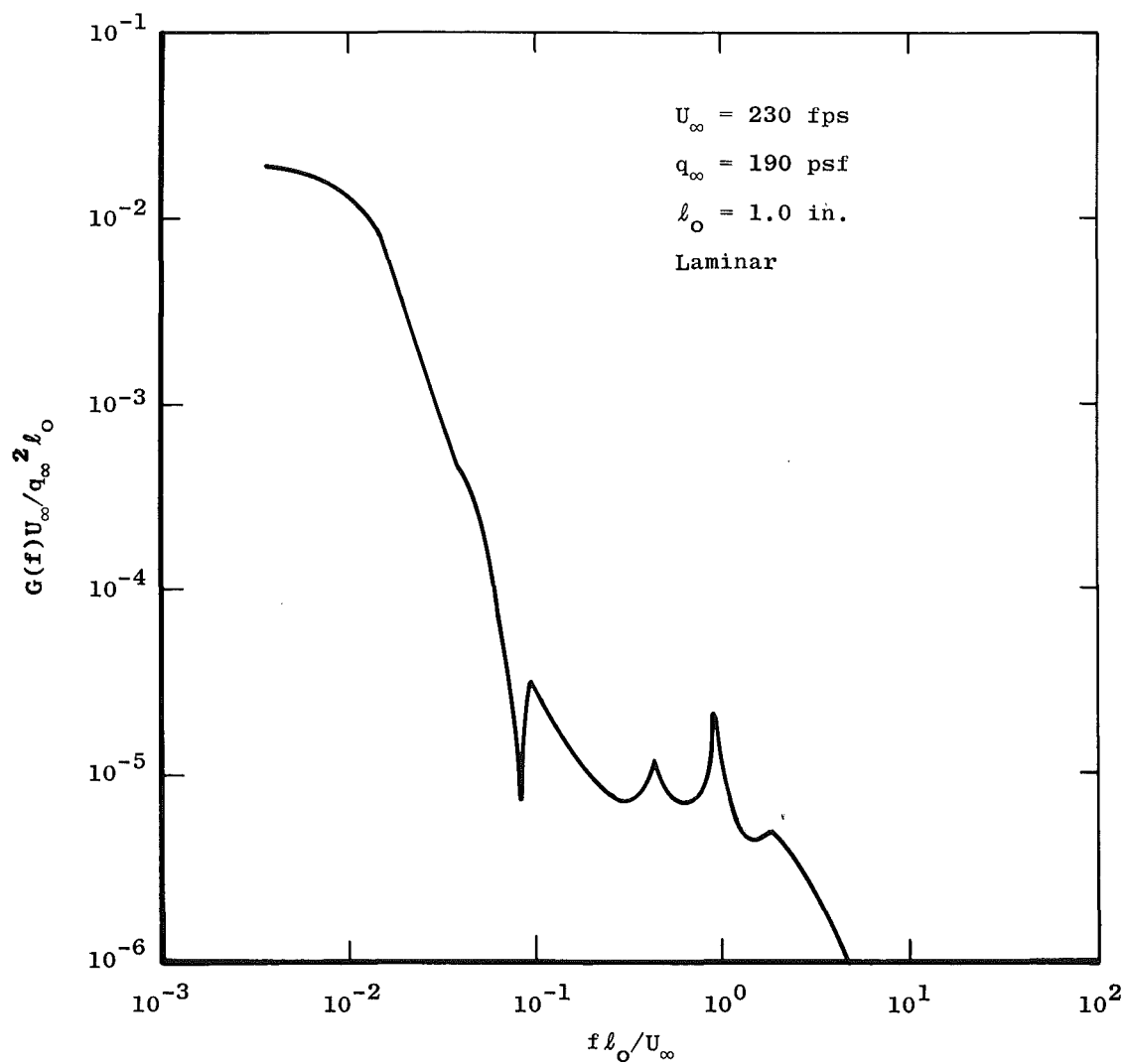
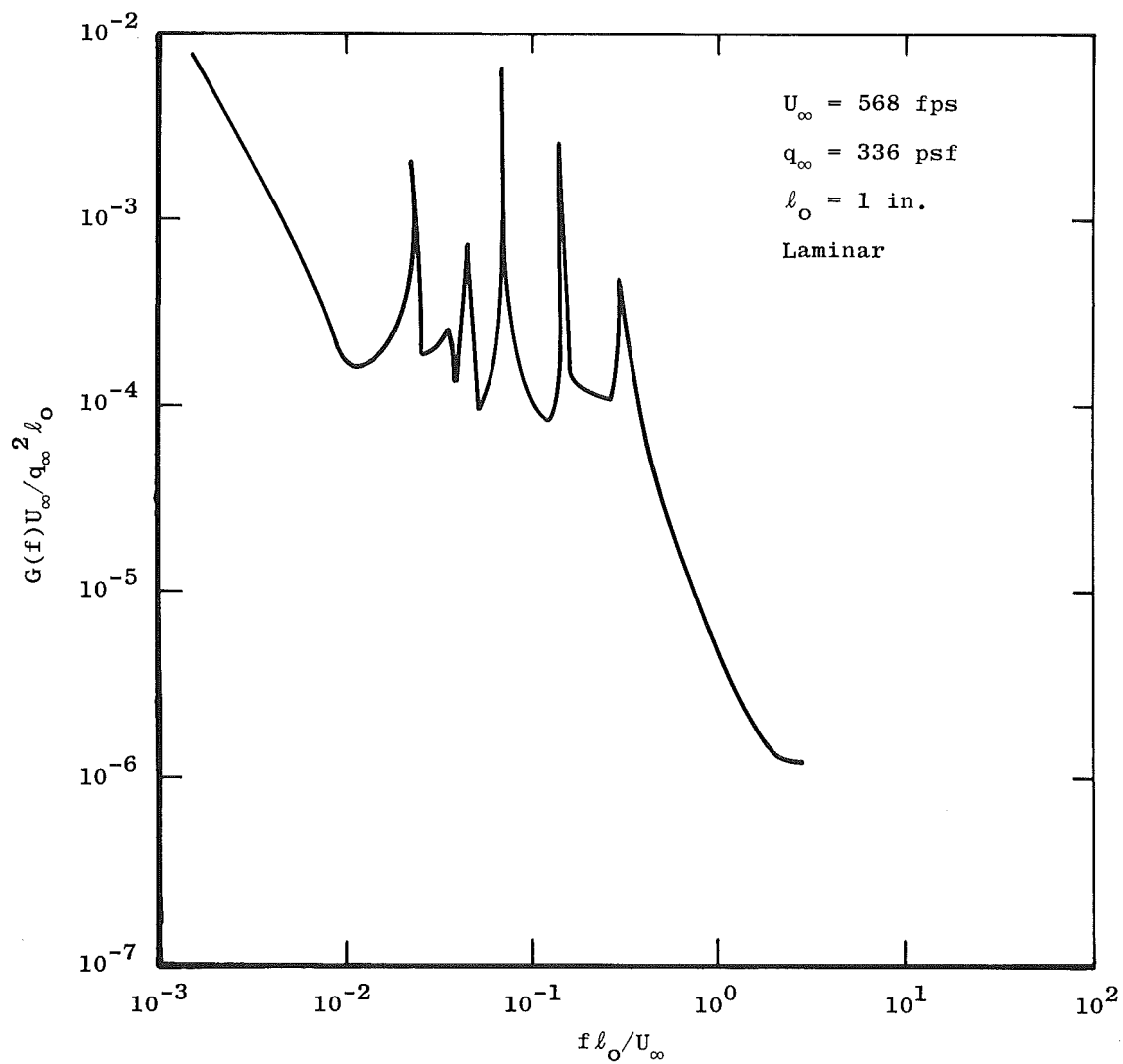


Figure 30. Noise levels in the NASA/Ames 12 PT.

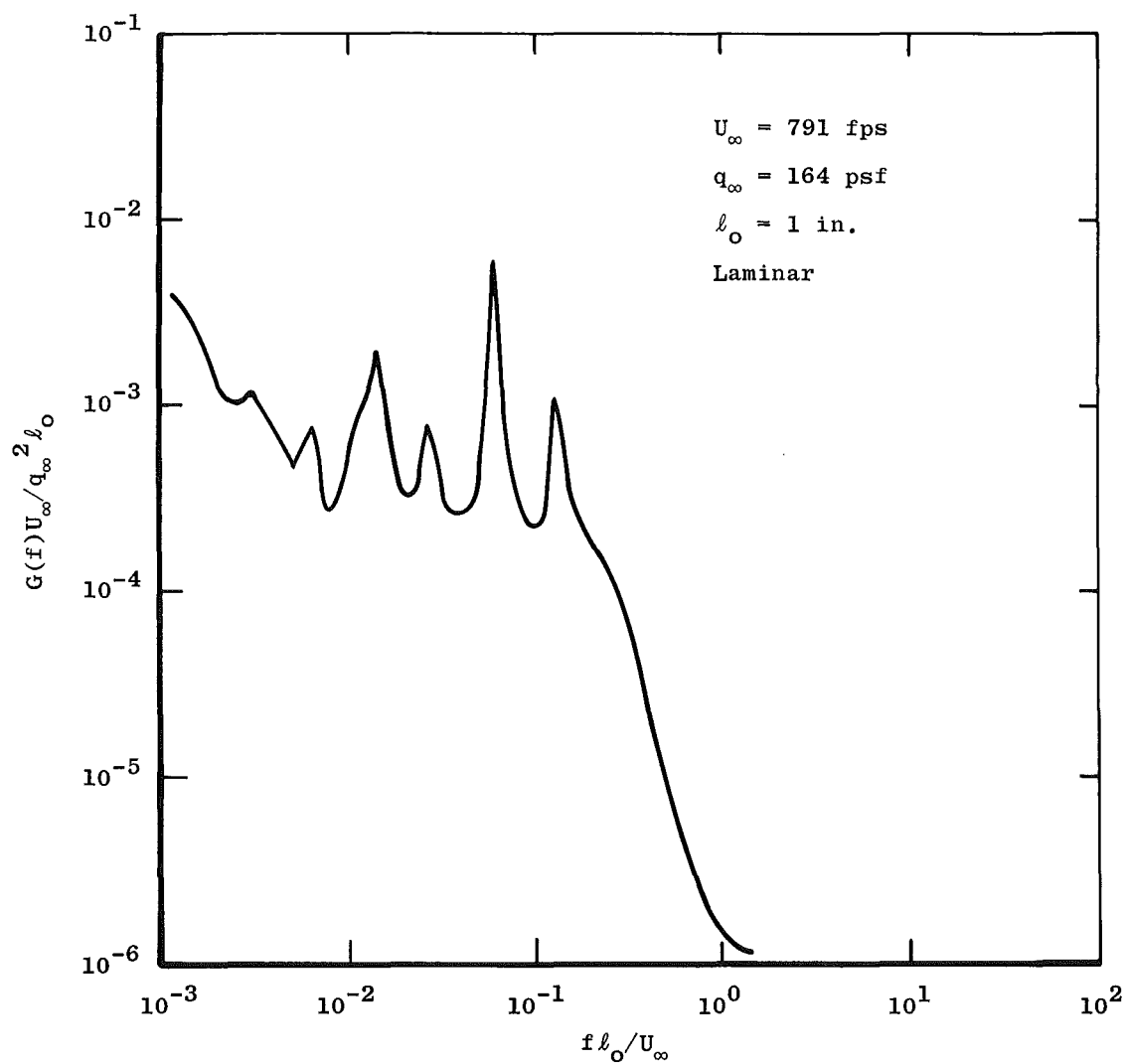


a. $M_{\infty} = 0.20$

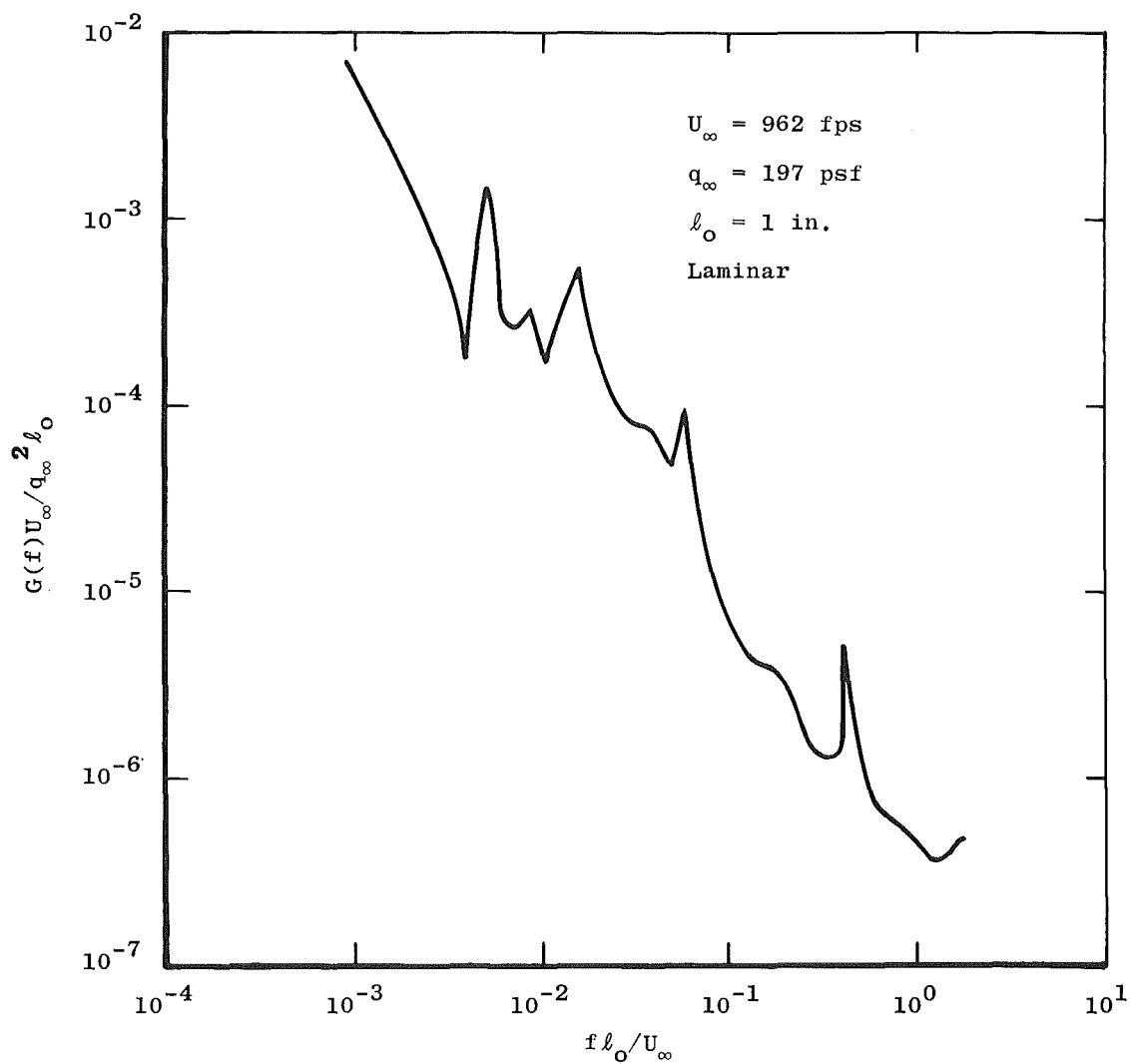
Figure 31. Power spectral density measurements in the NASA/Ames 12 PT.



b. $M_\infty = 0.50$
Figure 31. Continued.



c. $M_\infty = 0.70$
Figure 31. Continued.



d. $M_\infty = 0.90$
Figure 31. Concluded.

Table 6. NASA/Ames 12 PT Data

M_∞	U_∞ / ν_∞ $\times 10^{-6}$	ΔC_p , percent	$Re_t \times$ 10^{-6}	$Re_T \times$ 10^{-6}
0.20	1.42	1.20	2.62	3.48
0.20	3.00	1.29	3.10	3.66
0.20	3.50	—	3.27	3.74
0.50	1.50	—	3.45	4.14
0.50	1.95	1.13	3.41	4.28
0.50	2.98	1.28	3.62	4.43
0.70	2.04	1.53	3.48	4.16
0.70	2.27	1.73	3.57	4.37
0.90	1.95	0.56	—	—

RAE Farnborough 8 x 6

Data were acquired in the RAE Farnborough 8 x 6 wind tunnel using only the cone microphones and a fixed pitot probe affixed to the cone surface at 18.0 in. from the apex, opposite the forward microphone. The installation was as shown in Fig. 32. Because the fixed pitot probe generated a turbulent wake behind it, sublimation techniques were employed to verify that transition over the aft microphone was unaffected by the probe. Napthalene and acenaphthene were used as the indicators. A photograph of the turbulent wake made visible by this technique is shown in Fig. 33. The measurements were made by D. G. Mabey of RAE and were reported in Ref. 5. A portion of the results is repeated in this report for the purpose of tunnel-to-tunnel correlation.

Measurements indicating transition passage over the 18-in. location of the cone by the fixed pitot probe and forward microphone, respectively, are shown in Fig. 34 at $M_\infty = 0.3$ and 1.19. Here C_p from the pitot probe (defined as pitot pressure normalized by q_∞) is shown on the left-hand scale, and $\sqrt{p'^2}/q = \Delta C_p/100$ from the microphone is shown on the right-hand scale. Notable events in the transition process as observed by Mabey are indicated.

The predominant source of disturbances in this tunnel was found to be fan noise, concentrated at 140 Hz for $M_\infty = 0.6$. In order to minimize confusion between the fan noise and the increase in amplitude associated with transition, a tunable high-pass filter with a cutoff setting of about 200 Hz was used for the microphone data during transition detection. Use of the filter made the oscillations (in particular, turbulent spots) more readily identifiable.

Mabey found the end-of-transition Reynolds numbers, Re_T , from the fixed pitot probe to be in reasonably good agreement with those from the microphone. The Re_T data are presented in Fig. 35. The ΔC_p data are presented in Fig. 36. As was observed in Ref. 5, the surface imperfections and slightly bent cone tip existing during this test had an undeterminable degree of influence on the results. This influence apparently caused earlier transition, rendering these data uncorrelatable with those from other facilities.

Photo Courtesy of the
Royal Aircraft Establishment,
Farnborough, England

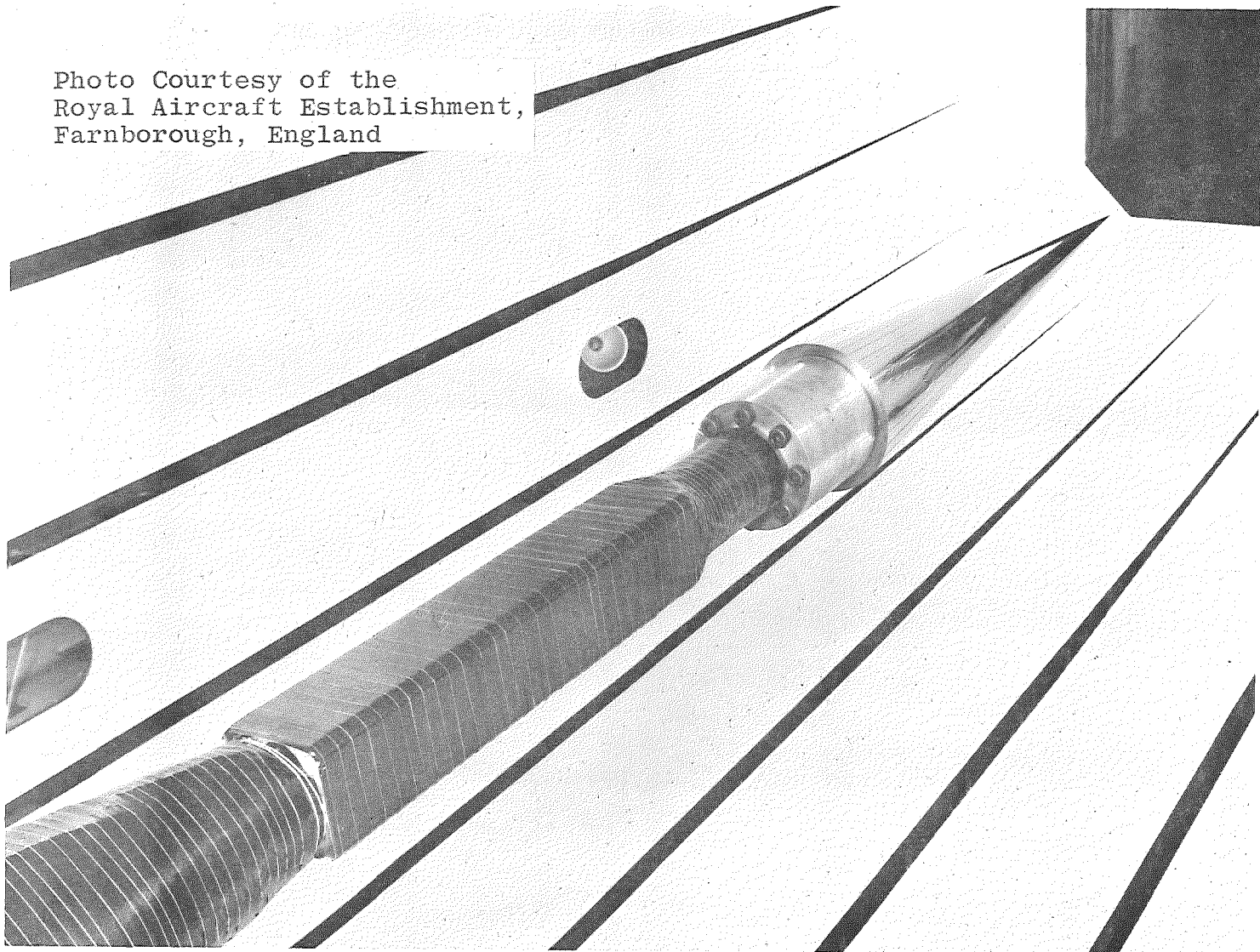


Figure 32. Photograph of the cone installed in the RAE Farnborough 8 x 6.

Photo Courtesy of the
Royal Aircraft Establishment,
Farnborough, England

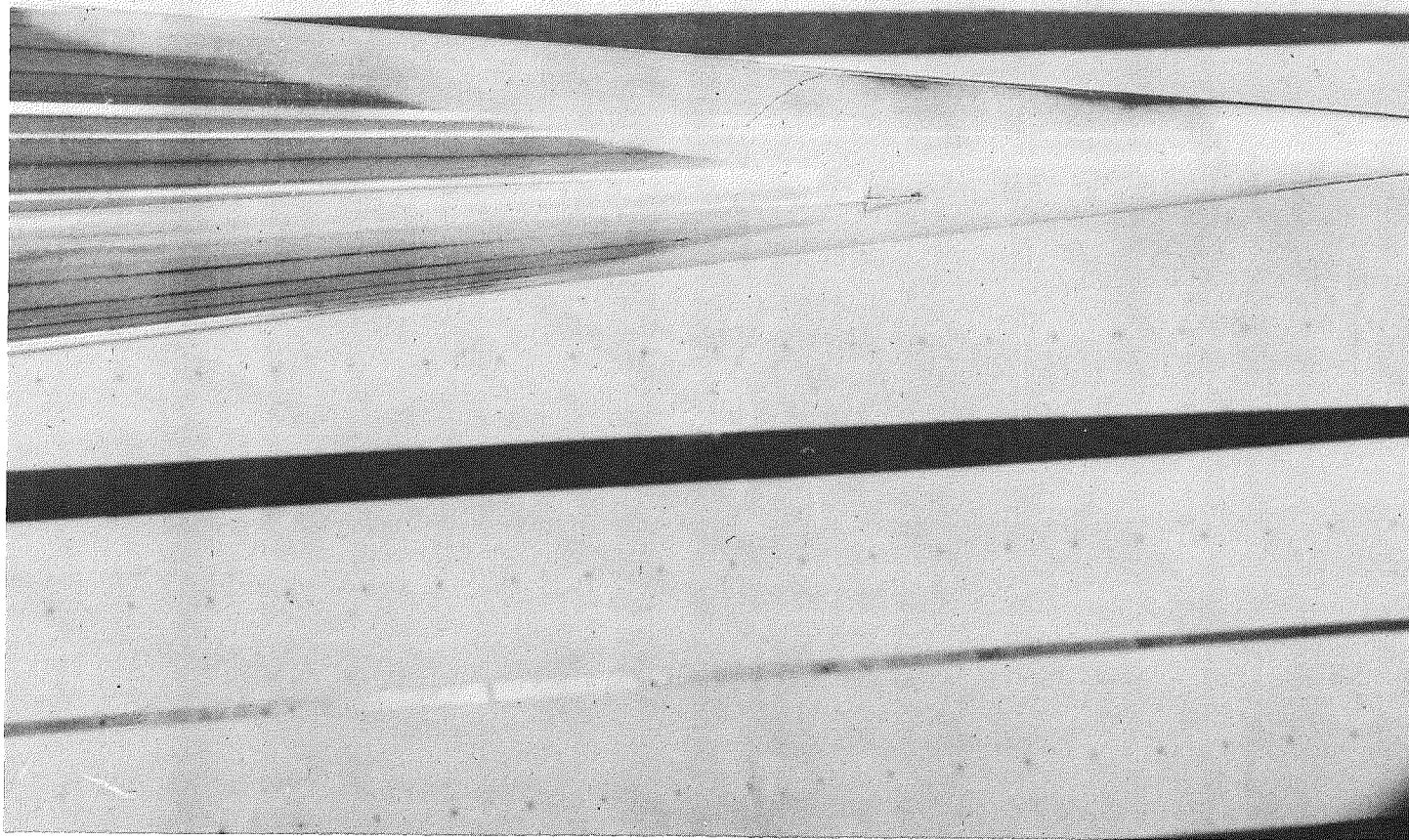
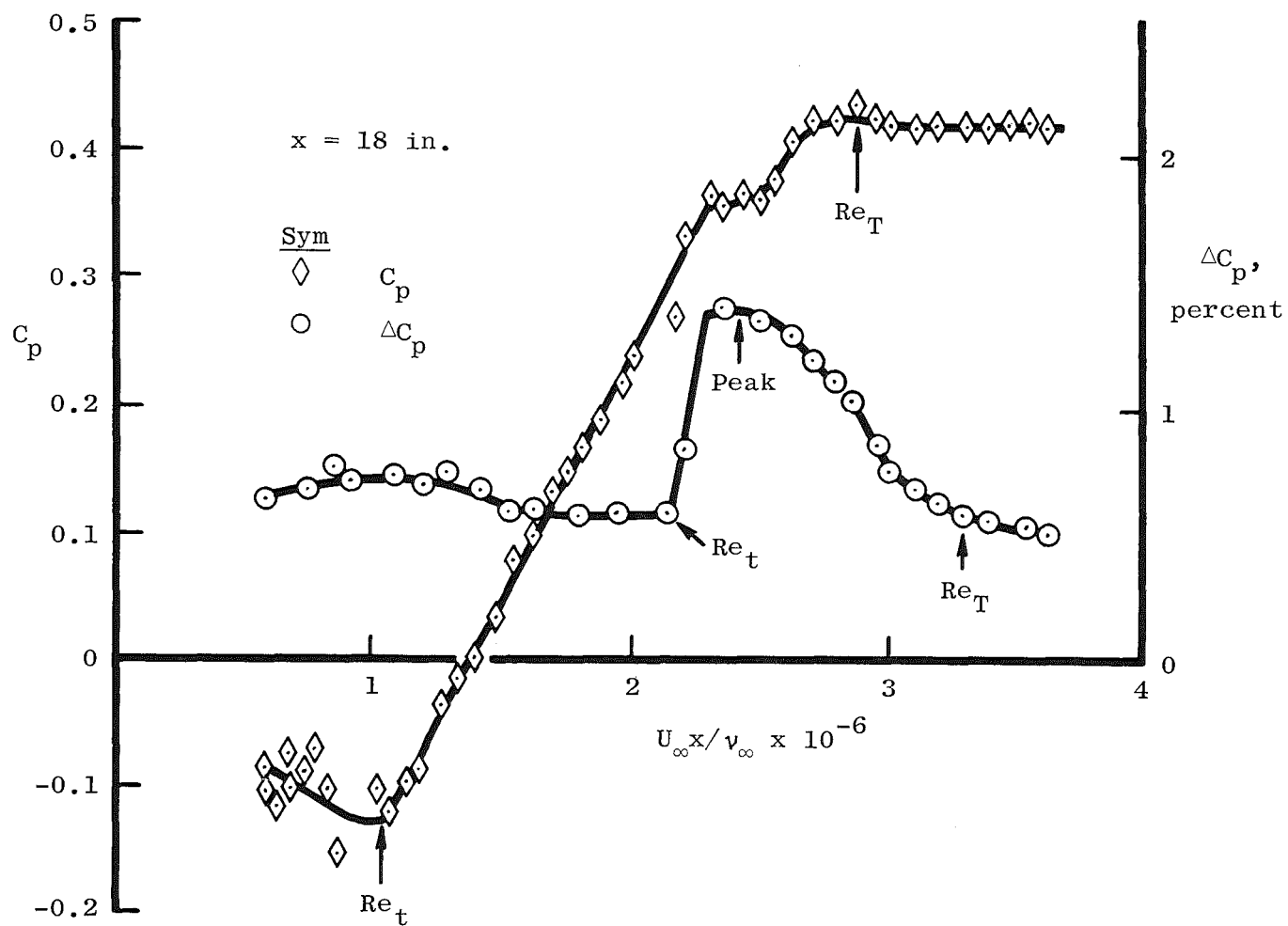
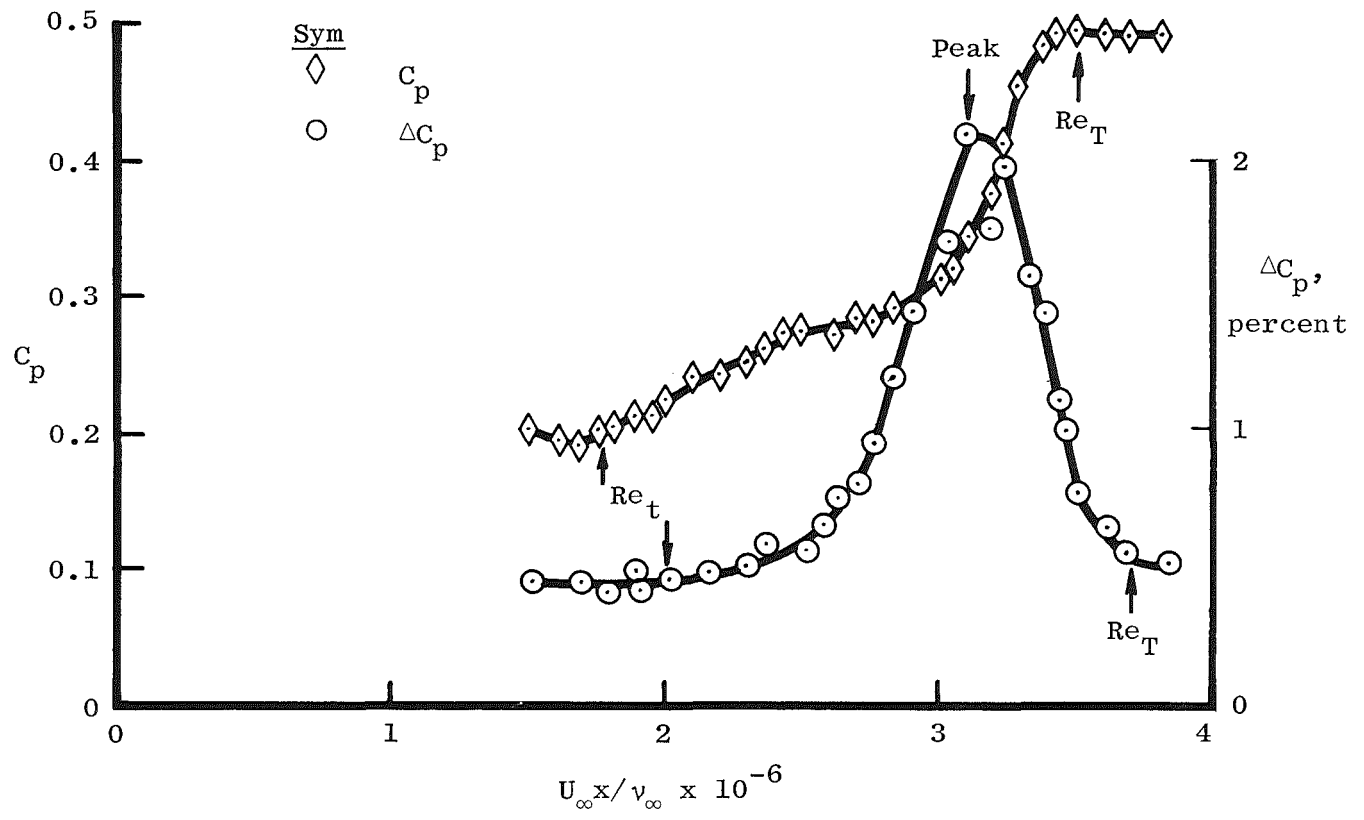


Figure 33. Photograph of the sublimation pattern behind the fixed pitot probe attached to the cone surface.



a. $M_\infty = 0.30$

Figure 34. Comparison of the cone microphone and the fixed pitot probe data in the RAE Farnborough 8 x 6.



b. $M_\infty = 1.19$
Figure 34. Concluded.

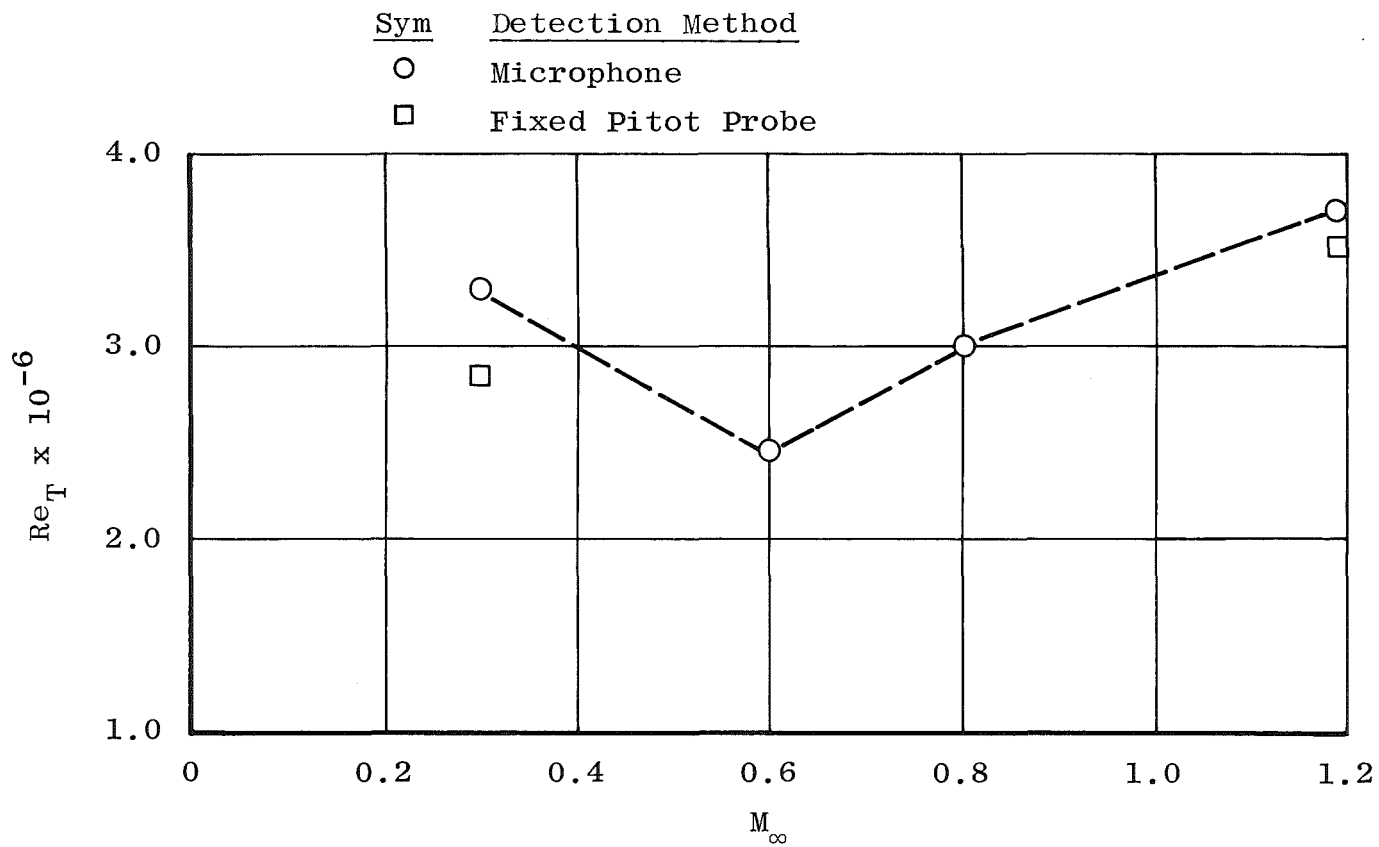


Figure 35. End-of-transition Reynolds numbers in the RAE Farnborough 8 x 6.

Note: Peak near $M_\infty = 0.6$ is due to 140-Hz fan noise.

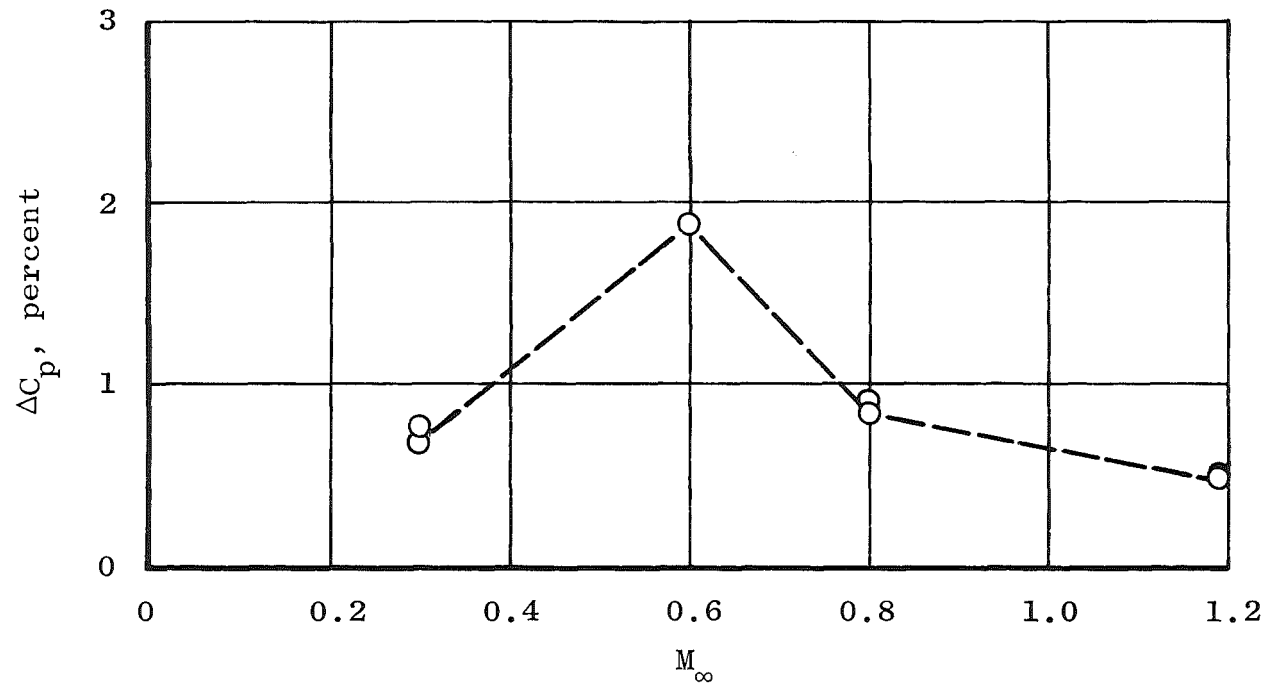


Figure 36. Noise levels in the RAE Farnborough 8 x 6.

3.3.2 Group 2 Tunnels: Transonic, Porous

AEDC/PWT Tunnel 4T

There were three test entries of the cone in AEDC 4T, spanning six years. During the first entry, the tunnel was operated normally. During the second and third entries, controlled acoustic disturbance variations were attempted by three methods:

1. discrete-frequency siren noise addition from four high power 50-watt speakers,
2. sealing of the porous test section walls using tape on the airstream surface of all four walls, and
3. installation of a wire screen overlay on the airstream side of the test section walls.

Both the tape and the wire screen overlay gave effective suppression of the porous wall edgetones (Ref. 6) and a measurable shift in transition Reynolds number. The results of the siren noise tests, during which frequencies were varied between 500 Hz and 8 kHz, were entirely negative. The four speakers were placed behind the test section walls inside the plenum chamber, and at full power there was no case of any flow condition in the tunnel where the siren sound pressure amplitude was sufficiently high to register above the test section background level.

Photographs of the cone installed in AEDC 4T during walls-taped and wire screen overlay experiments are shown in Fig. 37. In Fig. 38, end-of-transition Reynolds numbers, Re_T , are shown for normal operation, walls taped, and walls with screen overlay. The porosity, τ , was variable and represents the optimum porosity schedule for the test section walls. (See Table 7 for the variations in τ with M_∞ .) Different optimum porosity settings of $\tau = 3$ percent for $M_\infty = 1.0$ to 1.2, and 4 percent for $M_\infty = 1.3$, were determined in a tunnel calibration with screen overlay prior to this cone entry. The data for normal tunnel operation, open symbols, indicate that a strong variation exists in Re_T with M_∞ and that a slight variation also exists in Re_T with U_∞/ν_∞ . The influence of the walls-taped and wire screen overlay configurations was to hold Re_T near constant in this tunnel at 3.5 to 3.8×10^6 , for Mach numbers up to 1.1. These tests in AEDC 4T have served not only to characterize transition Reynolds number trends in this particular tunnel but to show that particular isolated acoustic disturbances predominant in this tunnel have a measurable influence on cone transition.

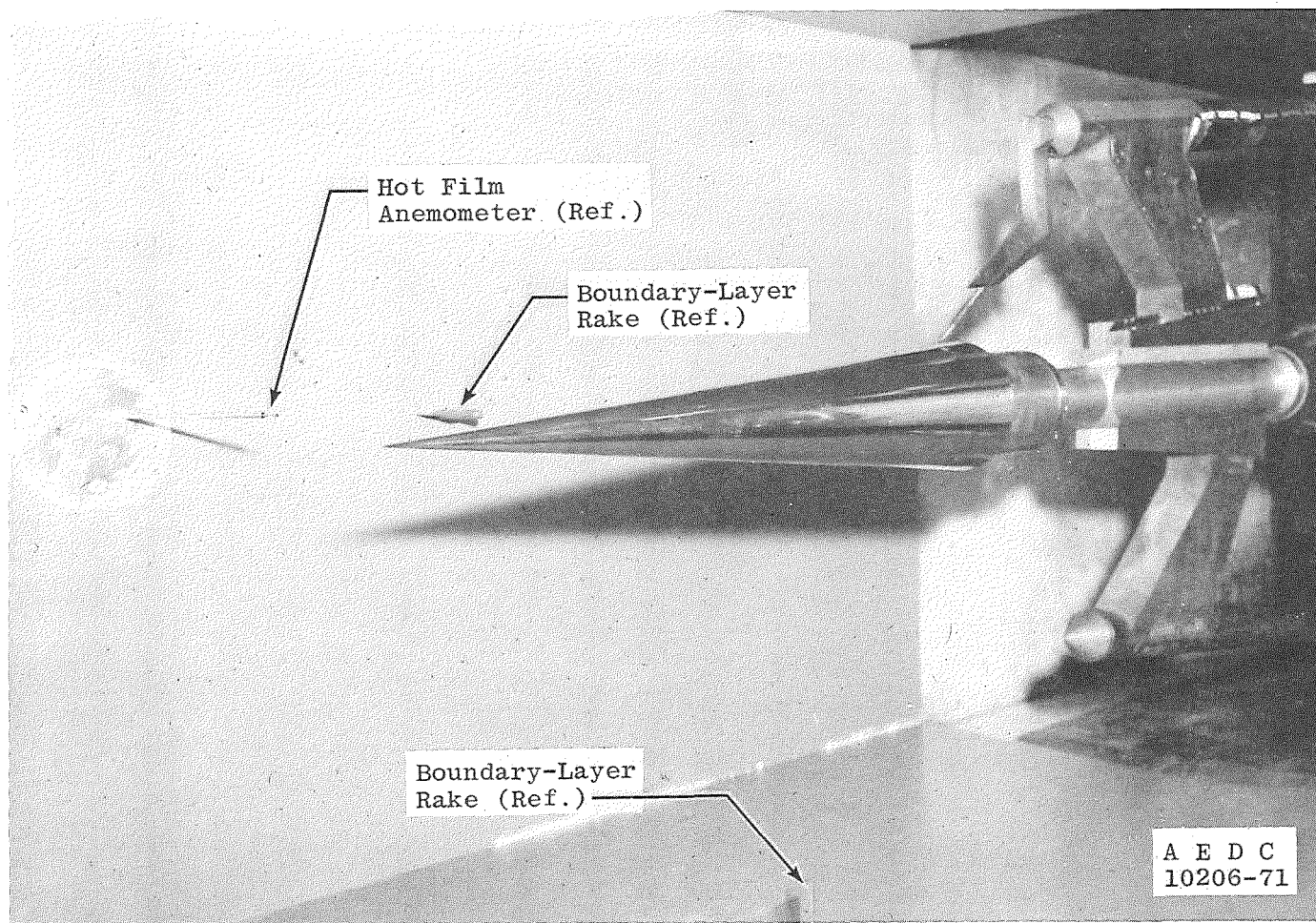
Onset-of-transition Reynolds numbers, Re_t , are shown in Fig. 39, reflecting about the same variations as the Re_T data. The change in transition locations is clear from these

wall-noise suppression tests. In the presentation of data in Figs. 38 and 39, a weighting of the data toward the first and third entries was made, as there was evidence in the second-entry data that a hot-film probe in the test section (installed for an attempt to measure velocity fluctuations) had an influence on the cone transition location. Because of the shedding of turbulence from the probe, it was furthermore judged that the hot-film data were invalidated by the vibratory motions experienced by the probe.

The variation in ΔC_p at these same flow conditions is presented in Fig. 40, and it is clearly shown that the wire screen and walls-taped cases yielded comparably lowered noise levels. Typical spectra recorded by the microphones for normal walls and taped walls are shown for Mach numbers from 0.3 to 0.8 in Fig. 41. While there was a reduction in amplitude across the full spectrum from 100 Hz to 10 kHz, it is particularly to be noted that the narrow-band (discrete) components dominating the normal wall spectra at $\tau = 6$ percent were eliminated.

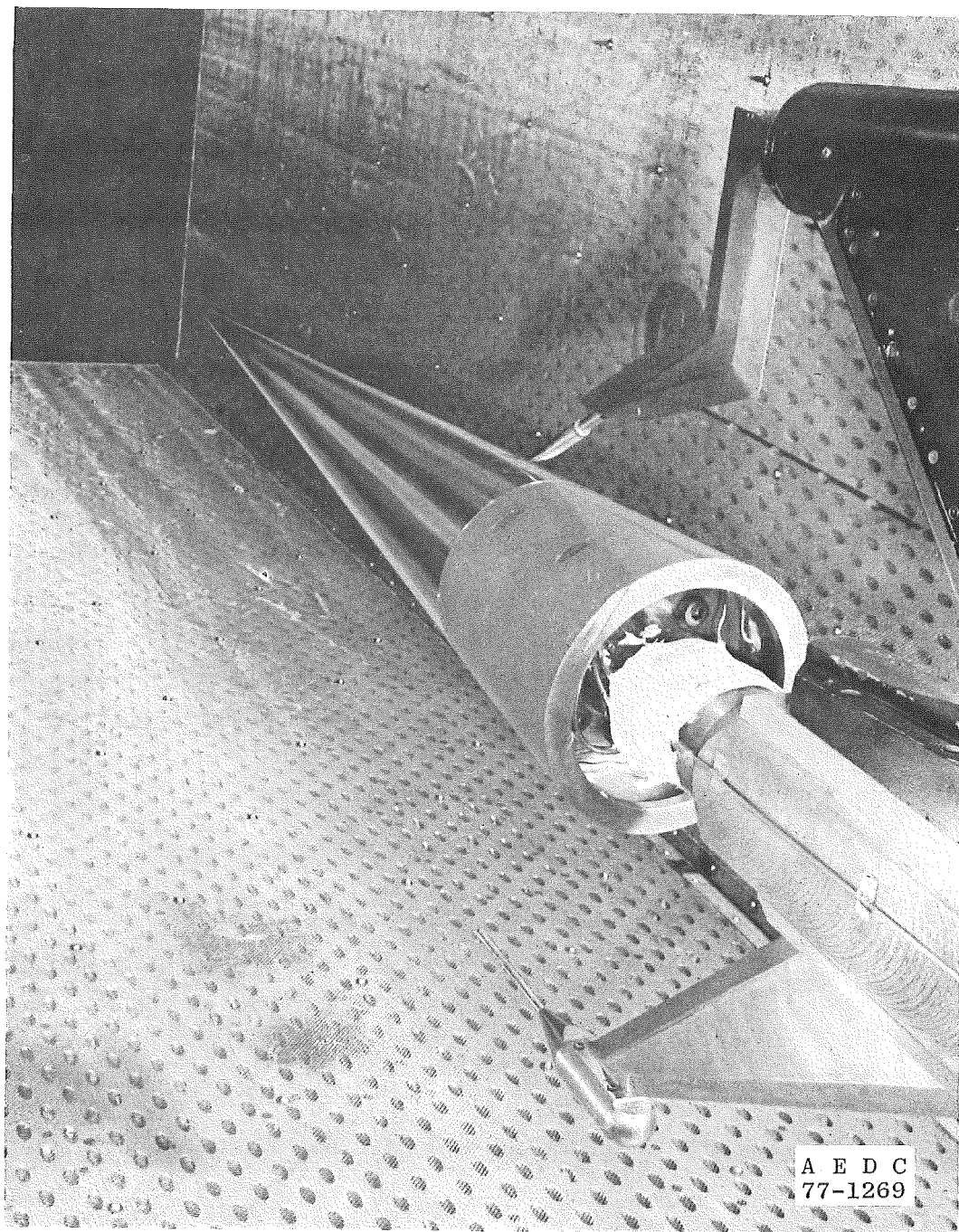
The walls-taped Re_T data are given only for $M_\infty \leq 0.7$ because of possible blockage interference effects for $M_\infty > 0.7$. Although the wire screen overlay permitted test section ventilation and operation to M_∞ as high as 1.3 at reduced noise levels, the pitot probe data providing transition detection also indicated the existence of many shock waves impinging on the cone. These shock waves probably emanated from the bolt heads which secured the screens in place in this temporary-type installation. A more permanent screen installation could utilize adhesive bonding such as has been described by Schutzenhofer and Howard for the NASA/Marshall Space Flight Center 14-in. Transonic Tunnel at Huntsville, Alabama (see Ref. 7).

A complete set of tabulated data is given in Table 7.

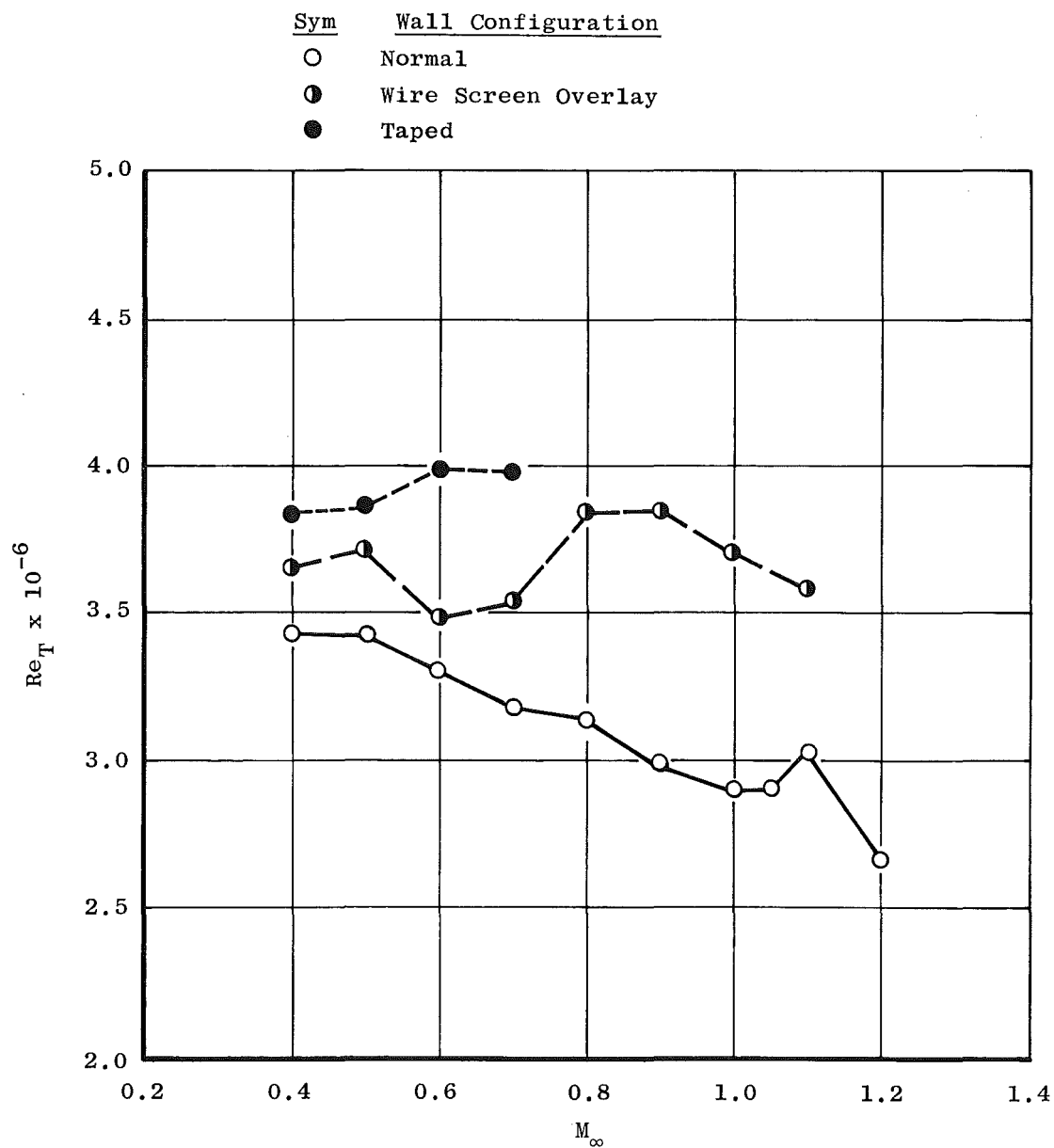


a. Entry with walls taped

Figure 37. Photographs of the cone installed in AEDC/PWT Tunnel 4T with tape and wire screen on the tunnel walls.

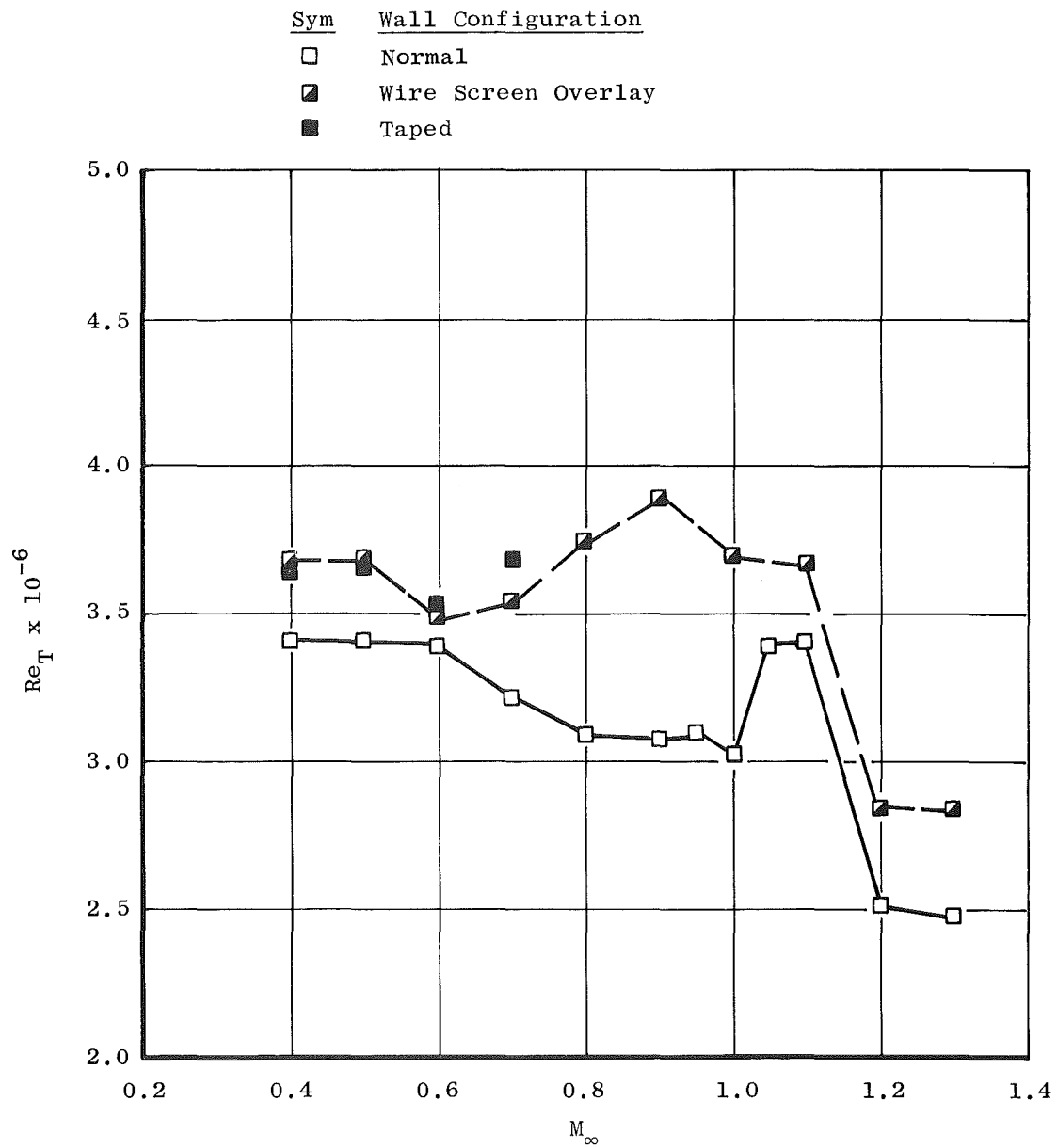


b. Entry with wire screen overlay
Figure 37. Concluded.

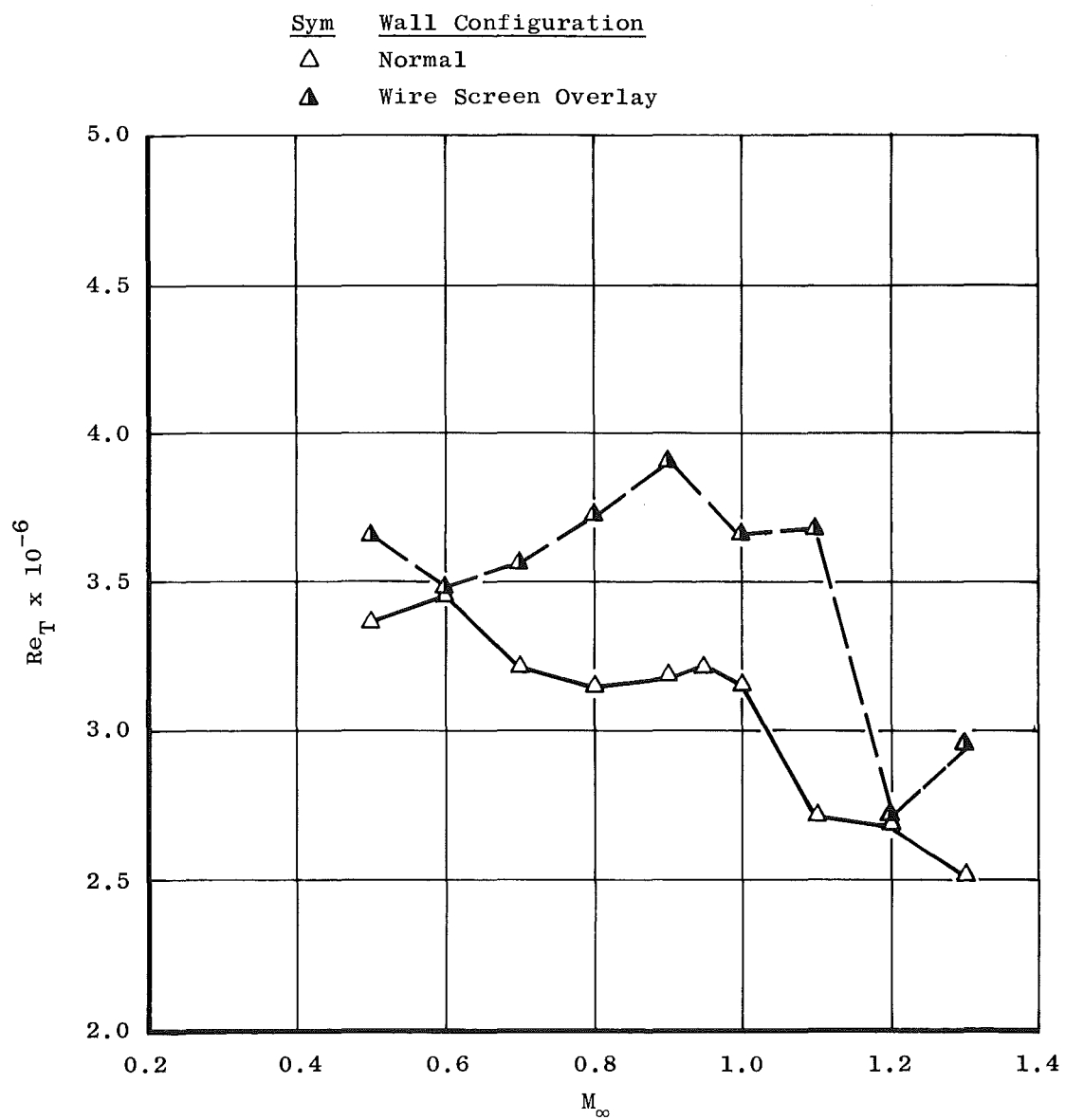


a. $U_\infty/\nu_\infty = 2.0 \times 10^6$

Figure 38. End-of-transition Reynolds numbers in AEDC/PWT 4T.



b. $U_\infty/\nu_\infty = 3.0 \times 10^6$
 Figure 38. Continued.



c. $U_\infty/\nu_\infty = 4.0 \times 10^6$
 Figure 38. Concluded.

Sym	$U_{\infty}/v_{\infty} \times 10^{-6}$
○	2.0
□	3.0
△	4.0

Open Symbols: Normal Wall Configuration
 Solid Symbols: Walls Taped
 Half Closed Symbols: Wire Screen Overlay

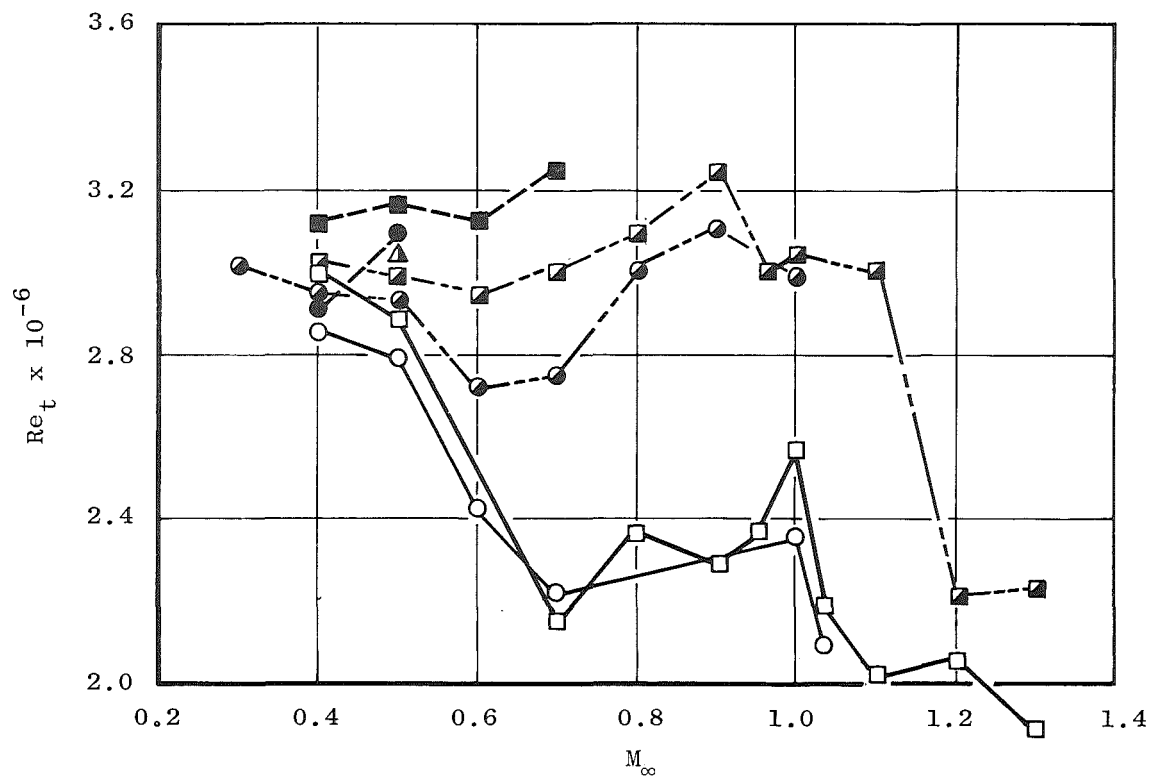
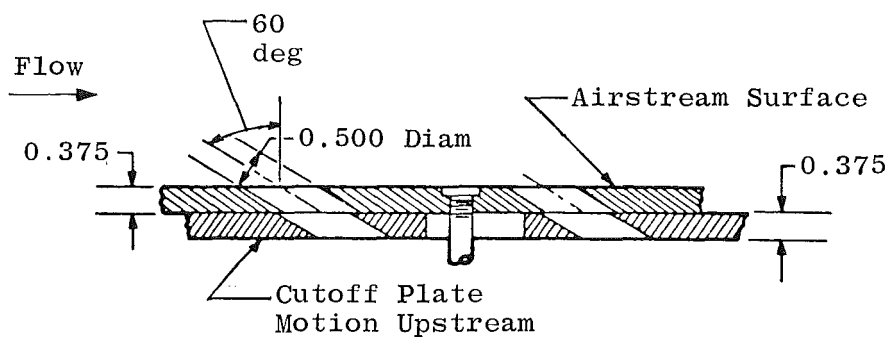
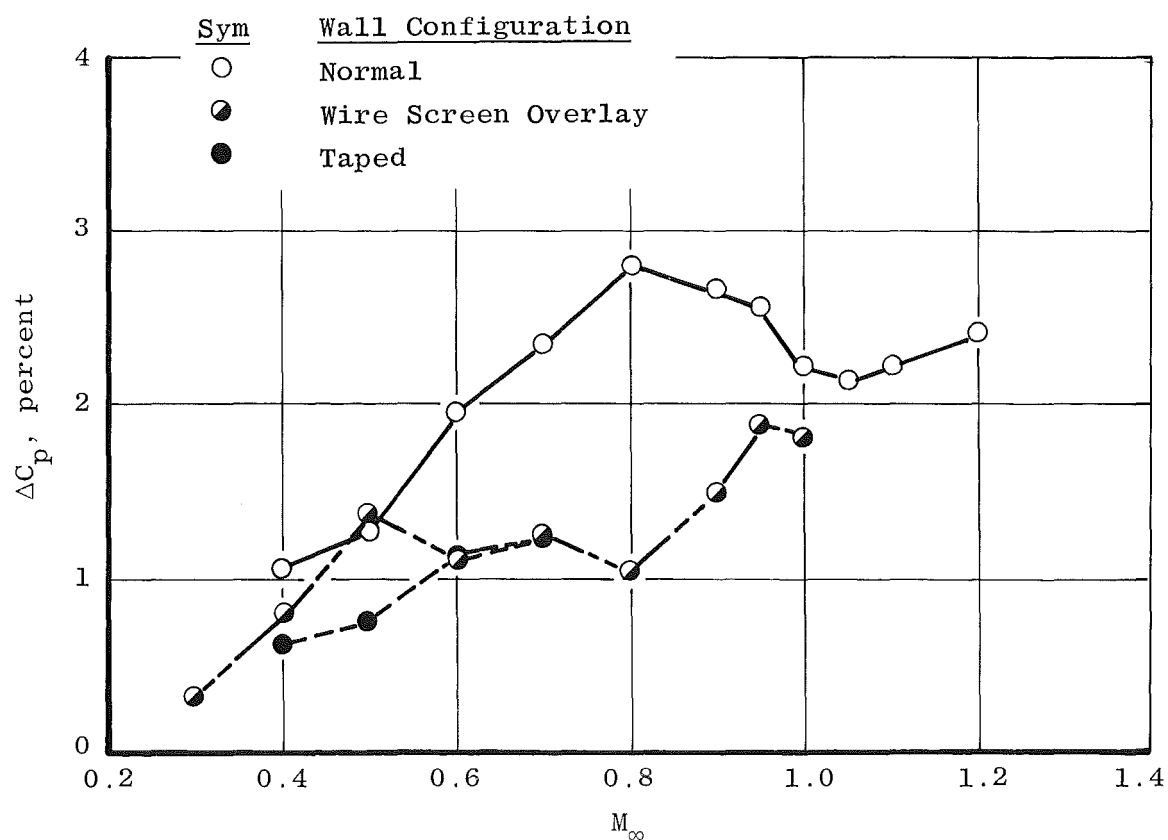


Figure 39. Onset-of-transition Reynolds numbers in AEDC/PWT 4T.

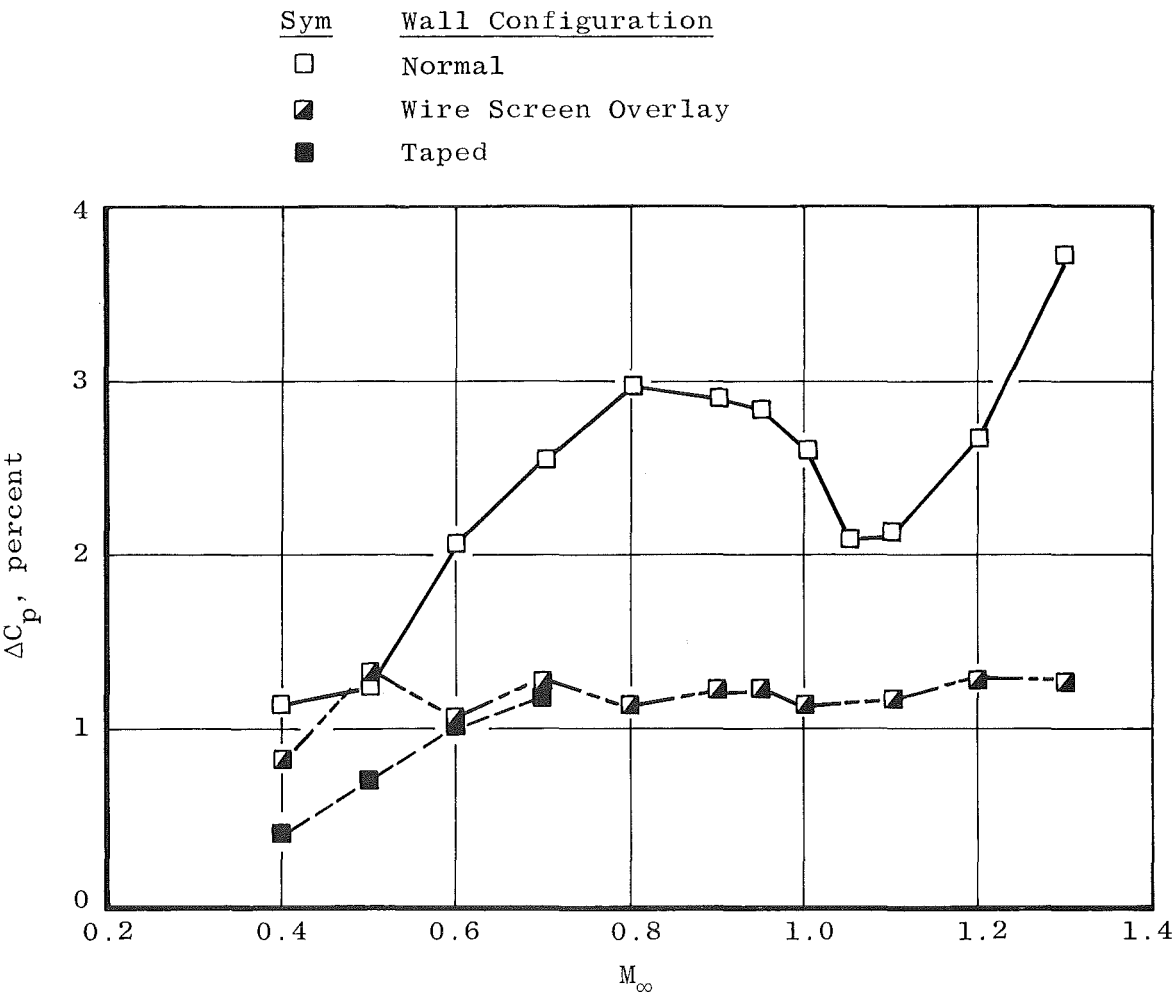


All Dimensions in Inches

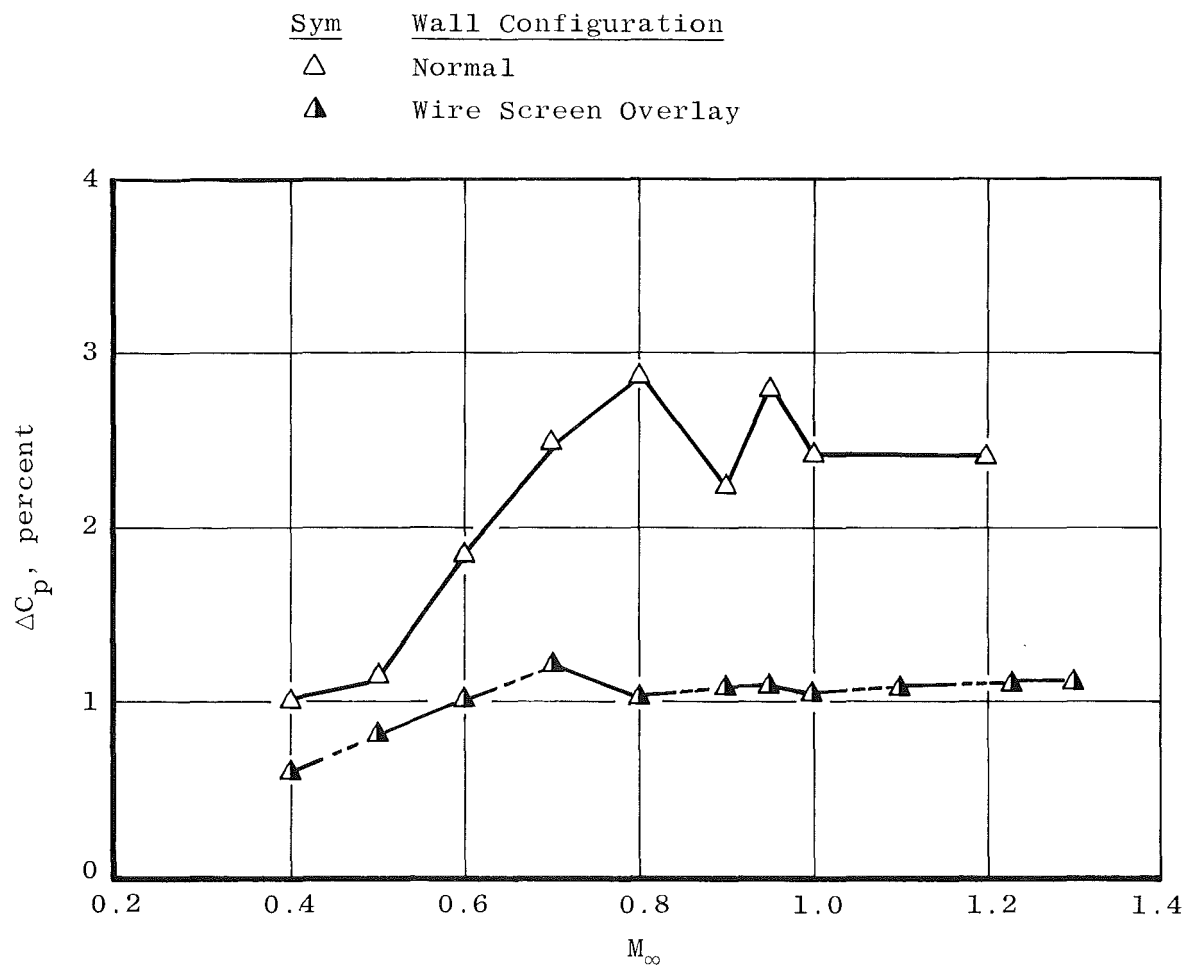


a. $U_\infty/\nu_\infty = 2.0 \times 10^6$

Figure 40. Noise levels in AEDC/PWT 4T.



b. $U_\infty/\nu_\infty = 3.0 \times 10^6$
Figure 40. Continued.



c. $U_\infty/\nu_\infty = 4.0 \times 10^6$
 Figure 40. Concluded.

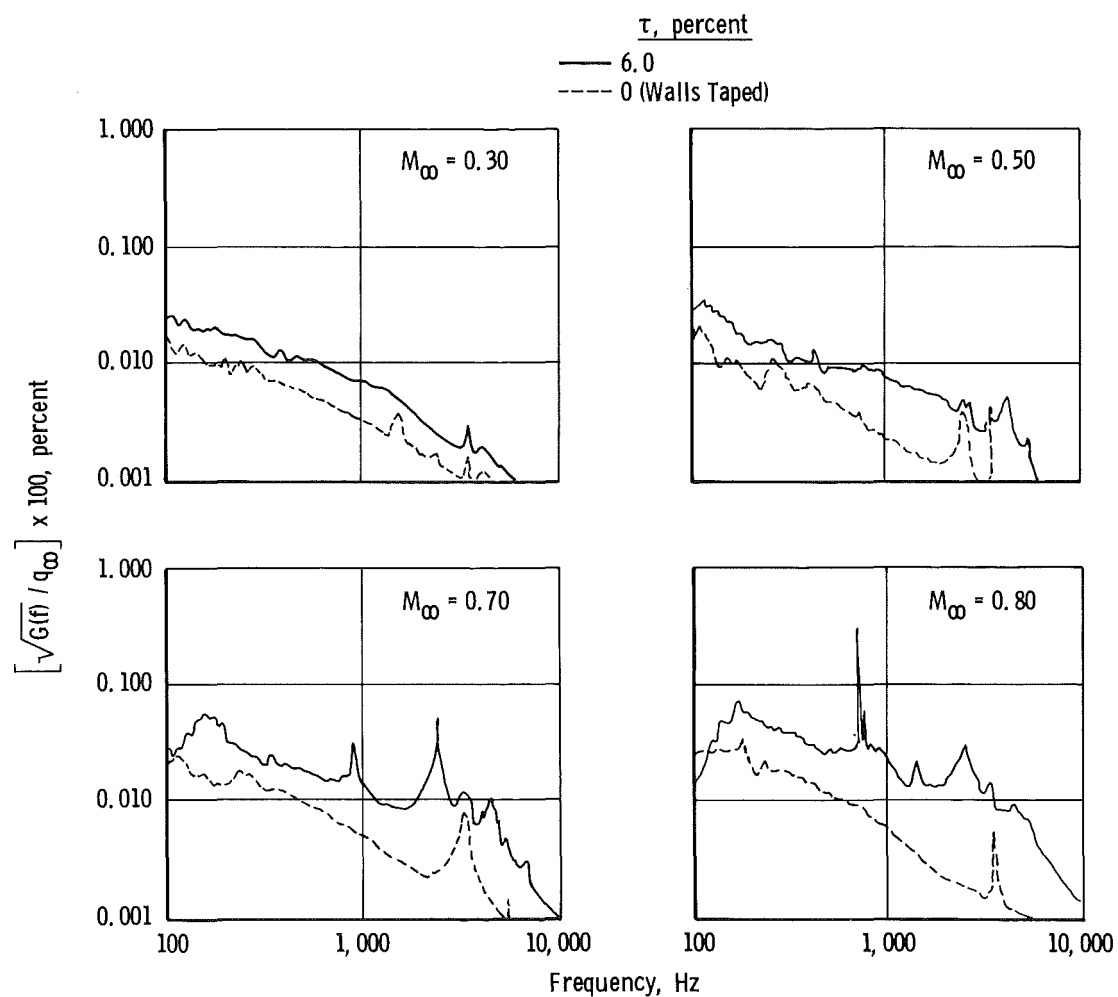


Figure 41. Fourier spectrum measurements in AEDC/PWT 4T.

Table 7. AEDC/PWT Tunnel 4T Data

First Entry					
M_∞	U_∞ / v_∞ $\times 10^{-6}$	ΔC_p , percent	τ , percent	$Re_t \times$ 10^{-6}	$Re_T \times$ 10^{-6}
0.30 ↓	1.924	-	6	2.597	3.046
	1.593	-	↓	-	3.916
	1.951	1.2	↓	2.276	3.089
	2.041	1.2	↓	2.466	3.231
0.40 ↓	2.443	1.6	6	2.748	3.359
	2.072	1.8	↓	2.676	3.505
	1.823	2.2	↓	2.659	3.646
	1.587	2.5	↓	2.519	3.359
	2.201	0.9	↓	2.512	3.760
	2.454	1.0	↓	-	3.477
	2.717	1.0	↓	2.706	3.962
0.50 ↓	2.919	1.3	6	2.761	3.406
	2.508	1.4	6	2.790	3.553
	2.523	7.1	10	2.523	3.574
	2.523	4.1	8	-	-
	2.523	1.4	6	2.838	3.427
	2.523	3.6	4	2.849	3.553
	2.523	1.2	2	2.827	3.574
	2.523	2.1	0	2.880	3.679
	1.914	1.8	6	2.393	3.190
	1.660	1.6	6	2.559	3.528
	2.734	1.3	6	2.620	3.235
	2.735	1.3	6	2.781	3.396
	2.735	1.9	4	2.826	3.487
	2.735	1.8	3	2.906	3.533
	2.735	1.2	2	2.917	3.510
	2.540	1.3	6	2.731	3.471
	2.472	2.2	4	2.812	3.502
	2.480	2.0	3	2.790	3.451
	3.010	1.3	6	2.584	3.386
	3.340	1.2	↓	2.728	3.591
	3.610	1.2	↓	2.813	3.550
	3.850	1.2	↓	3.144	3.593
0.55 ↓	2.892	1.0	6	2.939	3.519
	2.756	2.9	4	2.790	3.422
	2.724	2.4	3.5	2.792	3.382
	2.752	2.3	3	2.890	3.417
0.60 ↓	3.376	1.4	6	2.757	3.320
	2.845	1.4	↓	2.750	3.343
	2.515	1.6	↓	2.662	3.374

Table 7. Continued
First Entry, Continued

M_∞	U_∞/v_∞ $\times 10^{-6}$	ΔC_p , percent	τ , percent	$Re_t \times$ 10^{-6}	$Re_T \times$ 10^{-6}
0.60 ↓	2.152	1.7	6	2.367	3.049
	1.940	1.6	↓	2.668	3.751
	3.514	1.3	↓	2.811	3.309
	3.838	1.2	↓	2.910	3.422
	4.159	1.2	↓	2.946	3.466
	4.426	1.2	↓	3.172	3.688
	5.148	1.2	↓	—	—
0.70 ↓	3.719	1.8	6	2.665	3.161
	3.127	1.7	↓	2.528	3.205
	2.768	1.9	↓	2.503	3.183
	2.438	1.9	↓	2.438	3.108
	2.129	1.9	↓	2.324	3.158
	3.674	1.5	↓	2.663	3.184
	4.038	1.5	↓	2.692	3.230
	4.390	1.4	↓	2.744	3.256
	4.740	1.4	↓	2.844	3.279
	5.077	1.4	↓	2.962	3.258
0.80 ↓	4.010	2.0	6	2.640	—
	3.393	1.9	↓	2.528	3.136
	2.963	2.0	↓	2.469	3.111
	2.614	2.1	↓	2.353	2.941
	2.244	2.0	↓	2.487	3.086
0.90 ↓	4.201	1.7	6	—	—
	3.536	1.7	↓	2.578	3.123
	3.196	1.8	↓	2.557	3.196
	2.753	2.0	↓	2.420	3.051
	2.403	1.8	↓	2.303	3.044
0.95 ↓	4.262	1.6	6	—	—
	3.658	1.7	↓	2.591	3.109
	3.279	1.7	↓	2.582	3.142
	2.818	1.7	↓	2.419	3.029
	2.457	1.7	↓	2.344	3.051
1.00 ↓	4.365	1.5	6	—	—
	3.736	1.6	6	2.491	2.989
	3.698	1.2	1.5	2.650	3.174
	3.256	1.2	1.5	2.483	3.039
	3.235	1.5	6	2.507	3.046
	2.919	1.9	6	2.481	3.065
	2.890	1.4	1.5	2.432	2.986
	2.482	1.3	1.5	2.172	2.792
	2.467	1.8	6	2.282	2.981

Table 7. Continued
First Entry, Concluded

M_∞	U_∞ / v_∞ $\times 10^{-6}$	ΔC_p , percent	τ , percent	$Re_t \times$ 10^{-6}	$Re_T \times$ 10^{-6}
1.05 ↓	3.737	1.1	2	2.849	3.457
	3.289	1.4	2	2.878	3.453
	3.349	1.6	6	2.484	3.014
	2.845	1.8	6	2.430	2.964
	2.859	1.2	2	2.692	3.240
	2.475	1.3	2	2.454	3.011
	2.532	1.7	6	2.363	2.996
1.10 ↓	4.307	1.6	6	—	—
	3.774	1.6	6	2.422	2.799
	3.751	1.7	2.5	2.829	3.407
	3.321	1.7	2.5	2.864	3.487
	3.359	1.7	6	2.267	2.771
	2.914	1.7	6	2.210	2.841
	2.878	1.6	2.5	2.722	3.358
	2.501	1.4	2.5	2.564	3.210
	2.533	1.7	6	2.269	2.913
1.20 ↓	4.303	2.2	6	—	—
	3.811	2.4	6	2.382	2.699
	3.797	1.6	4.8	2.421	2.658
	3.341	1.6	4.8	2.199	2.784
	3.384	1.7	6	2.155	2.707
	2.878	2.2	6	1.871	2.590
	2.897	1.8	4.8	2.137	2.713
	2.524	1.8	4.8	1.977	2.545
	2.587	1.8	6	2.048	2.652
1.30 ↓	4.256	2.1	6	—	—
	3.786	2.3	6	—	2.461
	3.769	1.6	7	2.198	2.356
	3.324	1.6	7	1.911	2.410
	3.360	1.5	6	2.100	2.604
	2.864	1.8	6	1.838	2.506
	2.922	1.9	7	1.802	2.411
	2.515	1.9	7	1.781	2.389
	2.539	1.7	6	1.841	2.539

Second Entry

0.40 ↓	1.624	0.75	6	—	3.901
	1.964	0.79	↓	2.635	3.863
	2.031	0.93		2.870	3.733
	2.253	0.95		2.952	3.772
	2.943	0.79		3.018	3.734

Table 7. Continued
Second Entry, Continued

M_∞	U_∞/v_∞ $\times 10^{-6}$	ΔC_p , percent	τ , percent	$Re_t \times$ 10^{-6}	$Re_T \times$ 10^{-6}
0.50 ↓	1.636 1.914 2.006 2.192 2.448 2.708 2.955 3.868	1.05 1.18 1.21 1.29 1.22 1.24 1.25 1.21	6 ↓	- - - 2.795 2.856 2.870 2.901 3.192	3.260 3.390 3.433 3.468 3.594 3.544 3.377 3.487
0.60 ↓	1.871 2.009 2.194 2.527 2.785 3.018 3.110	1.83 1.80 1.80 1.83 1.85 1.88 1.87	6 ↓	2.526 2.428 2.476 2.548 2.132 2.108 2.195	3.823 3.241 3.075 3.077 2.572 2.426 2.495
0.70 ↓	1.989 2.064 2.413 2.779 2.913 3.115 3.456	2.51 2.51 2.50 2.49 2.45 2.46 2.48	6 ↓	2.304 2.387 2.505 2.404 2.159 2.258 2.339	2.882 2.939 2.976 2.856 2.625 2.540 2.625
0.80 ↓	1.903 2.246 2.610 2.993 3.369 3.750	2.79 2.77 2.77 2.76 2.79 2.78	6 ↓	- - 2.557 2.369 2.358 2.555	3.253 2.987 2.982 2.843 2.670 2.680
0.90 ↓	2.011 2.367 2.406 2.765 2.978 3.150 3.524	2.68 2.69 2.63 2.64 2.70 2.72 2.71	6 6 5 6 ↓	- - - 2.408 - 2.284 2.384	2.858 2.922 2.691 2.915 2.795 2.717 2.590
0.95 ↓	1.965 1.975 2.397 2.430 2.784 2.952	2.63 2.32 2.68 2.36 2.68 2.37	6 1.5 6 1.5 6 1.5	- - - - 2.407 -	2.847 2.913 2.901 2.815 2.860 2.925

Table 7. Continued
Second Entry, Continued

AEDC-TR-78-44

M_∞	U_∞/v_∞ $\times 10^{-6}$	ΔC_p , percent	τ , percent	$Re_t \times$ 10^{-6}	$Re_T \times$ 10^{-6}
0.95 ↓	2.987 3.248 3.611	2.67 2.64 2.80	6 ↓	2.367 2.355 -	2.760 2.726 2.666
1.00 ↓	1.999 1.997 1.995 2.451 2.435 2.862 2.969 2.984 3.254	2.76 2.42 1.94 2.63 2.05 2.77 2.82 2.18 2.79	6 6 1.5 6 1.5 6 6 1.5 6	- - 2.365 - 2.433 2.570 - 2.200 2.850	2.930 2.787 2.621 3.018 2.780 3.080 3.050 2.758 3.340
1.05 ↓	1.970 1.975 2.472 2.844 2.976 3.206	2.37 1.63 2.83 2.86 2.86 2.89	6 2 6 ↓	- - 2.580 2.160 2.220 -	3.067 2.700 3.412 2.500 2.430 2.030
1.10 ↓	2.487 2.511 2.896 2.953 2.965 3.313 3.709 3.980	2.70 - 3.44 - 2.92 2.91 3.39 2.92	6 2.5 6 2.5 6 ↓	1.679 - 1.954 - 1.977 2.194 - -	1.902 2.170 2.210 2.318 2.251 2.408 2.661 2.965
1.20 ↓	1.988 1.983 2.522 2.503 2.938 2.983 2.940 3.325 3.391	2.00 - 2.68 - 2.63 2.66 - 2.67 -	6 4.8 6 4.8 6 6 4.8 6 4.8	- - 1.997 1.922 2.115 2.139 - - -	2.250 2.210 2.480 2.440 2.490 2.501 2.360 2.502 2.370
<u>Walls Taped</u>					
0.40 ↓	1.611 1.834 2.018 2.053 2.295 3.018	0.52 0.53 0.53 0.59 - 0.47	0 ↓	2.807 2.904 3.075 - 3.114 3.105	3.828 3.807 3.947 3.923 3.917 3.446

Table 7. Continued
Second Entry, Concluded

M_∞	U_∞/v_∞ $\times 10^{-6}$	ΔC_p , percent	τ , percent	$Re_t \times$ 10^{-6}	$Re_T \times$ 10^{-6}
0.50 ↓	1.660 1.952 2.042 2.241 2.477 2.723 2.978 3.934	0.50 0.71 0.74 0.85 0.90 0.77 0.67 0.62	0 ↓	- - 3.096 3.114 3.324 3.240 3.156 -	3.794 3.806 3.851 3.881 4.089 3.816 3.618 3.670
0.60 ↓	1.896 2.035 2.250 2.576 2.876 3.085 3.169	1.13 1.18 1.28 1.13 1.09 1.07 1.07	0 ↓	- - - - 3.048 3.135 -	4.140 4.255 3.707 3.510 3.507 3.511 3.537
0.70 ↓	2.028 2.111 2.440 2.803 3.050 3.143 3.466	1.19 1.22 1.42 1.20 1.19 1.19 1.19	0 ↓	- - - 3.249 3.228 3.249 3.458	3.953 3.551 3.861 3.525 3.672 3.674 3.683

Third Entry

0.40 ↓	1.991 2.923 3.312	1.034 1.027 1.099	5 ↓	2.704 2.898 -	3.451 3.337 3.395
0.60 ↓	1.991 3.171 3.826	1.918 1.918 2.045	5 ↓	2.655 2.933 -	3.335 3.369 3.475
0.70 ↓	2.104 2.982 3.834	2.320 2.318 2.478	5 ↓	2.507 2.758 -	3.156 3.206 3.291
0.80 ↓	2.017 2.957 3.851	2.776 2.997 2.864	5 ↓	2.437 2.711 -	3.059 3.129 3.273
0.90 ↓	2.011 3.001 4.010	2.695 2.950 2.035	5 ↓	2.346 2.638 -	2.916 3.126 3.241

Table 7. Continued
Third Entry, Continued

M_∞	U_∞/v_∞ $\times 10^{-6}$	ΔC_p , percent	τ , percent	$Re_t \times$ 10^{-6}	$Re_T \times$ 10^{-6}
0.95	2.459	2.544	5	2.479	3.064
↓	3.004	2.873	↓	-	-
	3.961	2.782		-	3.202
1.00	1.992	2.182	1.5	2.158	2.681
↓	2.984	2.568	↓	2.499	3.432
	4.002	2.417		2.685	3.135
1.05	2.057	2.117	2	2.040	2.674
1.05	2.959	2.104	2	2.811	3.440
1.10	2.949	2.143	2.5	2.458	3.416
1.20	2.495	2.417	4.77	1.996	2.453
↓	2.892	2.720	↓	2.003	2.555
	3.948	2.405		2.221	2.698
1.30	2.971	3.730	6	1.882	2.488

Third Entry, Continued: Walls with Wire Screen Overlay

0.30	1.898	0.485	6	3.163	3.828
0.30	2.383	0.865	6	2.999	3.733
0.40	1.493	0.667	6	2.899	3.633
↓	1.999	0.817	↓	2.932	3.598
	2.290	0.916		2.863	3.702
	2.500	0.985		2.958	3.604
	2.995	0.787		2.970	3.719
↓	3.503	0.689	↓	3.065	3.620
0.50	1.693	0.784	6	2.984	3.711
↓	1.996	0.827	↓	2.894	3.659
	2.789	0.834		2.987	3.649
	2.999	0.842		3.074	3.724
↓	3.988	0.818	↓	3.074	3.656
0.60	1.543	1.032	6	2.765	3.485
↓	2.041	1.119	↓	2.721	3.453
	2.524	1.063		2.755	3.386
	3.174	1.045		3.002	3.518
↓	3.933	1.027	↓	2.983	3.671
0.70	1.533	1.288	6	7.734	3.488
↓	2.052	1.303	↓	2.770	3.540
	2.521	1.346		2.836	3.445
↓	3.002	1.288	↓	2.977	3.577

Table 7. Concluded
Third Entry, Concluded: Walls with Wire Screen Overlay

M_∞	U_∞/v_∞ $\times 10^{-6}$	ΔC_p , percent	τ , percent	$Re_t \times$ 10^{-6}	$Re_T \times$ 10^{-6}
0.70	3.528	1.218	6	2.969	3.616
0.70	3.913	1.242	6	3.000	3.620
0.80	2.040	-	6	3.009	3.706
↓	2.257	1.258	↓	3.159	3.896
	2.268	1.078		3.005	3.780
	3.529	1.028		-	-
	3.809	1.038		-	3.492
	3.940	-		3.185	3.710
↓	3.965	0.993	↓	-	3.535
0.90	1.475	-	6	3.085	3.835
↓	1.965	1.639	↓	3.111	3.815
	2.456	1.496		3.193	3.848
	2.941	1.209		3.235	3.872
	3.415	1.226		3.202	3.870
↓	3.843	1.181	↓	3.138	3.843
0.95	2.514	1.863	6	3.080	3.834
↓	3.081	1.246	↓	3.004	3.761
	4.055	1.184		-	-
1.00	2.042	-	3	2.978	3.727
↓	2.551	1.278	↓	2.997	3.678
	3.020	1.151		3.020	3.750
	3.453	1.093		2.964	3.654
↓	3.958	1.059	↓	-	-
1.11	2.180	2.049	3	3.270	3.779
↓	2.594	2.529	↓	3.026	3.675
	3.018	2.343		3.018	3.823
	3.508	1.160		2.982	3.683
↓	3.892	1.150	↓	2.724	3.665
1.23	2.421	1.516	3	2.542	3.006
↓	2.980	-	↓	2.210	2.682
	3.325	1.318		2.078	2.826
	2.828	1.347		2.286	2.852
↓	3.845	1.292	↓	2.275	2.724
1.31	2.403	1.634	4	-	2.864
↓	2.795	1.475	↓	2.096	2.679
	3.273	1.372		2.400	2.782
↓	3.773	1.285	↓	2.452	2.987

ONERA 6 x 6 S-2 Modane

The cone test in the ONERA 6 x 6 S-2 Modane complemented rather extensive investigations of dynamic flow quality which the French have been conducting in that tunnel. The test performed with the cone was likewise extensive, including many secondary parameter variations (e.g., U_∞/ν_∞ at constant M_∞ , varied cone roll angle, ϕ , varied compressor speed at constant M_∞ , varied second throat position, varied wall porosity, and walls taped). The S-2 tunnel is a transonic facility similar in many respects to AEDC 4T except that only the top and bottom test section walls are perforated, the sidewalls being solid. The porosity variation feature is slightly different, τ being variable from 0 to 6 percent in the ONERA S-2 Modane and from 0 to 10 percent in AEDC 4T. In the ONERA tunnel, the sliding cutoff plates for adjusting porosity translate downstream, whereas in AEDC 4T they translate upstream.

The tests in the ONERA S-2 Modane were conducted by X. Vaucheret and are reported in part in Ref. 8. Certain results obtained by Vaucheret are presented here for correlation in this report.

End-of-transition and onset-of-transition Reynolds numbers are presented in Fig. 42 as a function of M_∞ at a constant $p_t = 0.5$ bar, $\tau = 6$ percent. Also shown in Fig. 42 is the variation in transition Reynolds number at $M_\infty = 0.8$ for varied τ values.

The fluctuating pressure levels, ΔC_p , measured by the cone microphones are shown in Fig. 43 for the same flow conditions of $p_t = 0.5$ bar, $\tau = 6$ percent. Microphones were also installed on the sidewalls of the test section: one between perforations on a perforated wall, one upstream of the perforations on the same wall, and one on a solid sidewall at the same tunnel axial station as the one on the perforated wall. These measurements yielded useful information on the directivity and extent of propagation of the wall-generated edgetones, which were predominant in this tunnel. The data from these three wall-mounted microphones are shown in Fig. 44 compared to the cone-aft microphone. Also shown in Fig. 44 are the walls-taped data, which indicate a substantial reduction in test section noise level and good agreement with Lowson's turbulent boundary-layer pressure fluctuation empirical correlation (Ref. 9),

$$\Delta C_p = 0.6 / (1 + 0.14 M_\infty^2).$$

The variation in amplitudes, ΔC_p , as a function of porosity, τ , for $M_\infty = 0.80$ and 0.95 is shown in Fig. 45. Maximum ΔC_p occurred on the cone (M2); minimum amplitude occurred on the perforated wall ahead of the perforations (M5), indicating attenuation of the upstream propagation of the sound.

The change in ΔC_p on the cone as U_∞/ν_∞ varied from 2.0×10^6 to 7.2×10^6 at $\tau = 6$ percent, $M_\infty = 0.80$ and 0.95 , was small, as shown in Fig. 46.

Selected Fourier spectra from the cone microphones are shown in Fig. 47 for M_∞ varied from 0.25 to 1.15 . The predominant spectral peaks identified by Vaucheret as edgetones (similar to those in other perforated-wall transonic tunnels) are clearly distinguishable in these spectra. As seen in Fig. 48, a variation in τ from 6 percent to 0.6 percent produced a significant change in spectral distribution because of shifts in edgetone harmonic content. For a more complete discussion of the harmonic family of edgetones, see Dougherty, Anderson, and Parker (Ref. 10).

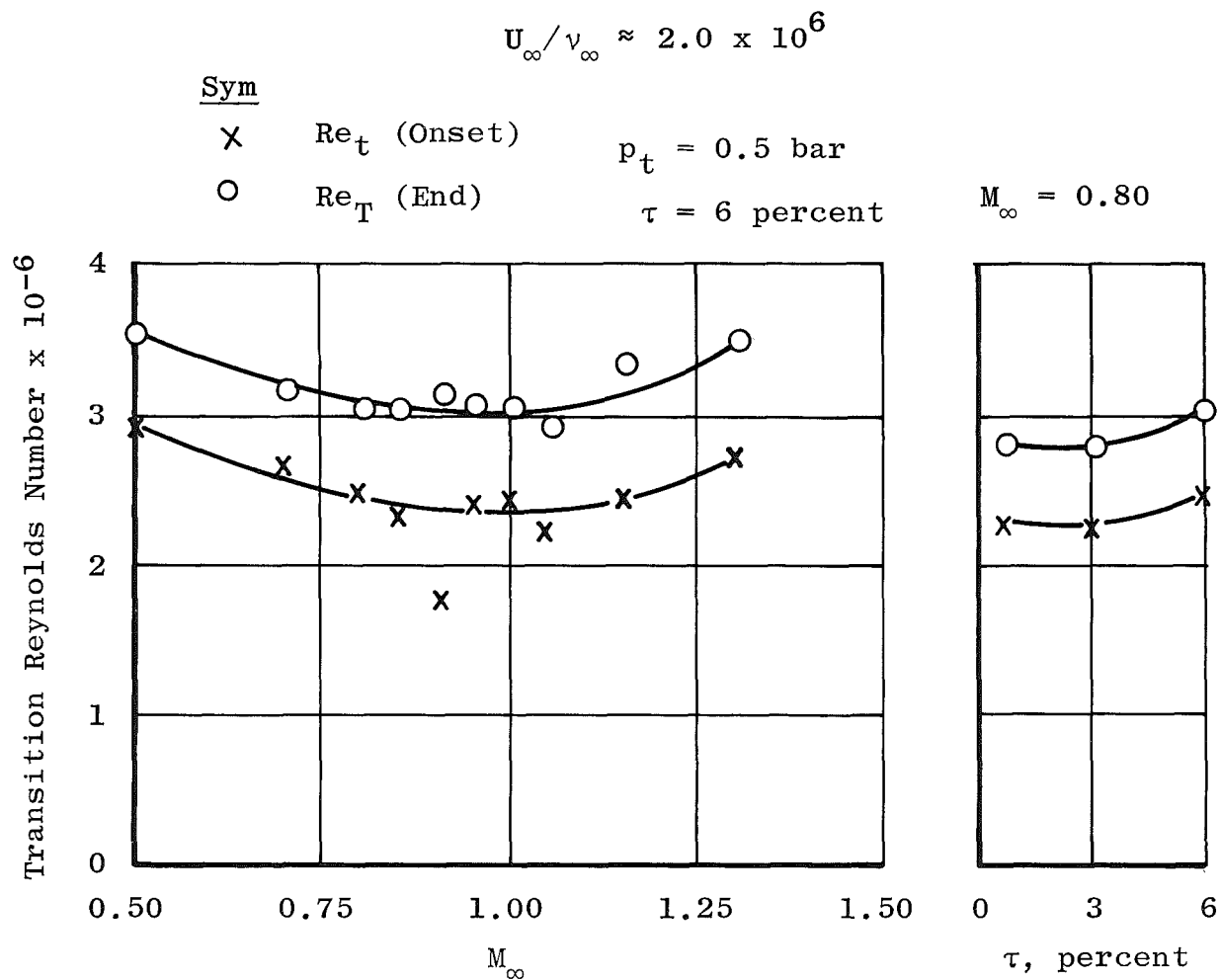


Figure 42. Transition Reynolds numbers in the ONERA 6 x 6 S-2 Modane.

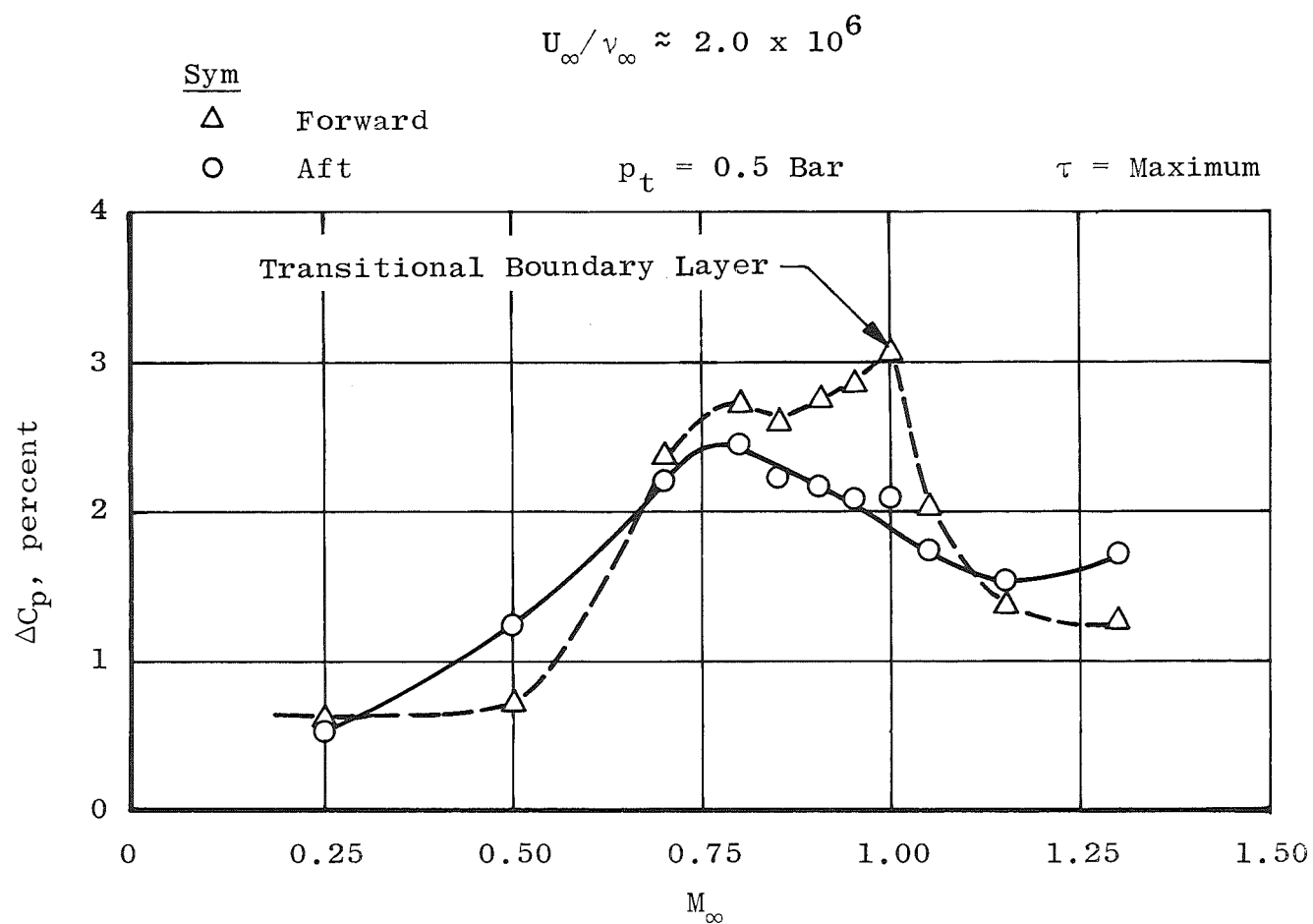
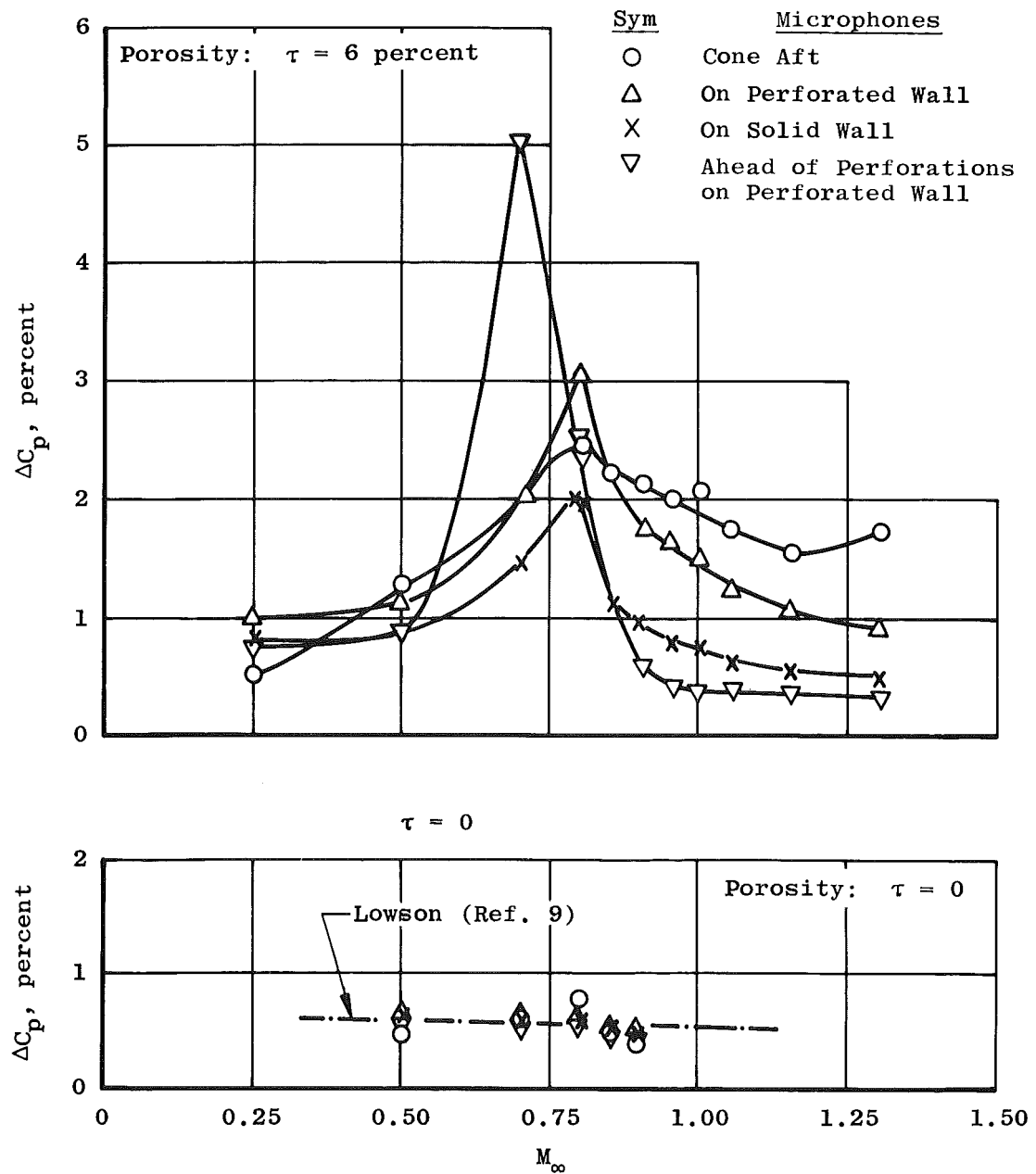


Figure 43. Noise levels in the ONERA 6 x 6 S-2 Modane measured by the cone microphones.



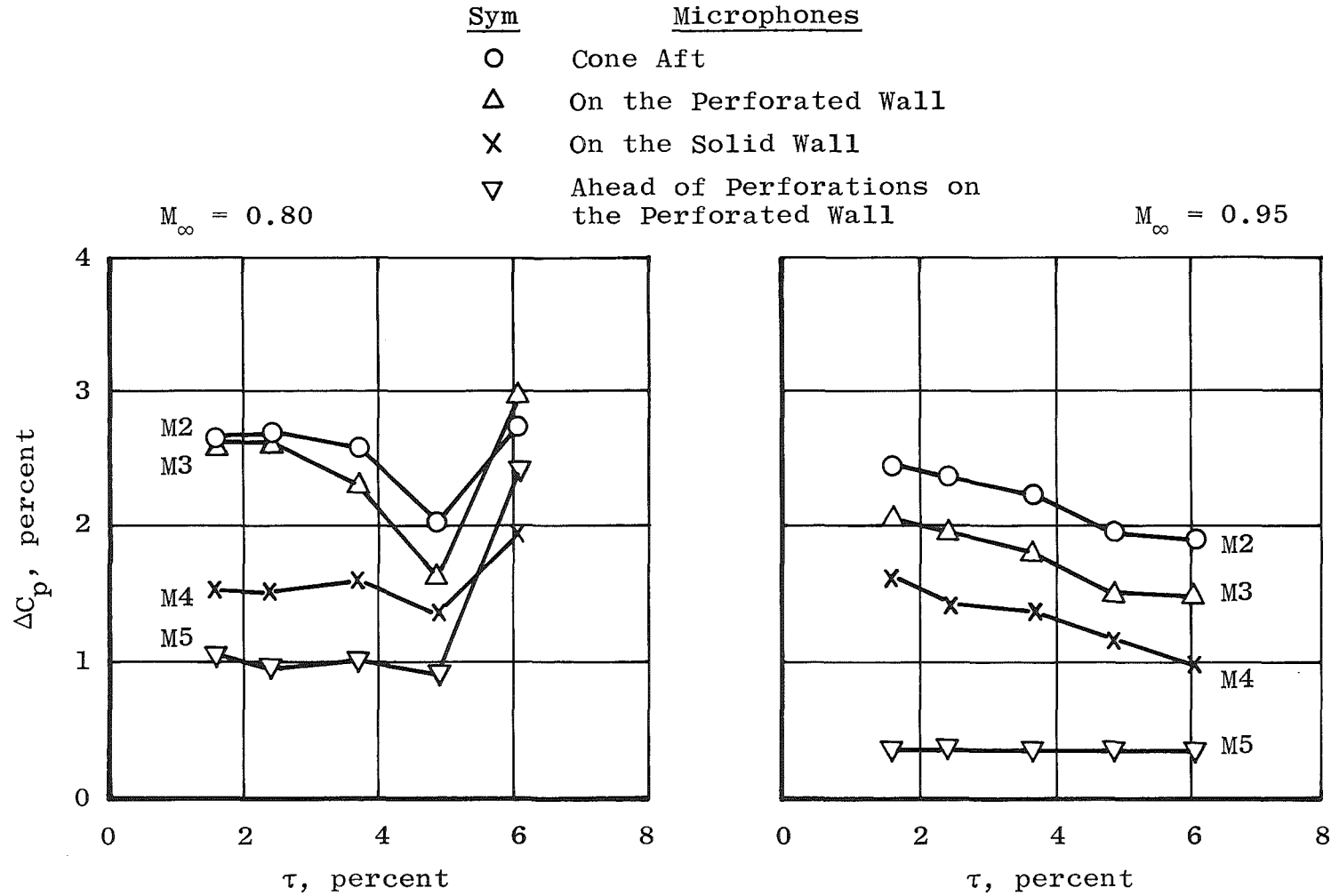


Figure 45. Noise levels in the ONERA 6 x 6 S-2 Modane measured at $M_\infty = 0.80$ and 0.95 at varied wall porosity.

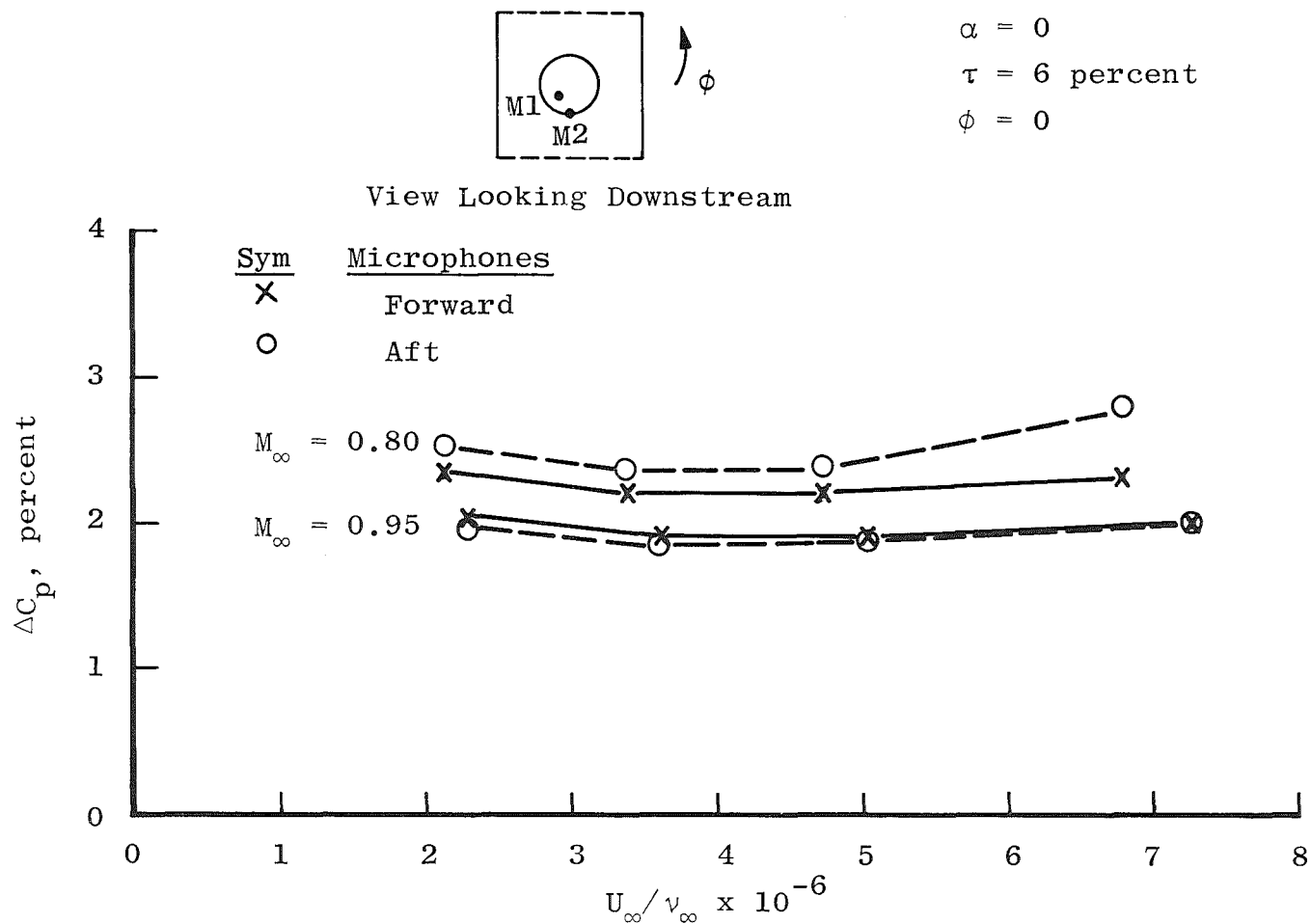


Figure 46. Variation in noise levels with U_∞/v_∞ in the ONERA 6 x 6 S-2 Modane measured by the cone microphones at $M_\infty = 0.80$ and 0.95 .

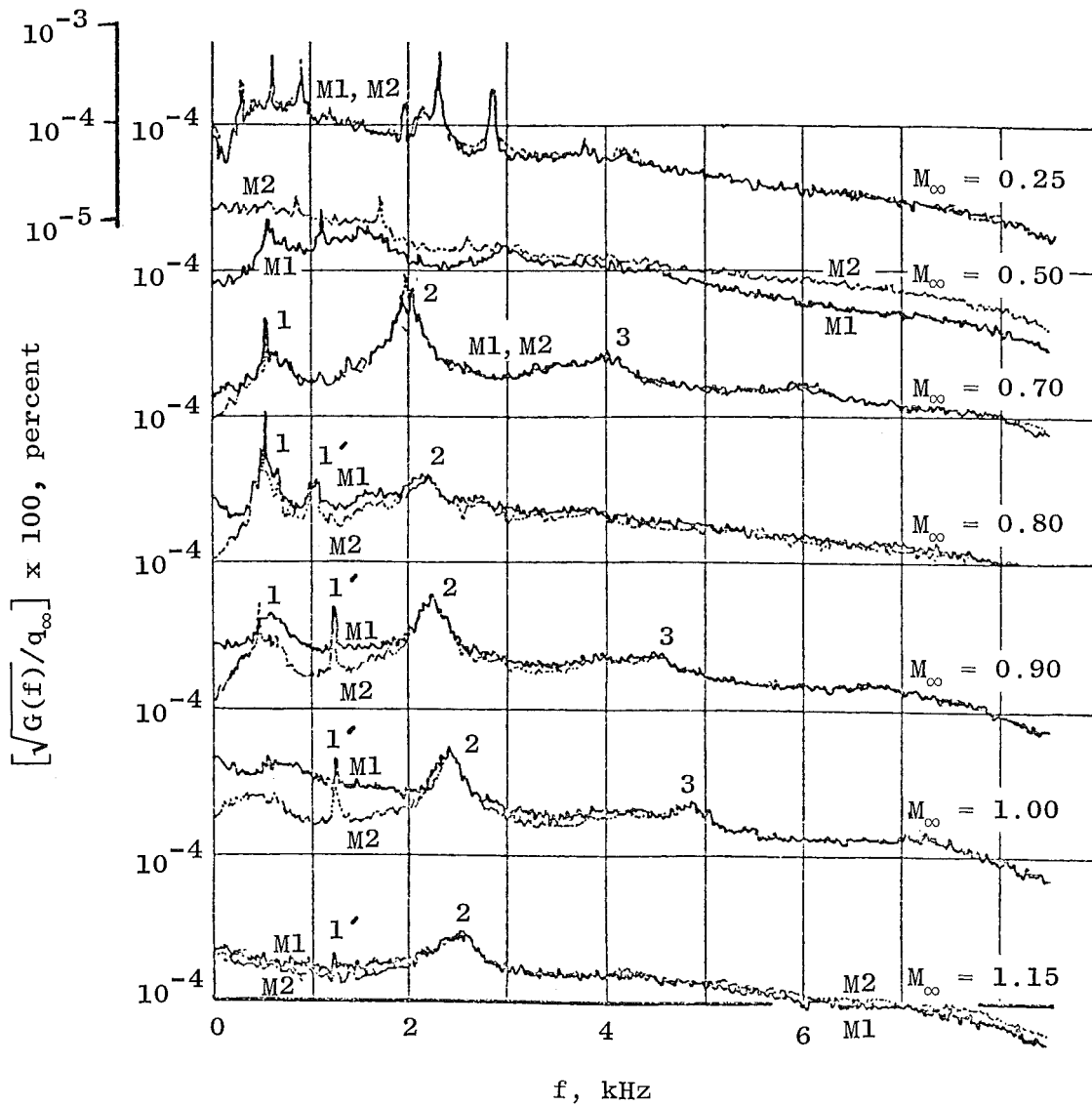


Figure 47. Fourier spectrum measurements in the ONERA 6 x 6 S-2 Modane.

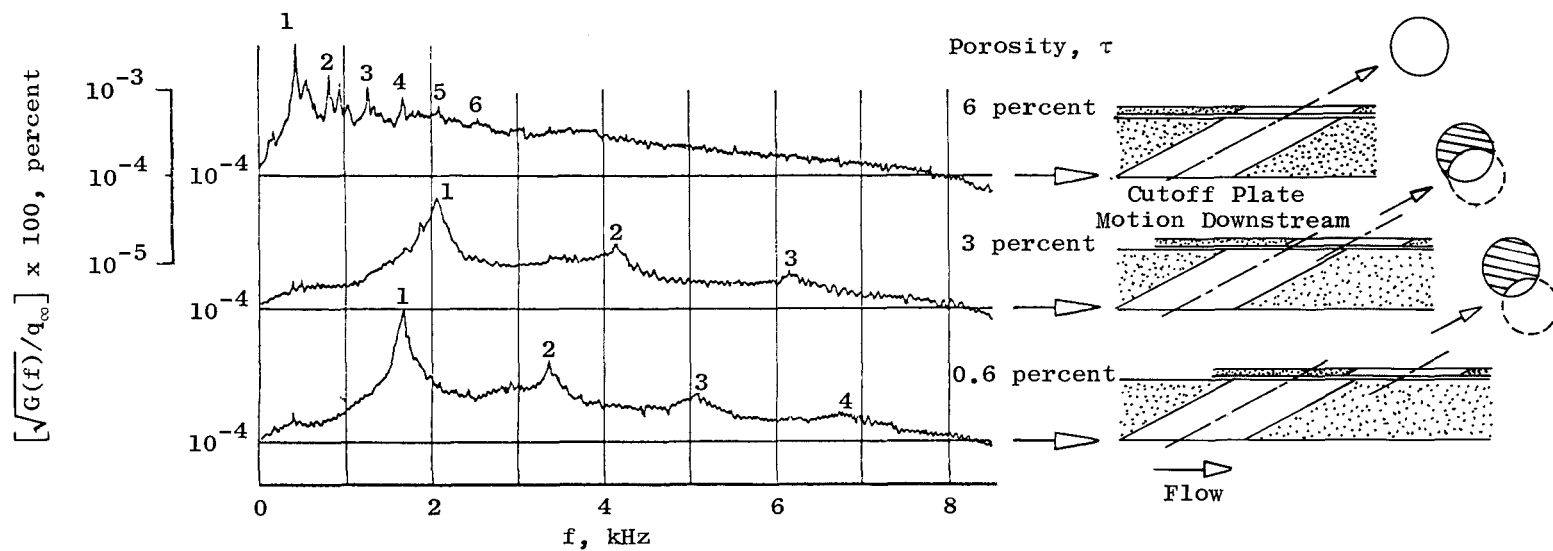


Figure 48. Effect of wall porosity variation on the power spectral density in the ONERA 6 x 6 S-2 Modane at $M_\infty = 0.80$.

ONERA 2.56 x 1.83 S-3 Modane

Because of the smaller size of the 2.56 x 1.83 S-3 Modane, the cone was tested without the traversing pitot probe mechanism; thus, no transition data were obtained. A complement of microphones similar to that used in the ONERA S-2 Modane tests was used by Vaucheret in this tunnel. In this manner, a basis of comparison was obtained for the flow environment in these two tunnels using the cone- and wall-mounted microphones.

Vaucheret's findings of the variation in ΔC_p with M_∞ from 0.25 to 1.0, $p_t = 1.15$ bar, are shown in Fig. 49. The wall porosities and hole sizes are different between horizontal and vertical walls in this tunnel. Noise levels, ΔC_p , are presented as a function of M_∞ for five microphone locations. (See the insert figure for microphone locations and wall porosity details). The change in ΔC_p with U_∞/ν_∞ at $M_\infty = 0.80$ and 0.95 is shown in Fig. 50, as U_∞/ν_∞ varied from 5.0×10^6 to 12.5×10^6 . Fourier spectra for the microphones are shown in Fig. 51 with certain narrow-band peaks (edgetones) being predominant. Both sets of holes (different size) emit tones.

Tests were also performed with the two sidewalls closed with tape and then with all four walls taped. As seen in Fig. 52, the levels of ΔC_p for a given M_∞ generally increased slightly when the walls were successively closed. Selected spectra for these walls-taped cases are shown in Fig. 53. Edgetones at high frequencies were suppressed as seen in Fig. 53 on the cone-aft and perforated-wall microphones, but the amplitudes in the low frequency range increased with tape application. This paradox in overall ΔC_p amplitudes seems to indicate that some of the fluctuations generated in the tunnel are cancelled by the open walls. The S-3 Modane is a blowdown tunnel, and this high level, low frequency noise is believed to originate in the stilling chamber.

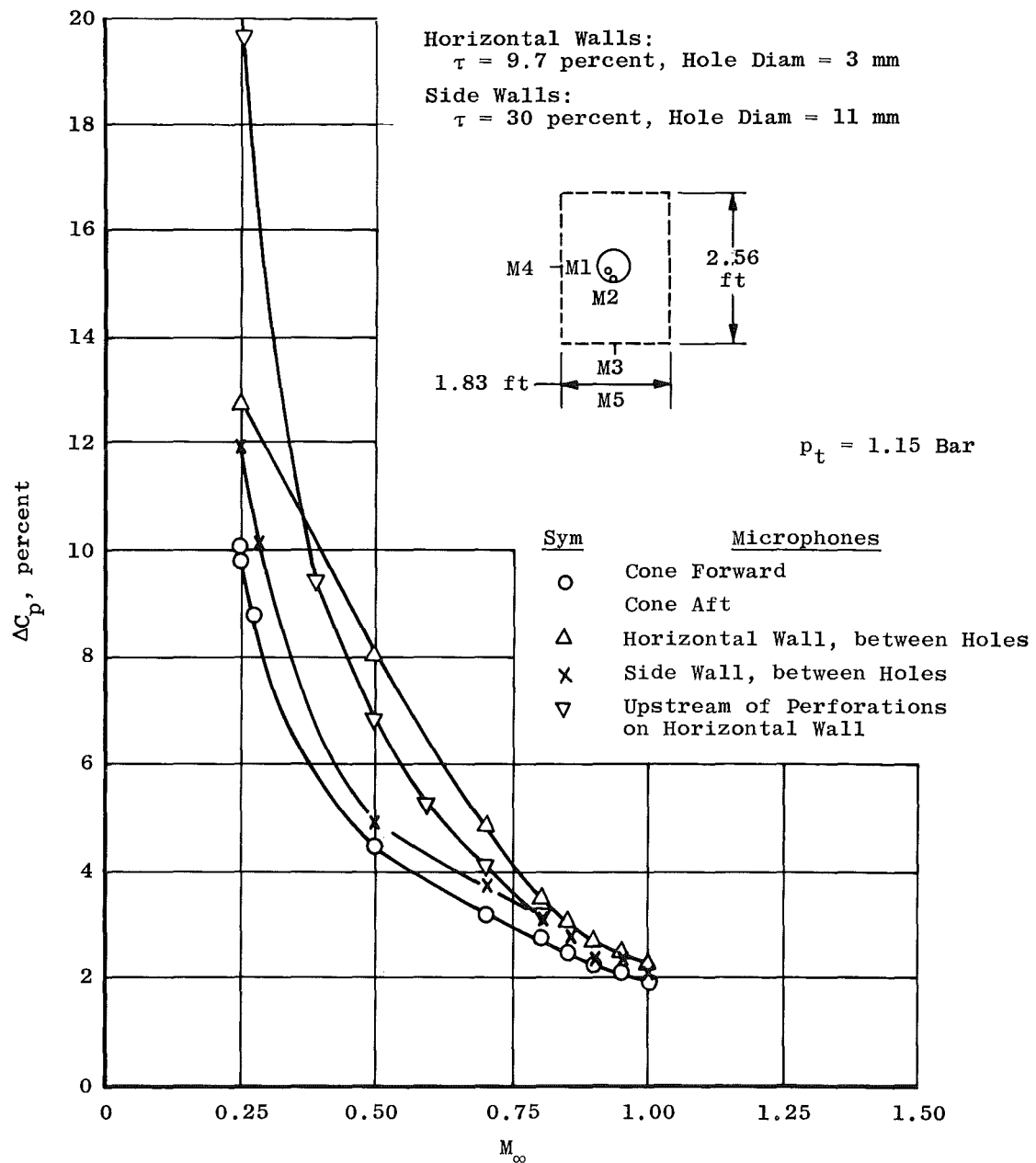


Figure 49. Noise levels in the ONERA 2.56 x 1.83 S-3 Modane.

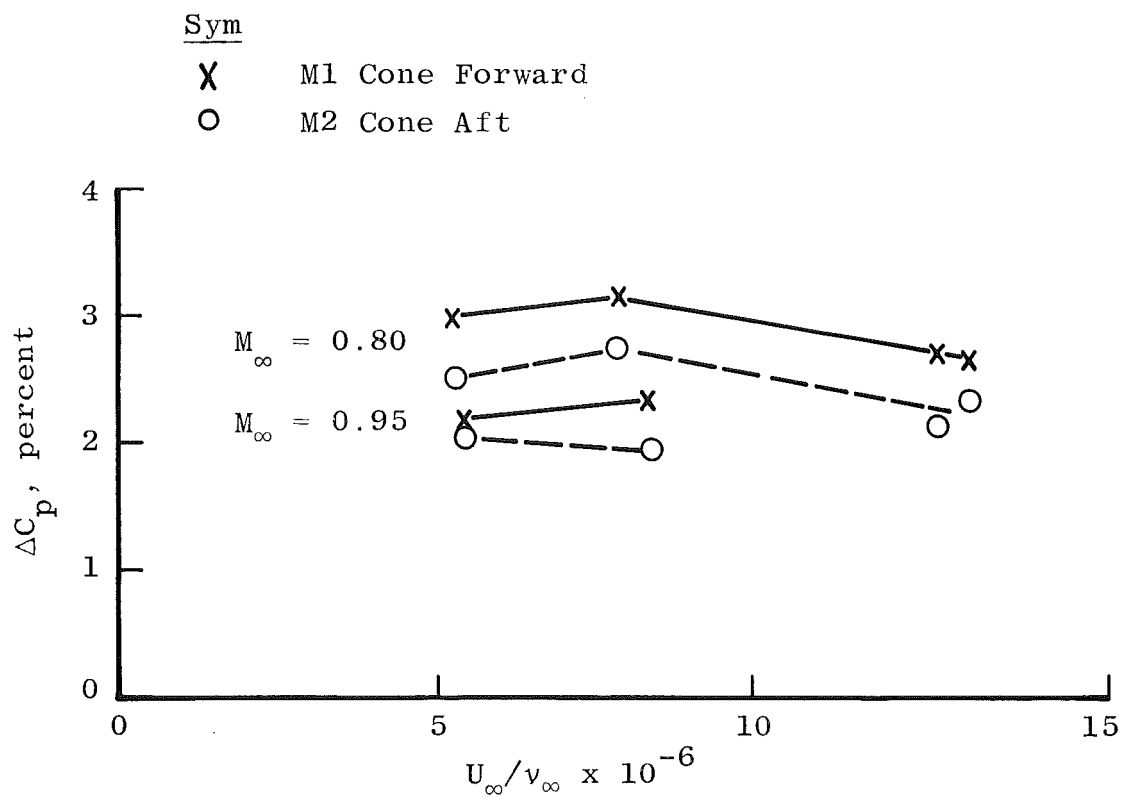


Figure 50. Variation in noise levels with U_∞/v_∞ in the ONERA 2.56 x 1.83 S-3 Modane at $M_\infty = 0.80$ and 0.95.

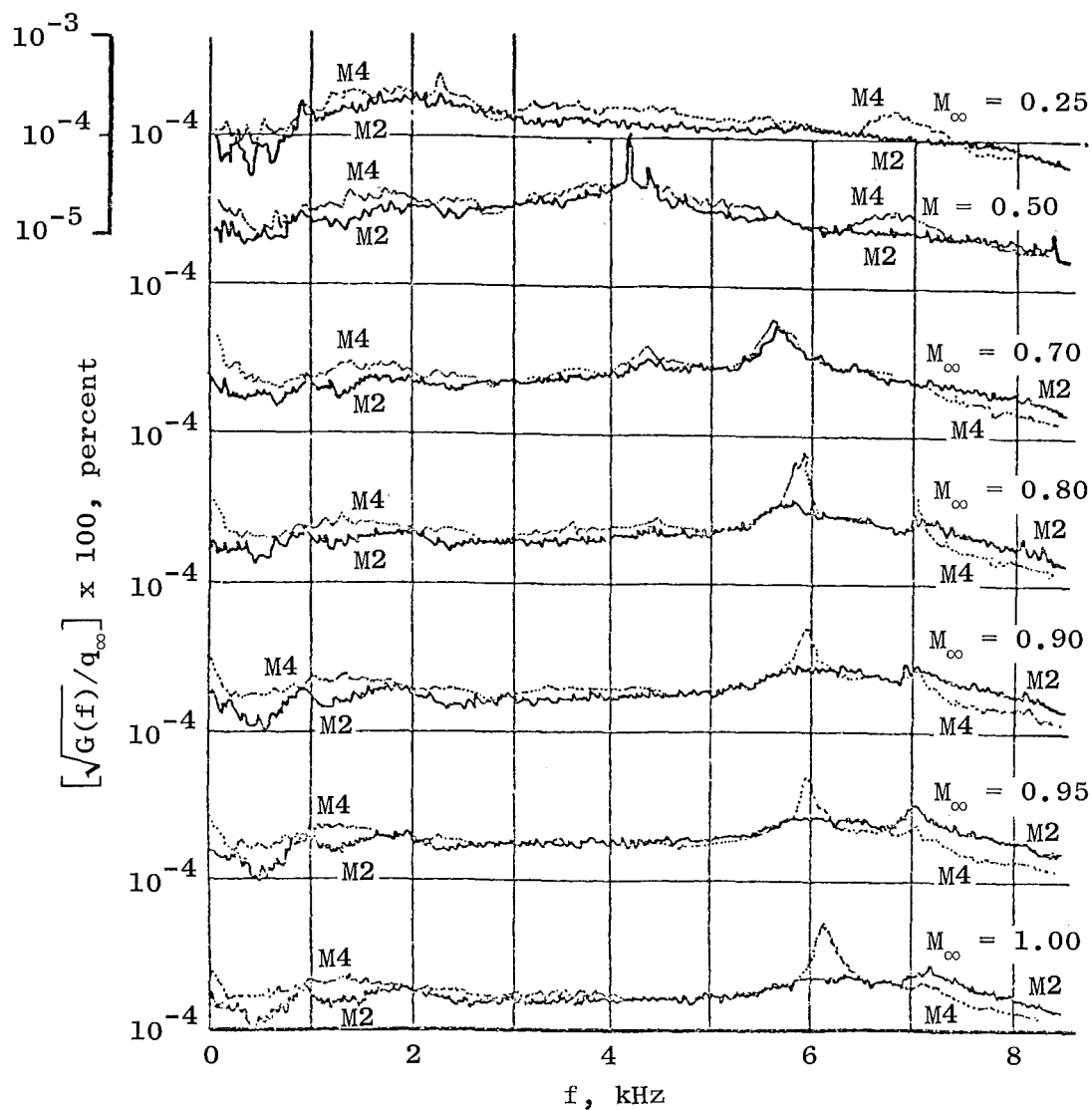


Figure 51. Fourier spectrum measurements in the ONERA 2.56 x 1.83 S-3 Modane.

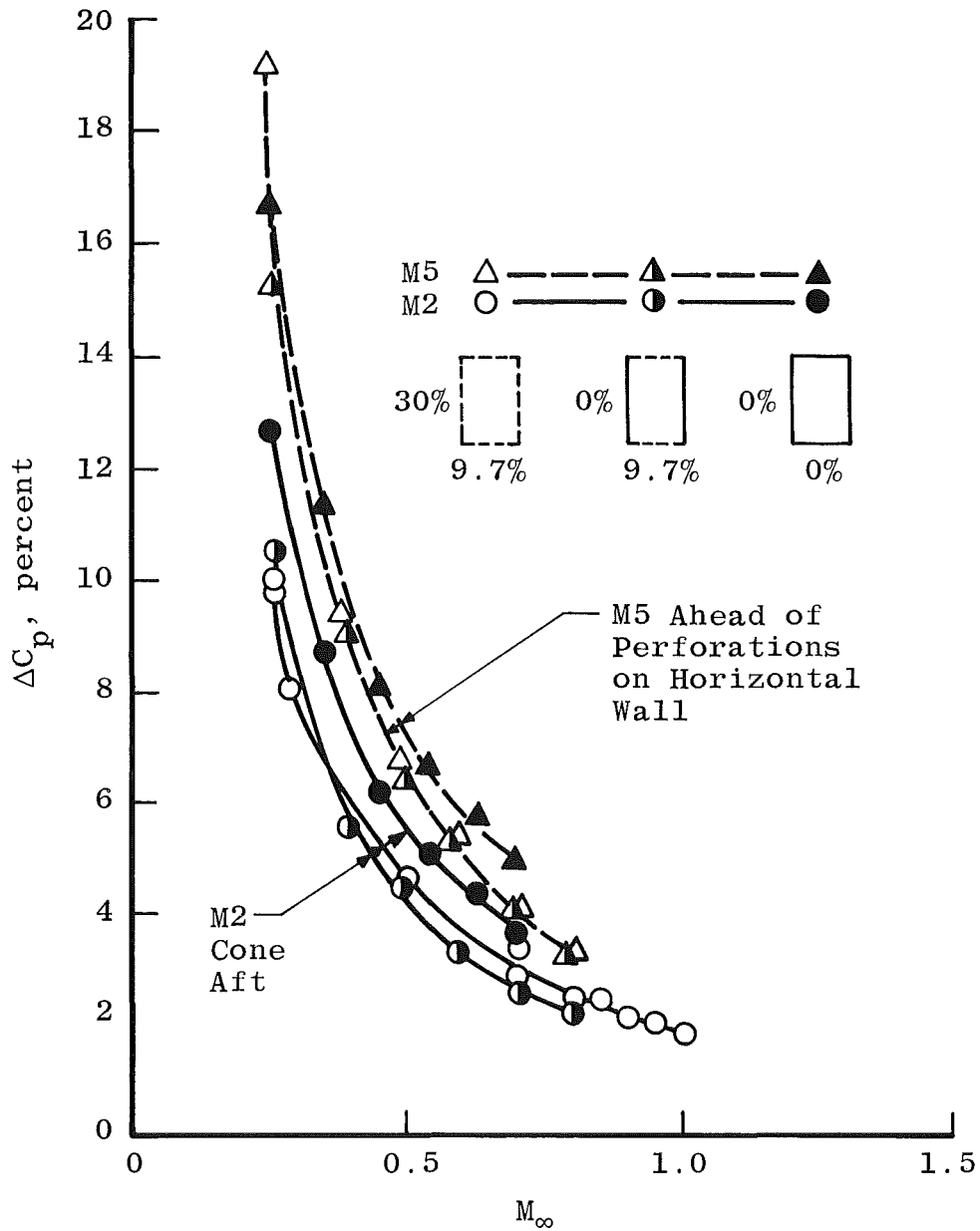


Figure 52. Effects of changing perforated to solid walls on the noise levels in the ONERA 2.56 x 1.83 S-3 Modane.

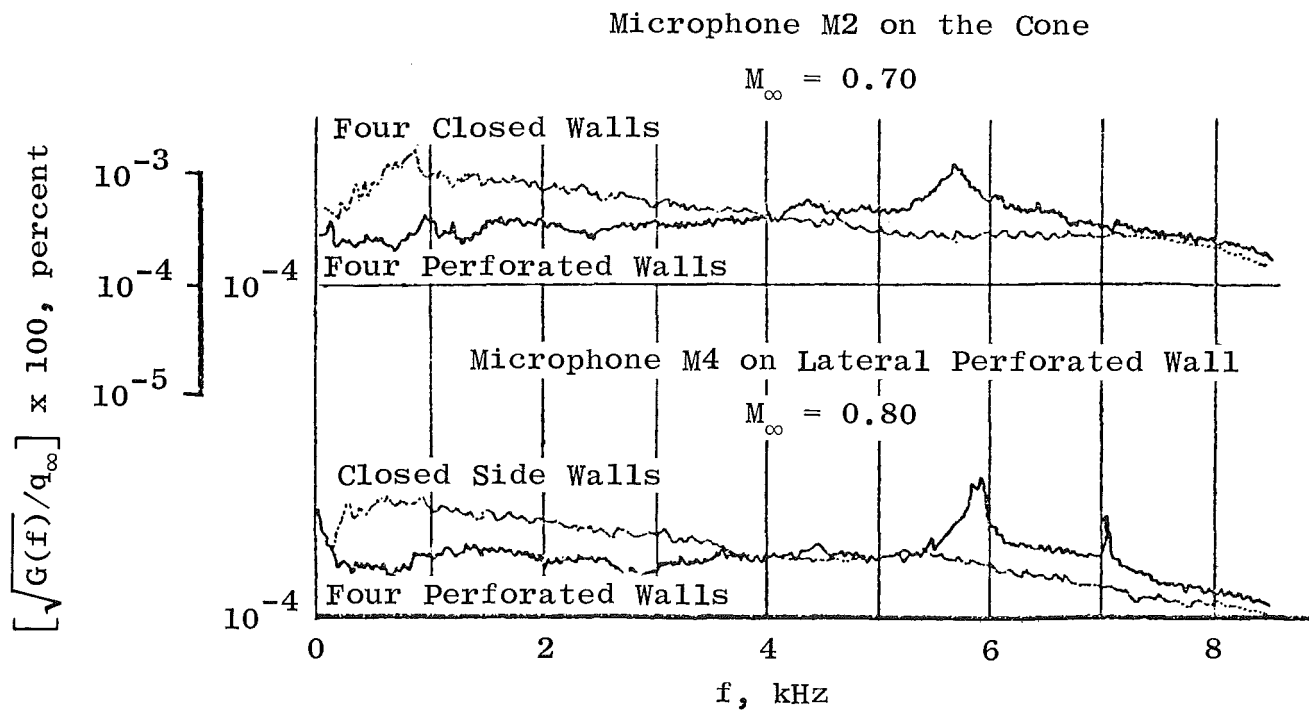


Figure 53. Fourier spectrum measurement comparisons for closed versus open walls at $M_\infty = 0.70$ and 0.80 in the ONERA 2.56×1.83 S-3 Modane.

AEDC/PWT Tunnel 16T

This transonic tunnel has two removable test section carts, the test sections being 16 ft square. Both cart sections are fitted with four perforated walls with $\tau = 6$ -percent fixed porosity. The principal difference between the two carts is the method of model support: one cart for sting mounting, the other for strut mounting. In the sting-support cart there are ribbed sidewalls with solid plates enlarging the cross section adjacent to the sting support mechanism with sufficient enlargement to compensate for the blockage of the mechanism. The strut-support cart has, therefore, a 23.5-percent longer porous zone than the sting-support cart. The cone was tested only in the sting-support cart. There were two separate entries of the cone in AEDC 16T, about two years apart. The second entry included a walls-taped test similar to those performed in AEDC 4T, ONERA S-2, and ONERA S-3. For normal tunnel operation, the two entries yielded basically repeatable results. A separate set of noise characteristics measurements was made in the strut-support cart to determine whether the noise levels in the two carts were about the same. These measurements were made under turbulent boundary-layer conditions on a centerline-mounted static pipe axially spanning the length of the test section and supported by guy wires.

Unit Reynolds number was varied by adjusting p_t at a near-constant T_t level of 570°R throughout both entries of the cone. End-of-transition Reynolds number, Re_T , is presented as a function of M_∞ at constant levels of U_∞/ν_∞ in Fig. 54. Walls-taped data at $U_\infty/\nu_\infty = 2.0 \times 10^6$ exhibit an appreciable increase in Re_T over the data at the same flow conditions for normal tunnel operation.

The onset-of-transition Reynolds number, Re_t , is shown in Fig. 55 for the same conditions as in Fig. 54, the only exception being that the Re_t data for $U_\infty/\nu_\infty = 4.0 \times 10^6$ have been omitted because the transition location is too far forward in this tunnel for valid pitot probe detection of the onset-of-transition point.

The noise levels measured by the cone microphones are presented in Fig. 56 in the form of ΔC_p versus M_∞ for U_∞/ν_∞ from 2.0×10^6 to 5.0×10^6 . The walls-taped data indicate that there was a substantial reduction in ΔC_p with wall noise (edgetone) removal. The data are presented in Table 8.

For comparison, data from the strut-support cart are presented in Fig. 57. These data are for U_∞/ν_∞ varied from 2.0×10^6 to 5.0×10^6 , M_∞ from 0.6 to 1.6. The noise levels measured on the cone in the sting-support cart are generally somewhat higher than those measured on the centerline pipe in the strut-support cart.

Selected cone microphone spectra are presented in Fig. 58 for M_∞ from 0.6 to 1.3. The predominant spectral components of narrow-band energy concentration in the Mach number range from 0.65 to 0.90 are the edgetones. Although not shown in Fig. 58, the walls-taped spectra revealed removal of these predominant peaks. The reduction in ΔC_p and attendant increases in Re_T and Re_t clearly indicate that these tones had a promoting influence on transition. The fundamental tone occurs at 530 Hz at a resonance condition (maximum in ΔC_p versus M_∞) which is at $M_\infty = 0.71$. Review of the spectra as M_∞ was varied in Fig. 58 clearly revealed the growth of this particular spectral component to its maximum amplitude near $M_\infty = 0.70$. Duct acoustic modes of the test section play a role in amplifying these wall-generated tones as described by Varner (Ref. 11).

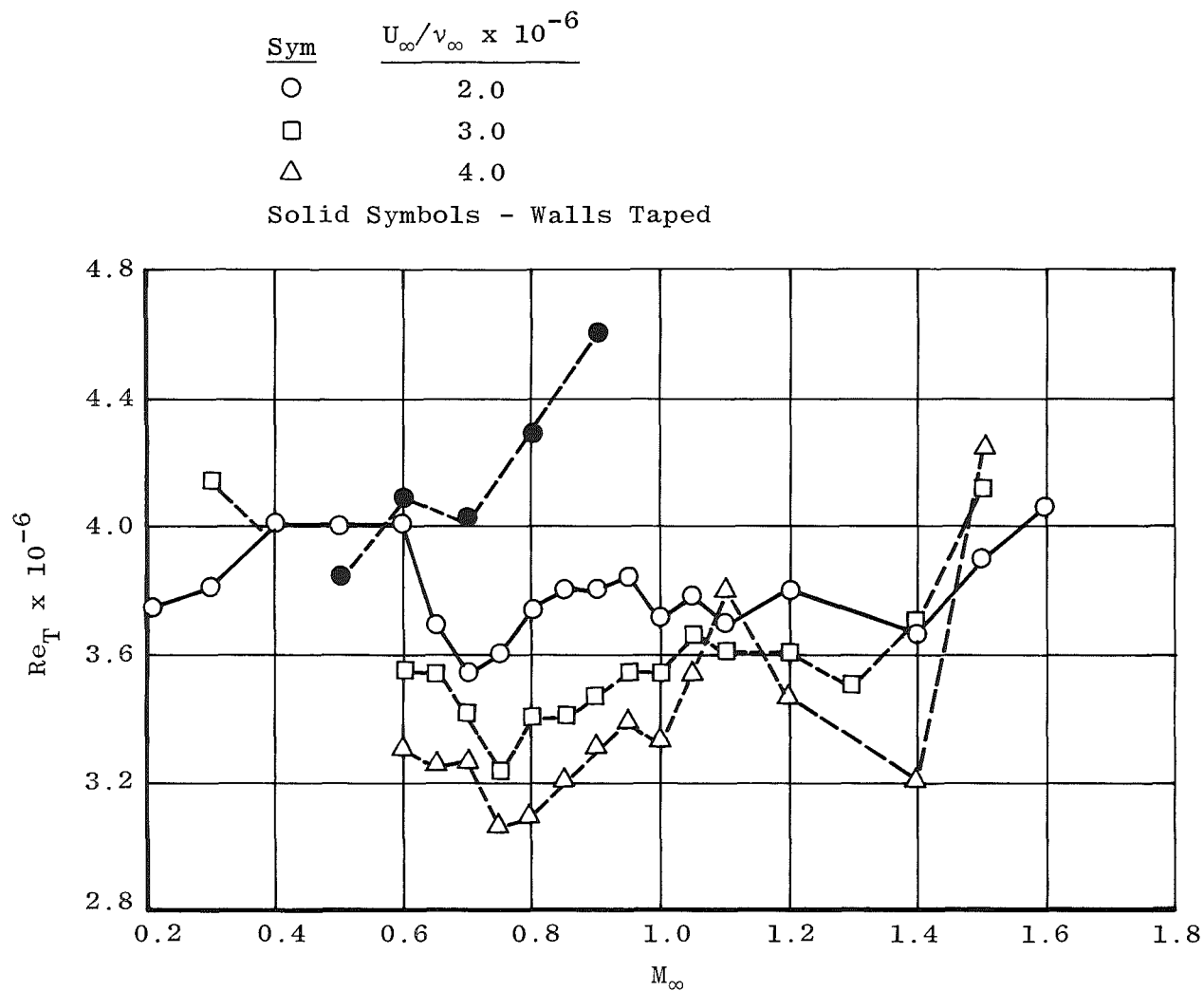


Figure 54. End-of-transition Reynolds numbers in AEDC/PWT Tunnel 16T.

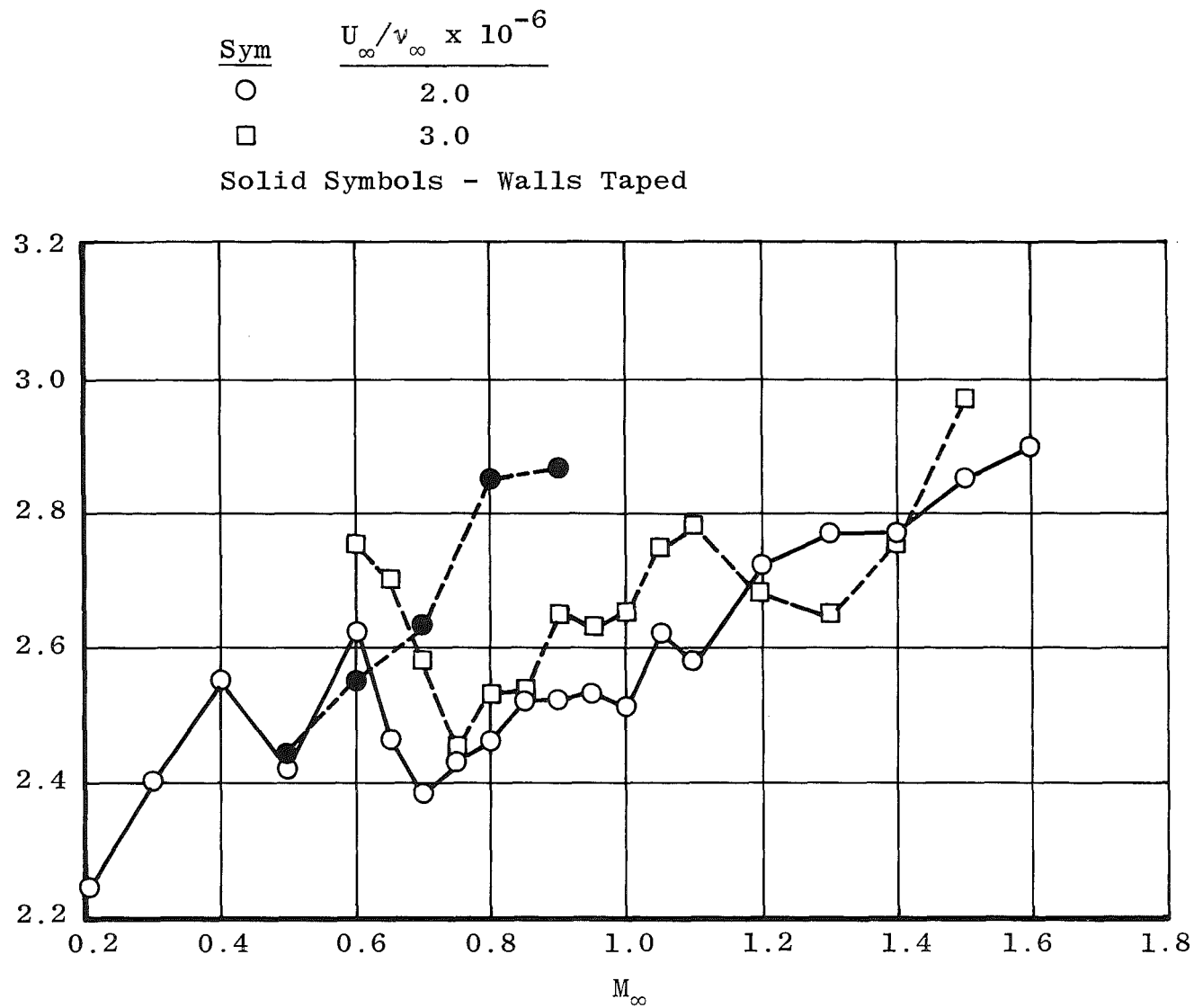


Figure 55. Onset-of-transition Reynolds numbers in AEDC/PWT Tunnel 16T.

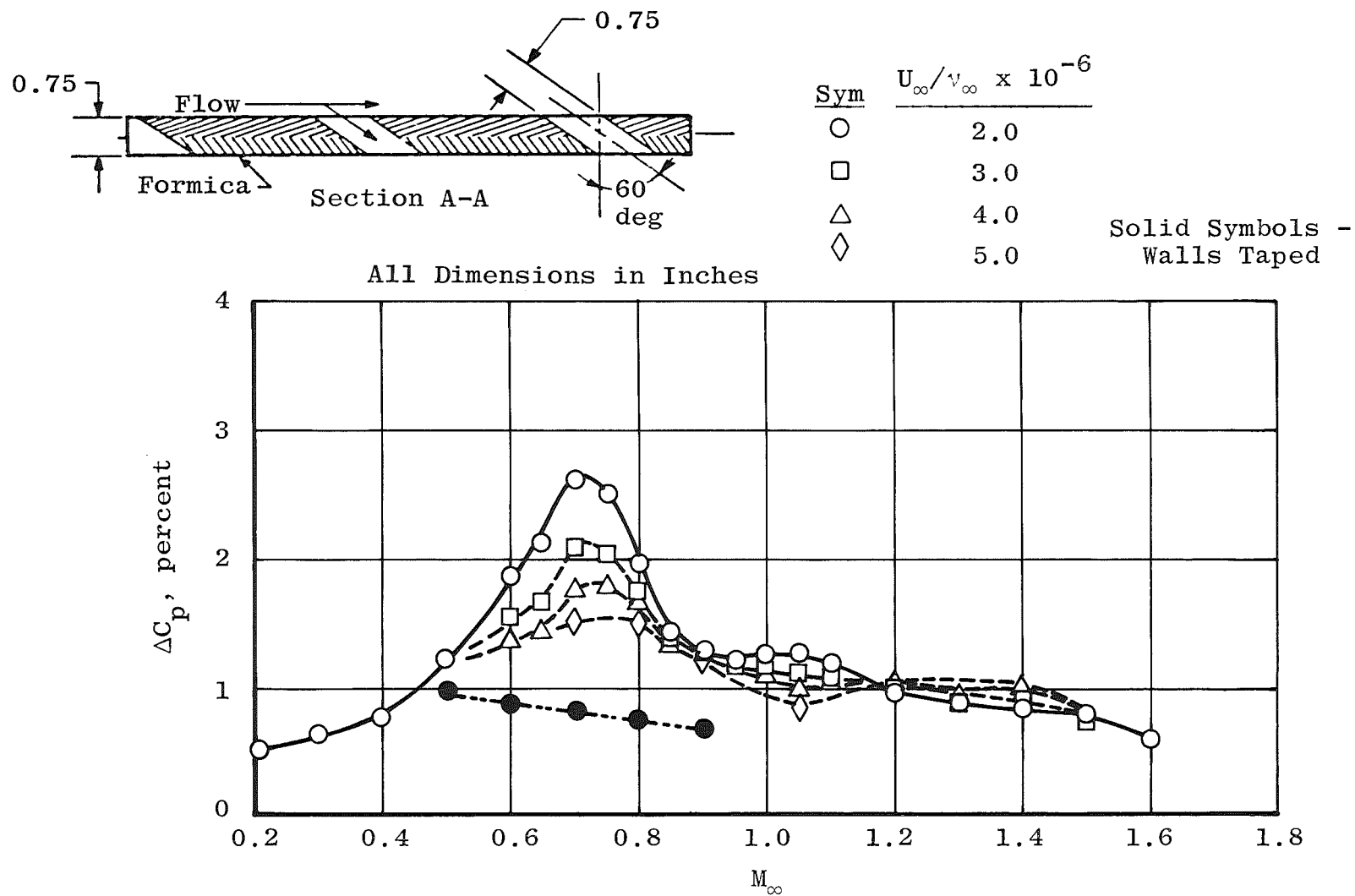


Figure 56. Noise levels in AEDC/PWT Tunnel 16T (sting-support cart).

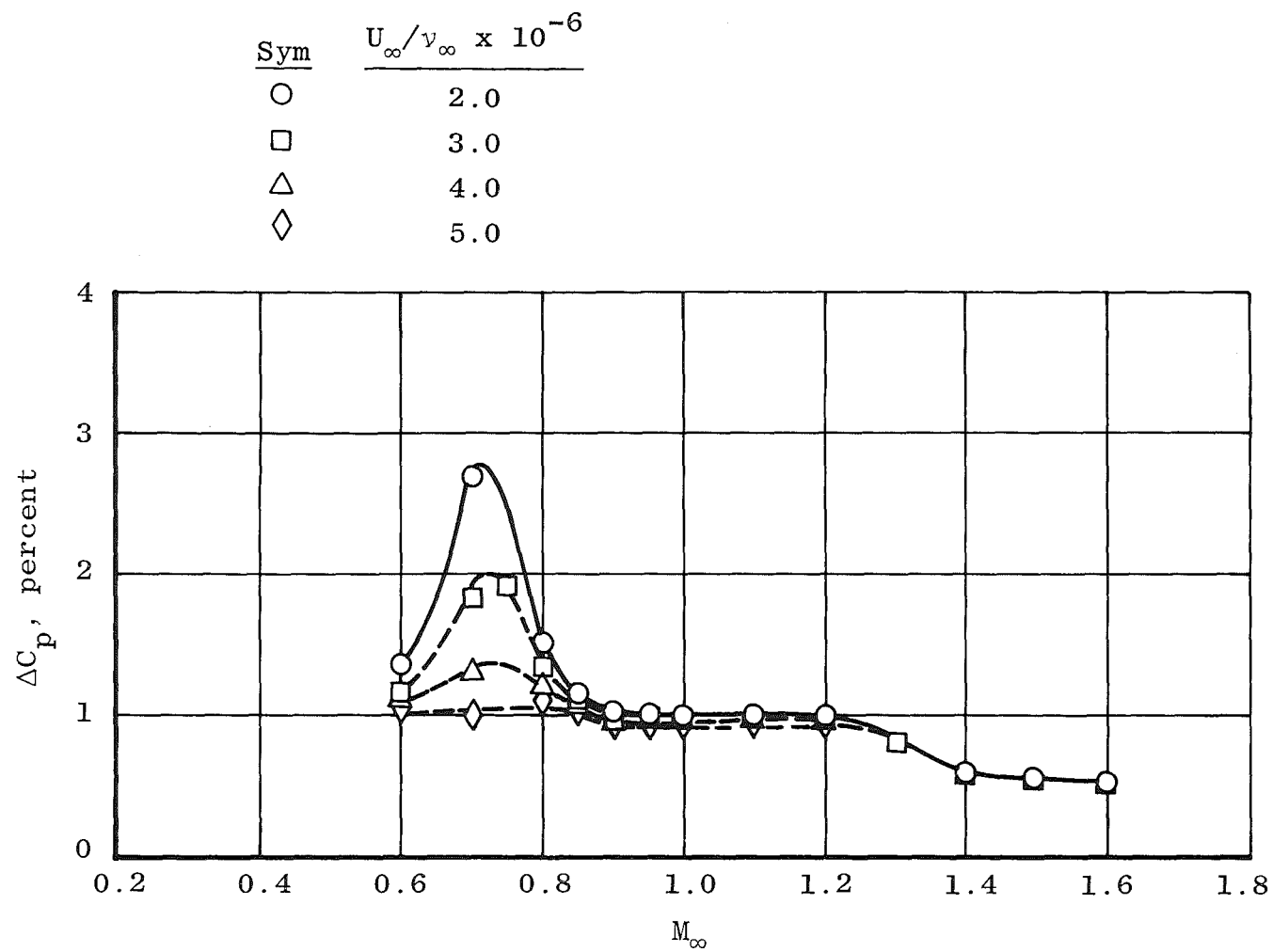


Figure 57. Noise levels in AEDC/PWT Tunnel 16T (strut-support cart).

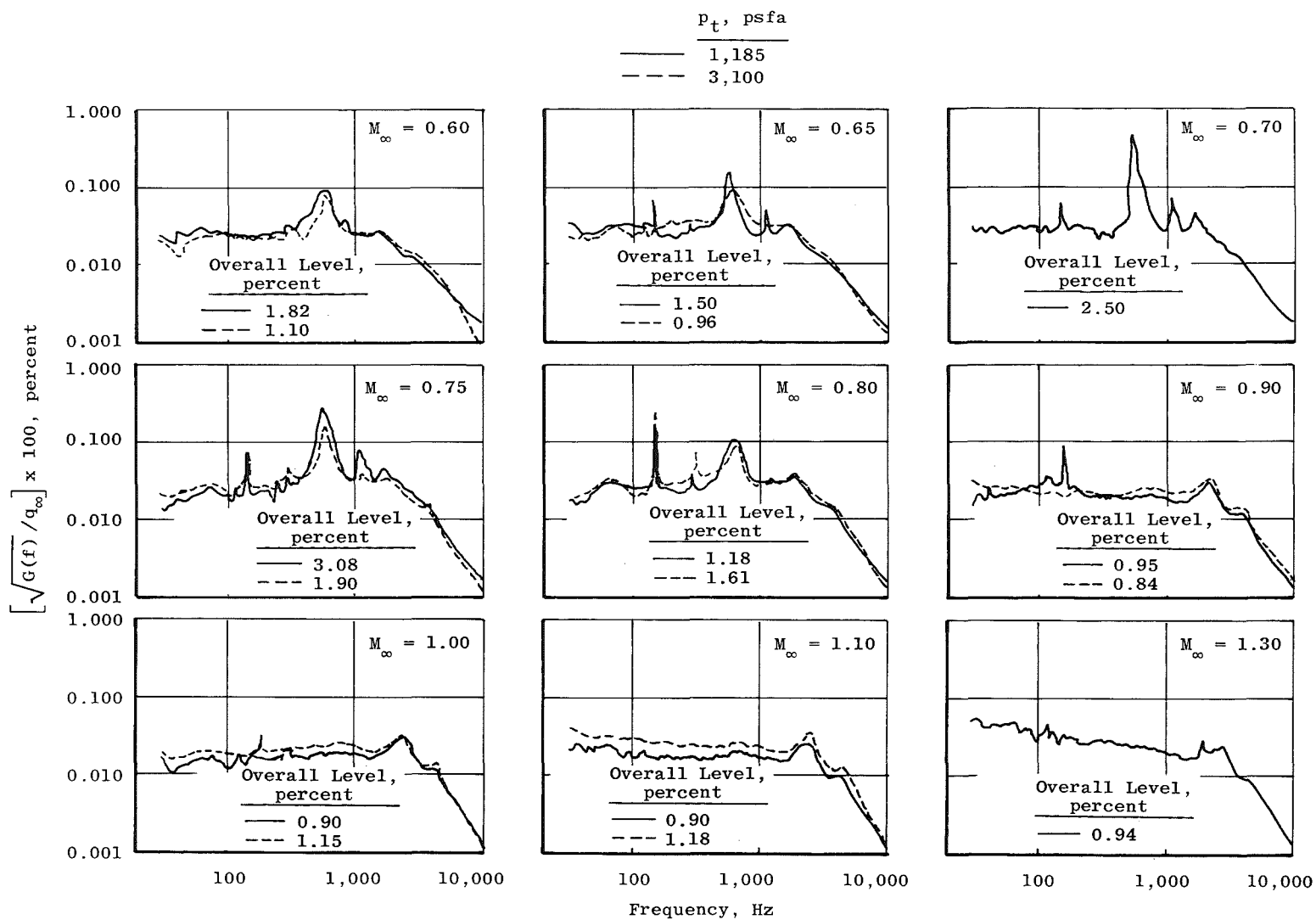


Figure 58. Fourier spectrum measurements in AEDC/PWT 16T (sting-support cart).

Table 8. AEDC/PWT Tunnel 16T Data

First Entry

M_∞	U_∞ / v_∞ $\times 10^{-6}$	ΔC_p , percent	$Re_T \times$ 10^{-6}	$Re_T \times$ 10^{-6}
0.60 ↓	1.660	1.88	2.63	4.13
	1.992	1.88	2.73	4.58
	2.204	1.84	2.63	3.92
	2.480	1.67	2.66	3.72
	2.805	1.60	2.66	3.60
	3.145	1.52	2.81	3.55
	3.649	1.45	2.87	3.38
0.65 ↓	3.641	1.49	2.93	3.38
	3.316	1.56	2.82	3.52
	2.995	1.67	2.68	3.57
	2.659	1.84	2.65	3.64
	2.331	2.01	2.57	3.68
	1.993	2.12	2.46	3.69
	1.670	2.26	2.42	3.68
0.70 ↓	1.753	2.73	2.33	3.53
	2.084	2.58	2.42	3.53
	2.423	2.26	2.46	3.44
	3.111	2.05	2.61	3.37
	3.462	1.87	2.67	3.32
	3.808	1.81	2.87	3.23
	4.003	1.70	2.91	3.22
0.75 ↓	1.488	2.58	2.44	3.95
	2.177	2.38	2.72	4.03
	2.879	2.05	2.44	3.22
	3.609	1.91	2.48	3.08
	3.963	1.81	2.78	3.17
	4.135	1.74	2.81	2.97
0.80 ↓	3.354	1.74	2.57	3.29
	3.731	1.67	2.59	3.12
	4.103	1.67	2.97	3.11
	2.972	1.77	2.72	3.63
	2.233	1.91	2.57	3.78
	1.855	1.98	2.46	3.74
0.85 ↓	1.918	1.41	2.52	3.81
	2.302	1.43	2.53	3.55
	3.070	1.38	2.54	3.37
	3.443	1.34	2.66	3.38
	3.830	1.31	2.82	3.25
	4.210	1.31	3.11	3.27

Table 8. Continued
First Entry, Concluded

M_∞	$U_\infty/v_\infty \times 10^{-6}$	ΔC_p , percent	$Re_t \times 10^{-6}$	$Re_T \times 10^{-6}$
0.90 ↓	1.959 2.344 3.164 3.531 3.934 4.315	1.27 1.31 1.24 1.20 1.20 1.27	2.47 2.56 2.66 2.69 3.80 -	3.82 3.58 3.43 3.37 3.31 3.30
0.95 ↓	2.012 2.397 3.197 3.606 4.012	1.24 1.17 1.17 1.17 1.13	2.55 2.52 2.67 2.70 2.91	3.90 3.58 3.54 3.46 3.38
1.00 ↓	2.030 3.254 4.073	1.20 1.10 1.04	2.54 2.68 2.82	3.48 3.47 3.28
1.10 ↓	2.485 3.318 4.151 2.068	1.07 1.05 1.03 1.10	2.66 2.85 3.27 2.49	3.68 3.72 3.81 3.71
1.20 ↓	2.080 2.496 3.345 3.974	1.06 1.06 1.06 1.06	2.76 2.58 2.65 2.70	3.68 3.46 3.48 3.31
1.30 ↓	2.093 2.500 3.320	1.06 1.03 1.06	2.77 2.61 2.50	3.47 3.83 3.33

Table 8. Continued

M_∞	Second Entry			
	U_∞/v_∞ $\times 10^{-6}$	ΔC_p , percent	$Re_t \times$ 10^{-6}	$Re_T \times$ 10^{-6}
0.20	2.027	0.47	2.24	3.74
0.30	1.877	0.41	2.31	3.64
0.30	2.668	0.36	2.67	4.03
0.40	1.382	0.52	2.66	3.23
0.40	2.426	0.45	2.45	3.38
0.50	1.100	0.77	2.74	-
↓	1.618	0.66	2.42	3.72
	2.123	0.71	2.41	4.01
0.60	1.234	2.15	2.60	-
↓	1.599	1.65	2.45	3.65
	1.827	1.40	2.57	3.73
	1.832	1.40	2.57	3.73
	3.223	1.20	2.93	3.63
↓	4.588	1.27	-	2.95
0.70	2.016	2.17	2.65	3.83
↓	2.028	2.17	2.40	3.81
	3.548	1.48	2.87	3.57
↓	5.052	1.43	-	3.15
0.80	1.731	1.70	2.35	3.45
↓	2.175	1.70	2.59	3.78
	2.184	1.70	2.43	3.51
↓	3.823	1.57	2.70	-
0.90	1.820	1.17	2.46	3.70
↓	2.295	1.17	2.76	3.99
	2.295	1.17	2.58	3.72
	4.020	1.15	-	-
↓	5.585	1.20	-	3.17
0.95	1.851	1.16	2.48	3.55
↓	2.295	1.14	2.72	3.86
	2.348	1.14	2.57	3.74
1.00	1.853	1.31	2.50	3.71
↓	2.370	1.23	2.73	4.01
	2.370	1.23	2.61	3.73
↓	3.176	1.10	2.70	3.70

Table 8. Continued
Second Entry, Continued

M_∞	U_∞ / v_∞ $\times 10^{-6}$	ΔC_p , percent	$Re_t \times$ 10^{-6}	$Re_T \times$ 10^{-6}
1.05 ↓	1.884 2.396 2.403 2.417	1.28 1.13 1.10 1.08	2.62 2.70 2.32 2.84	3.58 3.77 3.23 4.00
1.10 ↓	1.911 2.418 2.424 2.444 3.237	1.10 1.38 1.01 1.05 1.05	2.58 2.62 2.71 2.85 2.75	3.63 2.62 3.71 - 3.51
1.20 ↓	1.906 2.432 2.441 2.450 3.255 4.166	0.92 0.87 0.95 1.02 0.88 1.03	2.53 2.73 2.79 2.69 2.62 2.66	3.93 3.81 3.81 3.68 3.35 3.45
1.30 ↓	1.911 2.378 2.385 2.432 4.156	0.86 0.91 0.82 0.82 0.88	3.12 2.78 3.12 2.74 2.66	4.31 - 4.36 3.93 3.02
1.40 ↓	1.883 2.338 2.348 2.348 3.207 4.109	0.80 0.85 0.85 0.95 0.92 1.02	2.70 2.88 2.89 2.89 2.71 2.29	3.41 3.74 3.83 3.95 3.65 3.14
1.50 ↓	1.748 2.349 2.358 2.358 3.104	0.80 0.75 0.75 0.75 0.69	2.83 2.84 2.75 2.87 3.11	3.83 3.95 3.84 3.92 4.28
1.60 ↓	1.520 1.710 2.263 2.293 2.306	0.52 0.53 0.58 0.57 0.57	3.11 2.92 2.87 2.86 2.71	- 4.05 4.04 3.88 -

Table 8. Concluded
Second Entry, Concluded (Walls Taped)

M_∞	$U_\infty/v_\infty \times 10^{-6}$	ΔC_p , percent	$Re_t \times 10^{-6}$	$Re_T \times 10^{-6}$
0.90	2.28	0.70	3.04	4.58
0.82	2.20	0.76	2.86	4.32
0.70	2.02	0.82	2.63	4.03
0.60	1.83	0.90	2.54	4.10
0.50	1.60	0.99	2.45	3.82

NASA/Ames 11 TWT

The cone was tested in four different entries in the NASA/Ames 11 TWT. These entries were performed over a five-year time span. The objective of repeated entries was primarily to determine what variations existed with axial position in the tunnel over a range in tunnel stations from 110 to 150 in. as measured from the nozzle throat. The results indicated that there was little or no variation in either transition Reynolds number or noise characteristics over this range in axial locations; the results also provided a fairly consistent set of data from the standpoint of repeatability in tunnel operation.

Photographs of the cone installation in the NASA/Ames 11 TWT are shown in Fig. 59. In one test, when the cone was at Sta. 110 in., a walls-taped experiment was performed to remove the slot-generated noise from the test section (Ref. 6). All of the measured data are presented in Table 9.

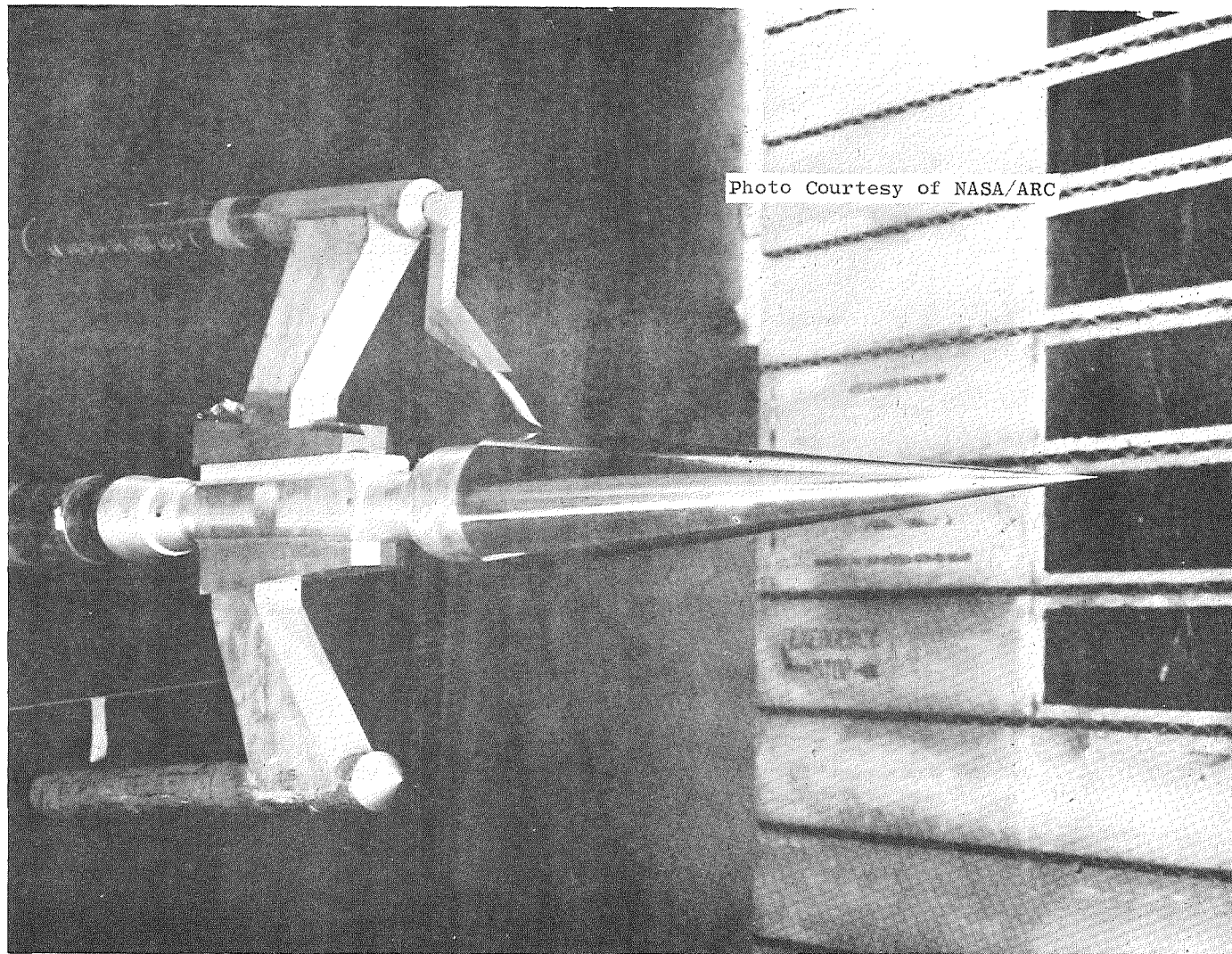
End-of-transition Reynolds number, Re_T , at the 110-in. location is shown in Fig. 60. Results are shown for normal tunnel operation and with slots closed. At $M_\infty = 0.90$ there is an intermediate point where the tape was removed from the two sidewalls, leaving the test section half open to the plenum. Onset of transition, Re_t , is shown in Fig. 61 for these same conditions with one omission, the half-open case at $M_\infty = 0.90$. The noise data, ΔC_p versus M_∞ , are shown for these same conditions in Fig. 62, and the result is clear that reduction of the slot-generated noise accompanies the increase in transition Reynolds number. Thus, there is clear indication that the acoustic disturbances occurring in this baffled, slotted-wall transonic tunnel have promotional influence on transition. Typical power density spectra from the two cone microphones are shown in Fig. 63 for M_∞ from 0.6 to 1.1. Three discrete spectral peaks occurring at approximately 2,600, 5,200, and 7,800 Hz are dominant; the lowest harmonic of these occurs at $fl_0/U = 0.76 \times 10^{-2}$ (2,600 Hz) at $M_\infty = 0.75$.

End-of-transition Reynolds number, Re_T , at the 122-in location* is presented in Fig. 64. Onset-of-transition Reynolds number, Re_t , is presented in Fig. 65. The noise level, ΔC_p , is presented in Fig. 66.

At the 133-in. location, data were acquired at levels of U_∞/ν_∞ up to 6.0×10^6 . End-of-transition Reynolds numbers are shown in Fig. 67, Re_t values are shown in Fig. 68, and ΔC_p values are shown in Fig. 69.

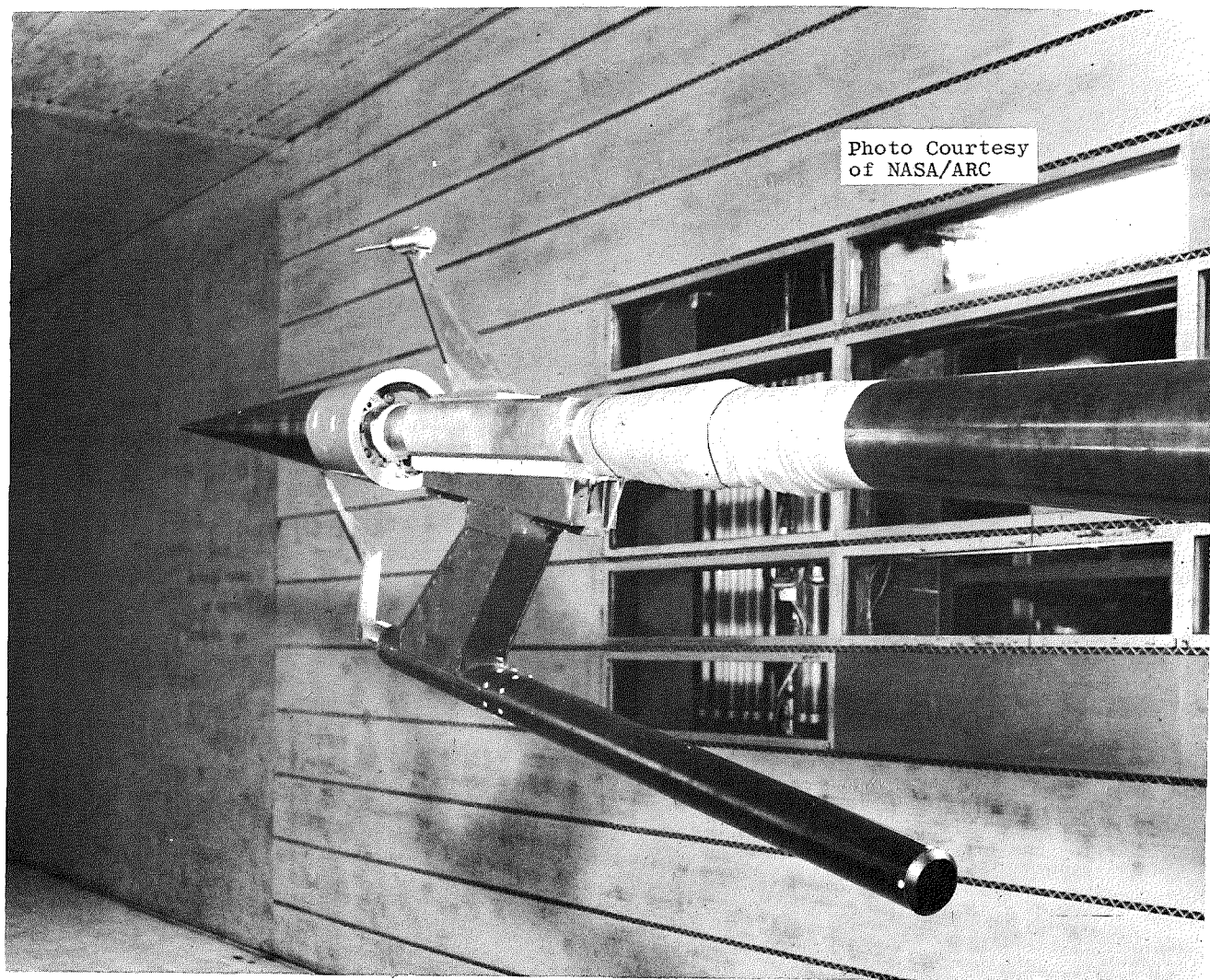
Finally, the data acquired at the 150-in. location are shown in Fig. 70 (Re_T), Fig. 71 (Re_t), and Fig. 72 (ΔC_p). At this and all other locations, it would seem that Re_T and Re_t generally have an inverse relationship to ΔC_p and that the noise level is invariant with U_∞/ν_∞ .

*Unpublished NASA/ARC data.



a. Third entry

Figure 59. Photographs of the cone installation in the NASA/Ames 11 TWT.



b. Fourth entry
Figure 59. Concluded.

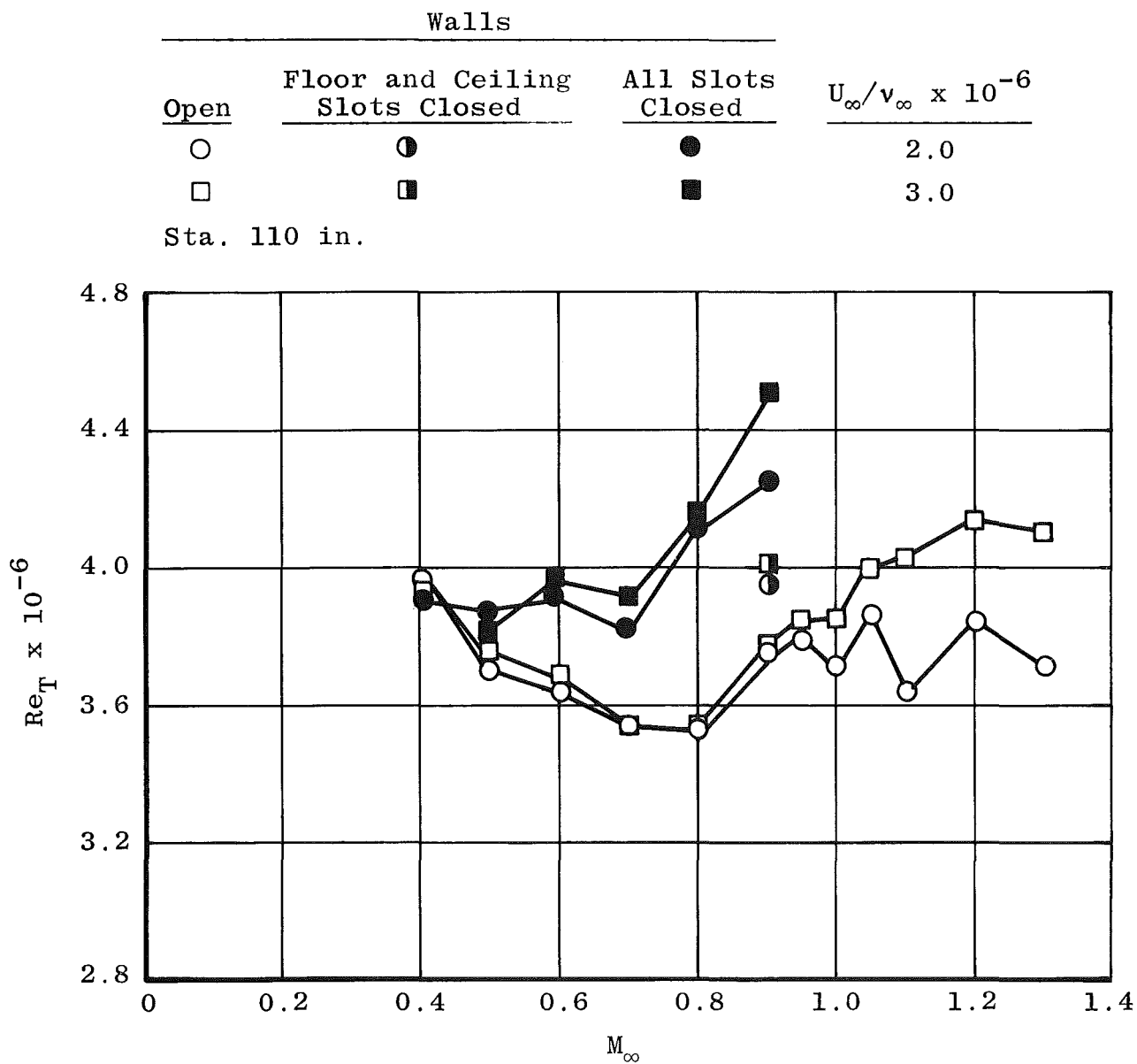


Figure 60. End-of-transition Reynolds numbers in the NASA/Ames 11 TWT at Sta. 110 in.

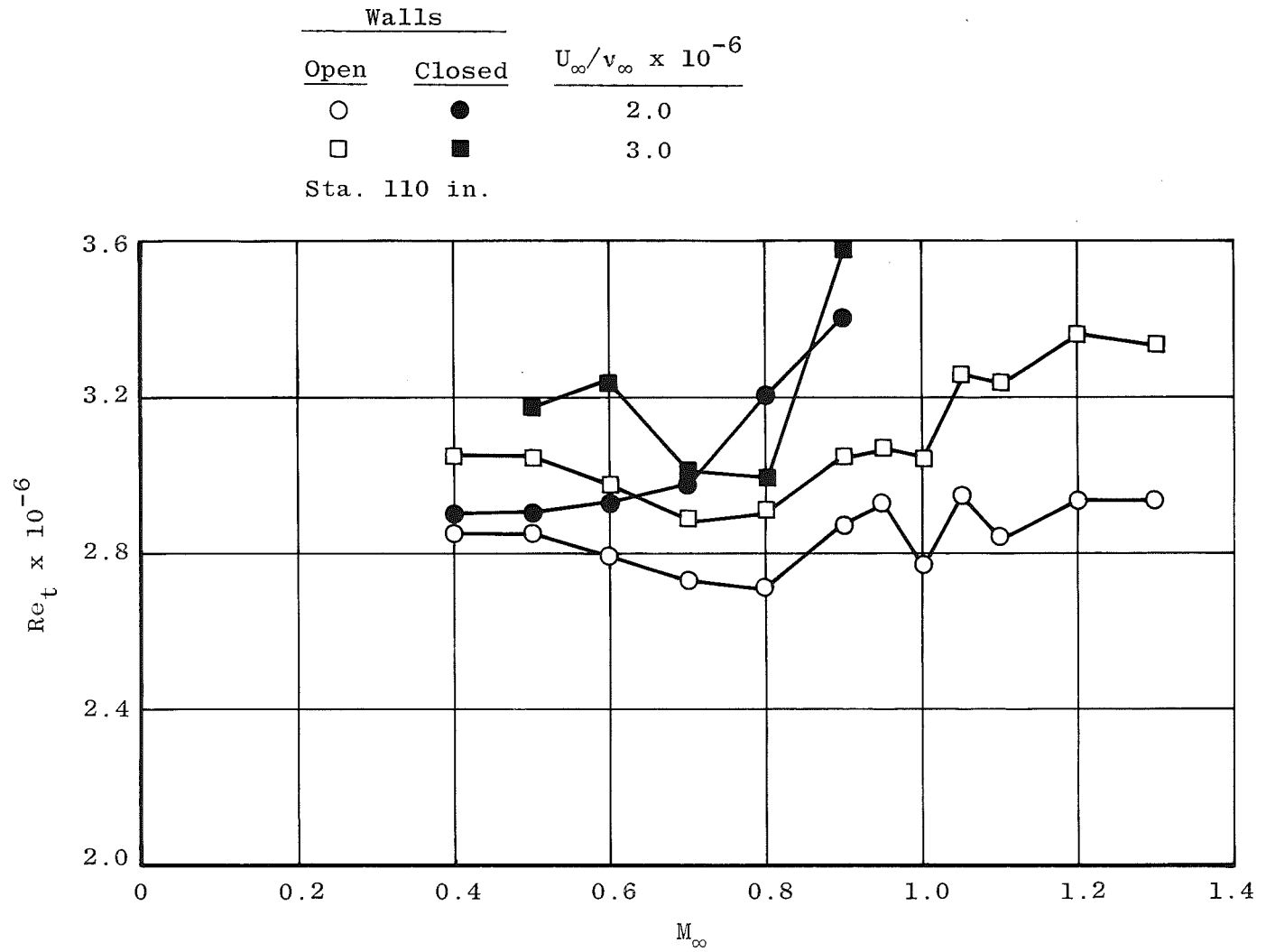


Figure 61. Onset-of-transition Reynolds numbers in the NASA/Ames 11 TWT at Sta. 110 in.

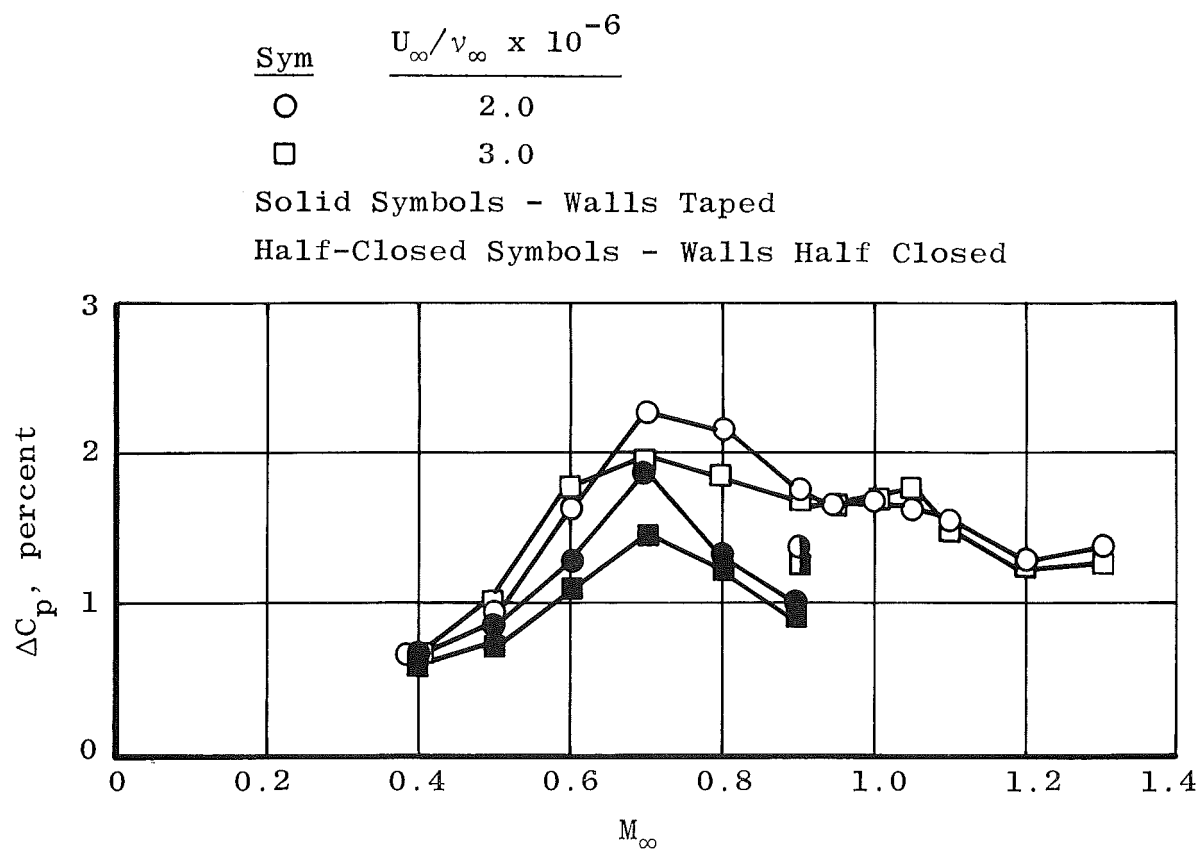
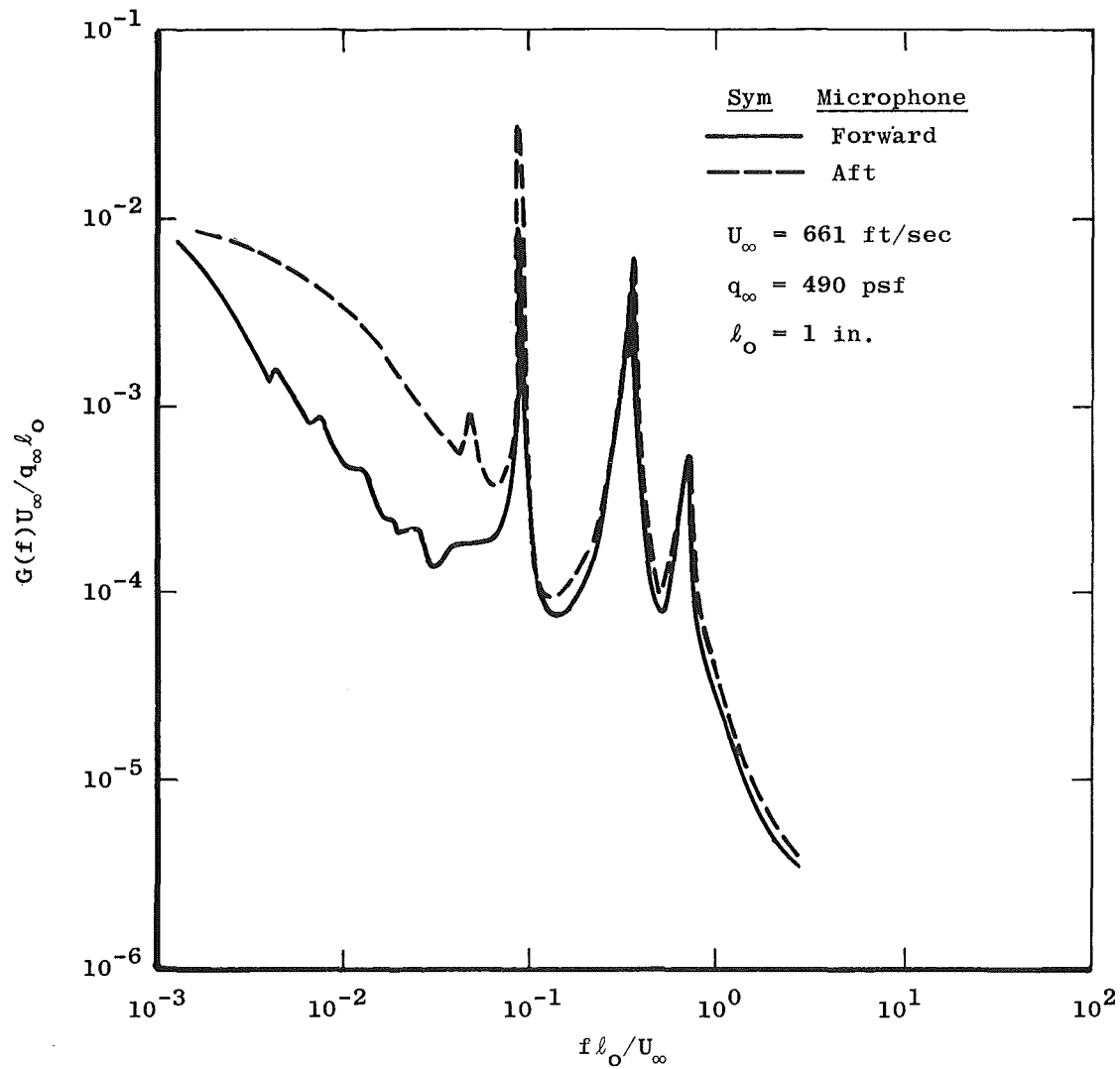
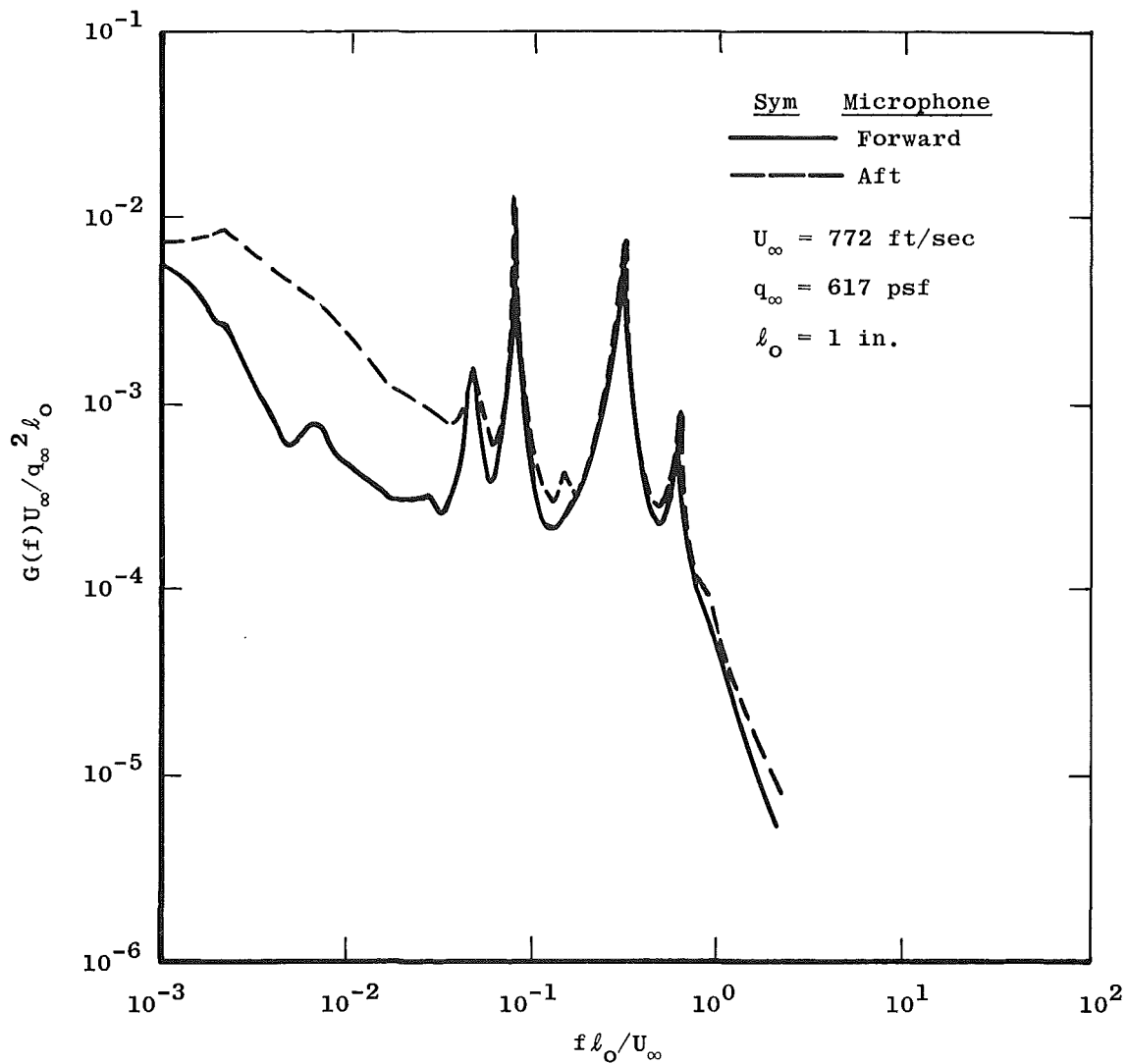


Figure 62. Noise levels in the NASA/Ames 11 TWT at Sta. 110 in.

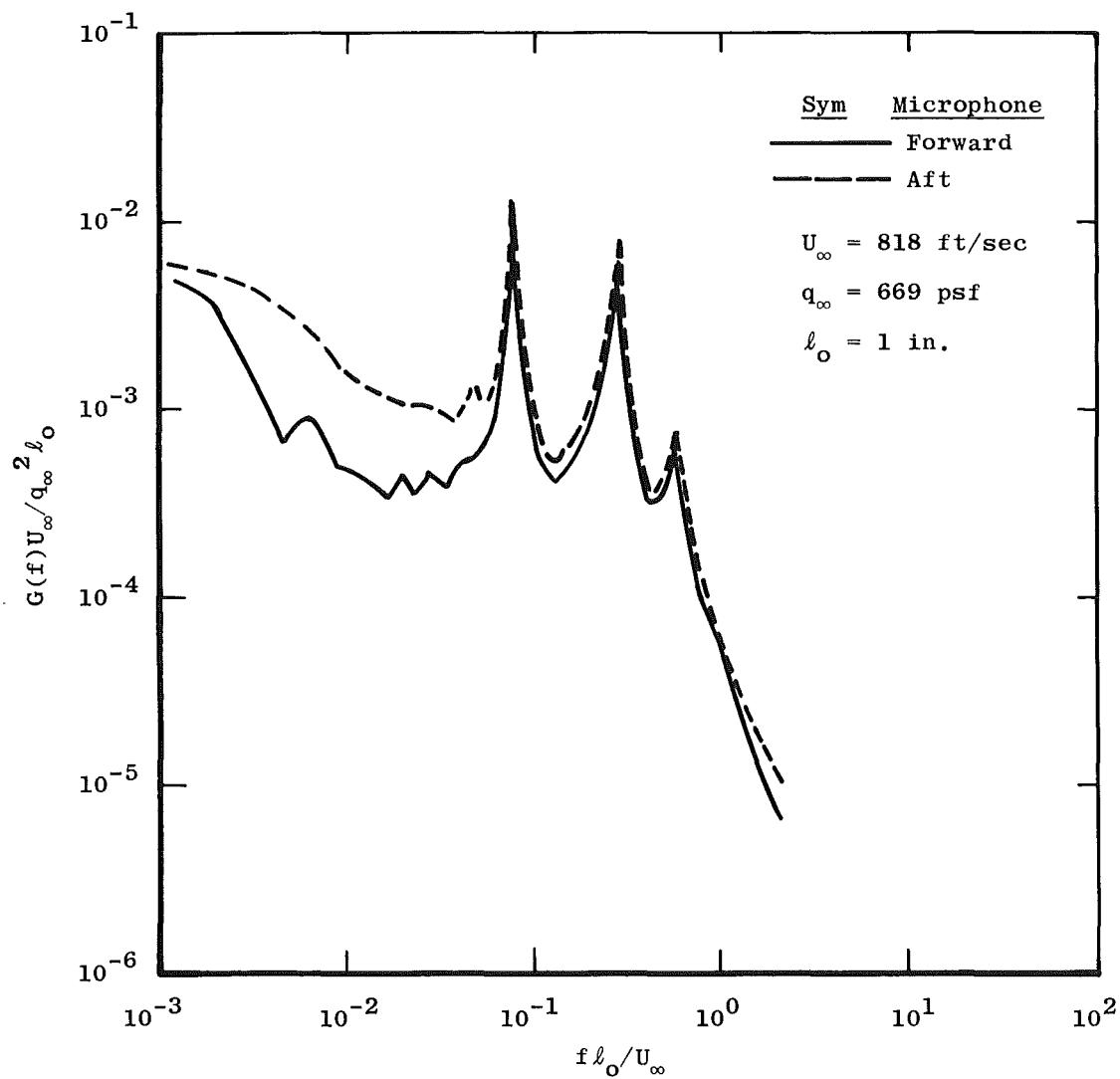


a. $M_{\infty} = 0.60$

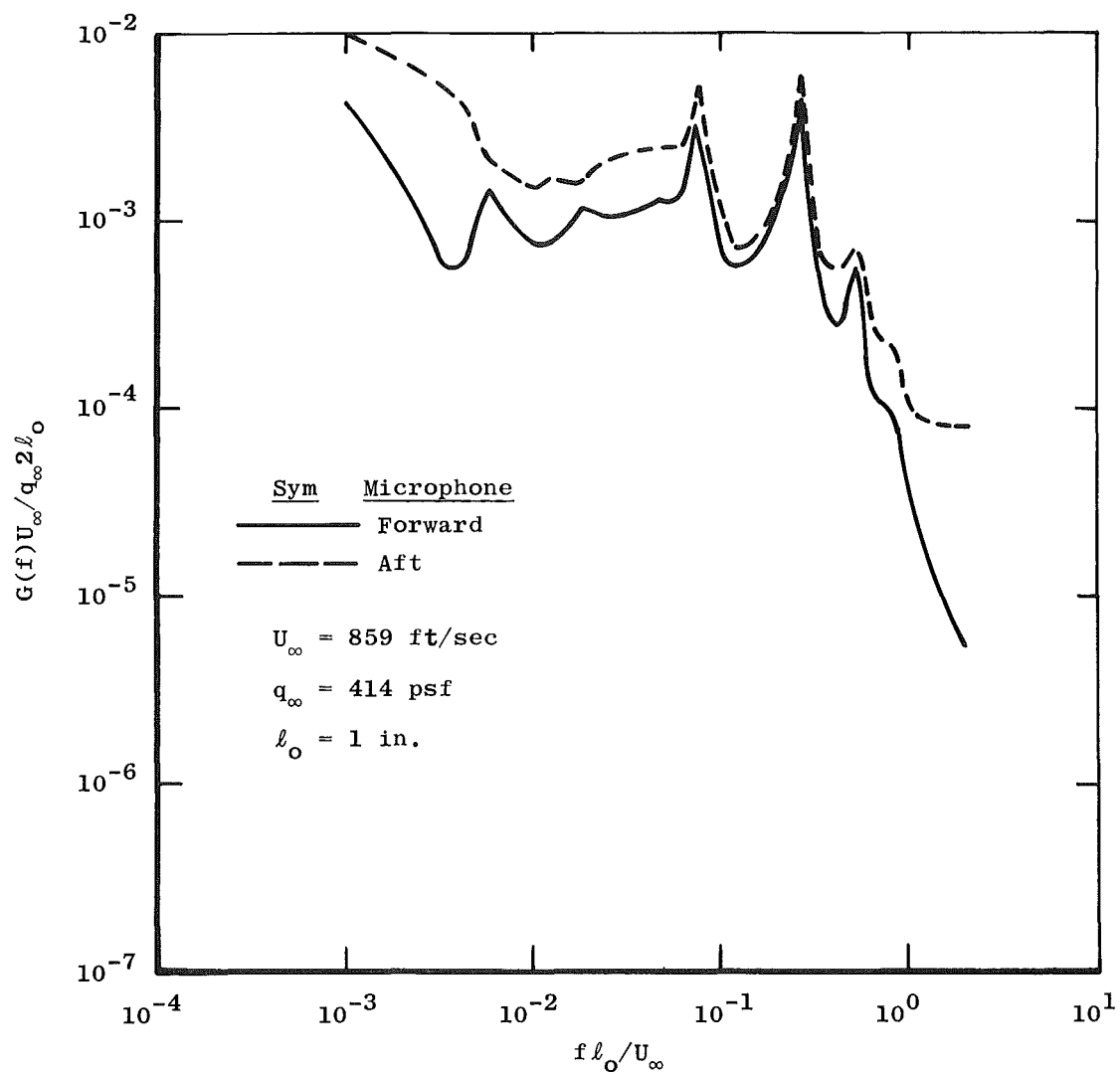
Figure 63. Typical power spectral density measurements in the NASA/Ames 11 TWT.



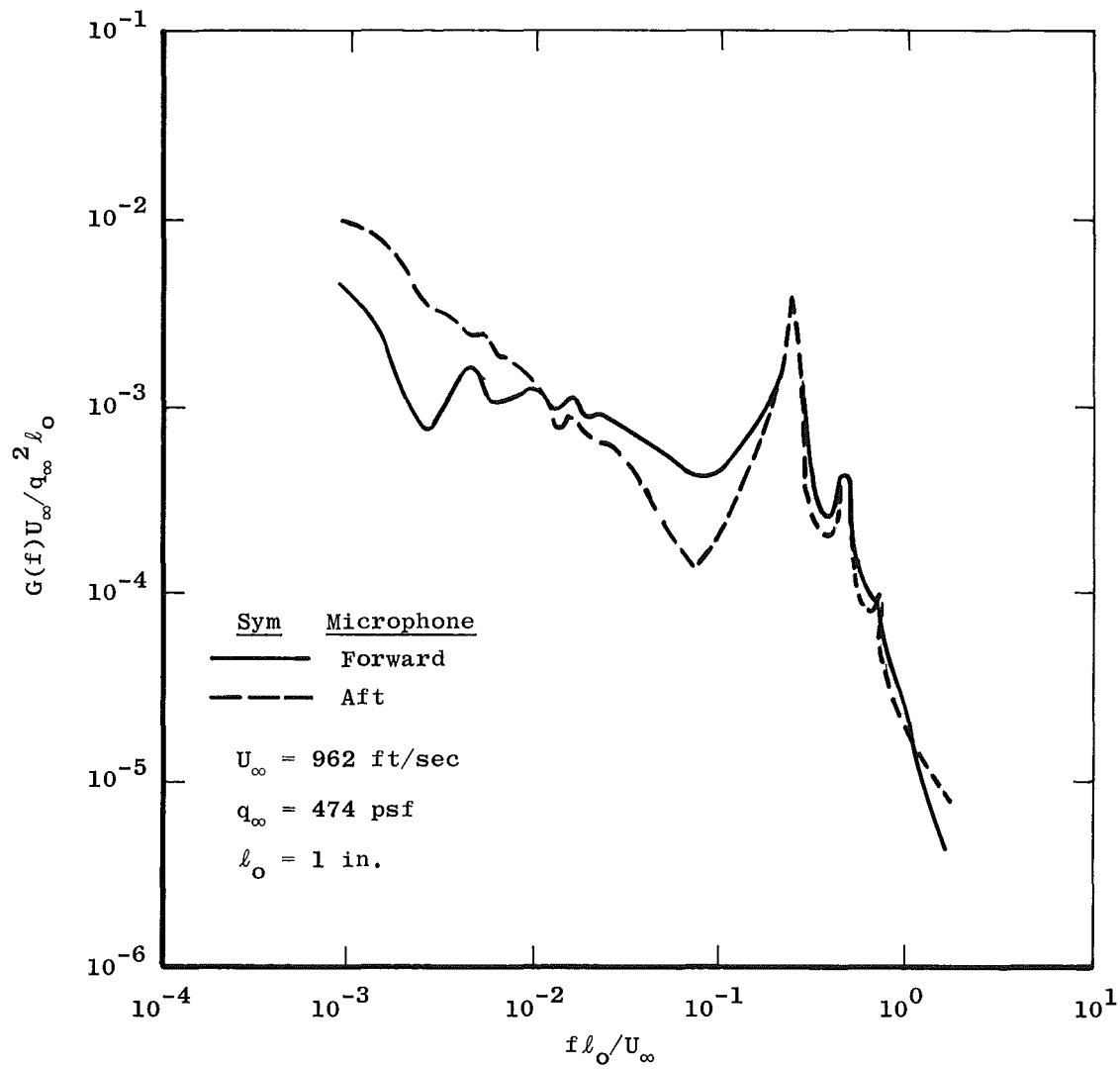
b. $M_\infty = 0.70$
Figure 63. Continued.



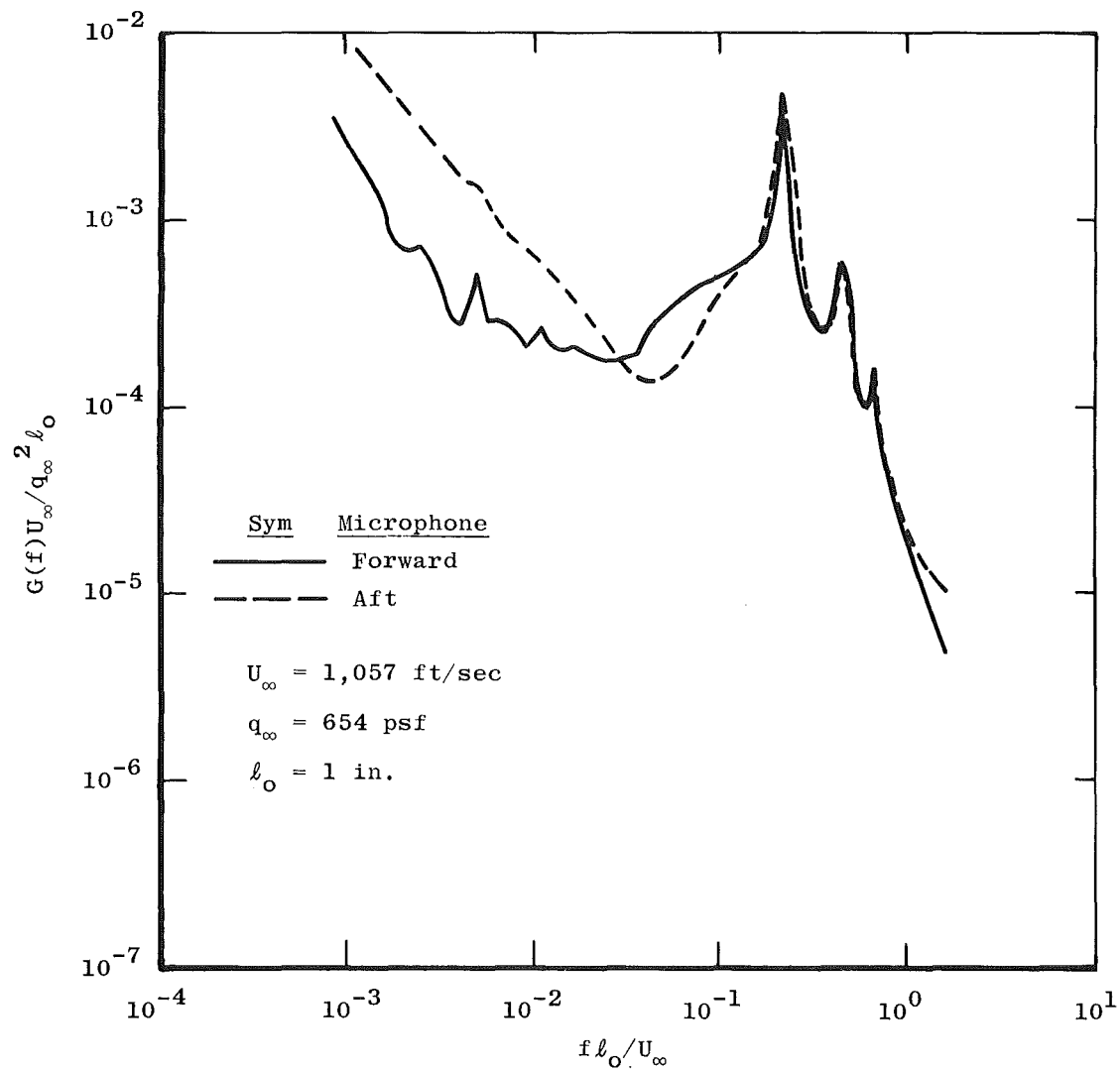
$c. M_\infty = 0.75$
 Figure 63. Continued.



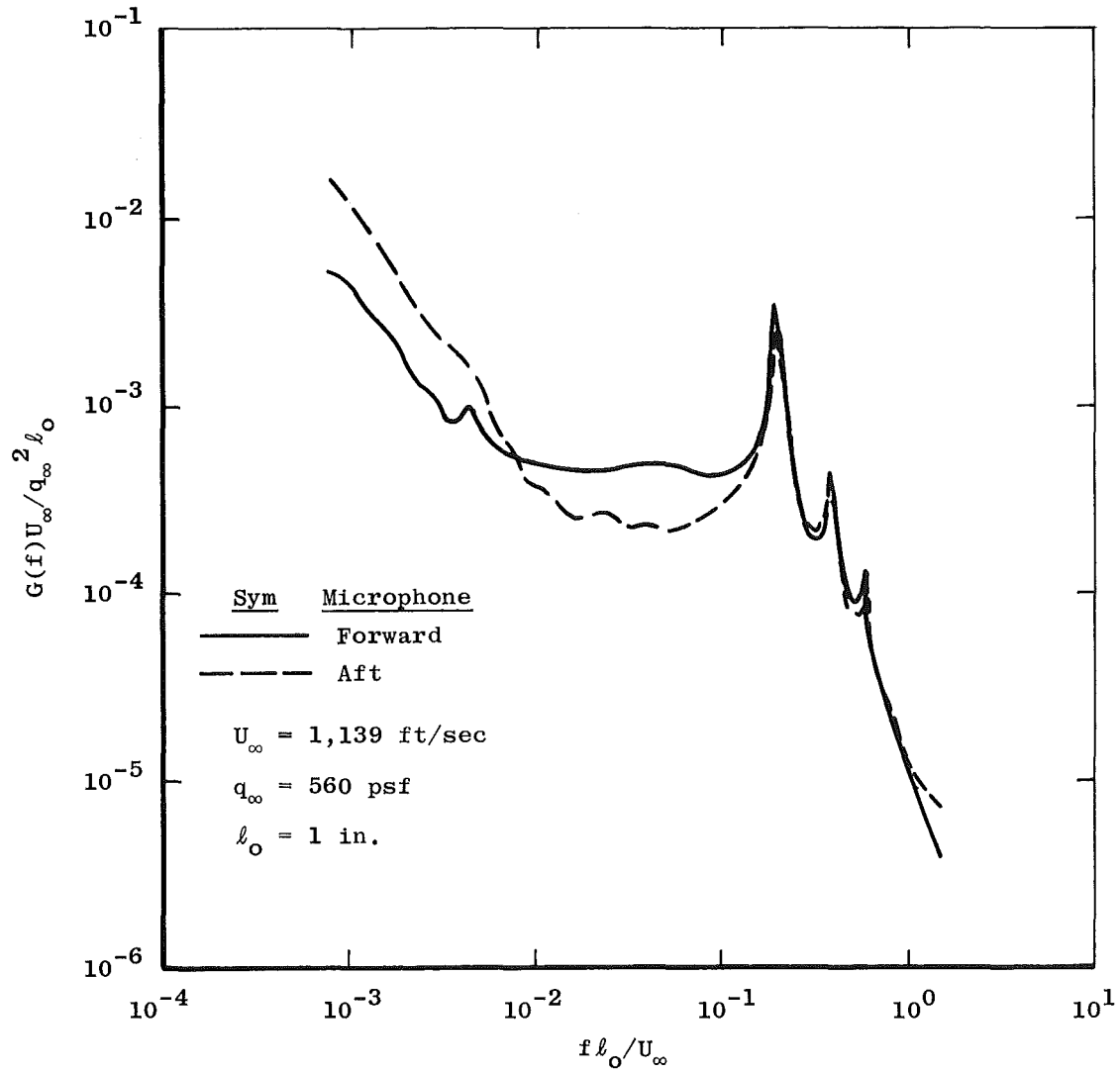
d. $M_{\infty} = 0.80$
 Figure 63. Continued.



e. $M_\infty = 0.90$
 Figure 63. Continued.



f. $M_\infty = 1.00$
 Figure 63. Continued.



g. $M_\infty = 1.10$
 Figure 63. Concluded.

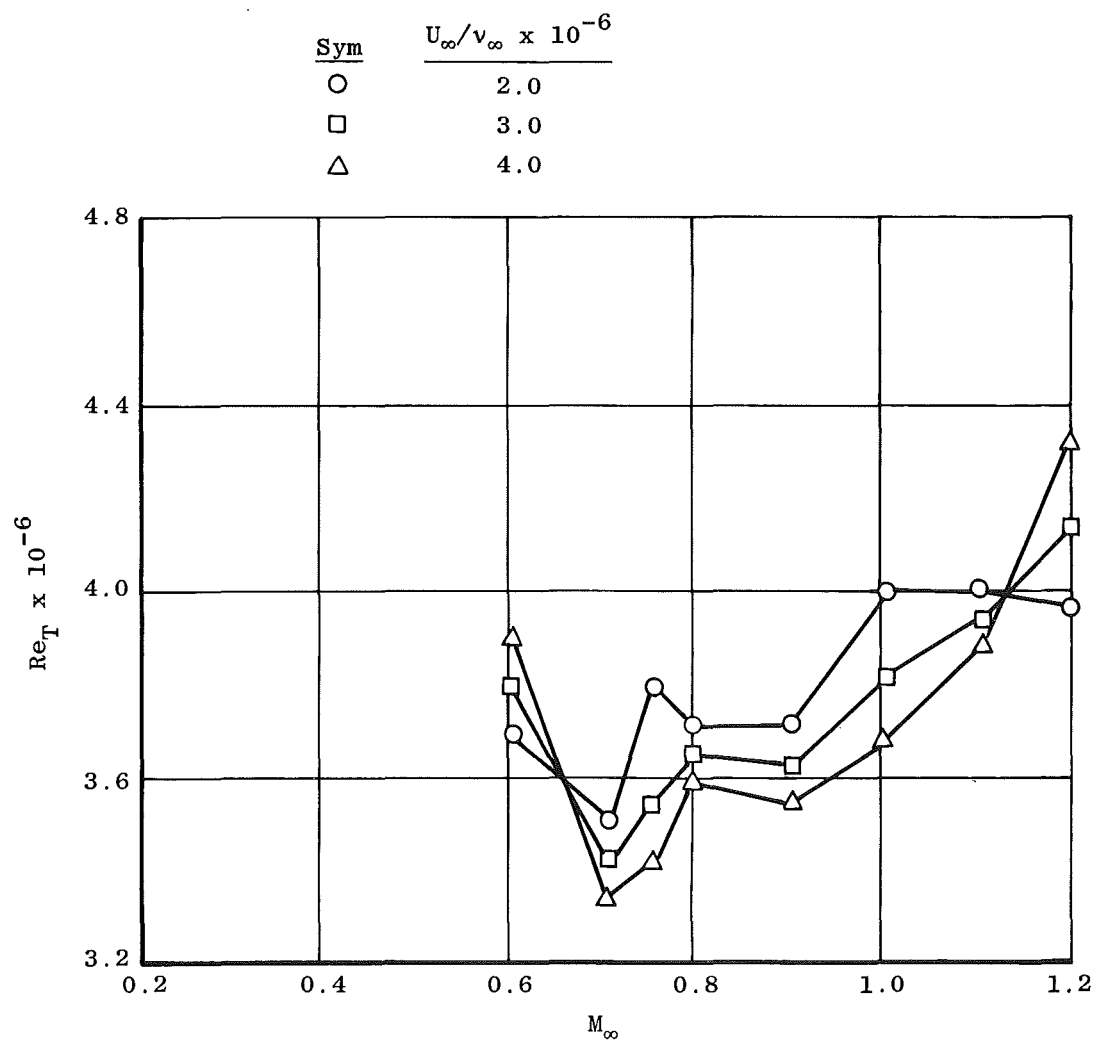


Figure 64. End-of-transition Reynolds numbers in the NASA/Ames 11 TWT at Sta. 122 in.

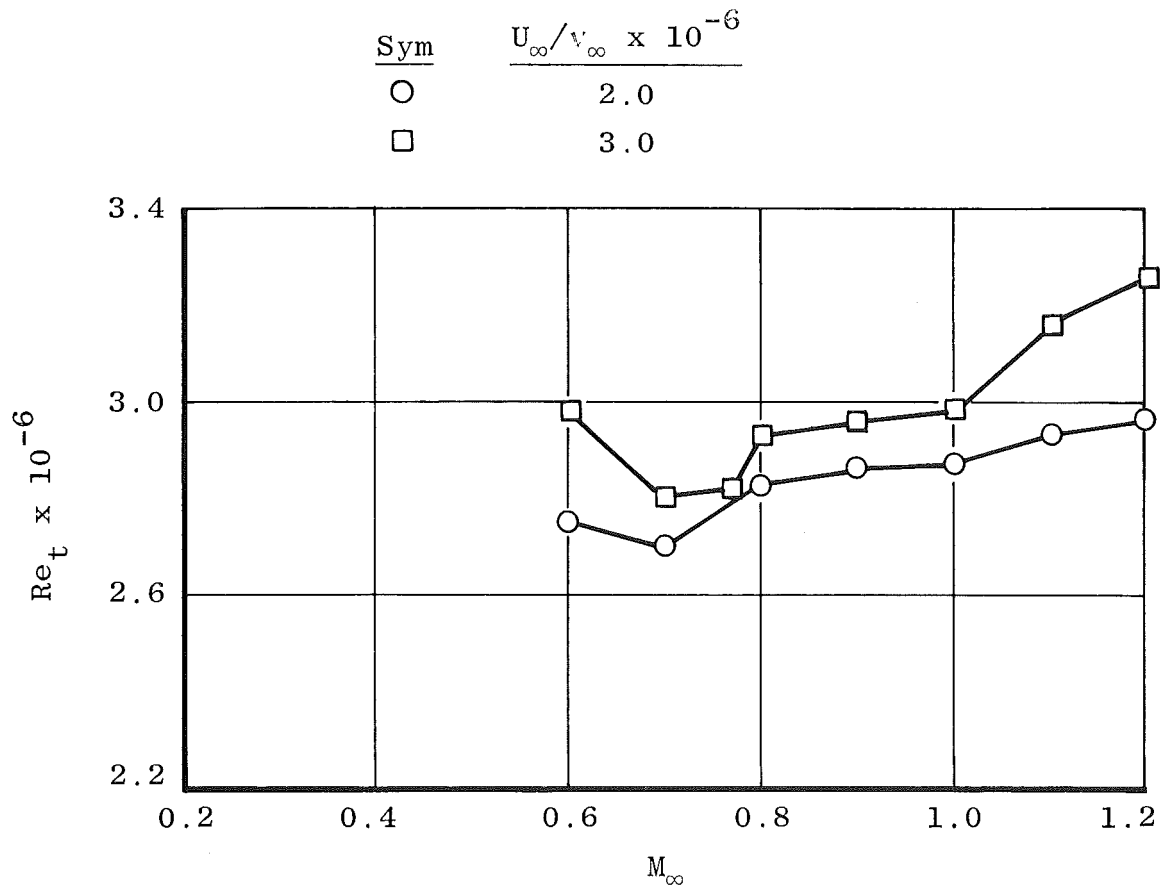


Figure 65. Onset-of-transition Reynolds numbers in the NASA/Ames 11 TWT at Sta. 122 in.

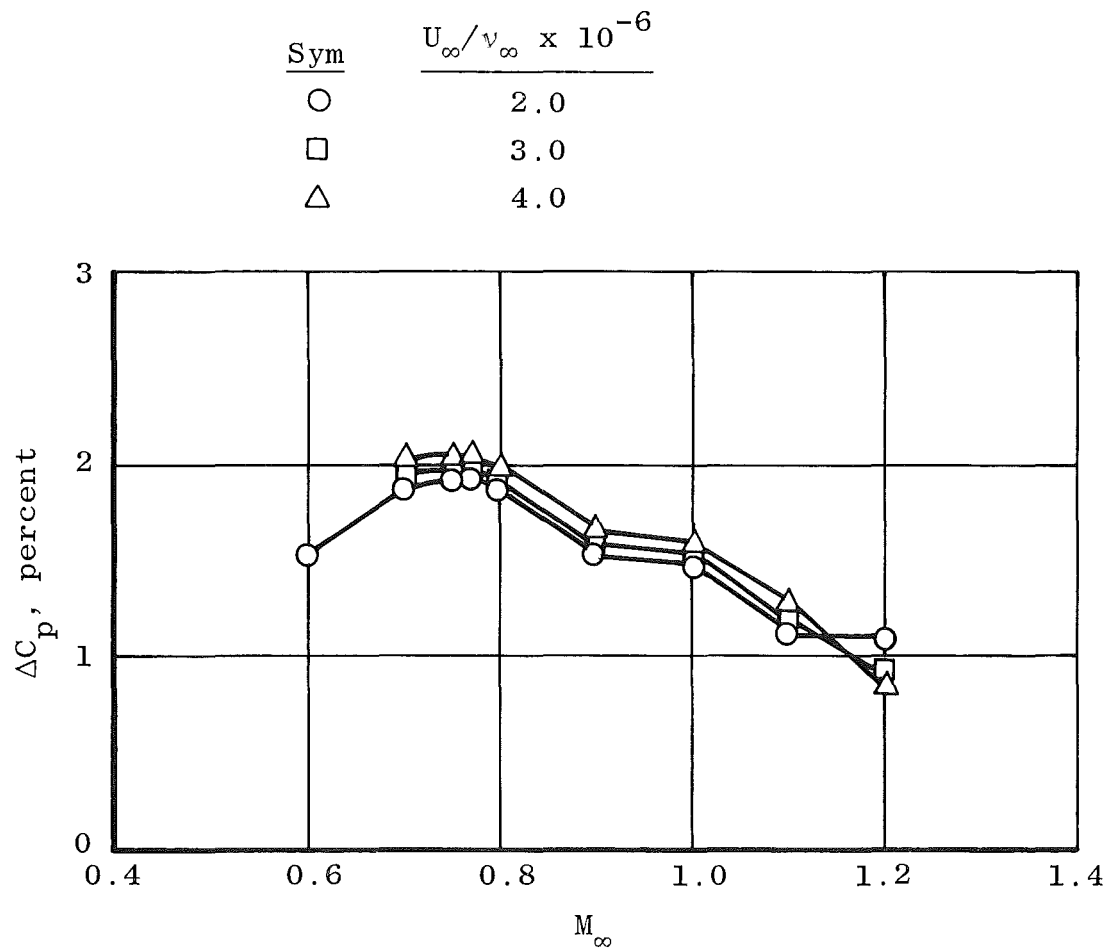


Figure 66. Noise levels in the NASA/Ames 11 TWT at Sta. 122 in.

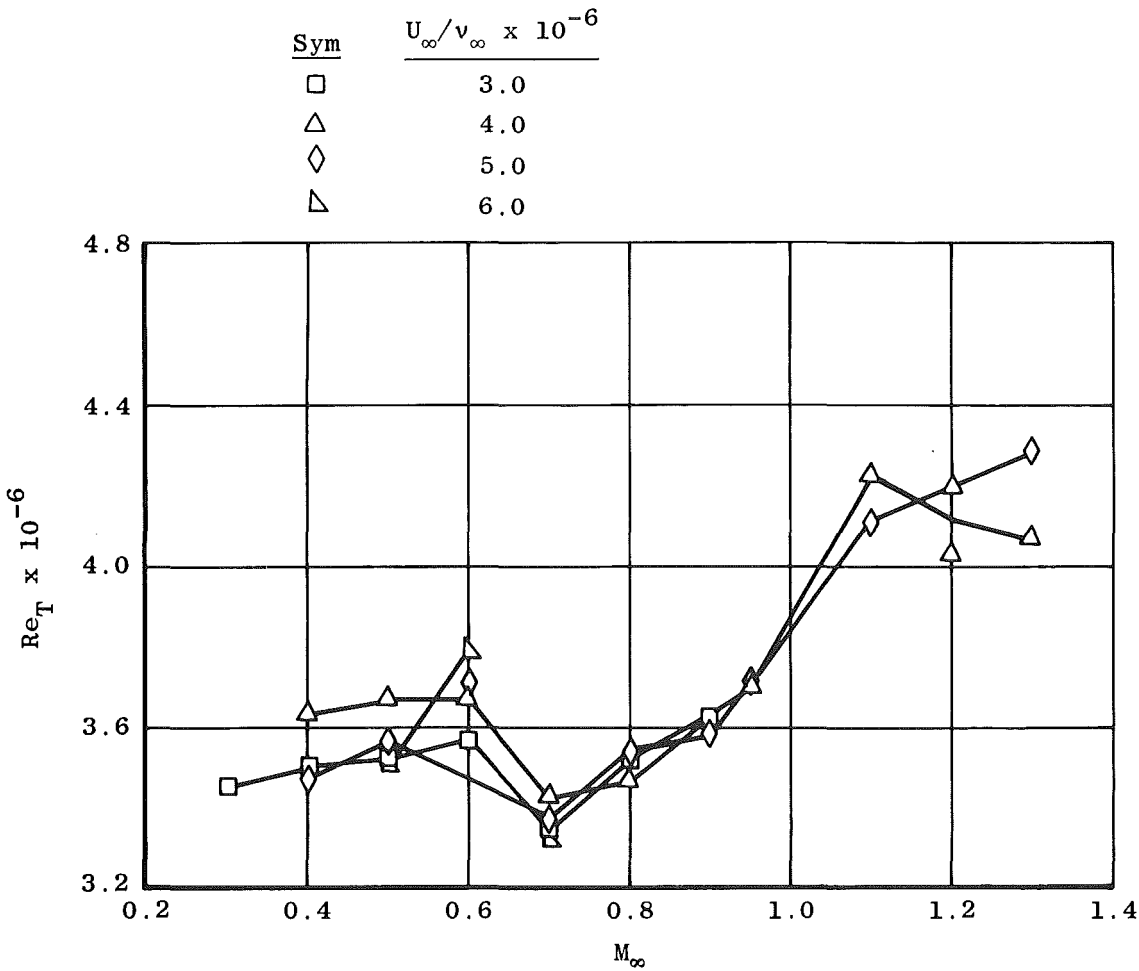


Figure 67. End-of-transition Reynolds numbers in the NASA/Ames 11 TWT at Sta. 133 in.

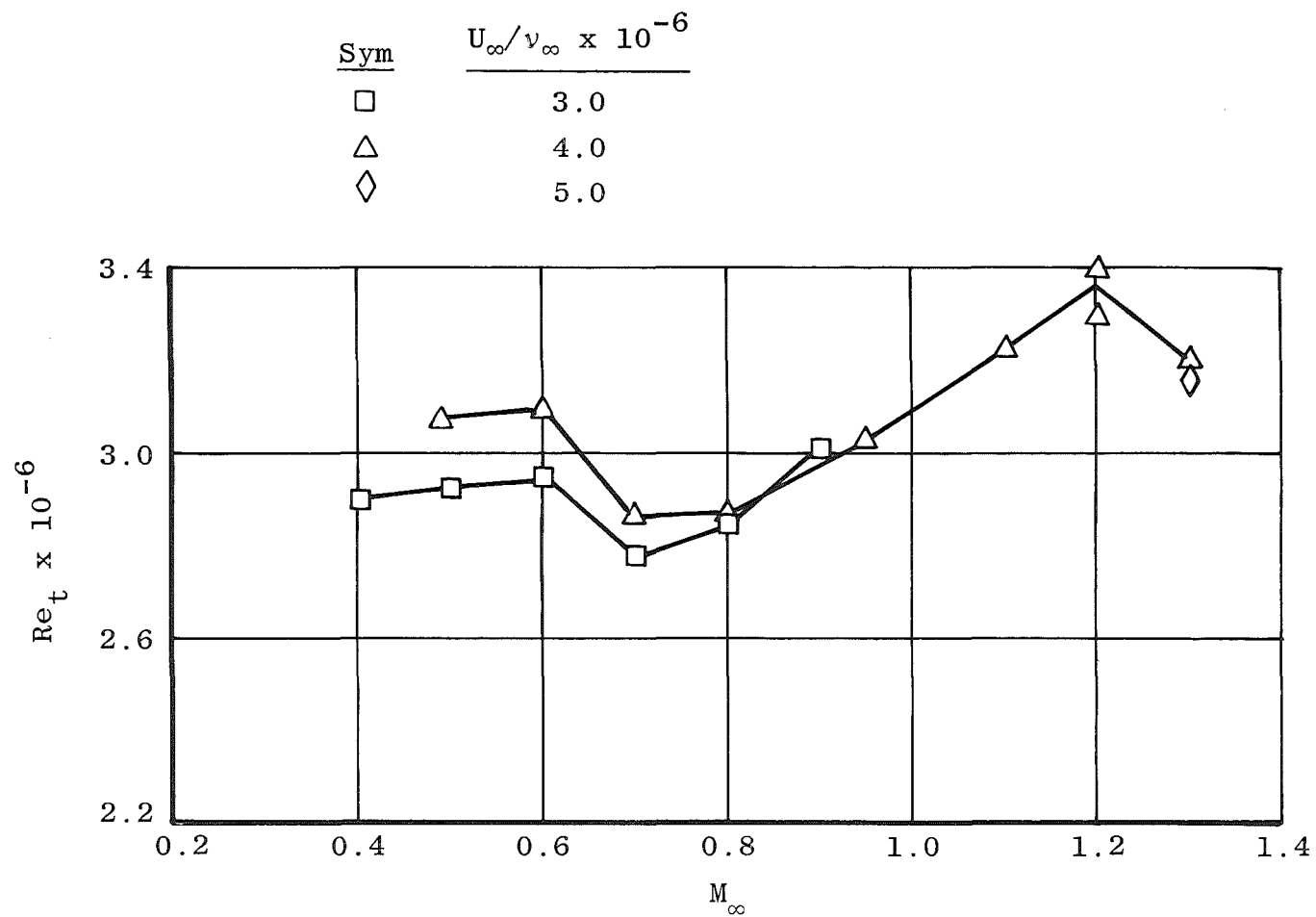


Figure 68. Onset-of-transition Reynolds numbers in the NASA/Ames 11 TWT at Sta. 133 in.

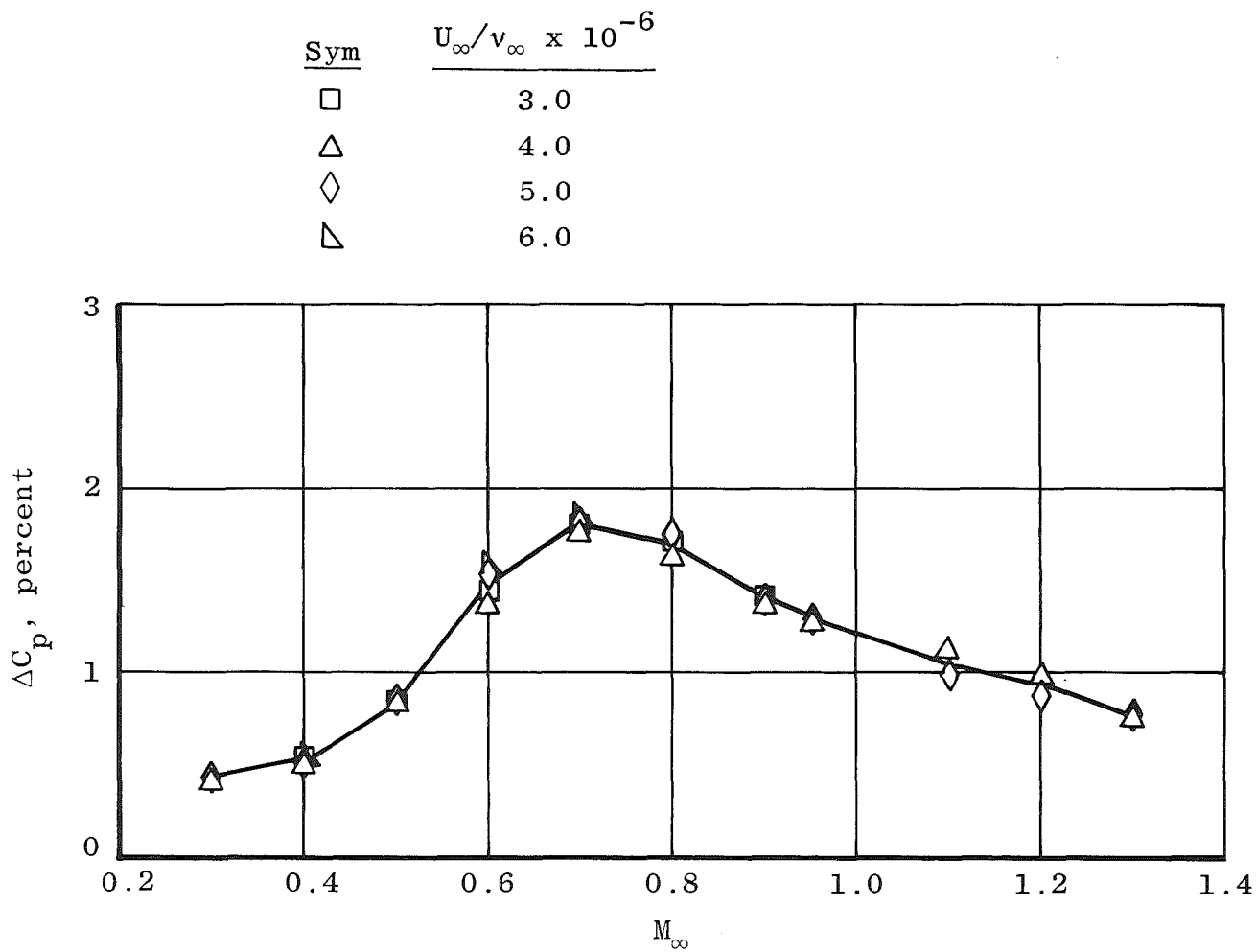


Figure 69. Noise levels in the NASA/Ames 11 TWT at Sta. 133 in.

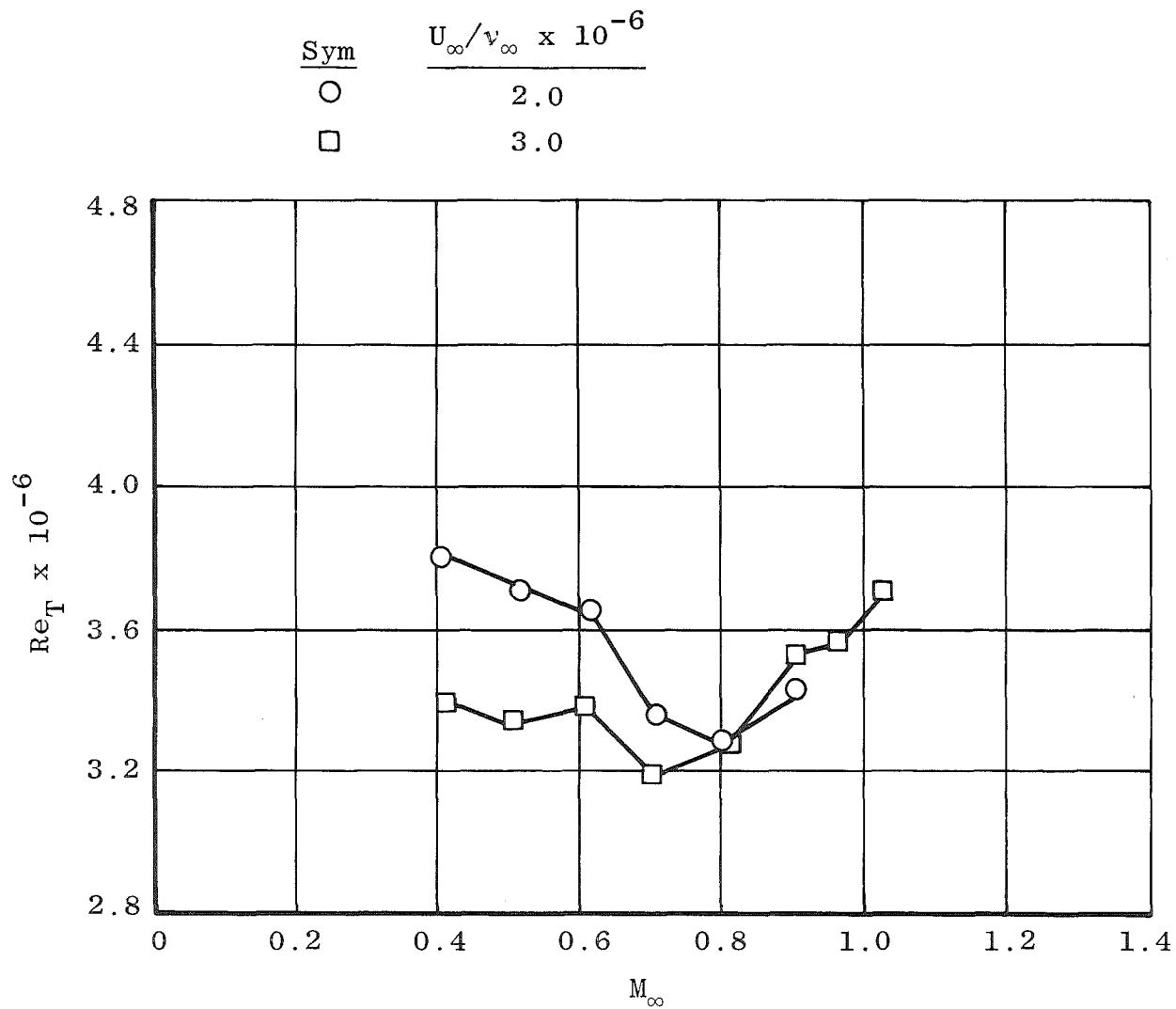


Figure 70. End-of-transition Reynolds numbers in the NASA/Ames 11 TWT at Sta. 150 in.

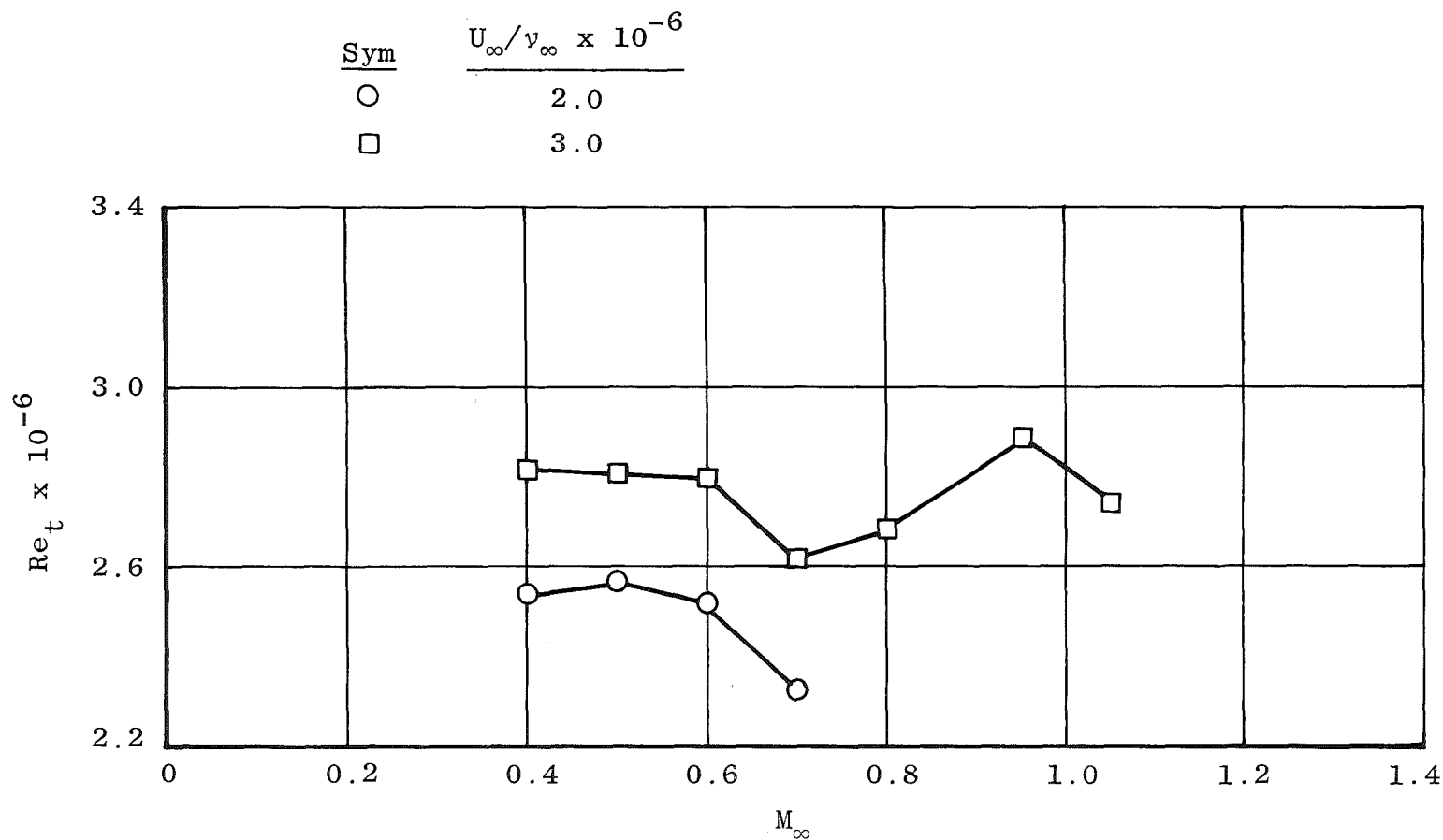


Figure 71. Onset-of-transition Reynolds numbers in the NASA/Ames 11 TWT at Sta. 150 in.

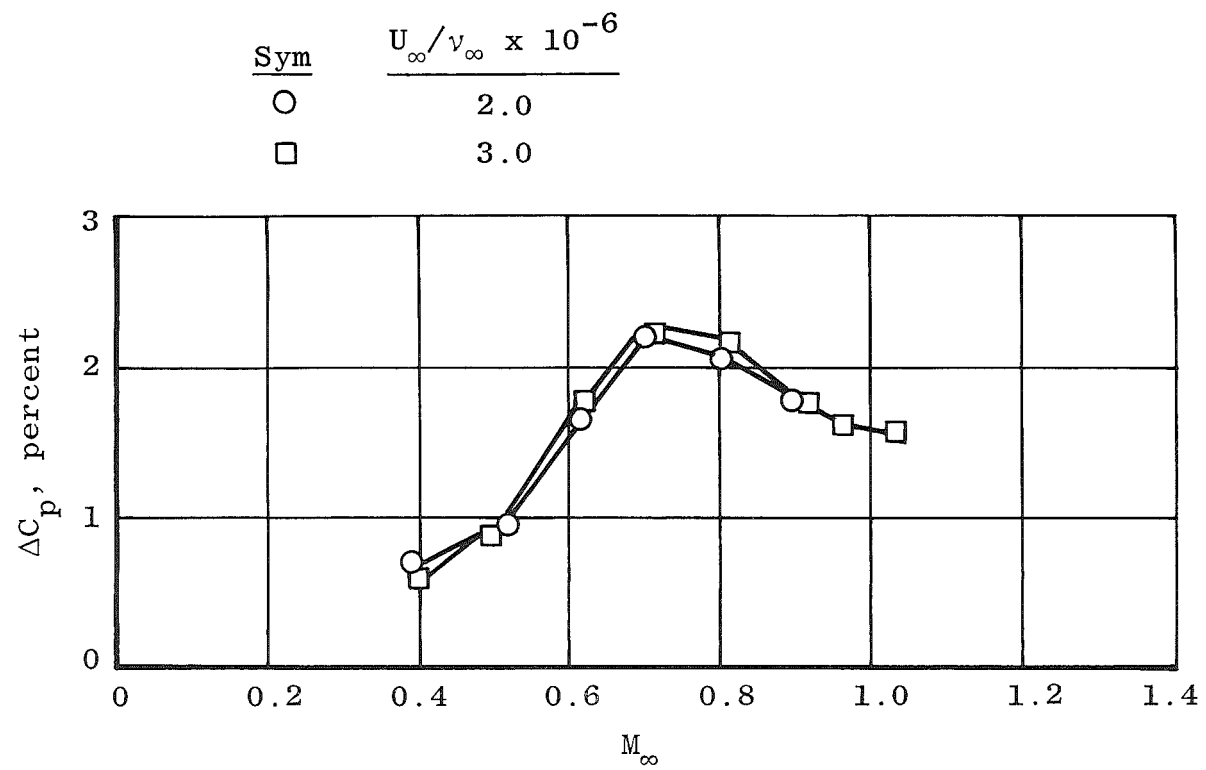


Figure 72. Noise levels in the NASA/Ames 11 TWT at Sta. 150 in.

Table 9. NASA/Ames 11 TWT Data

Station 110 in.

M_∞	U_∞/v_∞ $\times 10^{-6}$	ΔC_p , percent	$Re_t \times$ 10^{-6}	$Re_T \times$ 10^{-6}
0.40 ↓	2.99	0.768	3.05	3.68
	2.71	0.693	2.89	3.64
	2.50	0.656	2.89	3.73
	2.01	0.652	2.85	3.79
	1.49	0.717	2.78	3.50
0.50 ↓	1.60	1.295	2.76	3.59
	1.99	0.983	2.85	3.71
	2.47	0.971	2.93	3.75
	2.99	1.020	3.04	3.76
0.60 ↓	2.99	1.747	2.98	3.68
	2.75	1.801	2.97	3.67
	2.50	1.747	2.94	3.67
	2.01	1.611	2.80	3.66
	1.83	1.619	2.83	3.61
0.70 ↓	2.02	2.274	2.73	3.55
	2.49	2.300	2.76	3.59
	2.74	2.090	2.81	3.53
	3.00	1.940	2.89	3.55
0.80 ↓	3.24	1.550	—	3.59
	3.48	1.690	3.01	—
	2.99	1.830	2.92	3.62
	2.75	1.910	2.80	3.63
	2.50	2.067	2.83	3.61
	2.14	2.112	2.71	3.56
0.90 ↓	2.27	1.720	2.88	3.76
	2.48	1.678	2.89	3.84
	2.74	1.692	3.05	3.81
	2.99	1.818	3.05	3.79
0.95 ↓	2.29	1.636	2.95	3.80
	2.50	1.637	2.99	3.85
	2.74	1.624	3.04	3.86
	2.99	1.645	3.07	3.86
	3.24	1.703	3.11	3.86
	3.46	1.761	3.37	3.81
1.00 ↓	2.20	1.669	2.77	3.72
	2.48	1.740	2.89	3.78
	2.75	1.685	3.06	3.85
	2.99	1.666	3.04	3.86
	3.24	1.751	3.18	3.89
	3.50	1.949	3.36	3.82

Table 9. Continued
Station 110 in., Continued

M_∞	U_∞/v_∞ $\times 10^{-6}$	ΔC_p , percent	$Re_t \times$ 10^{-6}	$Re_T \times$ 10^{-6}
1.05 ↓	2.30	1.599	3.00	3.87
	2.50	1.657	3.04	3.94
	2.75	1.633	3.16	3.99
	2.99	1.763	3.26	4.09
	3.25	1.682	3.24	4.09
	3.49	1.948	3.36	4.10
	3.74	1.928	3.57	3.93
1.10 ↓	2.31	1.550	2.88	3.66
	2.49	1.534	2.95	3.80
	2.74	1.465	3.14	3.79
	2.99	1.486	3.23	4.04
	3.26	1.490	3.27	4.13
	3.51	1.556	3.45	4.12
	3.76	1.745	3.75	4.32
1.20 ↓	2.31	1.295	2.95	3.85
	2.51	1.269	3.07	4.04
	2.75	1.275	3.19	4.13
	3.00	1.270	3.37	4.14
	3.25	1.200	3.43	4.20
	3.49	1.201	3.62	4.30
	3.76	1.226	3.87	4.39
1.30 ↓	2.29	1.353	2.94	3.72
	2.50	1.275	3.11	3.92
	2.74	1.232	3.15	4.02
	2.99	1.228	3.38	4.11
	3.24	1.222	3.42	4.13
	3.74	1.242	-	3.90

Station 110 in., Continued (Walls Taped)

0.40 ↓	1.99	0.667	2.91	3.92
	2.51	0.683	2.98	3.89
	2.75	0.544	3.00	3.80
0.50 ↓	3.00	0.707	3.17	3.83
	2.26	0.748	2.58	3.84
	2.01	0.841	2.90	3.86
	1.60	0.870	-	3.83
0.60 ↓	1.84	1.123	-	3.91
	2.00	1.255	2.93	3.92
	2.50	1.167	3.12	3.92
	2.75	1.121	3.21	4.01
	3.01	1.060	3.24	3.96

Table 9. Continued
Station 110 in., Continued (Walls Taped)

M_∞	U_∞ / v_∞ $\times 10^{-6}$	ΔC_p , percent	$Re_t \times$ 10^{-6}	$Re_T \times$ 10^{-6}
0.70 ↓	3.98	1.392	-	-
	3.51	1.436	-	-
	3.02	1.439	3.12	3.93
	2.76	1.542	3.13	4.00
	2.51	1.500	3.06	3.87
	2.01	1.836	2.97	3.82
0.80 ↓	2.16	1.299	3.20	4.12
	2.48	1.302	3.28	4.22
	2.73	1.243	-	4.21
	2.99	1.250	3.34	4.16
0.90 ↓	2.23	0.985	3.42	4.26
	2.48	0.848	3.49	4.58
	2.48	0.813	3.46	4.57
	2.72	0.767	3.59	4.61
	2.98	0.808	3.58	4.53
	3.47	0.900	3.69	4.53
	3.72	0.795	3.04	-

Station 110 in., Concluded (Floor and Ceiling Only Taped)

0.90 ↓	2.24	1.350	-	3.96
	2.49	1.298	-	4.09
	2.73	1.298	-	4.12
	3.00	1.295	-	4.08
	3.49	1.444	-	4.07

Station 122 in.

0.60 ↓	1.780	1.548	2.789	3.619
	2.350	1.612	2.703	3.760
	3.223	1.690	3.223	4.230
	3.565	1.746	3.004	3.862
	4.128	1.789	-	3.784
	4.946	1.746	-	3.916

Table 9. Continued
Station 122 in., Continued

M_∞	U_∞ / v_∞ $\times 10^{-6}$	ΔC_p , percent	$Re_t \times$ 10^{-6}	$Re_T \times$ 10^{-6}
0.70 ↓	4.378	1.980	—	3.320
	3.643	1.937	—	3.370
	3.154	1.951	2.812	3.522
	2.495	1.909	2.641	3.493
	1.969	1.859	2.773	3.511
0.75 ↓	2.078	1.909	—	3.671
	2.705	1.965	—	3.674
	3.271	1.987	—	3.516
	3.920	1.881	—	3.463
	4.505	2.008	—	3.266
0.767 ↓	4.542	1.987	—	3.217
	3.928	1.923	2.880	3.404
	3.287	1.980	2.807	3.533
	2.666	1.902	—	3.488
	2.026	1.888	—	3.478
0.80 ↓	2.058	1.831	2.830	3.670
	2.724	1.817	2.837	3.655
	3.369	1.852	2.948	3.622
	4.021	1.859	—	3.585
	4.296	1.845	—	3.291
0.90 ↓	4.196	1.626	—	3.567
	3.507	1.612	—	3.595
	2.928	1.548	2.976	3.676
	2.146	1.838	2.861	3.648
1.00 ↓	2.222	1.513	2.870	3.629
	2.928	1.513	2.928	3.831
	3.614	1.555	3.040	3.795
	4.331	1.555	—	3.537
1.10 ↓	4.408	1.287	—	3.894
	3.689	1.251	3.197	4.027
	2.952	1.195	3.198	3.985
	2.247	1.159	2.884	3.970
1.20 ↓	2.261	—	2.902	3.862
	2.973	1.004	3.295	4.274
	3.498	0.940	3.207	3.935

Table 9. Continued
Station 133 in.

M_∞	U_∞/v_∞ $\times 10^{-6}$	ΔC_p , percent	$Re_t \times$ 10^{-6}	$Re_T \times$ 10^{-6}
0.29	3.735	0.39	—	3.486
0.40	4.928	0.50	—	3.491
↓	3.992	0.48	—	3.593
↓	3.964	0.48	—	3.733
↓	3.006	0.52	2.906	3.507
0.50	5.858	0.89	—	3.515
↓	3.985	0.89	3.088	3.653
↓	3.982	0.89	—	3.650
↓	3.953	0.88	—	3.722
↓	3.954	0.89	—	3.756
↓	2.989	0.90	2.914	3.512
0.60	5.947	1.52	—	3.816
↓	4.942	1.50	—	3.748
↓	3.978	1.30	3.116	3.713
↓	3.968	1.30	3.075	3.637
↓	2.996	1.37	2.946	3.570
0.70	5.917	1.88	—	3.304
↓	4.985	1.88	2.866	3.365
↓	3.987	1.82	2.857	3.422
↓	3.971	1.82	2.945	3.541
↓	3.004	1.86	2.779	3.354
0.80	5.939	—	—	3.415
↓	4.978	1.79	2.945	3.526
↓	4.011	1.70	2.875	3.476
↓	3.969	1.70	3.043	3.638
↓	3.006	1.77	2.856	3.507
0.90	5.026	1.27	3.057	3.602
↓	4.005	1.29	3.037	3.771
↓	3.983	1.29	2.954	3.651
↓	2.998	1.26	3.023	3.623
0.95	4.997	1.24	3.081	3.456
↓	3.995	1.20	3.063	3.795
↓	3.986	1.20	3.056	3.687
↓	2.497	—	2.809	3.600
1.10	5.013	1.00	3.467	4.136
↓	3.983	1.09	3.220	4.215
↓	3.973	1.10	3.476	4.238
↓	2.512	—	3.245	3.956

Table 9. Continued
Station 133 in., Concluded

M_∞	U_∞/v_∞ $\times 10^{-6}$	ΔC_p , percent	$Re_t \times$ 10^{-6}	$Re_T \times$ 10^{-6}
1.20	4.012	0.97	3.310	4.045
↓	3.982	0.97	3.385	4.181
	2.512	-	3.014	3.705
1.25	4.009	-	2.973	3.942
1.30	4.979	0.80	3.153	4.274
↓	4.006	0.78	3.238	4.006
	3.993	0.78	3.294	4.060
	2.497	-	2.976	3.808

Station 150 in.

0.40	1.492	0.504	-	3.72
↓	1.982	0.662	2.54	3.81
	2.476	0.581	2.69	3.38
	2.730	0.542	2.74	3.36
	2.978	0.578	2.82	3.34
	3.217	0.587	2.79	3.38
0.50	1.610	0.784	2.51	3.64
↓	1.985	0.954	2.56	3.76
	2.233	0.903	2.60	3.48
	2.506	0.933	2.66	3.44
	2.739	0.880	2.73	3.42
	2.964	0.906	2.80	3.34
	3.226	0.936	2.81	3.32
	3.480	0.974	-	3.42
0.60	1.85	1.549	2.50	3.61
↓	1.98	1.611	2.52	3.65
	2.51	1.585	2.64	3.44
	2.74	1.710	2.71	3.40
	2.98	1.729	-	3.38
	3.49	1.780	2.97	3.52
	3.98	-	-	3.58
0.70	2.01	2.171	2.32	3.35
↓	2.49	2.259	2.51	3.20
	2.98	2.243	2.61	3.18
	3.47	2.315	2.80	3.27
	3.99	2.368	2.91	3.29
0.80	2.13	2.024	-	3.28
↓	2.48	2.141	2.69	3.20
	2.98	2.188	2.89	3.28
	3.49	2.218	2.89	3.08
	4.00	1.182	2.93	-

Table 9. Concluded
Station 150 in. Concluded

M_∞	U_∞/v_∞ $\times 10^{-6}$	ΔC_p , percent	$Re_t \times$ 10^{-6}	$Re_T \times$ 10^{-6}
0.90 ↓	2.23	1.723	—	3.42
	2.49	1.695	2.67	3.56
	2.98	1.707	—	3.53
	3.49	1.729	—	3.60
	4.01	1.744	—	3.60
0.95 ↓	2.26	1.573	—	3.43
	2.50	1.614	2.50	3.54
	2.99	1.631	2.89	3.59
	3.51	1.651	2.82	3.63
	4.00	1.642	3.12	3.60
1.05 ↓	2.31	1.645	—	3.52
	2.75	1.680	2.72	3.69
	3.00	1.639	2.74	3.73
	3.49	1.653	3.54	3.78
	3.99	1.651	3.61	3.86

NASA/Ames 14 TWT

Data were acquired in the NASA/Ames 14 TWT at a nominal total pressure, p_t , of 2,130 psfa and total temperature, T_t , varying from 527 to 644°R as M_∞ was increased from 0.4 to 1.05. Consequently, U_∞/ν_∞ varied from approximately 2.6×10^6 to approximately 4.0×10^6 as M_∞ increased in this atmospheric tunnel. The same type of walls-taped experiment performed in the NASA/Ames 11 TWT was performed in this tunnel to search for further confirmation that the slot-generated noise influences cone transition.

End-of-transition Reynolds number, Re_T , is shown in Fig. 73 for 1) normal operation, 2) walls taped, and 3) only the floor and ceiling taped (i.e., half open). Onset-of-transition Reynolds numbers, Re_t , are presented for these same conditions in Fig. 74. The noise levels from the cone microphones, ΔC_p , are shown in Fig. 75. The supporting evidence is clear that the noise generated in baffled, slotted-wall transonic tunnels has a promoting influence on transition since the test section design of this tunnel is essentially identical to that of the NASA/Ames 11 TWT, only scaled up to a 14- x 14-ft-square test section. The noise spectra were similar except that the deeper slot baffle gave a fundamental tone of 1,900-Hz frequency instead of 2,600 Hz. The measured data are presented in Table 10.

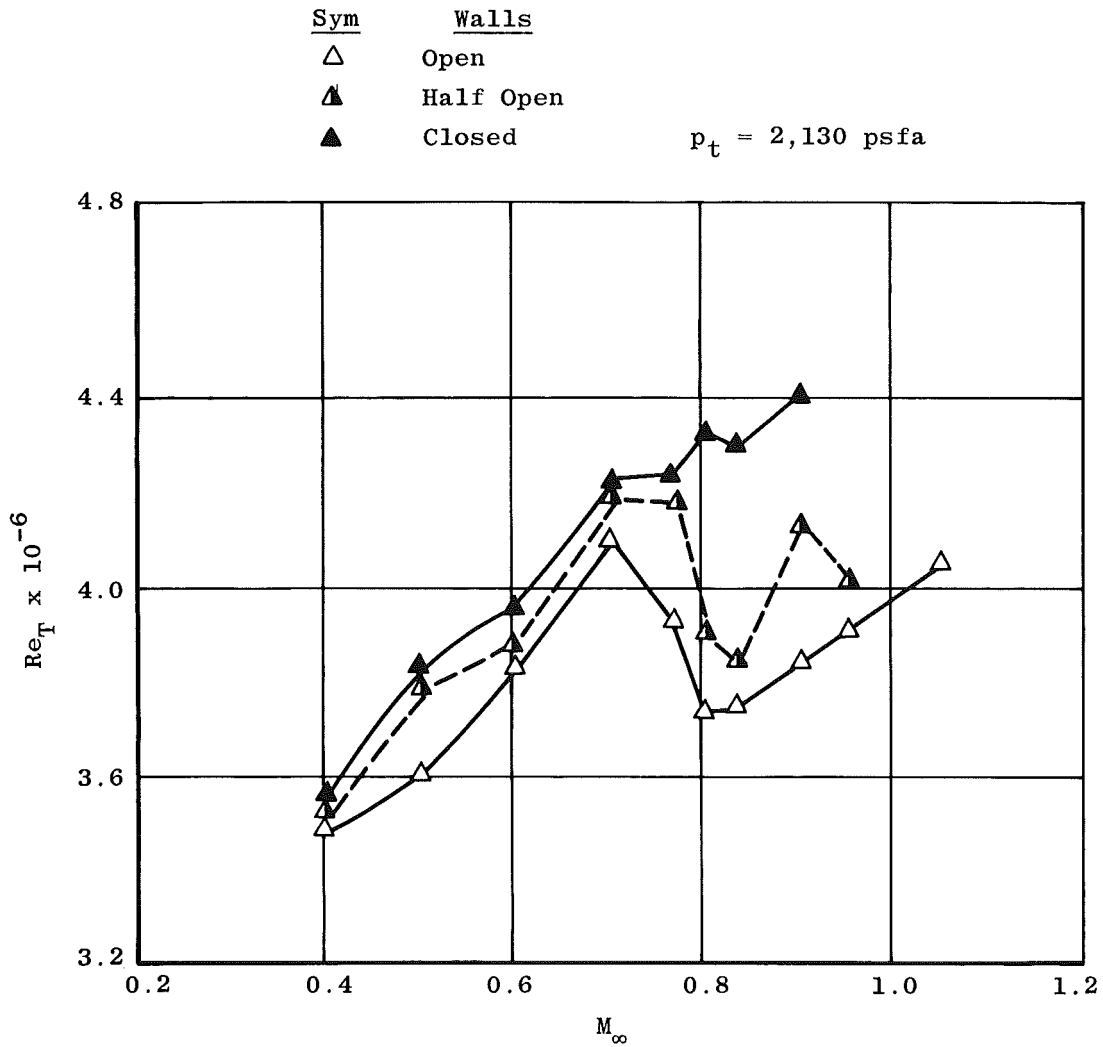


Figure 73. End-of-transition Reynolds numbers in the NASA/Ames 14 TWT.

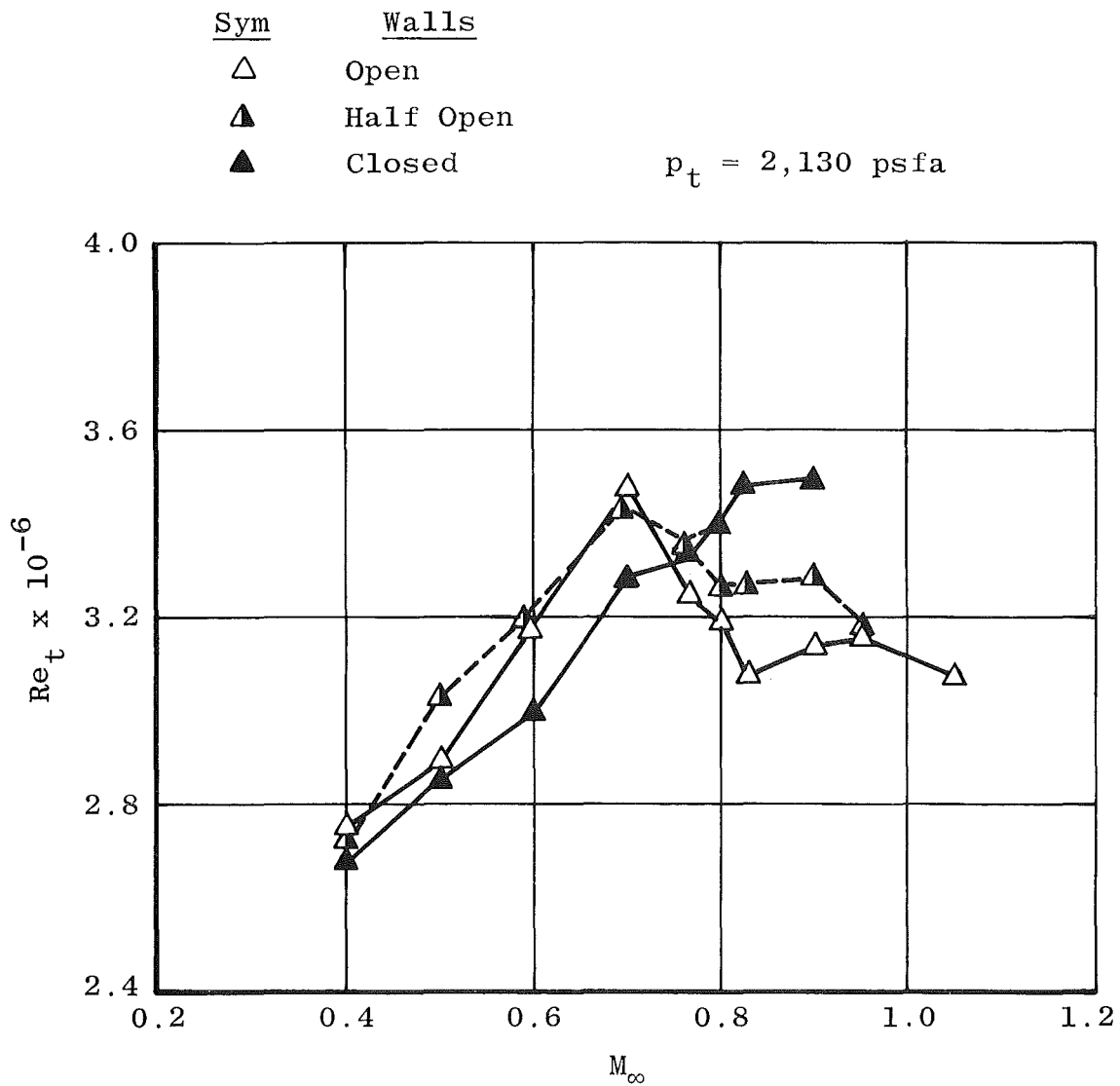


Figure 74. Onset-of-transition Reynolds numbers in the NASA/Ames 14 TWT.

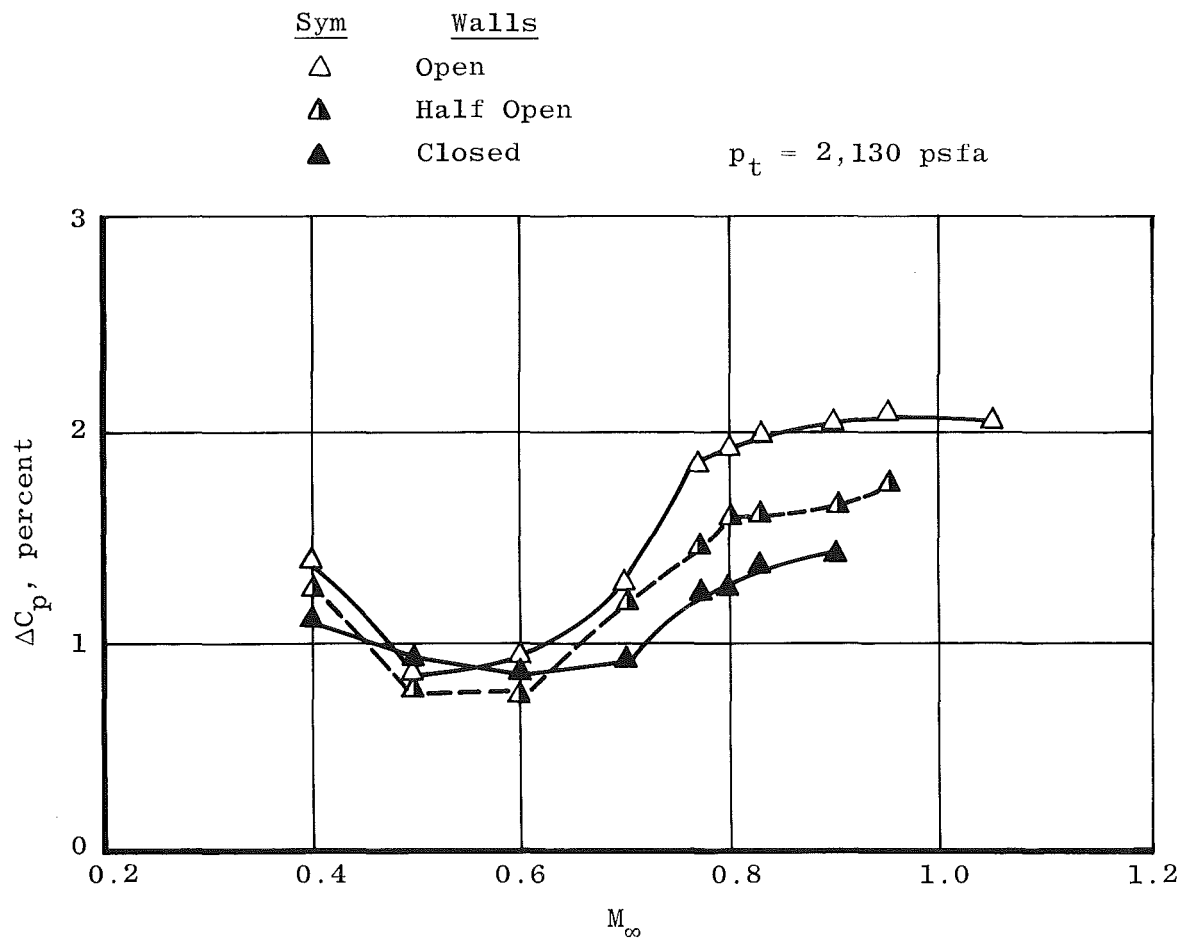


Figure 75. Noise levels in the NASA/Ames 14 TWT.

Table 10. NASA/Ames 14 TWT Data

M_∞	U_∞/v_∞ $\times 10^{-6}$	ΔC_p , percent	$Re_t \times$ 10^{-6}	$Re_T \times$ 10^{-6}
Open Walls				
0.403	2.518	1.370	2.749	3.505
0.502	2.987	0.885	2.875	3.604
0.593	3.339	0.940	3.160	3.840
0.700	3.597	1.253	3.457	4.127
0.768	3.731	1.887	3.262	3.930
0.800	3.793	1.910	3.190	3.741
0.829	3.844	1.975	3.071	3.748
0.902	3.879	2.030	3.136	3.847
0.950	3.860	2.072	3.168	3.914
1.049	3.793	2.043	3.064	4.042
Half-Open (Floor and Ceiling Taped)				
0.402	2.495	1.230	2.724	3.553
0.500	2.997	0.790	3.034	3.786
0.590	3.321	0.761	3.193	3.890
0.697	3.609	1.150	3.429	4.191
0.762	3.726	1.411	3.322	4.178
0.799	3.798	1.572	3.260	3.893
0.827	3.844	1.575	3.267	3.844
0.889	3.825	1.610	3.283	4.112
0.952	3.860	1.730	3.178	4.033
Four Walls Fully Taped				
0.397	2.597	1.090	2.684	3.559
0.499	3.052	0.930	2.841	3.838
0.599	3.443	0.876	2.984	3.934
0.700	3.742	0.901	3.290	4.220
0.767	3.838	1.223	3.326	4.238
0.797	3.920	1.260	3.381	4.345
0.804	3.871	1.280	3.380	4.310
0.822	3.980	1.305	3.483	4.312
0.829	3.934	1.311	2.721	4.298
0.899	3.950	1.399	3.486	4.379

Calspan 8 TWT

The Calspan 8 TWT has all four walls in the test section perforated with normal holes at 22.5-percent porous open area. These walls apparently also emit strong discrete acoustic disturbances similar to the edgetones found in the perforated-wall test sections with 60-deg inclined holes.

End-of-transition Reynolds number, Re_T , is presented in Fig. 76 for M_∞ varied from 0.6 to 0.95. Onset-of-transition Reynolds numbers, Re_t , are presented in Fig. 77. The noise data, ΔC_p , measured by the cone microphones are shown in Fig. 78. Reference data from another experiment in this tunnel given in Ref. 12 tend to confirm these values of ΔC_p measured on the cone. The tabulated data are in Table 11.

There is little apparent correlation in this tunnel between overall ΔC_p and Re_T and Re_t . This apparent paradox may be explained by closer examination of noise spectra shown in Fig. 79. As seen in Figs. 77a and b, there are discrete frequency components at nominally 700 and 1,300 Hz in the spectrum at the lower Mach numbers. These components may be associated with the tunnel drive compressors: 700 Hz with the variable speed main drive compressor, and 1,300 Hz with the fixed speed plenum exhaust auxiliary compressor. As M_∞ increased, these components diminished in amplitude to the broadband background level (see $M_\infty = 0.85$ and 0.95 , Figs. 79c and d). But there is a concentration of energy (near 6,400 Hz at $M_\infty = 0.6$ to 7,900 Hz at $M_\infty = 0.9$) which is believed to be wall-generated noise. The transition data seem to follow the amplitude variation of this component, which maximizes at $M_\infty = 0.85$.

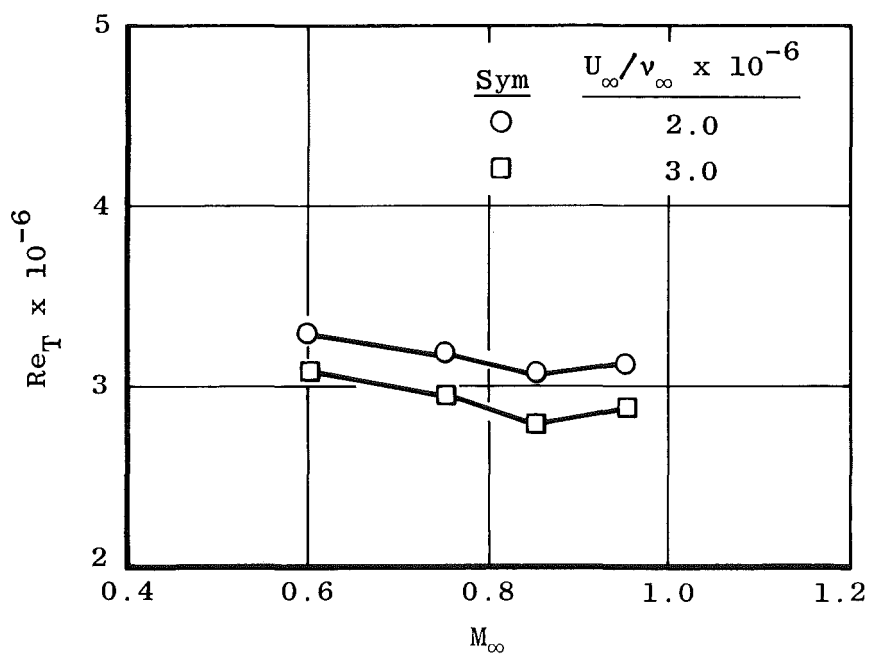


Figure 76. End-of-transition Reynolds numbers in the Calspan 8 TWT.

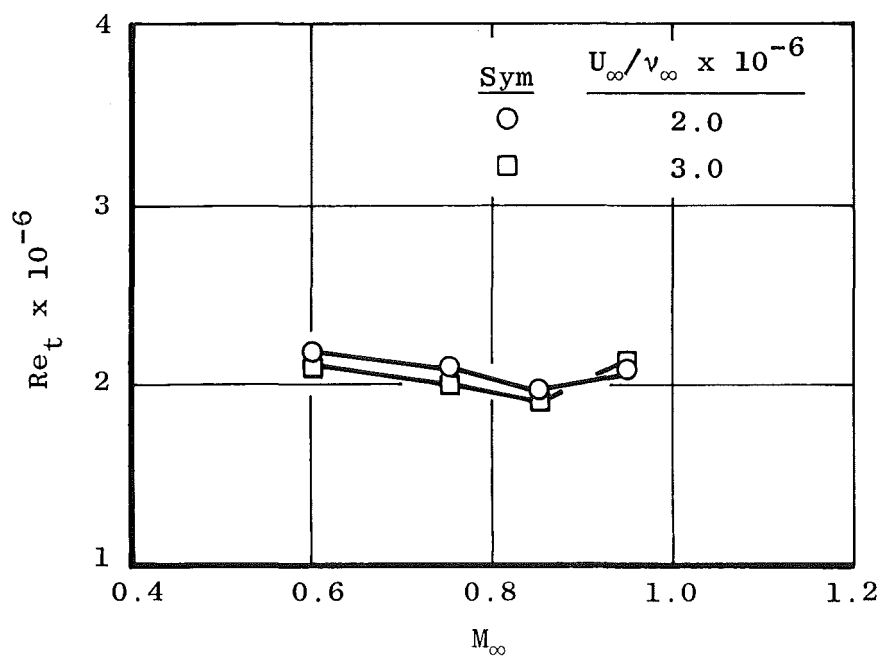


Figure 77. Onset-of-transition Reynolds numbers in the Calspan 8 TWT.

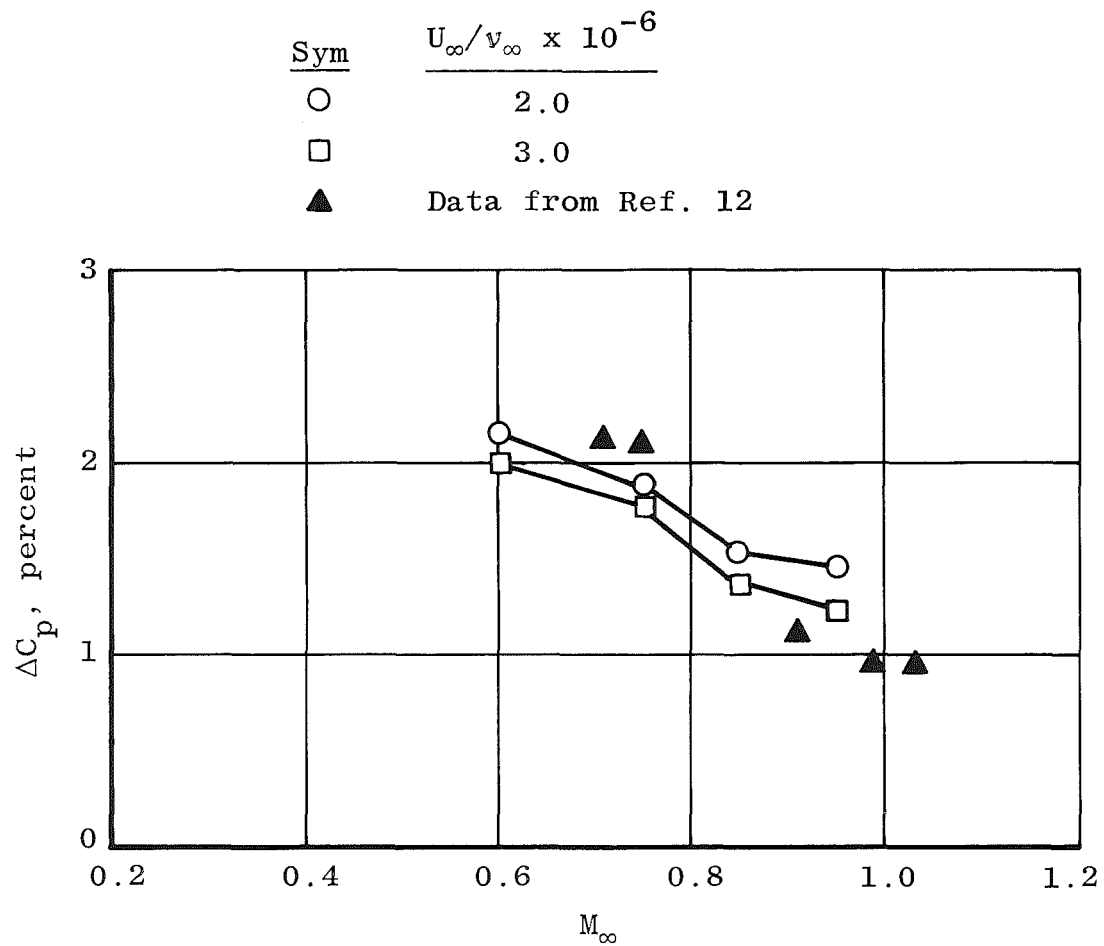
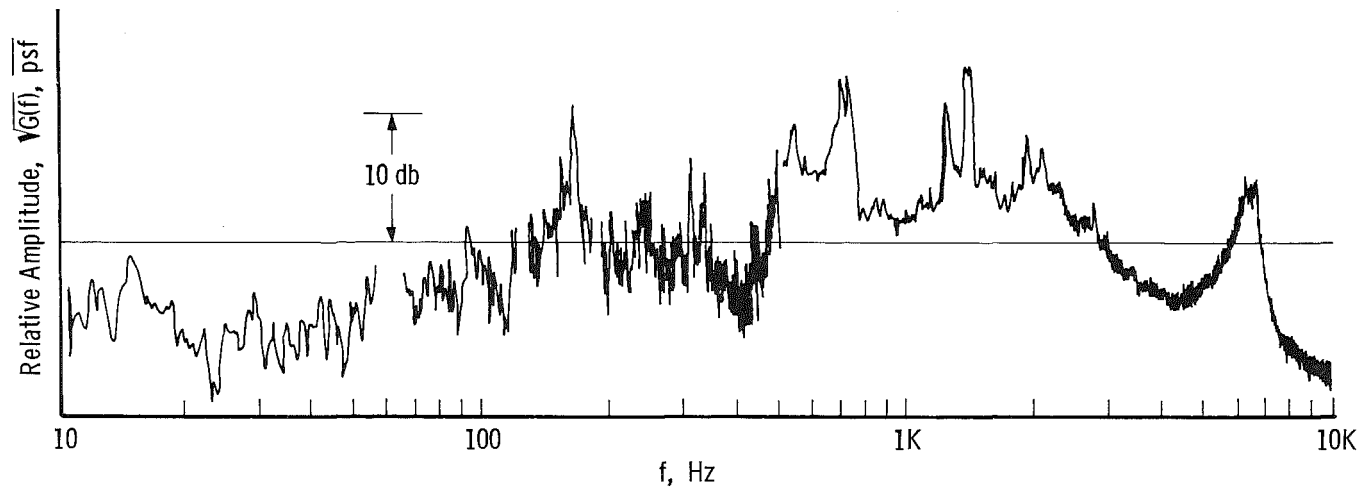
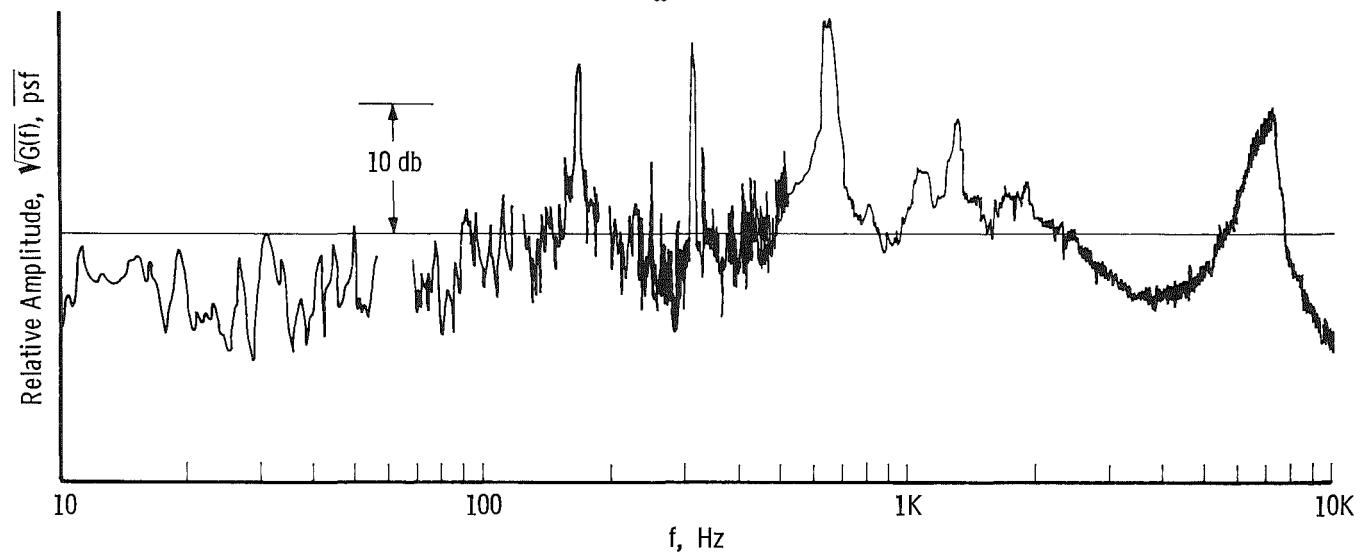


Figure 78. Noise levels in the Calspan 8 TWT.

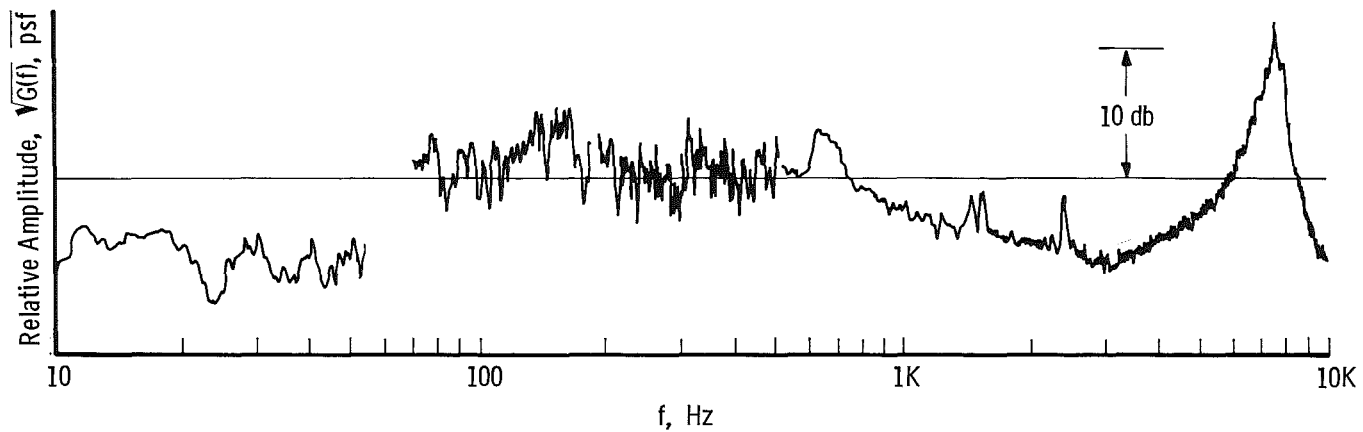


a. $M_\infty = 0.60$

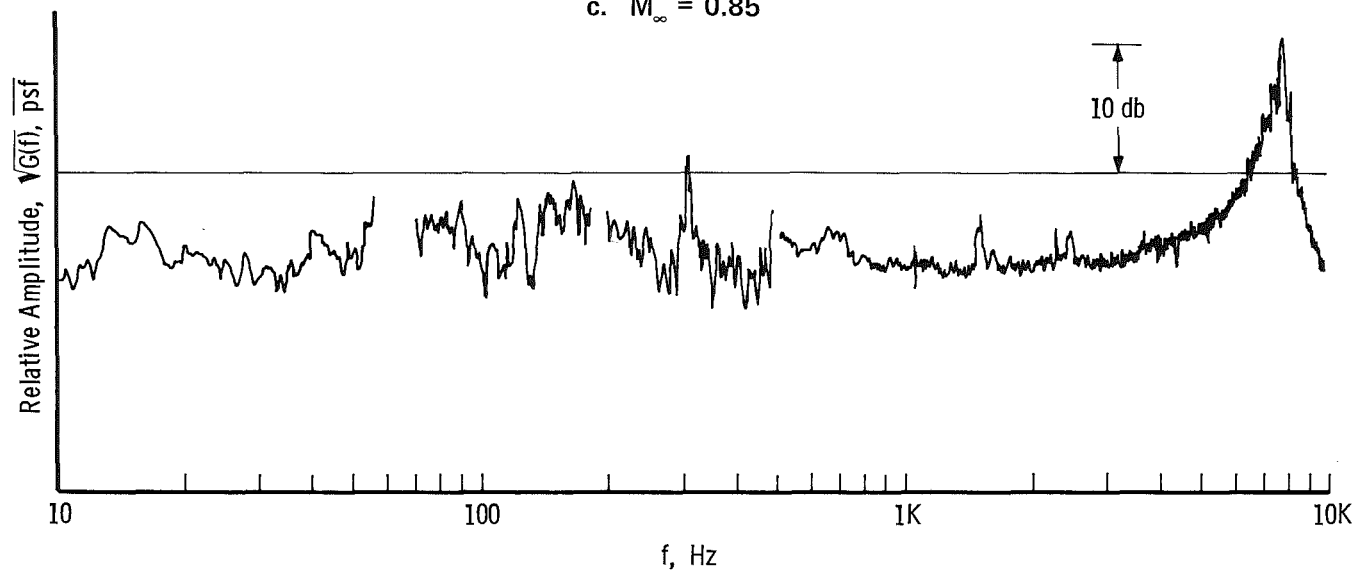


b. $M_\infty = 0.75$

Figure 79. Fourier spectrum measurements in the Calspan 8 TWT.



c. $M_\infty = 0.85$



d. $M_\infty = 0.95$

Figure 79. Concluded.

Table 11. Calspan 8 TWT Data

M_∞	$U_\infty/v_\infty \times 10^{-6}$	ΔC_p , percent	$Re_t \times 10^{-6}$	$Re_T \times 10^{-6}$
0.60 ↓	1.586	-	2.181	3.357
	1.906	2.29	1.969	3.240
	1.913	-	2.200	3.348
	2.222	2.05	2.111	3.222
	2.525	2.03	2.041	3.198
	2.538	2.03	2.136	3.003
	2.837	2.03	2.080	3.070
	2.858	1.99	2.286	3.215
	3.155	2.03	-	-
	3.171	1.97	2.418	3.224
0.75 ↓	1.466	-	2.101	3.237
	1.467	-	1.980	3.252
	2.184	2.04	2.000	3.220
	2.188	1.83	-	2.735
	2.915	1.76	-	2.988
	2.920	1.74	2.190	2.944
	3.648	1.83	-	2.812
0.85 ↓	1.952	1.98	1.985	3.070
	2.706	1.51	1.917	2.819
	3.492	1.35	-	2.765
	3.833	1.36	-	2.524
0.95 ↓	2.034	-	2.085	3.136
	2.426	1.34	2.000	3.033
	3.229	1.19	2.152	2.825

ARA, Ltd. Bedford 9 x 8

The ARA, Ltd. 9 x 8 transonic tunnel has 22.5-percent open, perforated walls with normal holes like the Calspan 8 TWT. The tunnel is an atmospheric tunnel, driven by a variable speed, two-stage fan which has 22 rotor blades and 20 prerotation stator blades on each stage. Noise data were acquired over a Mach number range from 0.2 to 1.4 (ΔC_p data) with p_t nominally 2,070 psfa and T_t varying from 478 to 521°R as M_∞ increased, yielding a range in U_∞/ν_∞ from approximately 1.5×10^6 to approximately 4.4×10^6 . Transition data were acquired at M_∞ ranging from 0.2 to 0.6 only. Results of the test are given by Jordan in Ref. 13.*

End, onset, and rms peak locations of transition are shown in Fig. 80. End (Re_T) and onset (Re_t) of transition Reynolds numbers are given in Fig. 81. The variation of ΔC_p with M_∞ measured by the cone microphones is shown in Fig. 82. There is a sharp peak in ΔC_p near $M_\infty = 0.68$.

Spectral decomposition of the microphone signals revealed the existence of low frequency components associated with the compressor. The fundamental tone identification is established in Fig. 83 as 20/rev; tones also exist at 40/rev, 60/rev, and 80/rev, but these components are not the predominant ones in the spectra. Associated with the sharp increase in ΔC_p near $M_\infty = 0.68$ is a harmonic family of discrete tones of which the fundamental occurs at 2,900 Hz at $M_\infty = 0.65$. The variation in amplitude of these tones with M_∞ is shown in Fourier spectral plots in Fig. 84. It is suspected that these tones, like the 7,600-Hz tone in the Calspan 8 TWT, are emitted by the test section walls (see also Ref. 14). However, the data acquired were not sufficient to verify what effect, if any, these disturbances have on transition.

*The data were obtained by R. Jordan and N. S. Dougherty, Jr.

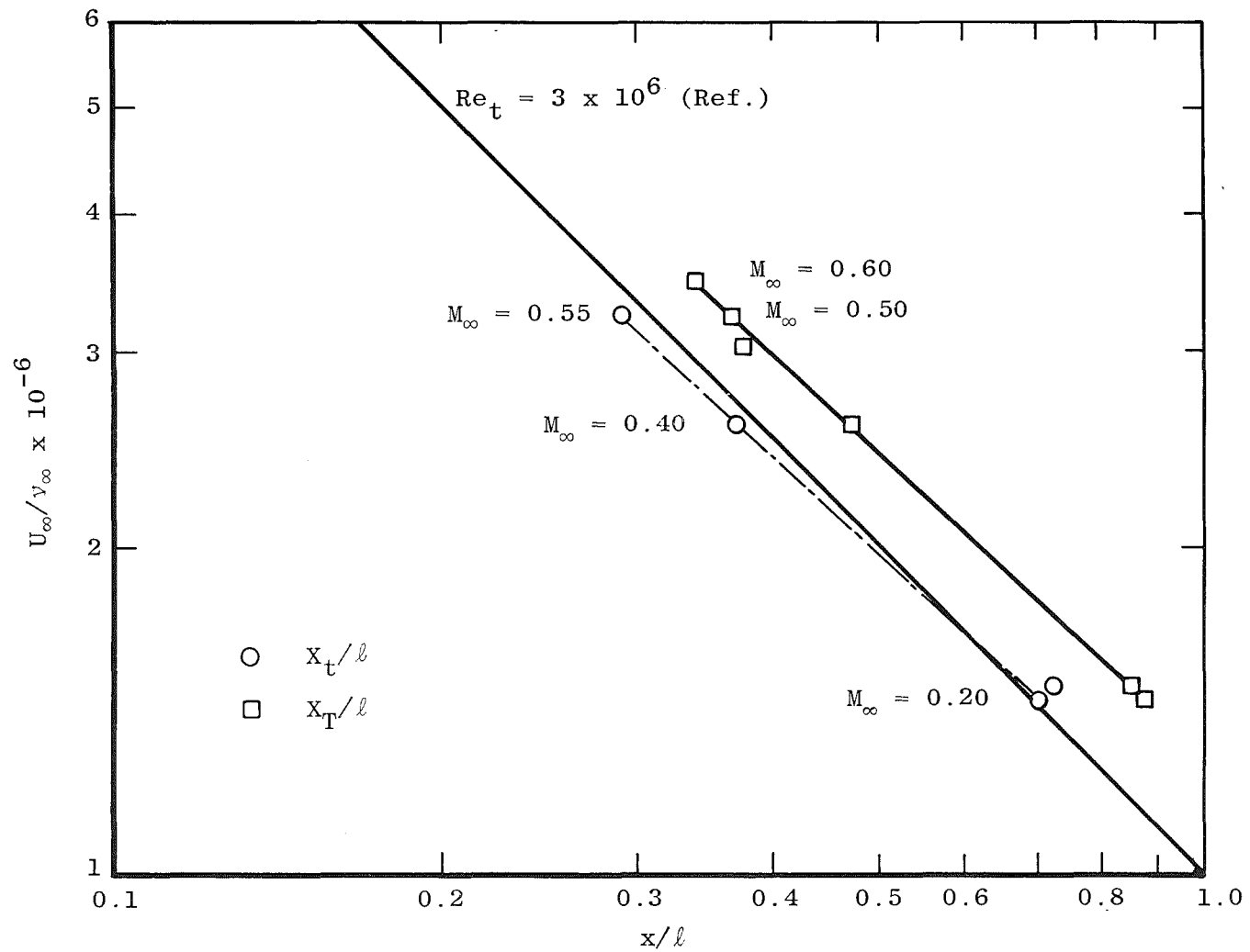


Figure 80. Transition locations on the cone in the ARA, Ltd. Bedford 9 x 8.

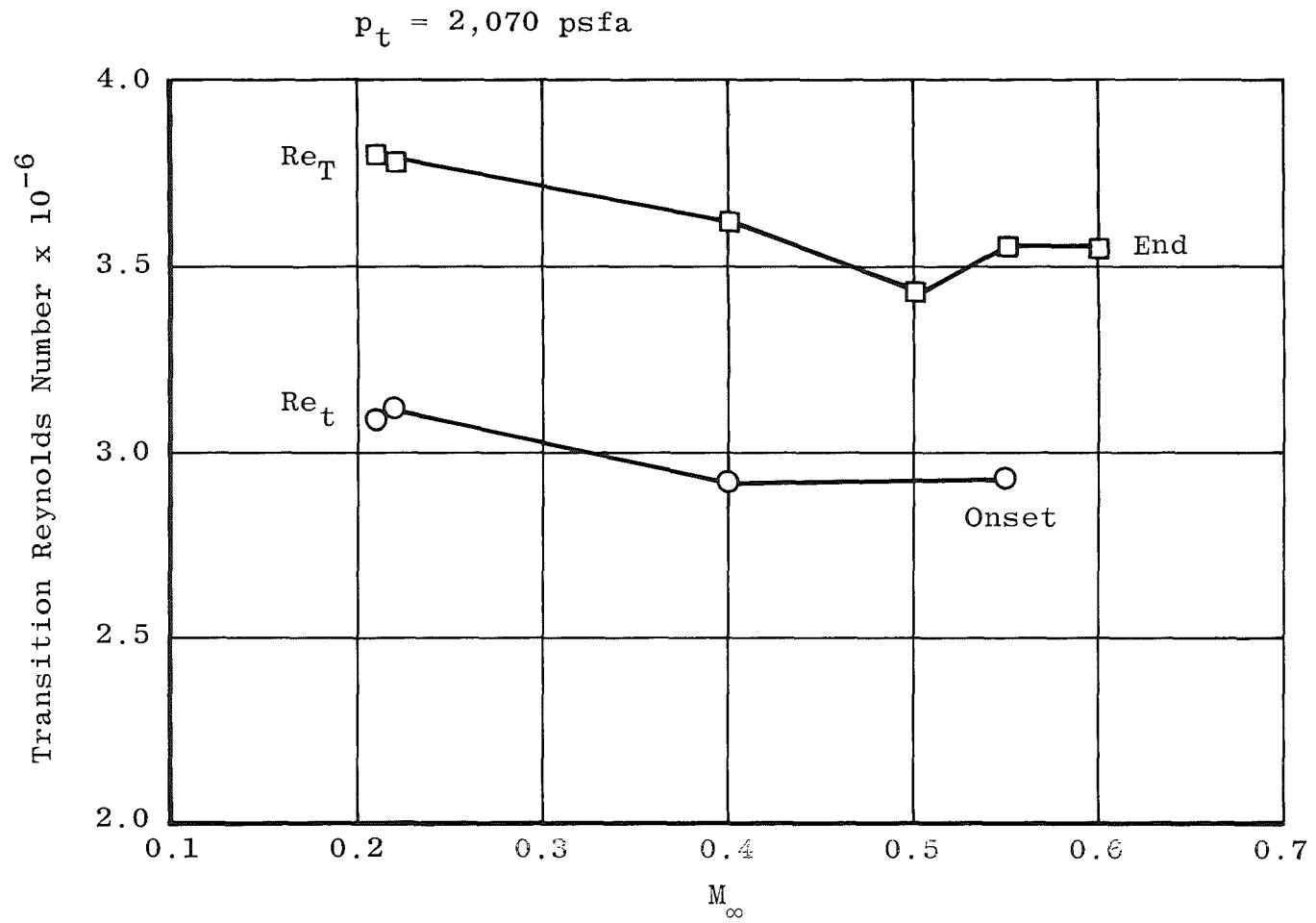


Figure 81. Transition Reynolds numbers in the ARA, Ltd.
Bedford 9 x 8.

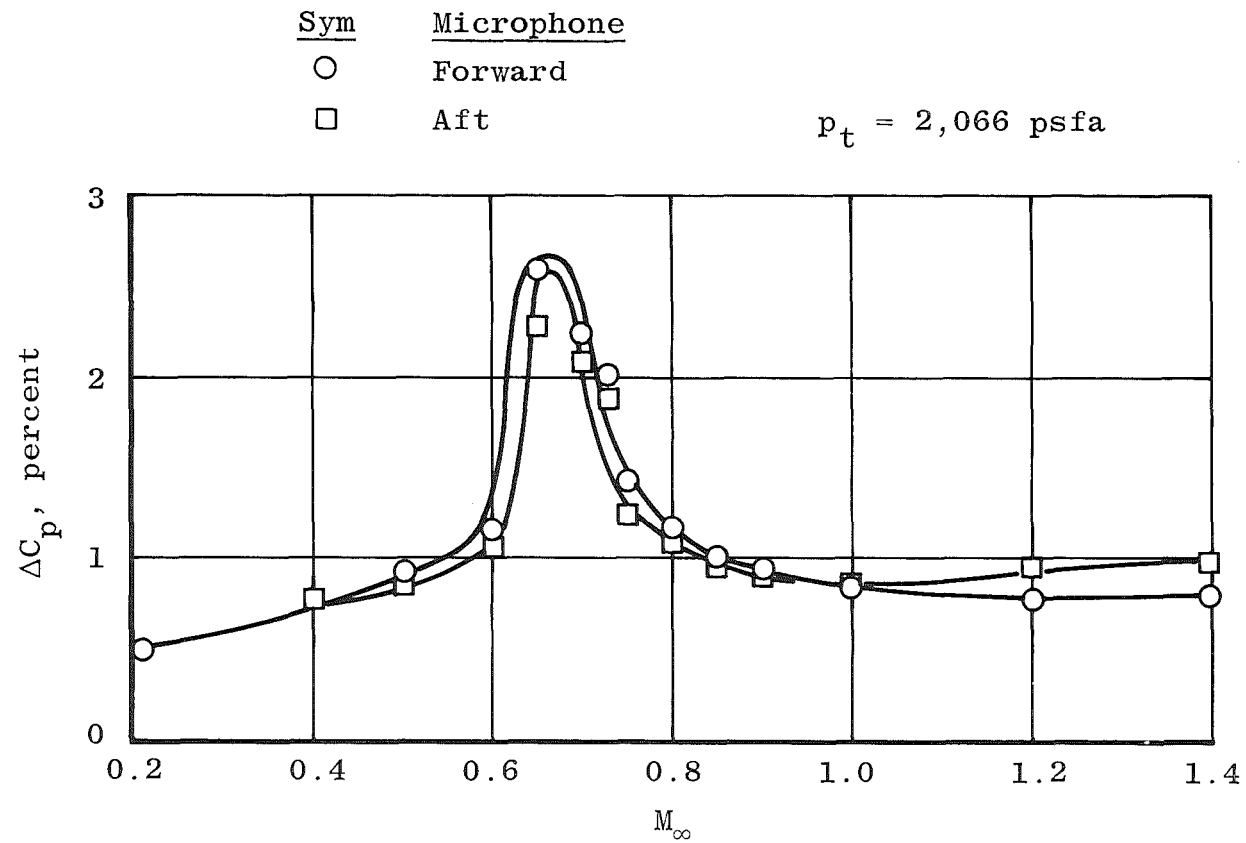


Figure 82. Noise levels in the ARA, Ltd. Bedford 9 x 8.

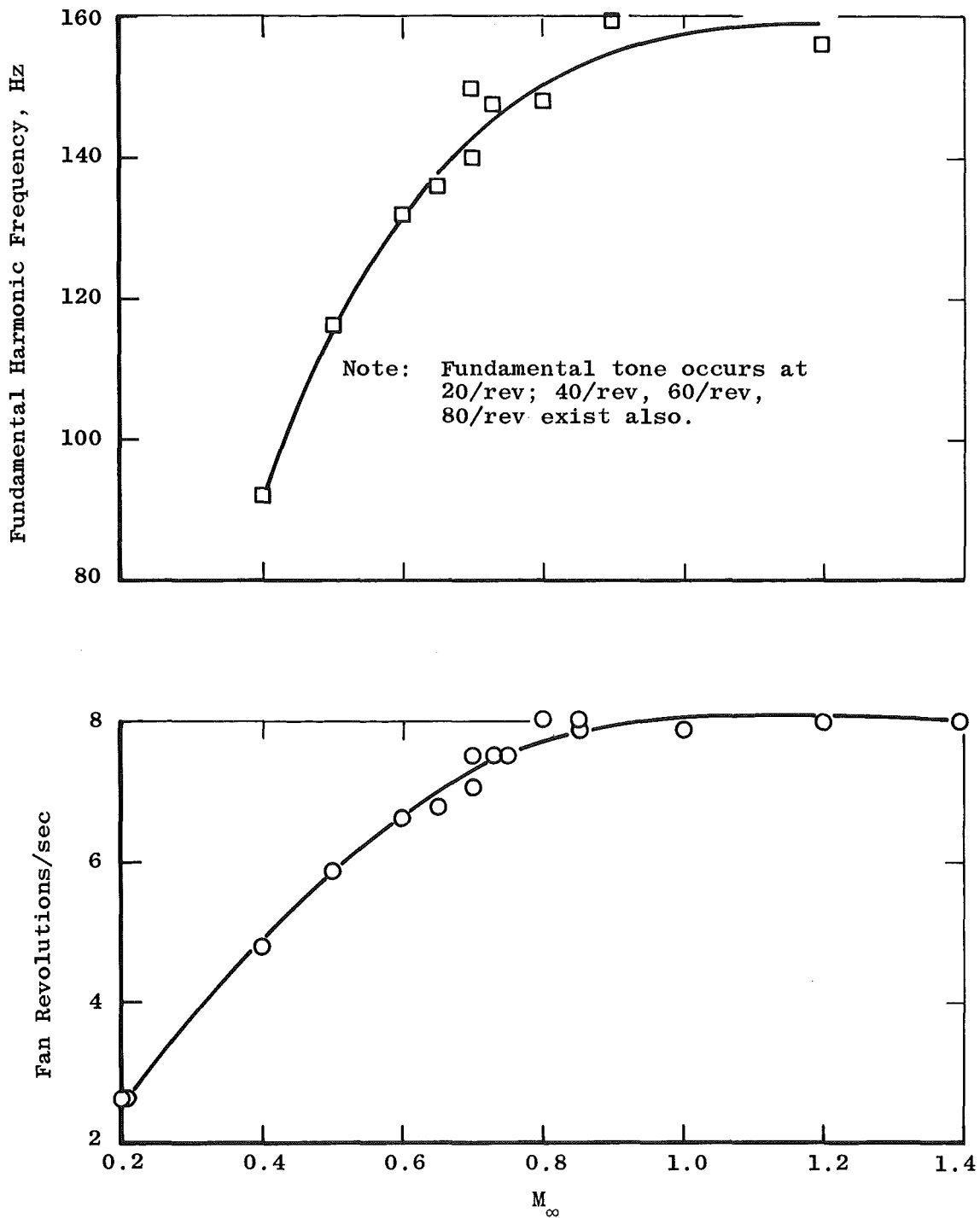


Figure 83. Fan tone identifications in the ARA, Ltd.
Bedford 9 x 8.

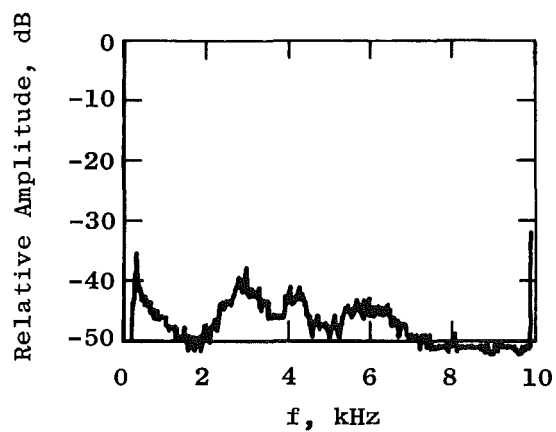
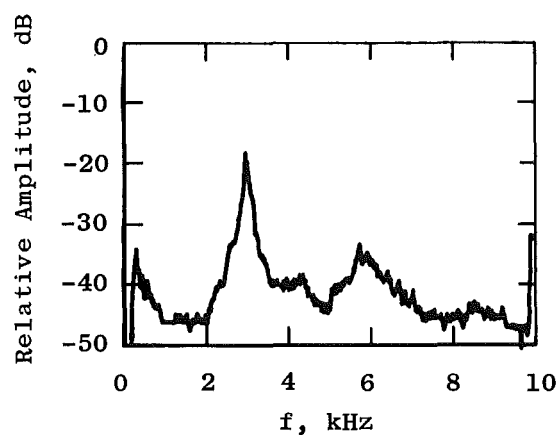
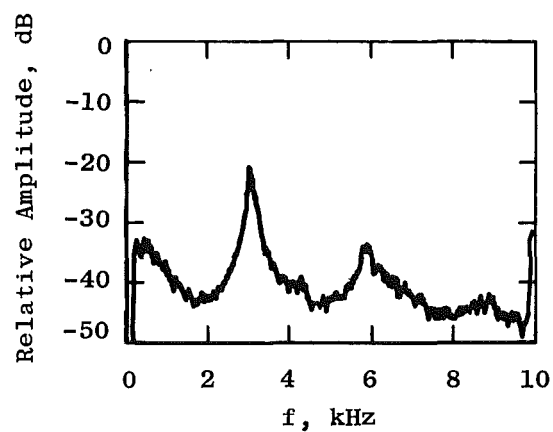
a. $M_\infty = 0.60$ b. $M_\infty = 0.65$ c. $M_\infty = 0.70$

Figure 84. Fourier spectrum measurements in the ARA, Ltd.
Bedford 9 x 8.

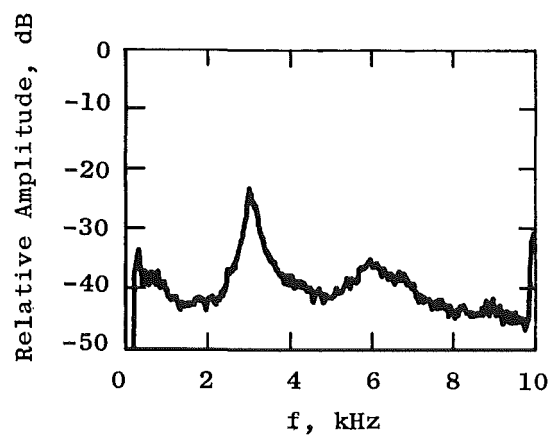
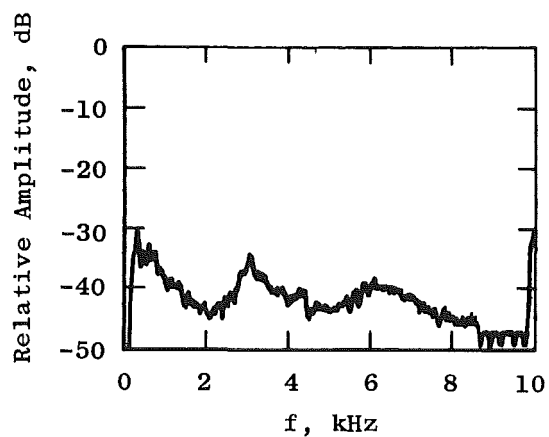
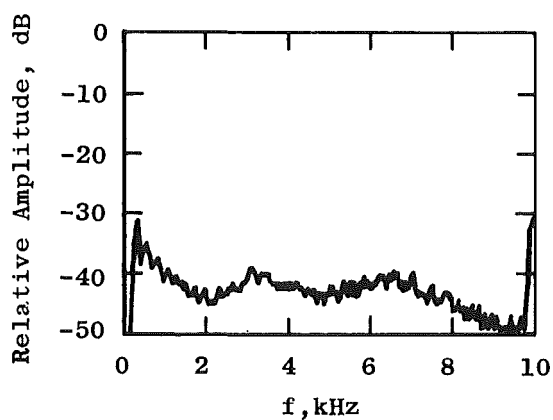
d. $M_{\infty} = 0.73$ e. $M_{\infty} = 0.75$ f. $M_{\infty} = 0.80$

Figure 84. Concluded.

3.3.3 Group 3 Tunnels: Supersonic, Two-Dimensional Nozzle

RAE Bedford 8 x 8 SWT

Data were acquired in this tunnel by D. G. Mabey of RAE and N. S. Dougherty, Jr. Transition detection was accomplished by means of the aft microphone signal, and the results are described in Ref. 5. The cone was installed in the tunnel as shown in Fig. 85, but the traversing pitot probe data were not used because of difficulties in detecting transition by that method. Although never proved conclusively, it is suspected that some surface scratches sustained on the 0-deg ray prior to the test (later polished out) caused a locally tripped boundary layer in the path of the probe. Circumferential contamination was apparently not complete to the 180-deg ray, where the aft microphone was located. Testimony to this conclusion is the apparently good correlation in other supersonic tunnels of the data obtained using the microphone with that using the pitot probe.

The results obtained at $M_\infty = 0.19, 0.6, 1.4,$ and 2.4 are shown in Figs. 86a, 86b, 87a, and 87b. Data are presented in the form of ΔC_p from the aft microphone versus U_∞/ν_∞ at the various Mach numbers. Arrows marking certain points in the ΔC_p profiles denote onset, rms peak, and end-of-transition Reynolds numbers, respectively. There are shifts in repeated segments of the data at both supersonic Mach numbers which are explained as follows. The desired variation in U_∞/ν_∞ was obtained by holding T_t constant and varying p_t . However, midway into the pressure excursion, it was noticed that the cone surface thermocouple indicated a slowly drifting temperature. Because some cone heat transfer was suspected, the excursion was terminated, and time was allowed for the cone surface temperature to achieve equilibrium, at which time a portion of the p_t excursion was repeated. The shift in the data was interpreted as indicative of the existence of heat transfer which would have altered transition location.

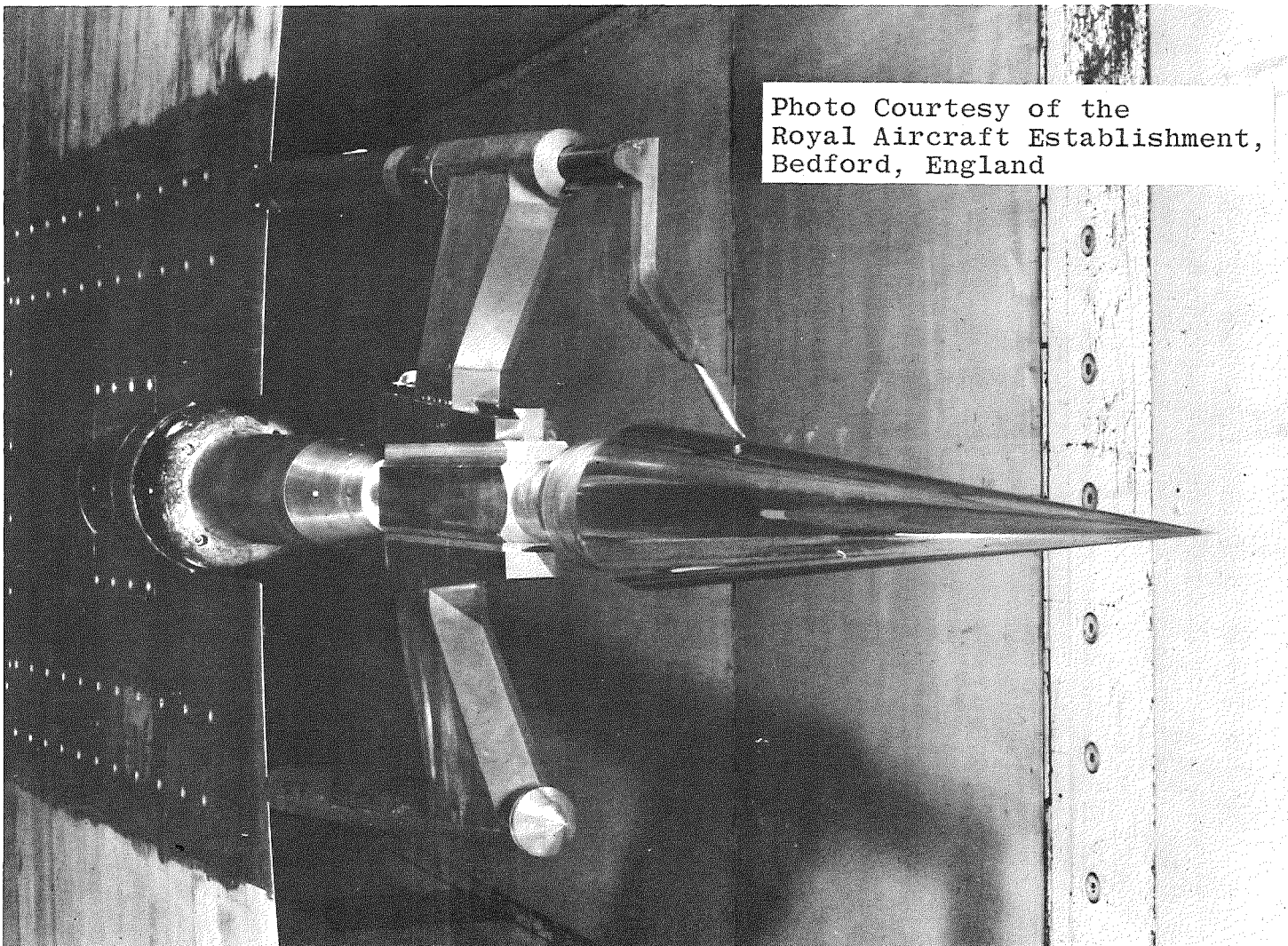
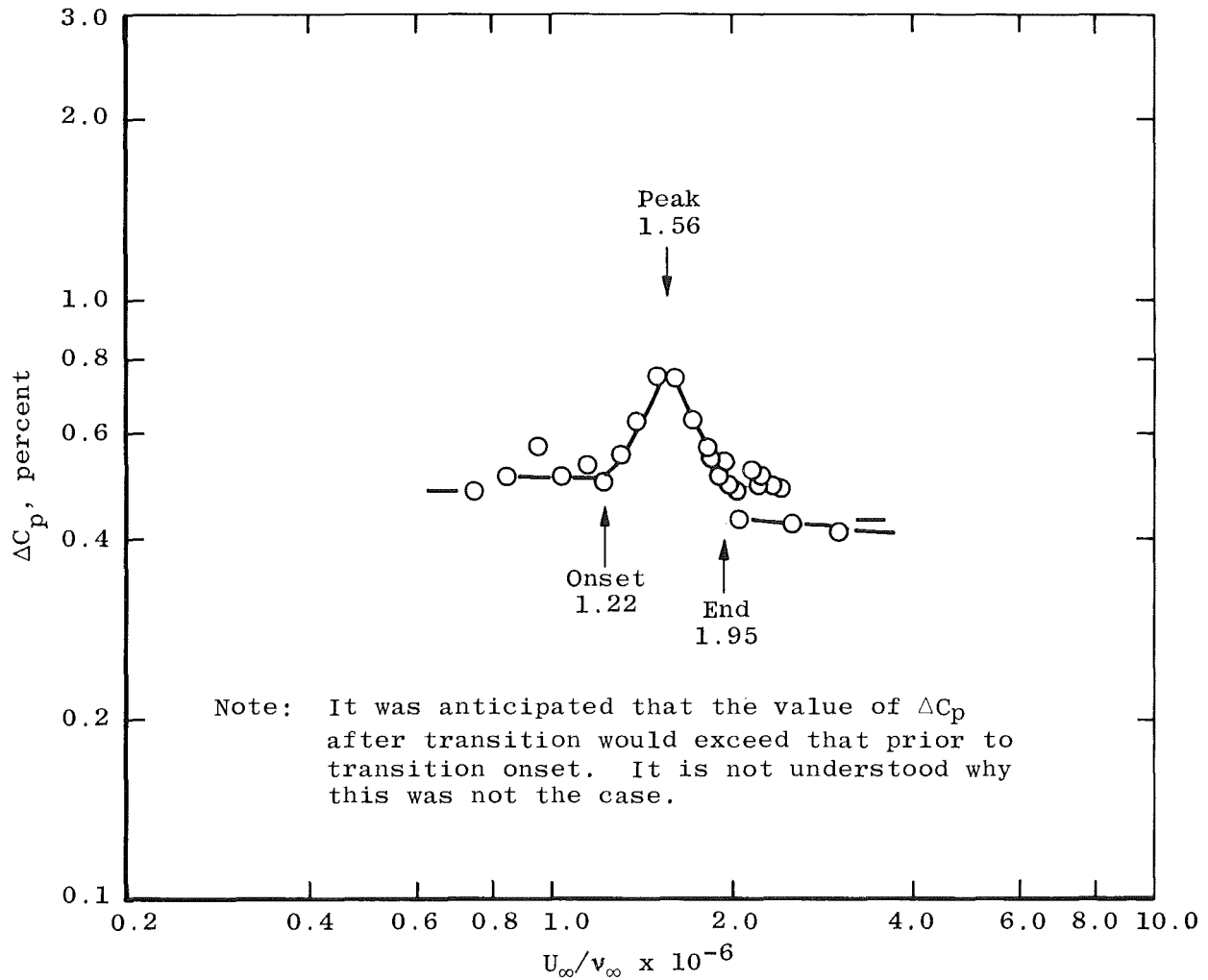
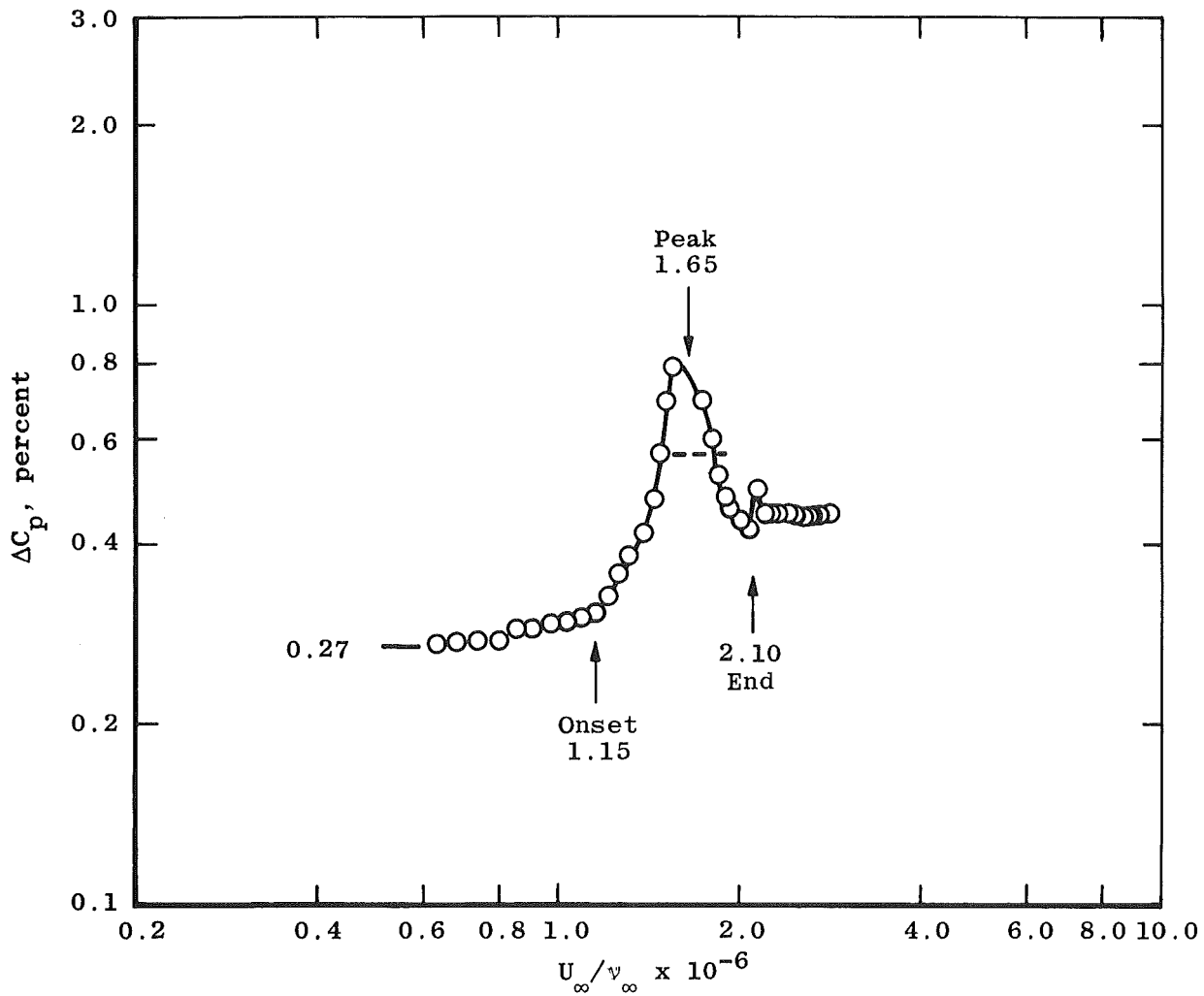


Figure 85. Photograph of the cone installation in the RAE Bedford 8 x 8 SWT.

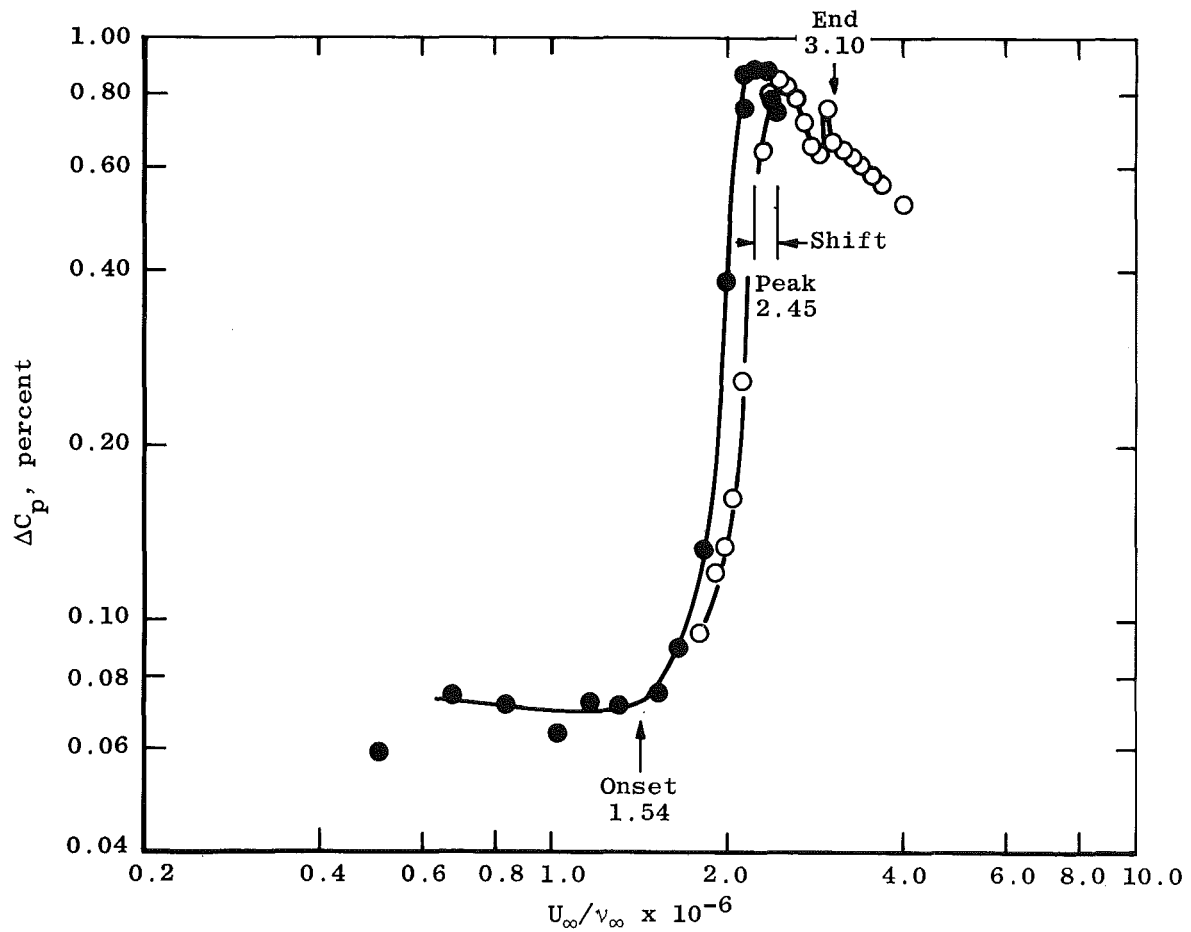


a. $M_\infty = 0.19$

Figure 86. Noise level as a function of U_∞/ν_∞ at $M_\infty = 0.19$ and 0.6 in the RAE Bedford 8 x 8 SWT.

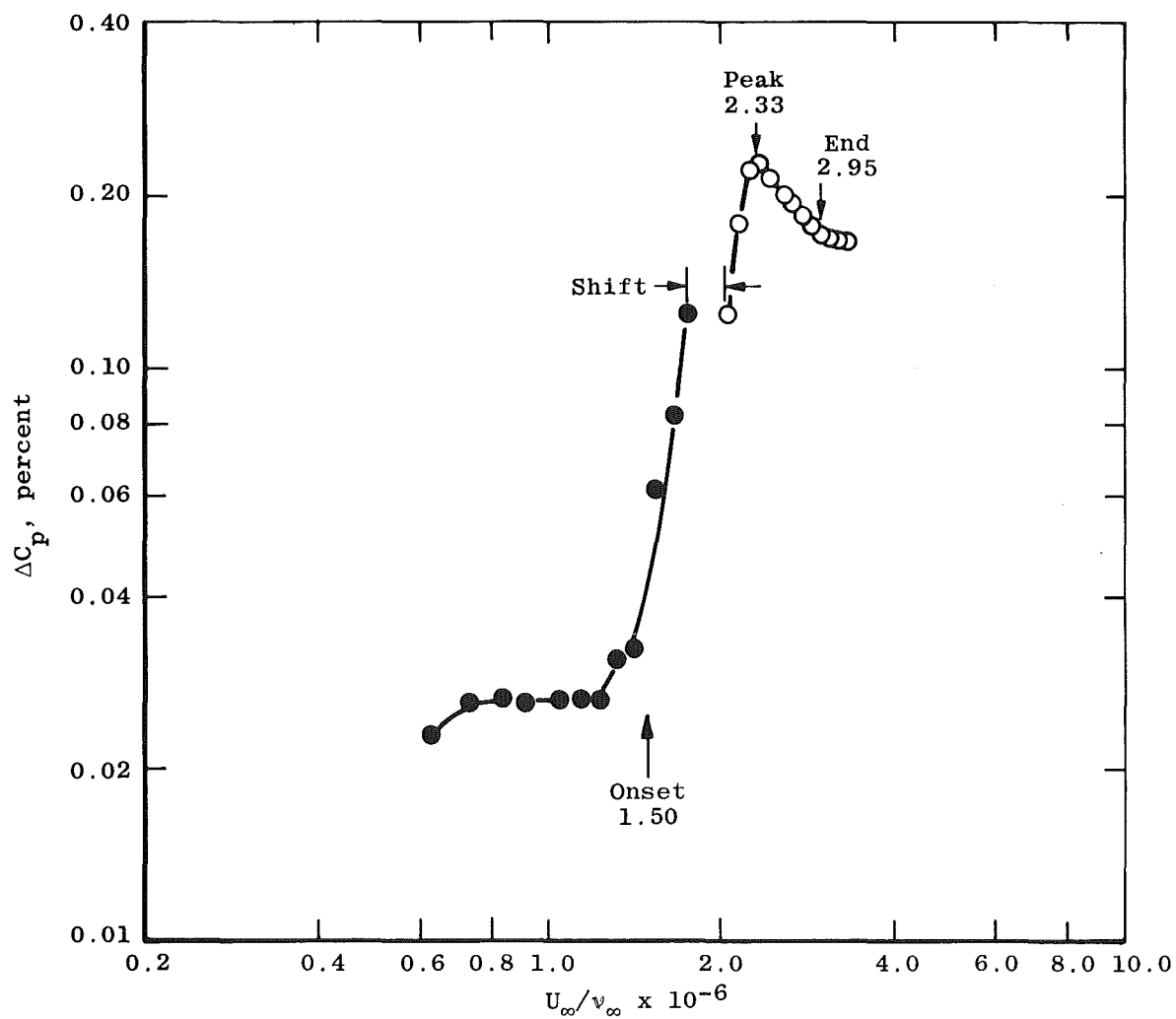


b. $M_\infty = 0.6$
Figure 86. Concluded.



a. $M_\infty = 1.4$

Figure 87. Noise level as a function of U_∞/ν_∞ at $M_\infty = 1.4$ and 2.4 in the RAE Bedford 8 x 8 SWT.



b. $M_\infty = 2.40$
Figure 87. Concluded.

NASA/Langley 4 SPT

Data were acquired in the NASA/Langley 4 SPT at two Mach numbers, 1.61 and 2.0. The data are presented in Table 12.

End-of-transition Reynolds number, Re_T , is presented as a function of U_∞/ν_∞ at $M_\infty = 1.6$ in Fig. 88. The onset-of-transition Reynolds number, Re_t , is presented in Fig. 89. The noise levels measured by the forward microphone and the projected laminar trend are shown for $M_\infty = 1.6$ in Fig. 90.

The same parameters in the same manner, Re_T , Re_t , and ΔC_p are presented for $M_\infty = 2.0$ in Figs. 91, 92, and 93, respectively.

There are apparent inconsistencies in the extent of the transition zone in these measurements which hold no ready explanations. Between Re_T and Re_t , it is Re_T that is believed to have the greater accuracy of measurement.

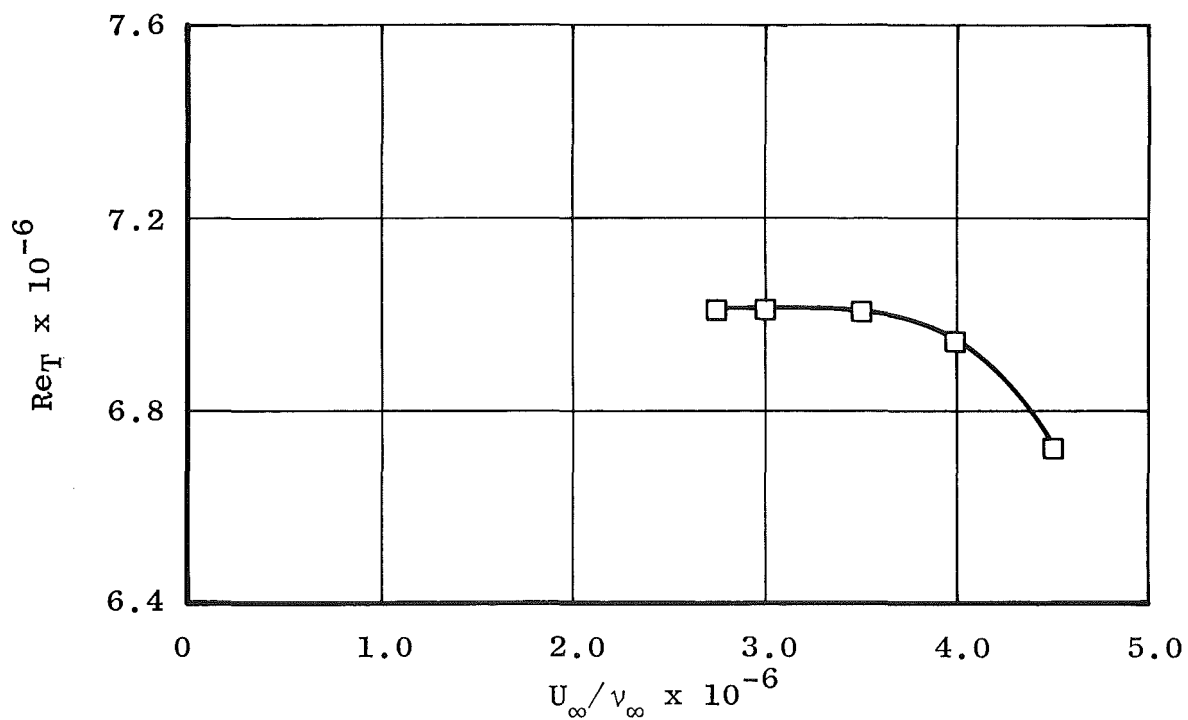


Figure 88. End-of-transition Reynolds numbers in the NASA/Langley 4 SPT at $M_\infty = 1.6$.

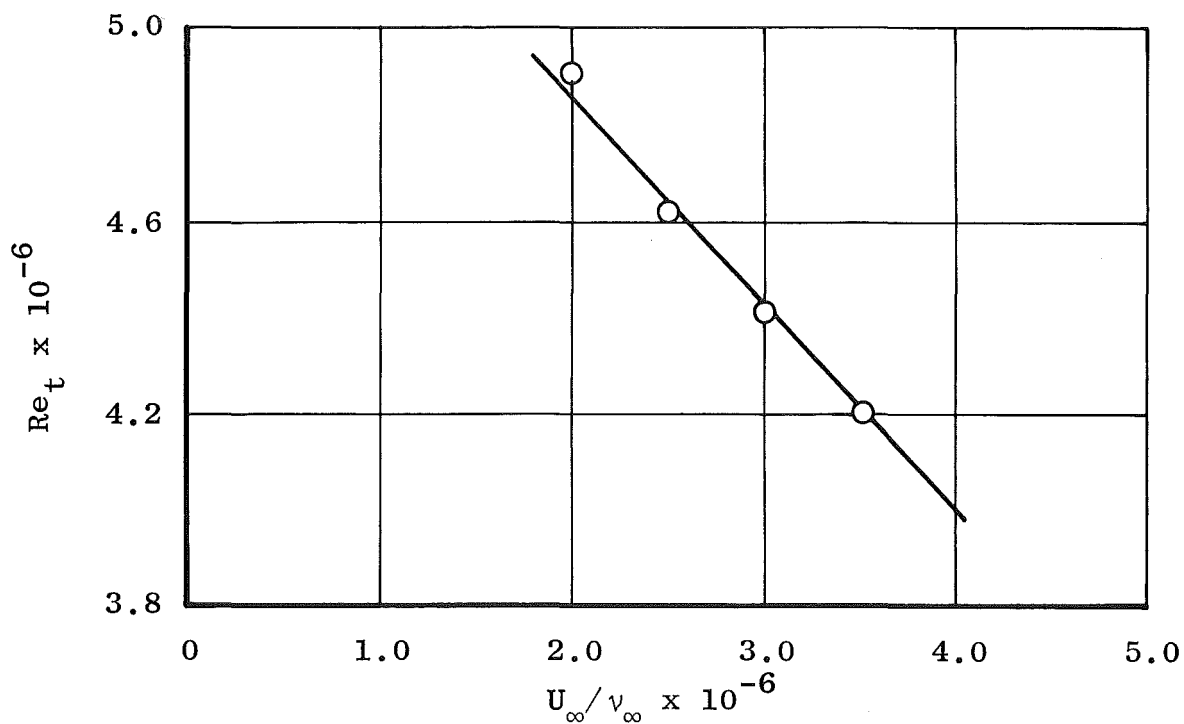


Figure 89. Onset-of-transition Reynolds numbers in the NASA/Langley 4 SPT at $M_\infty = 1.6$.

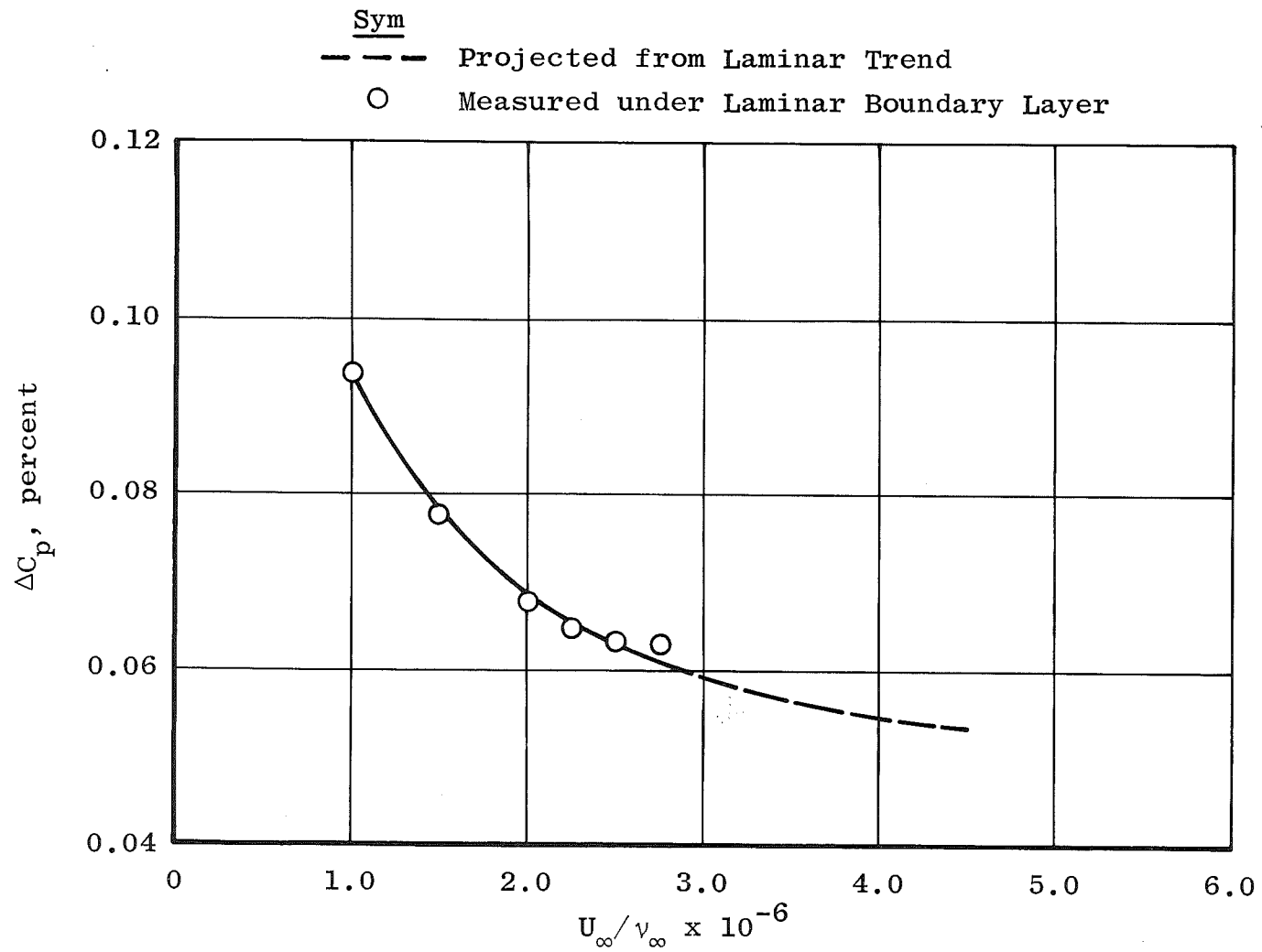


Figure 90. Noise levels in the NASA/Langley 4 SPT at $M_\infty = 1.6$.

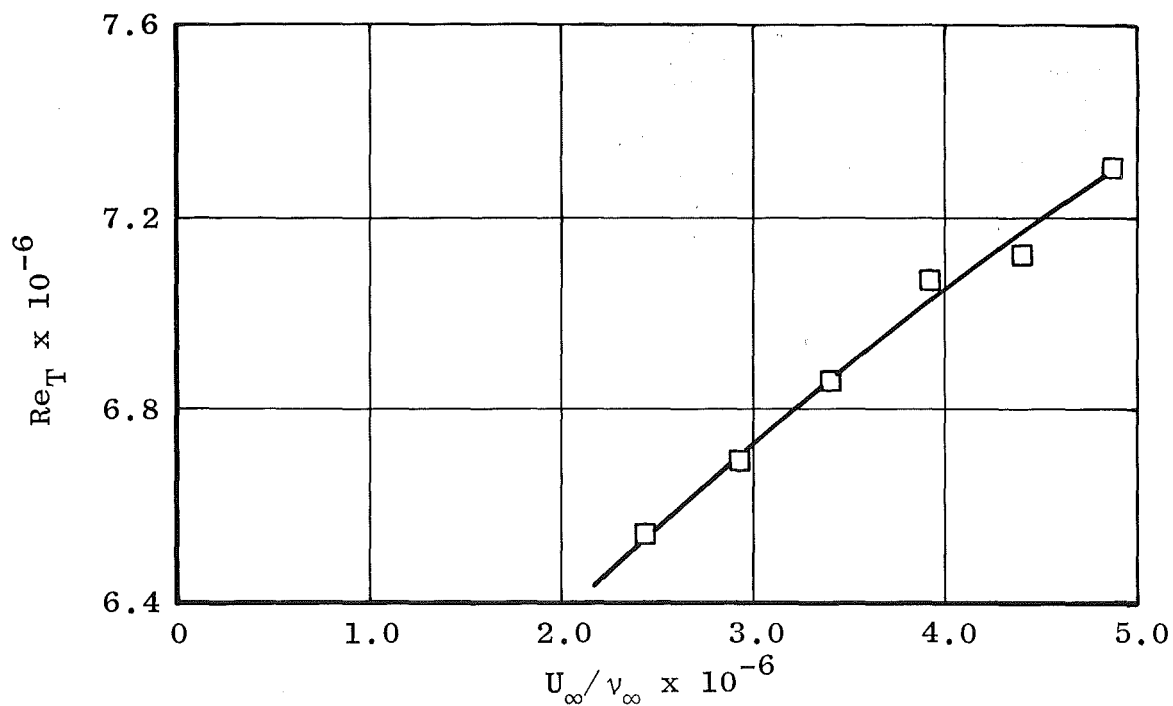


Figure 91. End-of-transition Reynolds numbers in the NASA/Langley 4 SPT at $M_\infty = 2.0$.

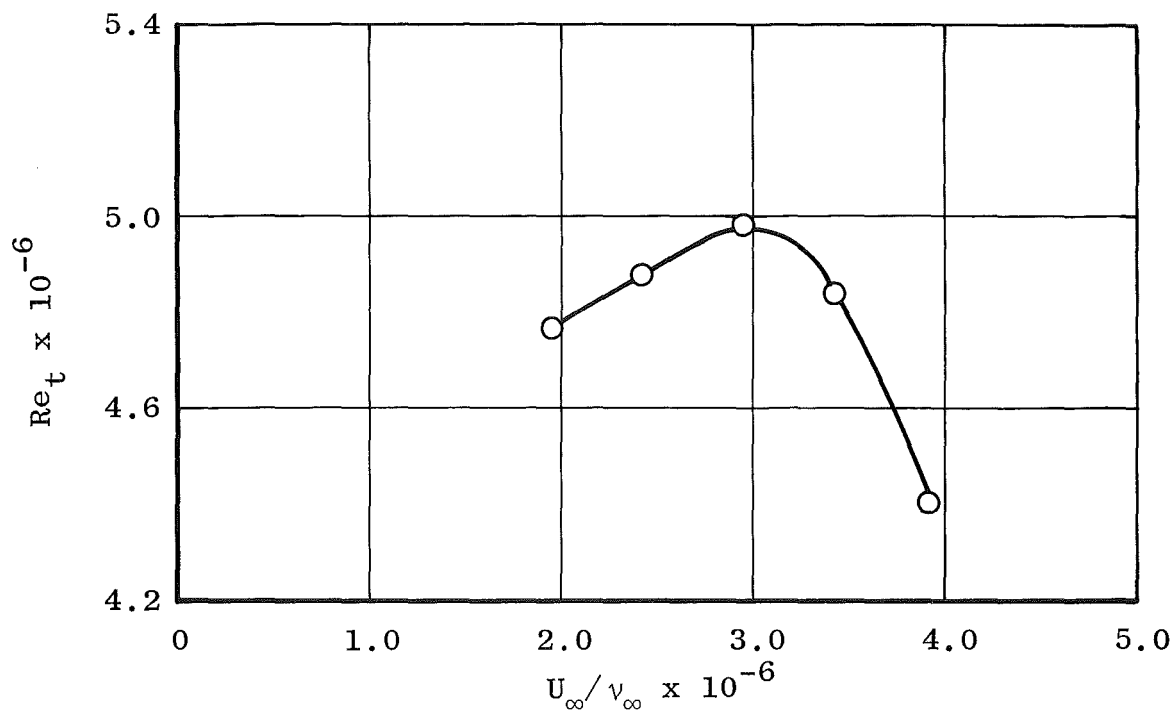


Figure 92. Onset-of-transition Reynolds number in the NASA/Langley 4 SPT at $M_\infty = 2.0$.

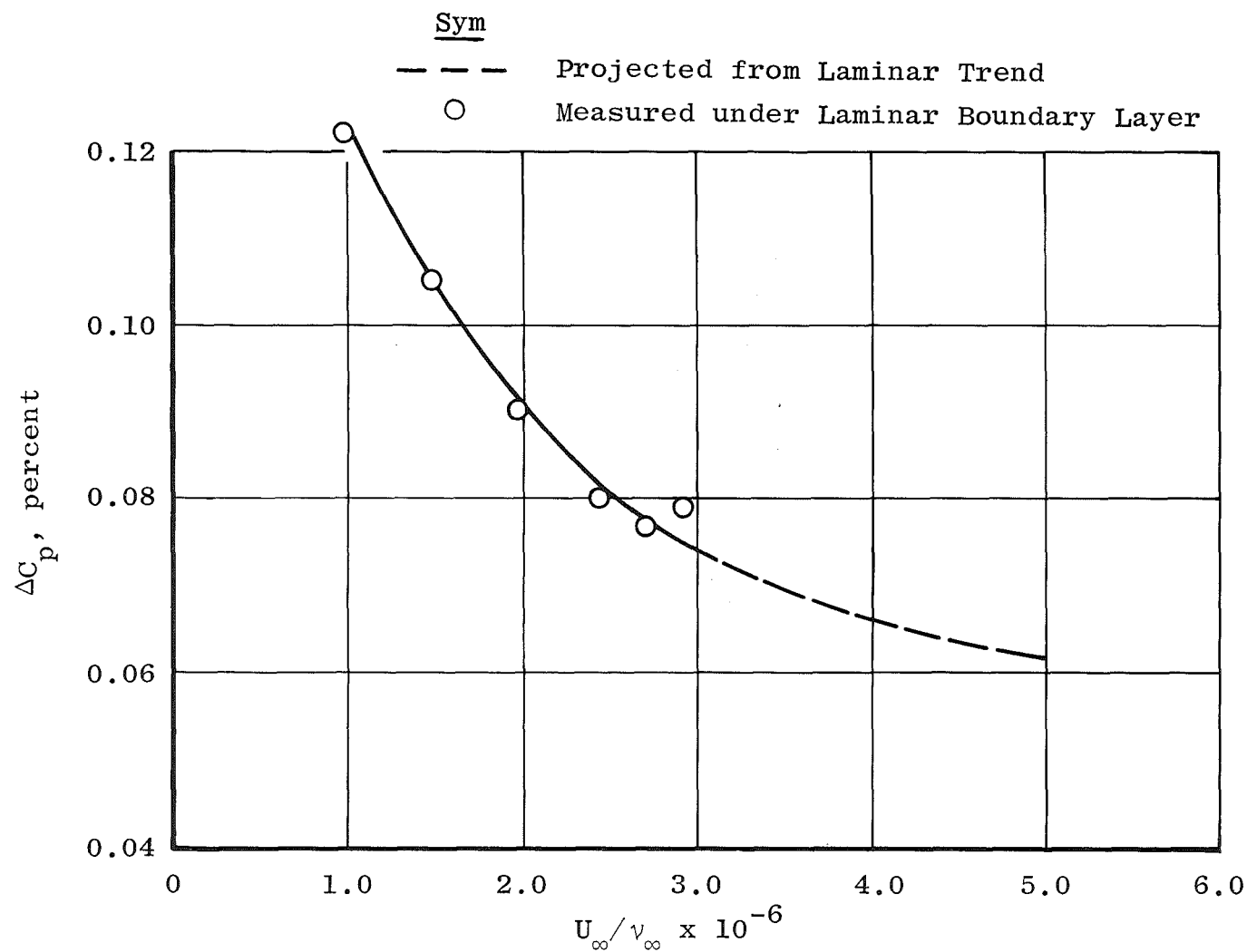


Figure 93. Noise levels in the NASA/Langley 4 SPT at $M_\infty = 2.0$.

Table 12. NASA/Langley 4 SPT Data

M_∞	U_∞/v_∞ $\times 10^{-6}$	ΔC_p , percent	$Re_t \times$ 10^{-6}	$Re_T \times$ 10^{-6}
1.61	0.992	0.093	-	-
	1.461	0.077	-	-
	1.478	0.077	-	-
	1.964	0.068	4.81	-
	2.204	0.065	4.44	-
	2.432	0.063	4.46	-
	2.689	0.063	4.55	6.86
	2.939	-	4.36	6.86
	3.431	-	3.83	6.89
	3.918	-	3.72	6.76
	4.168	-	3.13	6.46
	4.416	-	-	-
2.01	0.981	0.122	-	-
	1.473	0.105	-	-
	1.954	0.090	4.77	-
	2.439	0.080	4.88	6.54
	2.682	0.077	-	-
	2.928	0.079	4.98	6.69
	3.418	-	4.84	6.86
	3.909	-	4.40	7.07
	4.404	-	3.86	7.12
	4.875	-	3.29	7.31
	1.955	-	-	-
	1.465	-	-	-
	0.975	-	-	-

AEDC/PWT Tunnel 16S

Limited noise data on the cone-aft microphone were acquired in AEDC 16S. No pitot probe transition data were acquired on the cone since the probe indicated that the boundary layer was laminar over the entire cone for all test conditions. The maximum U_∞/ν_∞ obtainable in AEDC 16S is 2.2×10^6 ; thus, the cone was not long enough to acquire transition data.

A Kulite transducer was used in place of the Bruel and Kjaer microphones in this particular test. Only one sensor was operative.

The noise measurements made on the cone in AEDC 16S are shown in Fig. 94 as a function of U_∞/ν_∞ for M_∞ from 1.67 to 3.0. These data are suspected of being somewhat high in amplitude. A correlation of ΔC_p with wall boundary-layer characteristics presented by Laderman, Ref. 15, indicates lower levels in other supersonic tunnel measurements. Wall-mounted transducer data from AEDC 16S by Maestrello, et al., Ref. 16, are consistent with Ref. 15.

The trends with M_∞ and U_∞/ν_∞ , although absolute levels are in doubt, bear a self-consistency as they were used in Ref. 17 to collapse the hollow cylinder transition data in AEDC 16S (Ref. 2) indicating that the Re_T data on the cylinder follow the noise amplitude.

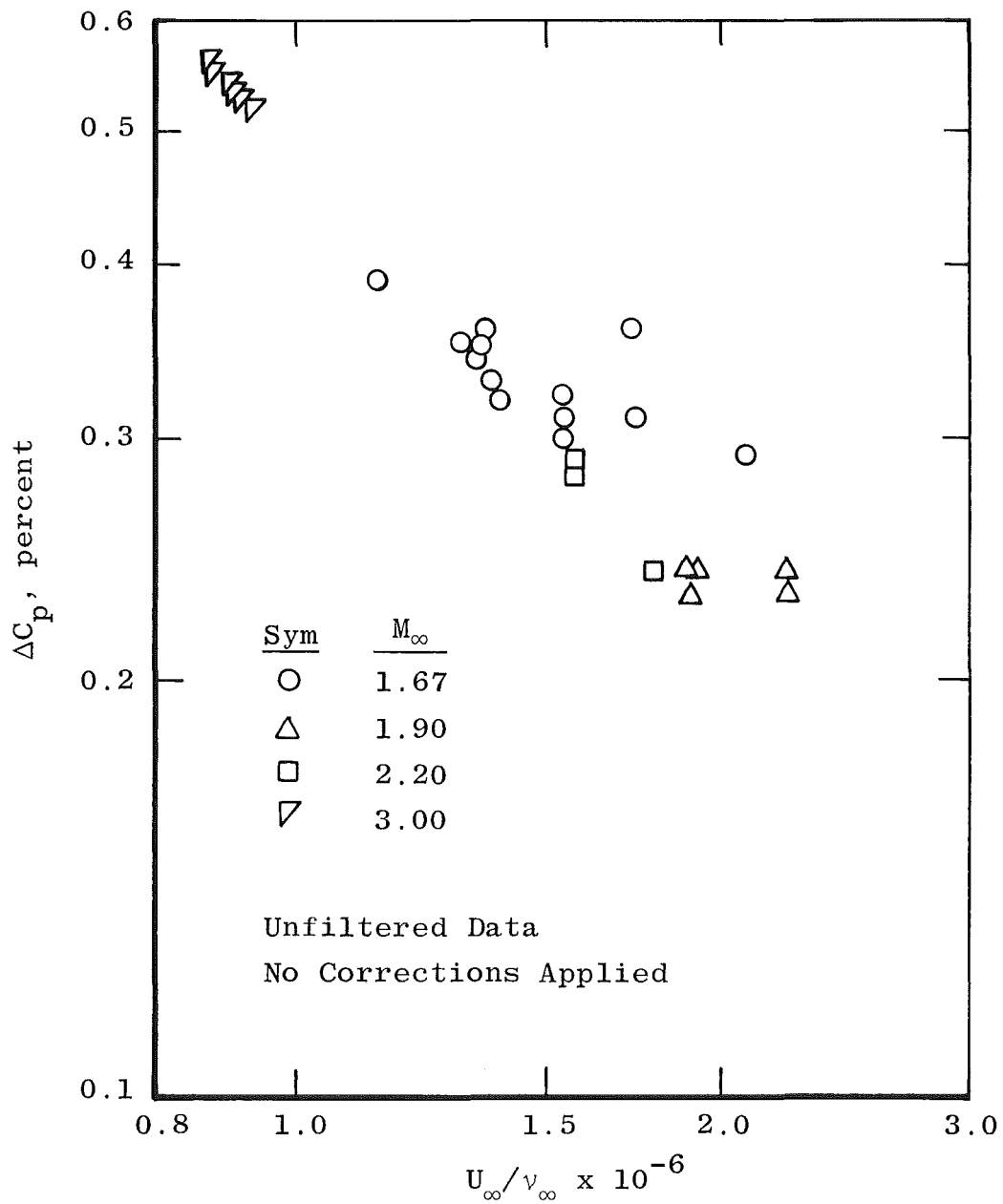


Figure 94. Noise levels in AEDC/PWT Tunnel 16S measured on the cone.

AEDC/VKF Tunnel A

A photograph of the cone installation in AEDC/VKF A is shown in Fig. 95. Transition data were acquired at M_∞ from 1.5 to 5.5. No noise level measurements were obtained, however, because of microphone diaphragm damage sustained by particulate contamination in the flow during these tests.

Transition Reynolds numbers, end and onset, are presented in Table 13. The data are presented as a function of U_∞/ν_∞ in Figs. 96 through 105. No explanation can be offered for the apparent variations in the extent of the transition zone as Re_T and Re_t appear to have opposite trends with U_∞/ν_∞ at some Mach numbers.

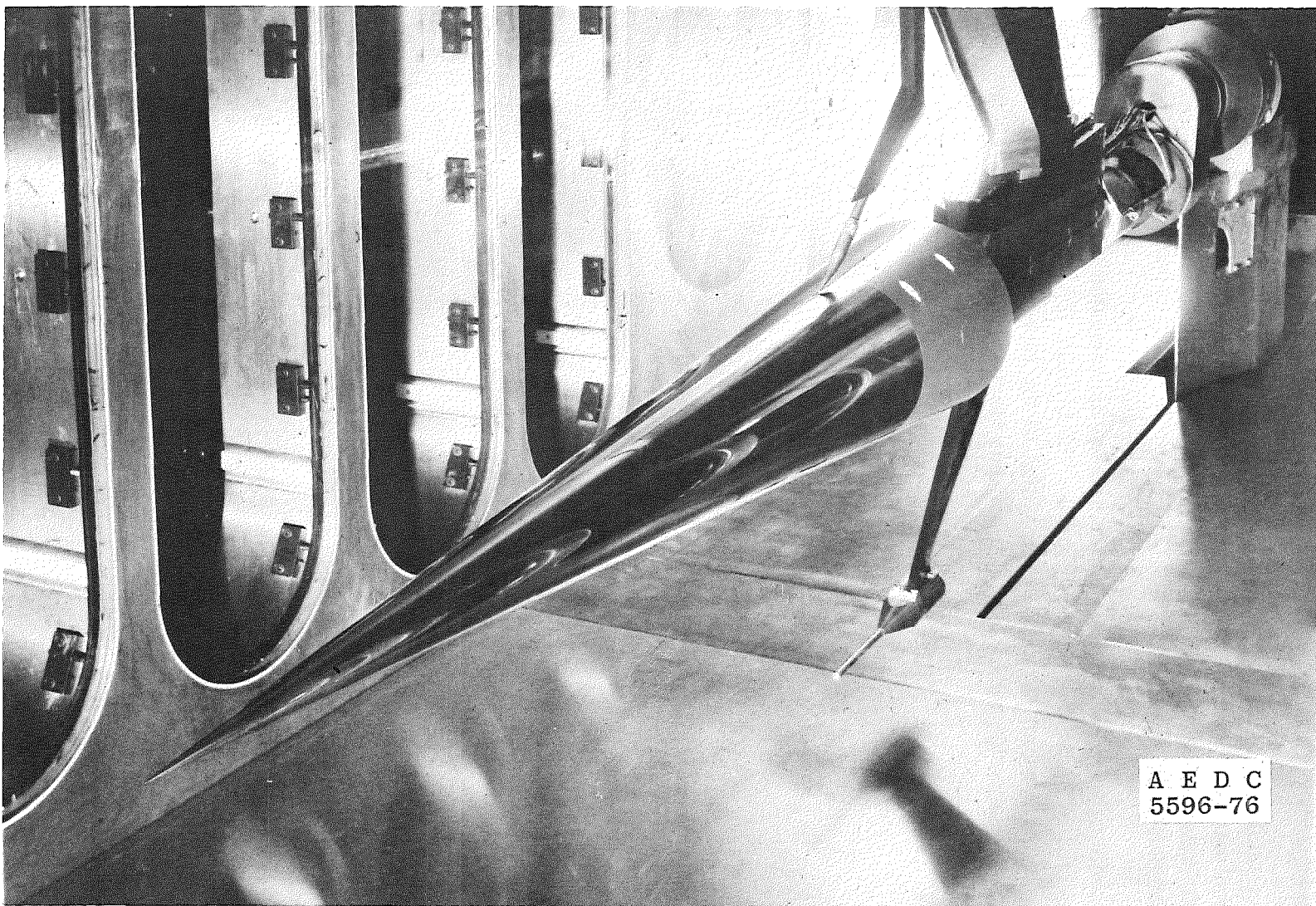


Figure 95. Photograph of the cone installation in AEDC/VKF Tunnel A.

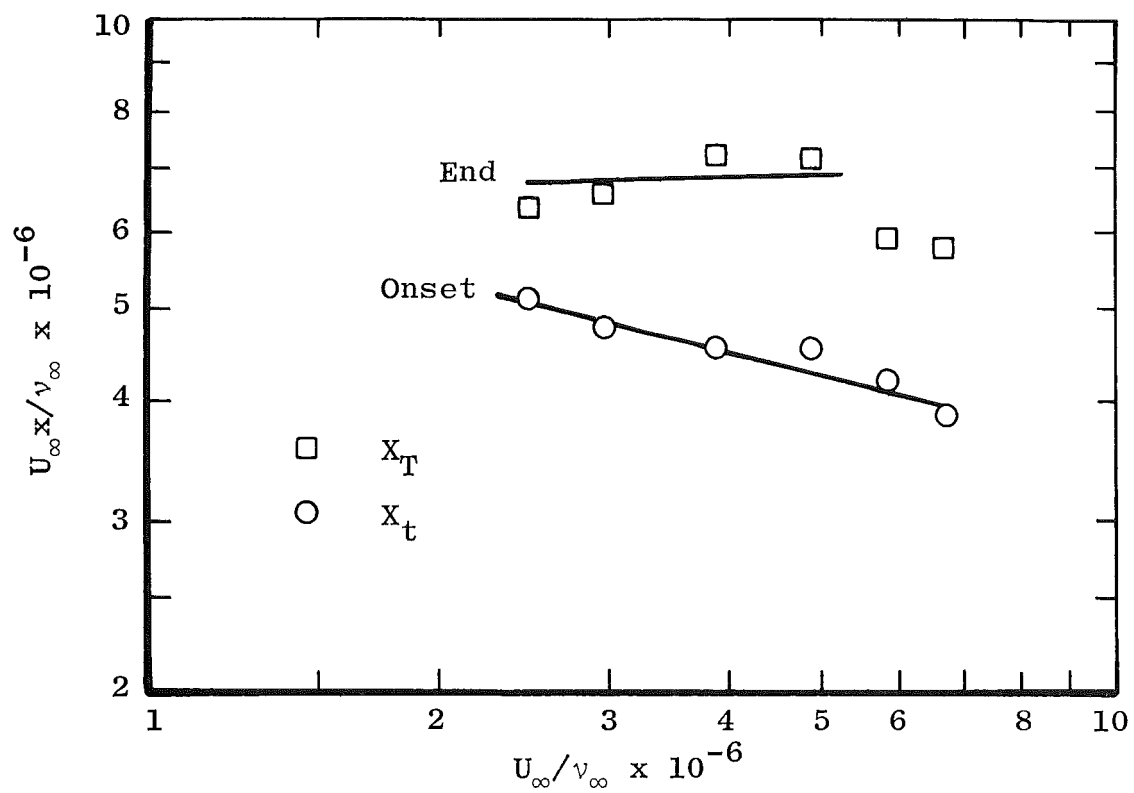


Figure 96. Transition Reynolds numbers in AEDC/VKF Tunnel A at $M_{\infty} \cong 1.5$.

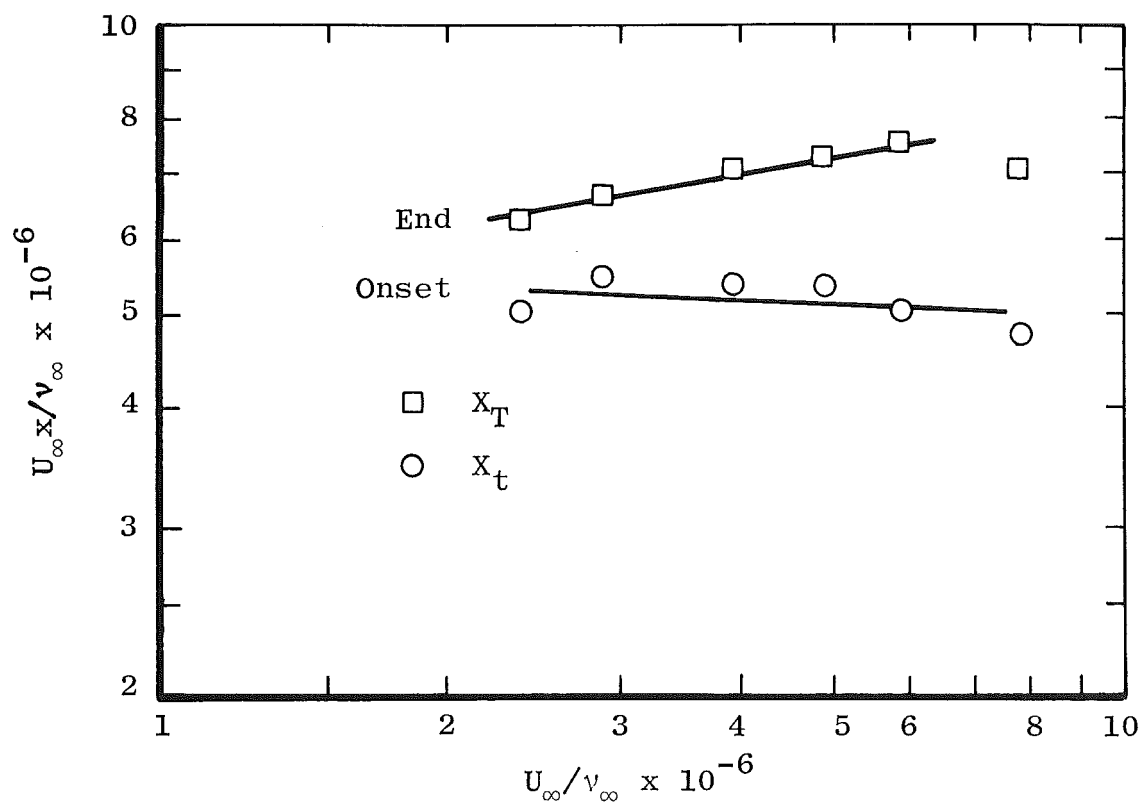


Figure 97. Transition Reynolds numbers in AEDC/VKF Tunnel A at $M_\infty \cong 1.7$.

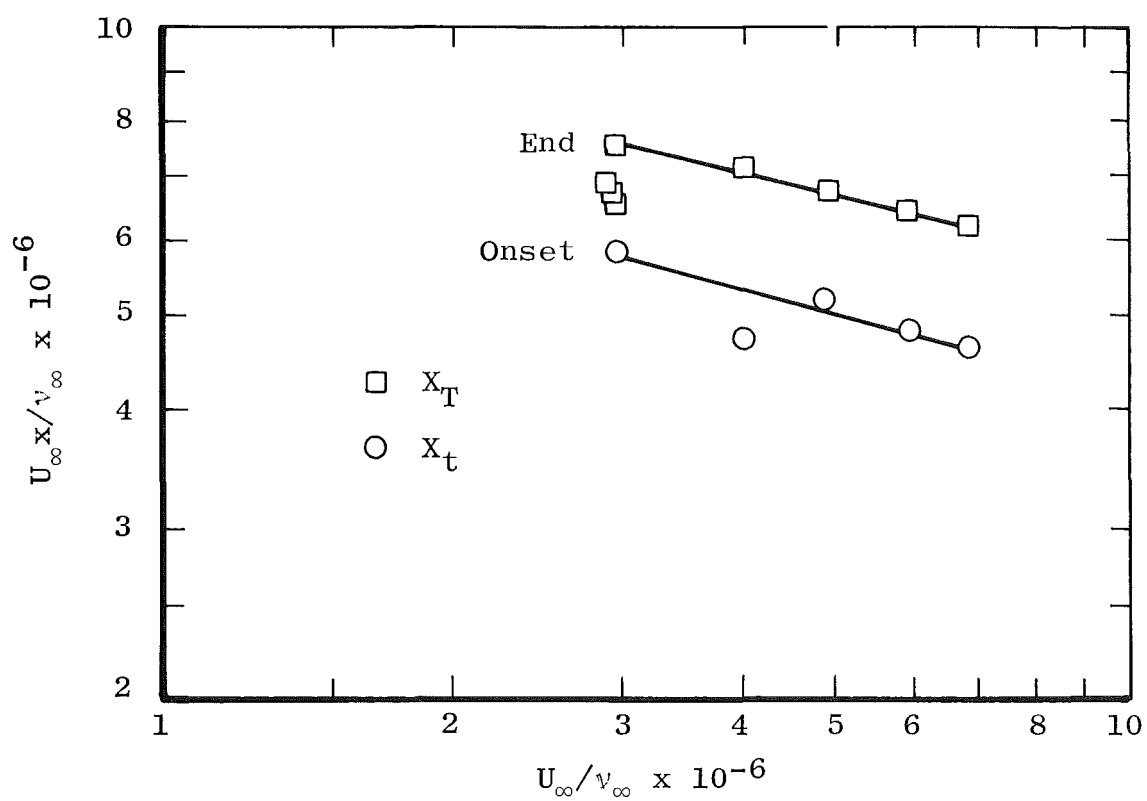


Figure 98. Transition Reynolds numbers in AEDC/VKF Tunnel A at $M_\infty \cong 1.96$.

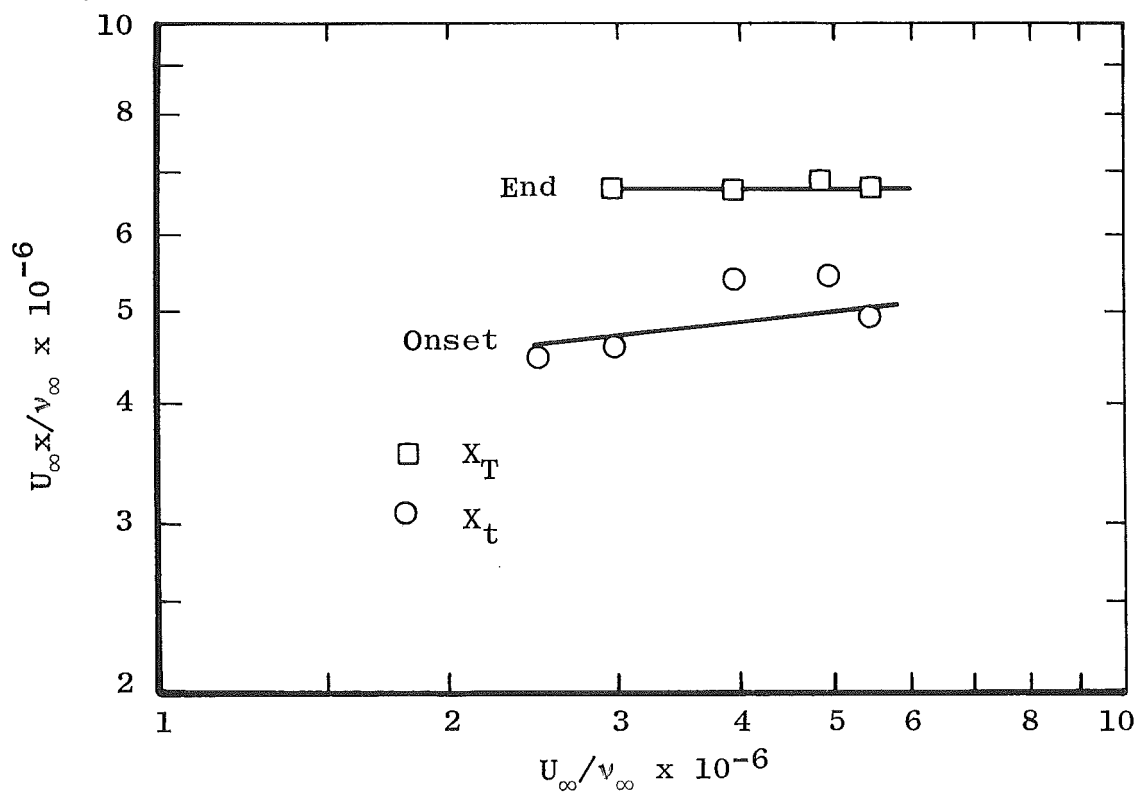


Figure 99. Transition Reynolds numbers in AEDC/VKF Tunnel A at $M_\infty \cong 2.47$.

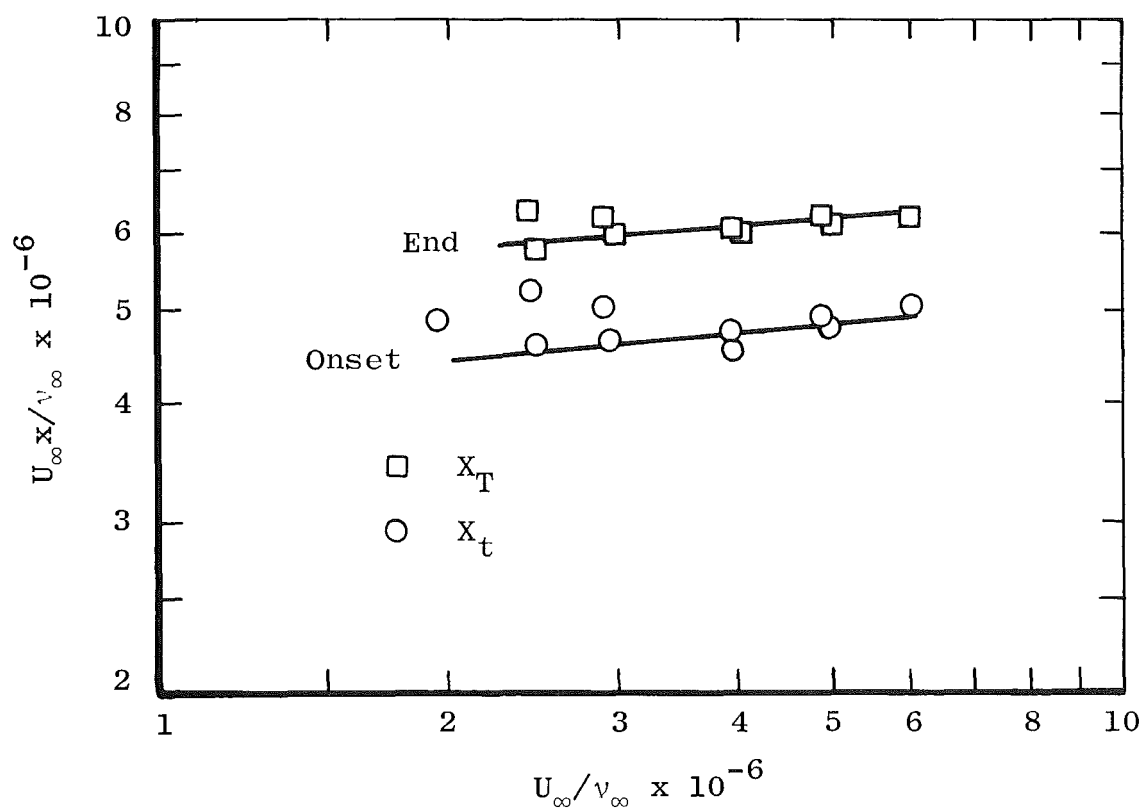


Figure 100. Transition Reynolds numbers in AEDC/VKF Tunnel A at $M_\infty \approx 2.98$.

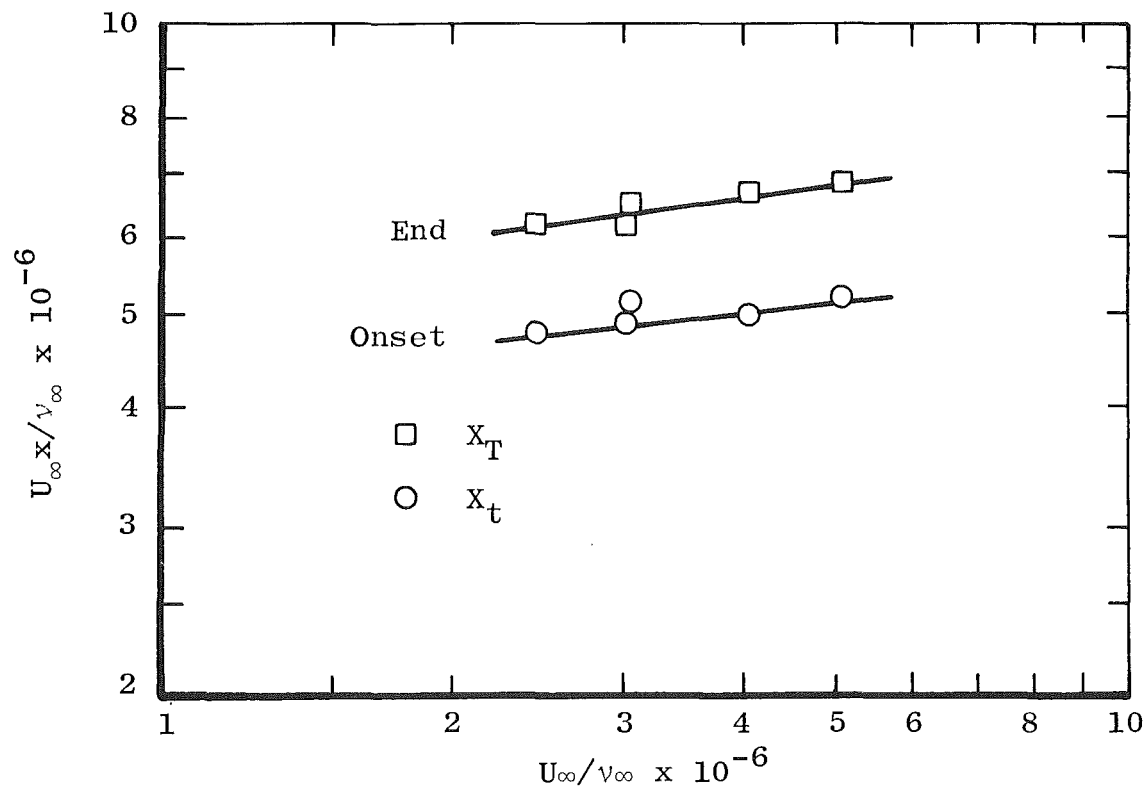


Figure 101. Transition Reynolds numbers in AEDC/VKF Tunnel A at $M_\infty \cong 3.22$.

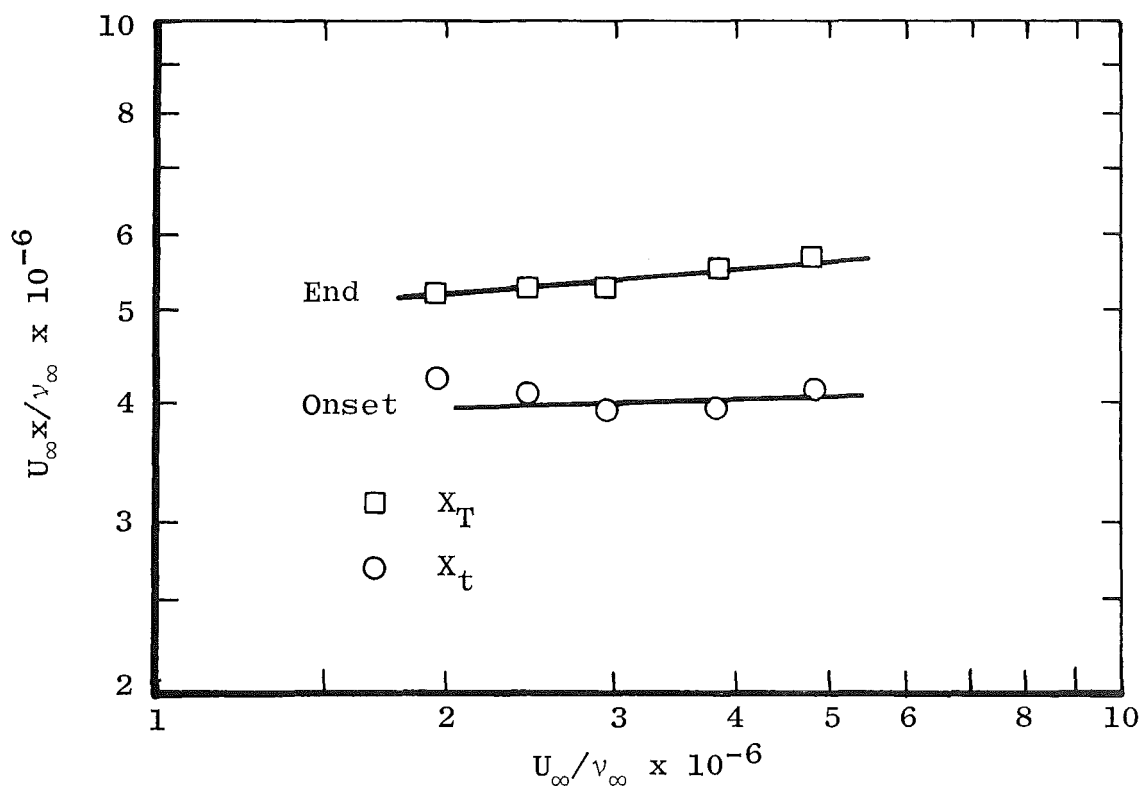


Figure 102. Transition Reynolds numbers in AEDC/VKF Tunnel A at $M_\infty \cong 3.45$.

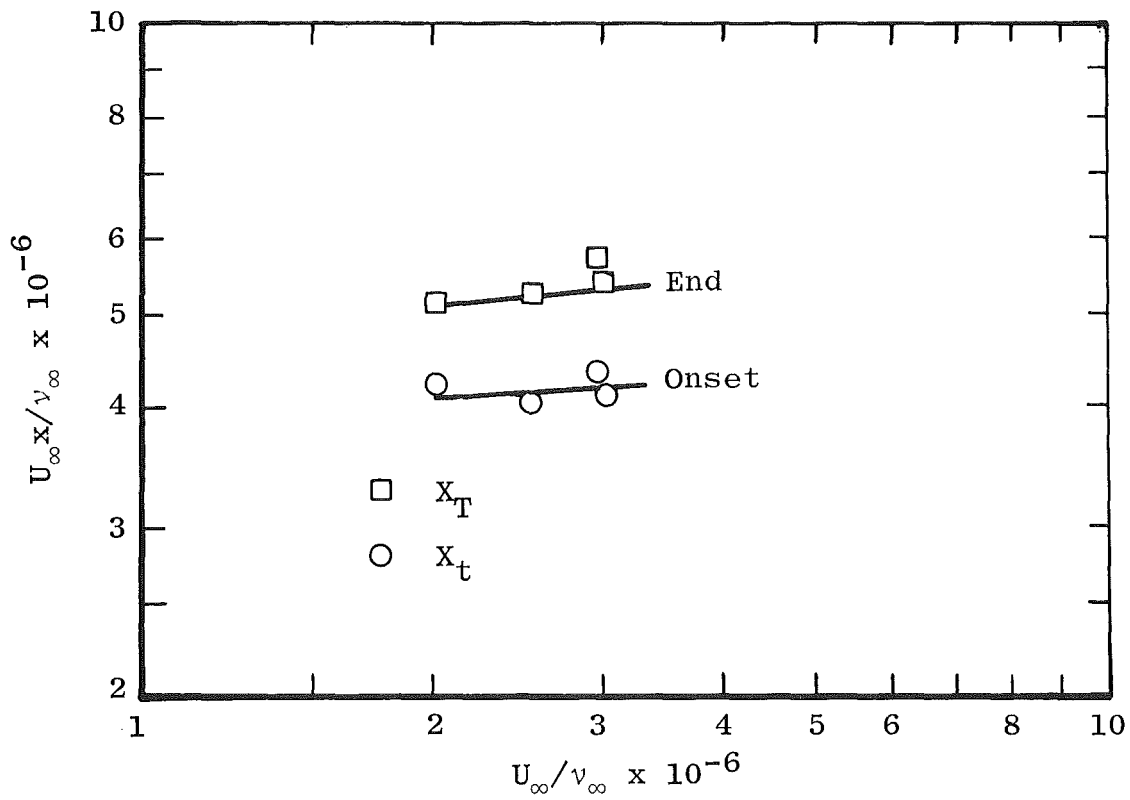


Figure 103. Transition Reynolds numbers in AEDC/VKF Tunnel A at $M_\infty \cong 4.05$.

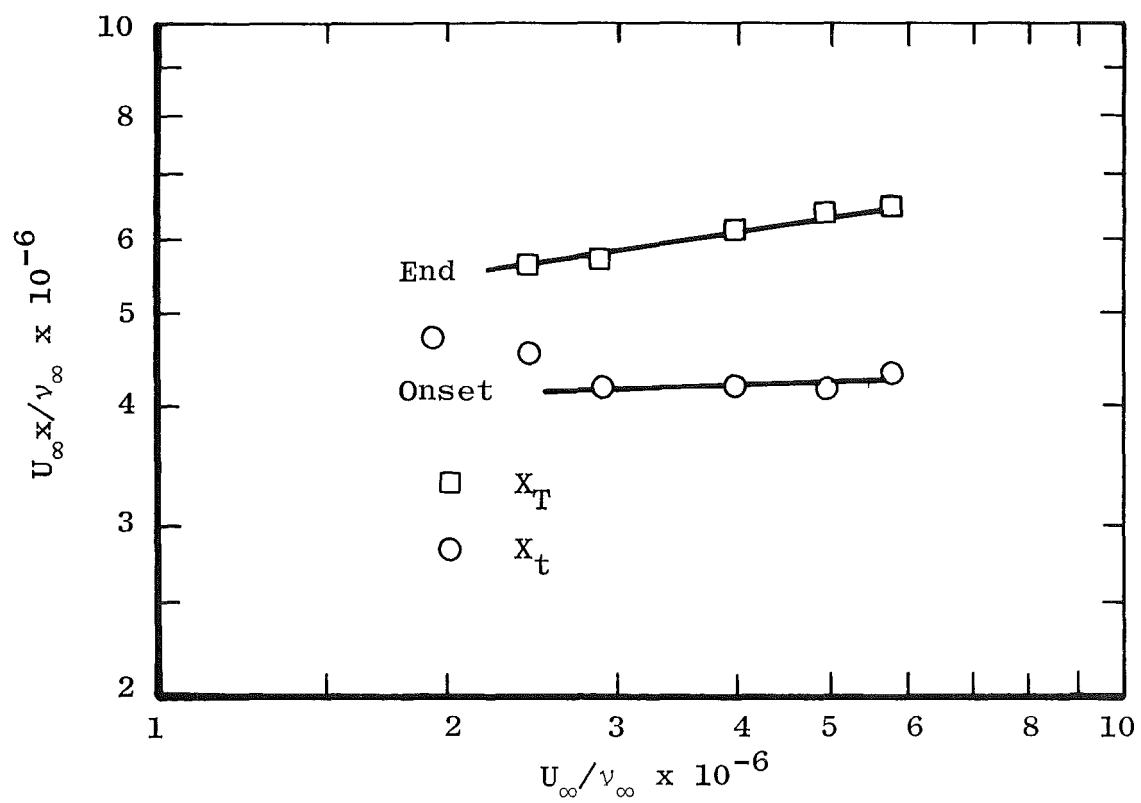


Figure 104. Transition Reynolds numbers in AEDC/VKF Tunnel A at $M_\infty \cong 4.48$.

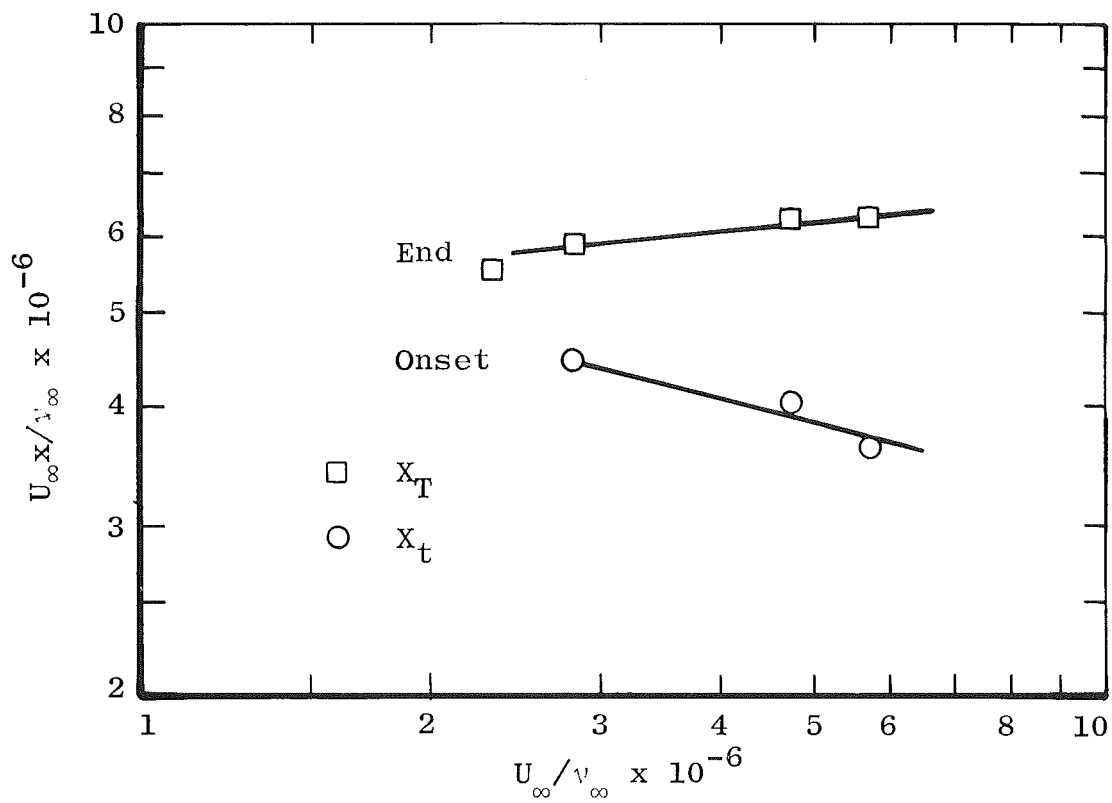


Figure 105. Transition Reynolds numbers in AEDC/VKF Tunnel A at $M_\infty \cong 5.05$.

Table 13. AEDC/VKF Tunnel A Data

M_∞	U_∞/v_∞ $\times 10^{-6}$	$Re_{t,x}$ 10^{-6}	$Re_{T,x}$ 10^{-6}
2.975	6.437	4.67	6.600
2.998	6.014	5.11	6.265
2.996	4.885	4.97	6.307
2.975	3.913	4.76	6.098
2.958	2.889	5.08	6.235
2.934	2.424	5.21	6.383
2.905	1.934	4.87	-
1.962	2.879	-	6.862
1.951	2.921	-	6.718
1.960	2.937	-	6.584
1.509	6.689	3.85	5.797
1.508	5.820	4.22	5.917
1.505	4.854	4.53	7.160
1.499	3.871	4.55	7.225
1.508	2.970	4.80	6.584
1.500	2.474	5.20	6.371
1.735	6.800	4.76	7.083
1.731	5.840	5.01	7.592
1.720	4.866	5.35	7.299
1.712	3.914	5.38	7.078
1.691	2.897	5.48	6.663
1.672	2.368	5.01	6.236
2.482	5.427	4.93	6.693
2.482	4.933	5.43	6.783
2.480	3.961	5.38	6.635
2.469	2.965	4.60	6.671
2.462	2.469	4.48	-
5.120	5.713	3.62	6.237
5.077	4.715	4.01	6.287
5.052	2.807	4.44	5.895
5.026	2.315	-	5.556

Table 13. Concluded

M_∞	U_∞ / v_∞ $\times 10^{-6}$	$Re_t \times$ 10^{-6}	$Re_T \times$ 10^{-6}
4.042	3.008	4.11	5.389
3.997	2.976	4.37	5.754
4.065	2.539	4.02	5.205
4.060	2.042	4.22	5.139
3.470	4.800	4.12	5.680
3.464	3.810	3.94	5.525
3.458	2.922	3.97	5.284
3.452	2.424	4.08	5.292
3.470	1.958	4.26	5.254
3.000	4.943	4.78	6.179
2.989	3.955	4.52	6.097
2.978	2.967	4.67	5.934
2.971	2.479	4.59	5.702
1.925	2.936	5.85	7.585
1.950	4.885	5.25	6.758
1.960	6.815	4.66	6.247
1.962	3.990	4.76	7.149
1.963	5.911	4.83	6.404
3.215	5.091	5.18	6.830
3.211	4.077	4.99	6.693
3.214	3.062	5.15	6.532
3.206	3.019	4.86	6.189
3.188	2.447	4.79	6.158
4.517	5.718	4.34	6.433
4.495	4.922	4.18	6.399
4.495	3.962	4.23	6.141
4.467	2.897	4.20	5.697
4.464	2.408	4.58	5.639
4.413	1.926	4.72	-
5.558	4.134	-	6.614
5.556	3.135	4.13	6.061

RAE Bedford 3 x 4 HSST

As in the RAE Bedford 8 x 8 SWT, transition was detected using the cone microphones since the traversing pitot probe mechanism was not installed for this test. Data were acquired at M_∞ from 2.5 to 4.5 with appropriate variations in U_∞/ν_∞ to move the transition region over both microphones. The measurements were made by D. G. Mabey of RAE, and the results are included in Ref. 5.

The data are presented in Figs. 106 through 110 as a function of $U_\infty x/\nu_\infty$, x being the appropriate dimension, either 18.0 or 26.0 in., of the placement of the respective microphone. End-of-transition locations are denoted by arrows at the appropriate value of $U_\infty x/\nu_\infty$.

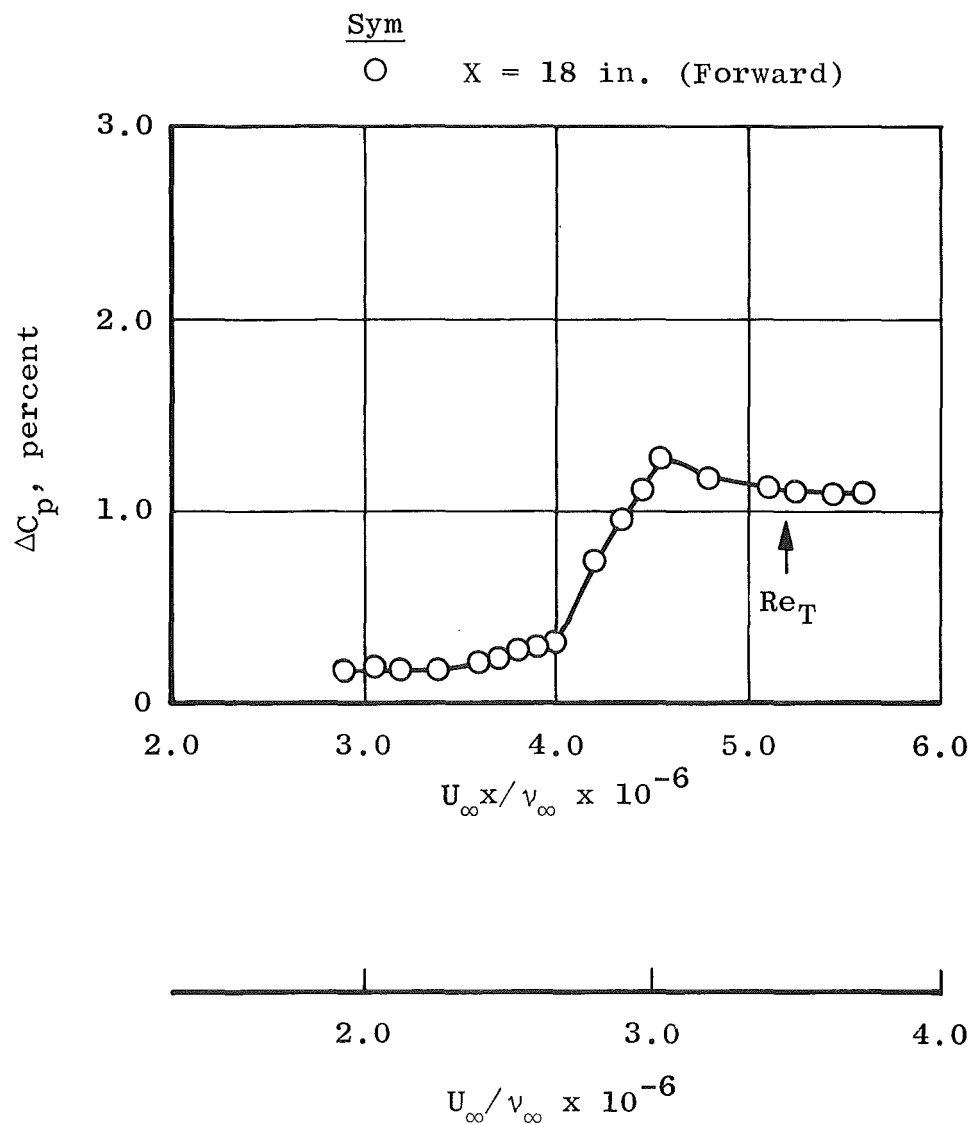


Figure 106. Noise levels as a function of U_∞/ν_∞ at $M_\infty = 2.5$ in the RAE Bedford 3 x 4 HSST.

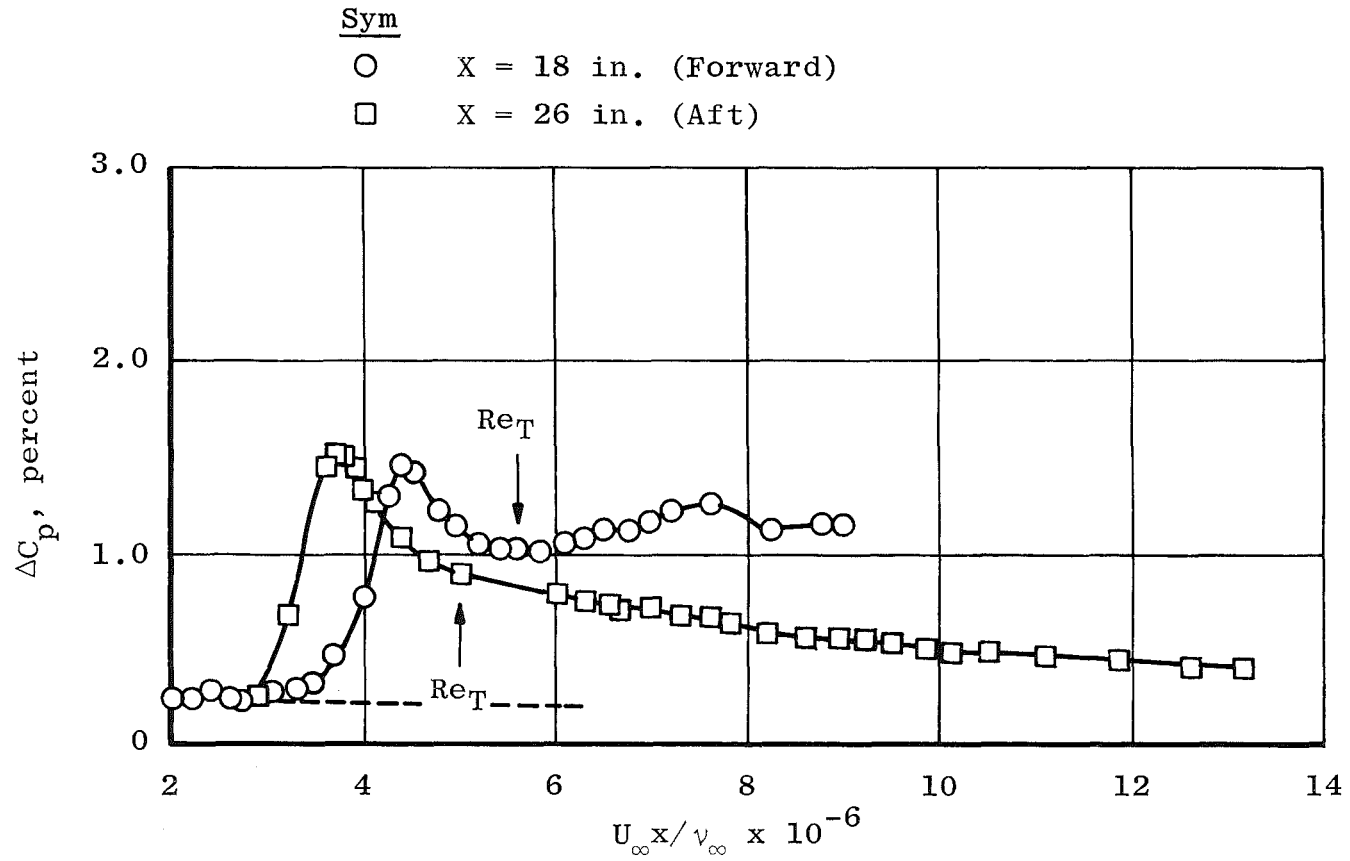


Figure 107. Noise levels as a function of U_∞/ν_∞ at $M_\infty = 3.0$ in the RAE Bedford 3 x 4 HSST.

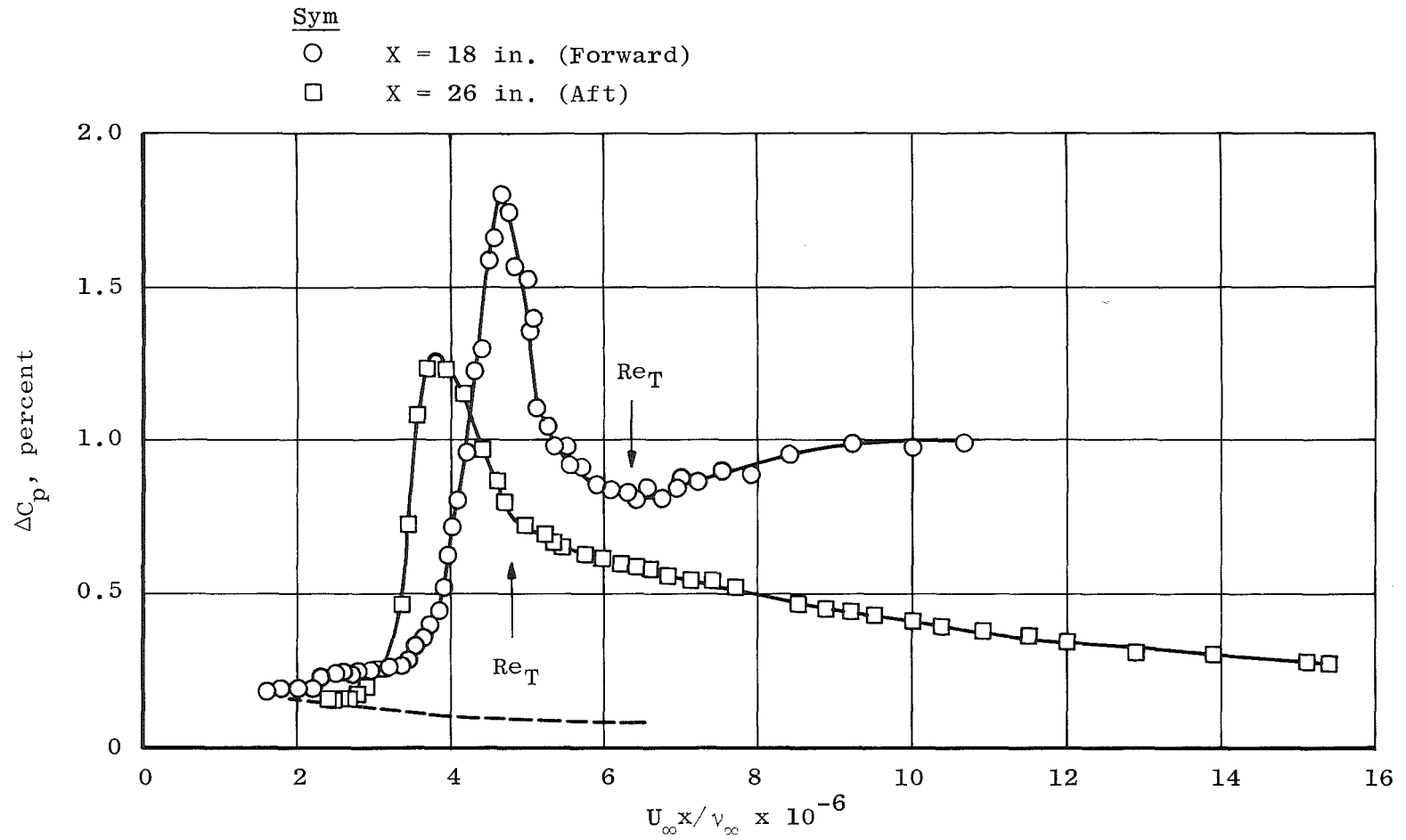


Figure 108. Noise levels as a function of $U_\infty x / \nu_\infty$ at $M_\infty = 3.5$ in the RAE Bedford 3 x 4 HSST.

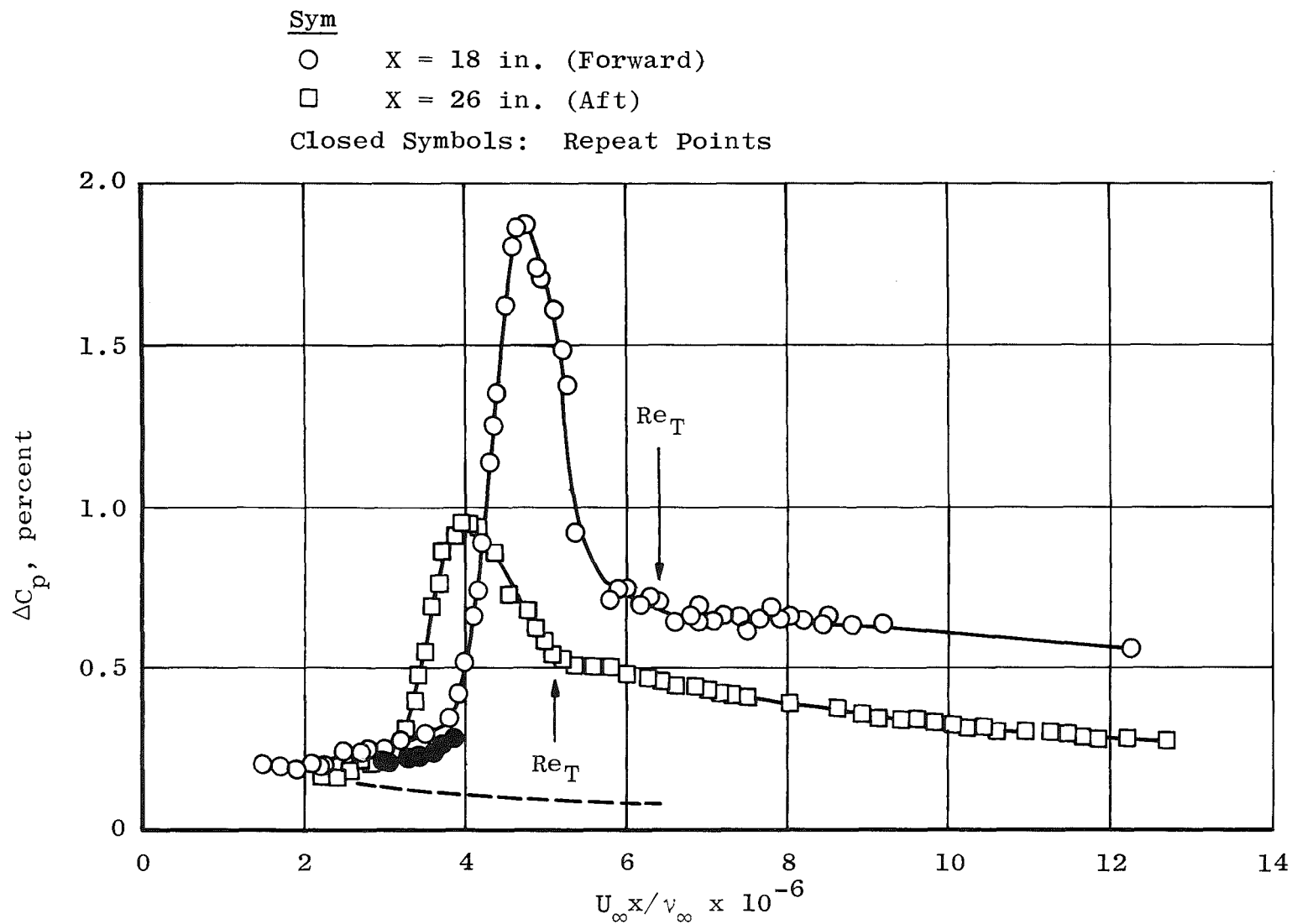


Figure 109. Noise levels as a function of U_∞/ν_∞ at $M_\infty = 4.0$ in the RAE Bedford 3 x 4 HSST.

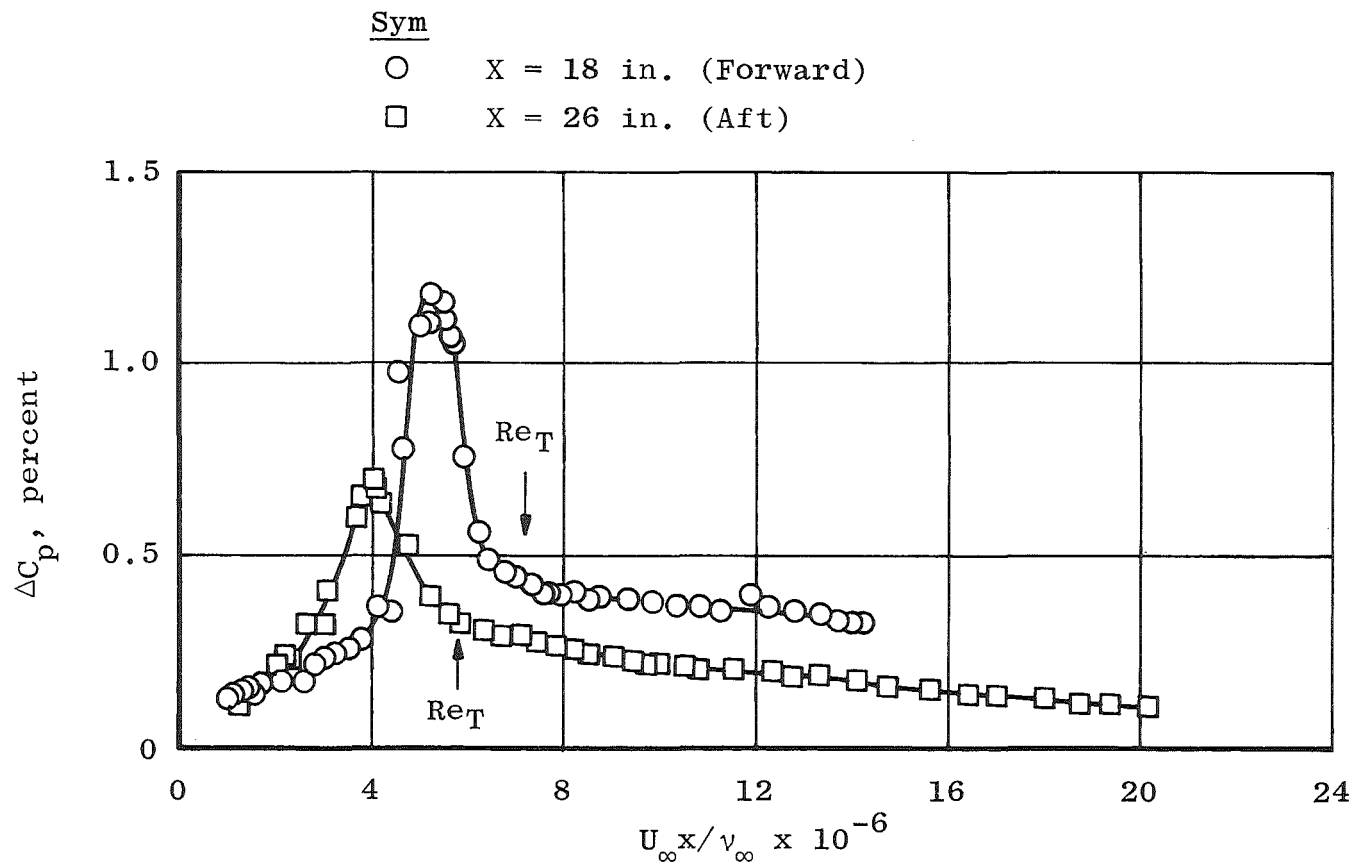


Figure 110. Noise levels as a function of U_∞/ν_∞ at $M_\infty = 4.5$ in the RAE Bedford 3 x 4 HSST.

3.3.4 Group 4 Tunnels: Supersonic, Sliding Block Nozzle

NASA/Ames 9 x 7 SWT

Both transition and noise data were acquired in this tunnel, the traversing pitot probe being used for detection of transition. Data were acquired over the full Mach number range from 1.5 to 2.5. A photograph of the model installation is shown in Fig. 111.

End, Re_T , and onset, Re_t , of transition Reynolds numbers are shown as a function of U_∞/ν_∞ at $M_\infty = 1.5, 1.6, 1.7, 1.8, 2.0, 2.2$, and 2.5 in Figs. 112 through 118. A smoothed envelope of the end-of-transition results at varied U_∞/ν_∞ is shown as a function of M_∞ in Fig. 119.

Noise measurements in the form of ΔC_p versus U_∞/ν_∞ are presented in Fig. 120. All of the data are presented in Table 14.

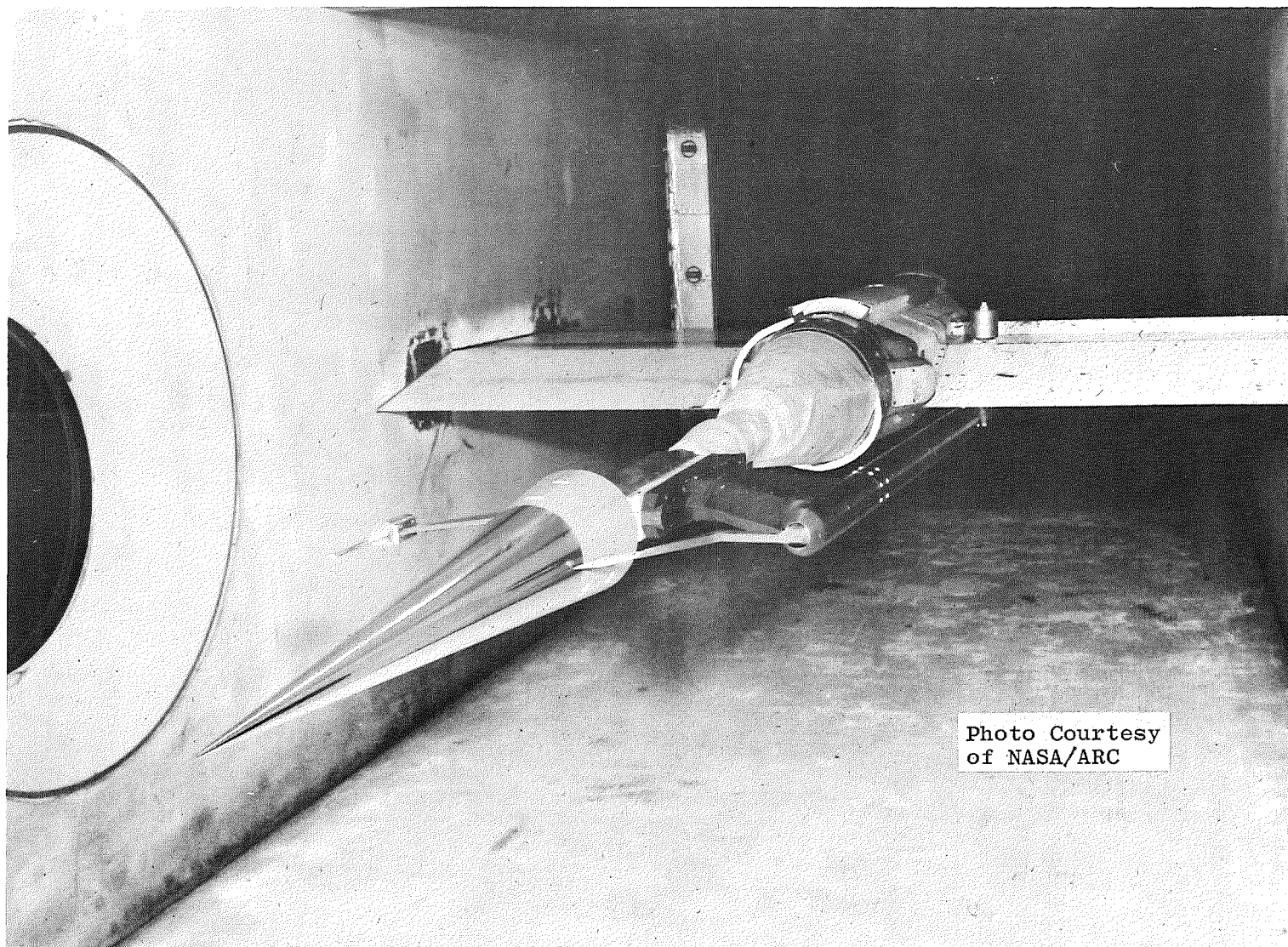


Photo Courtesy
of NASA/ARC

Figure 111. Photograph of the cone installation in the NASA/Ames 9 x 7 SWT.

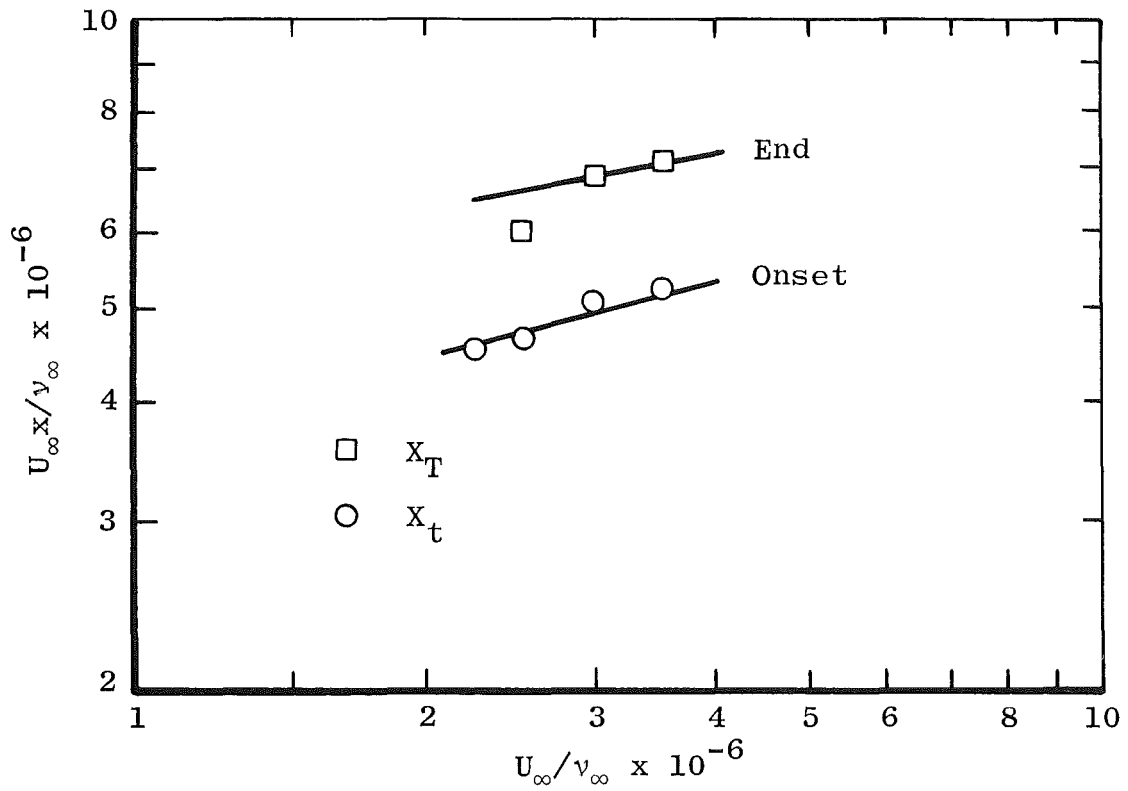


Figure 112. Transition Reynolds numbers at $M_\infty = 1.5$ in the NASA/Ames 9 x 7 SWT.

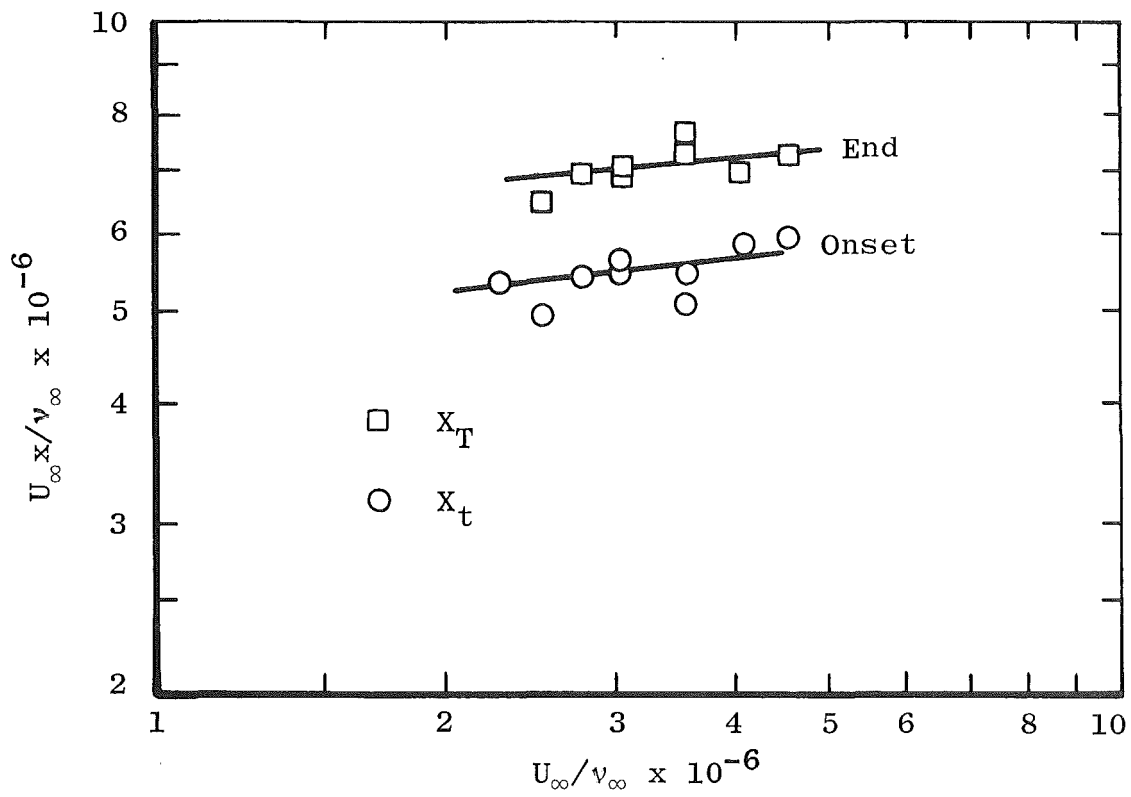


Figure 113. Transition Reynolds numbers at $M_\infty = 1.6$ in the NASA/Ames 9 x 7 SWT.

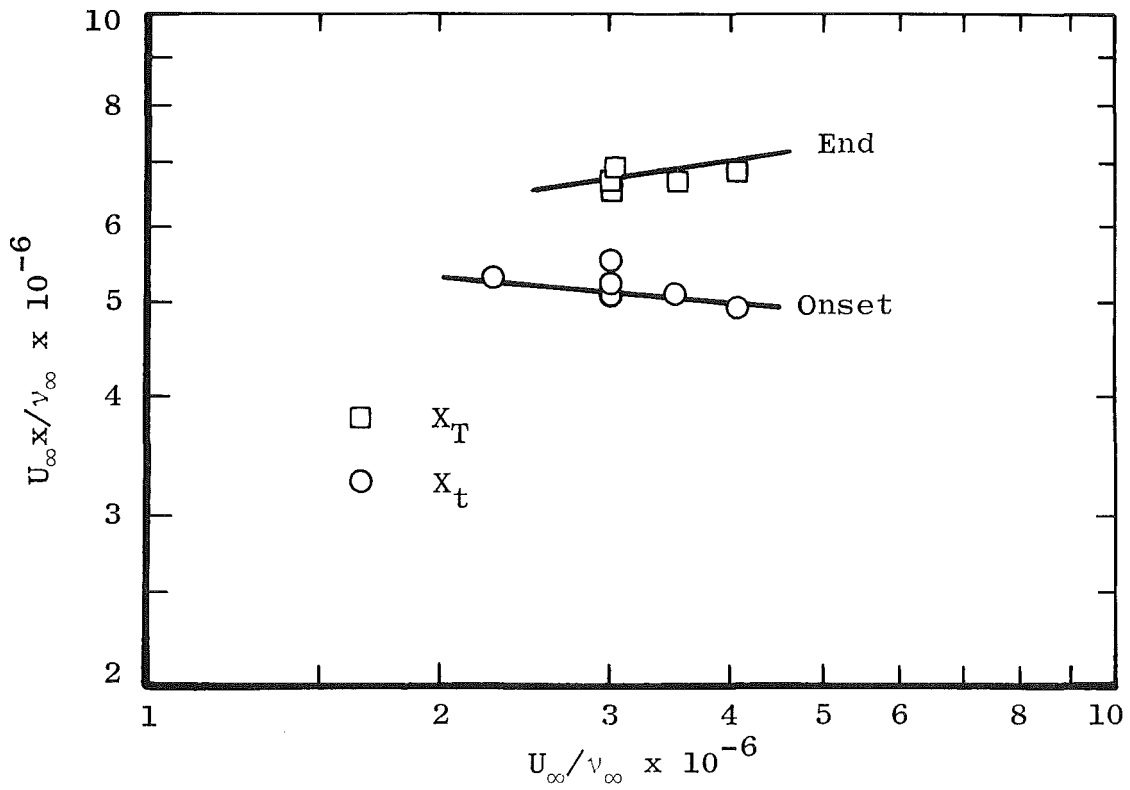


Figure 114. Transition Reynolds numbers at $M_\infty = 1.7$ in the NASA/Ames 9 x 7 SWT.

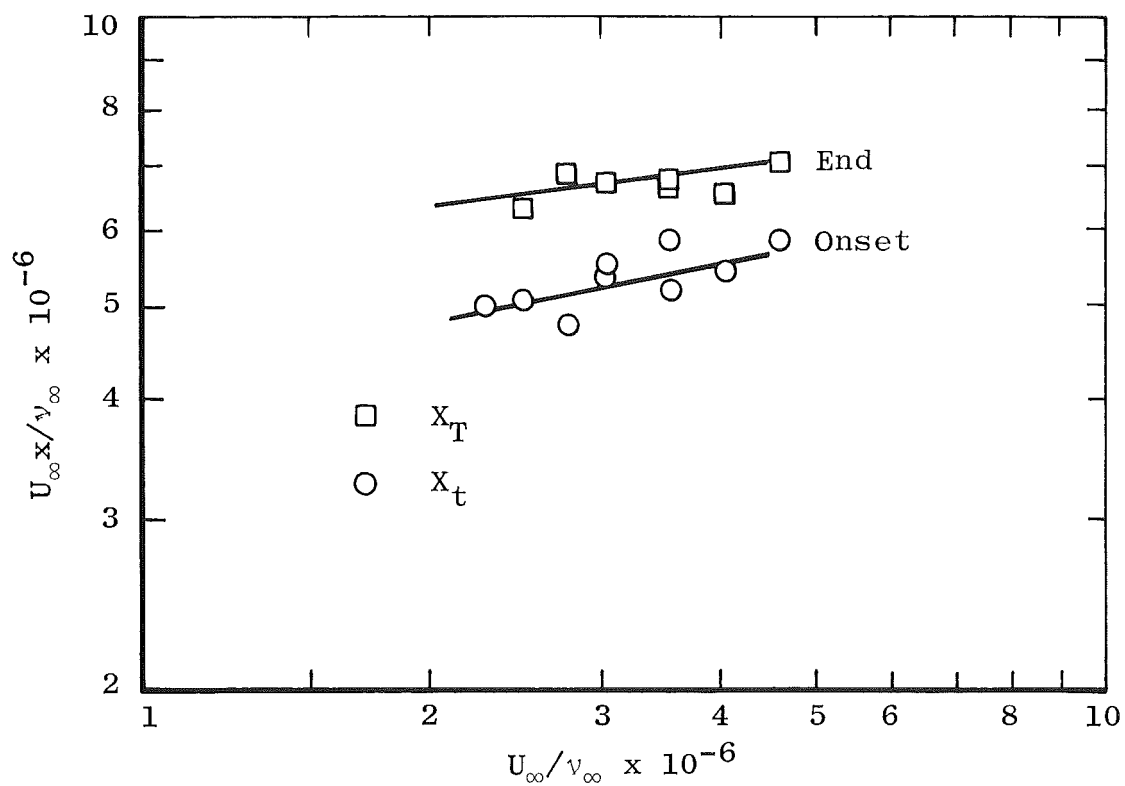


Figure 115. Transition Reynolds numbers at $M_\infty = 1.8$ in the NASA/Ames 9 x 7 SWT.

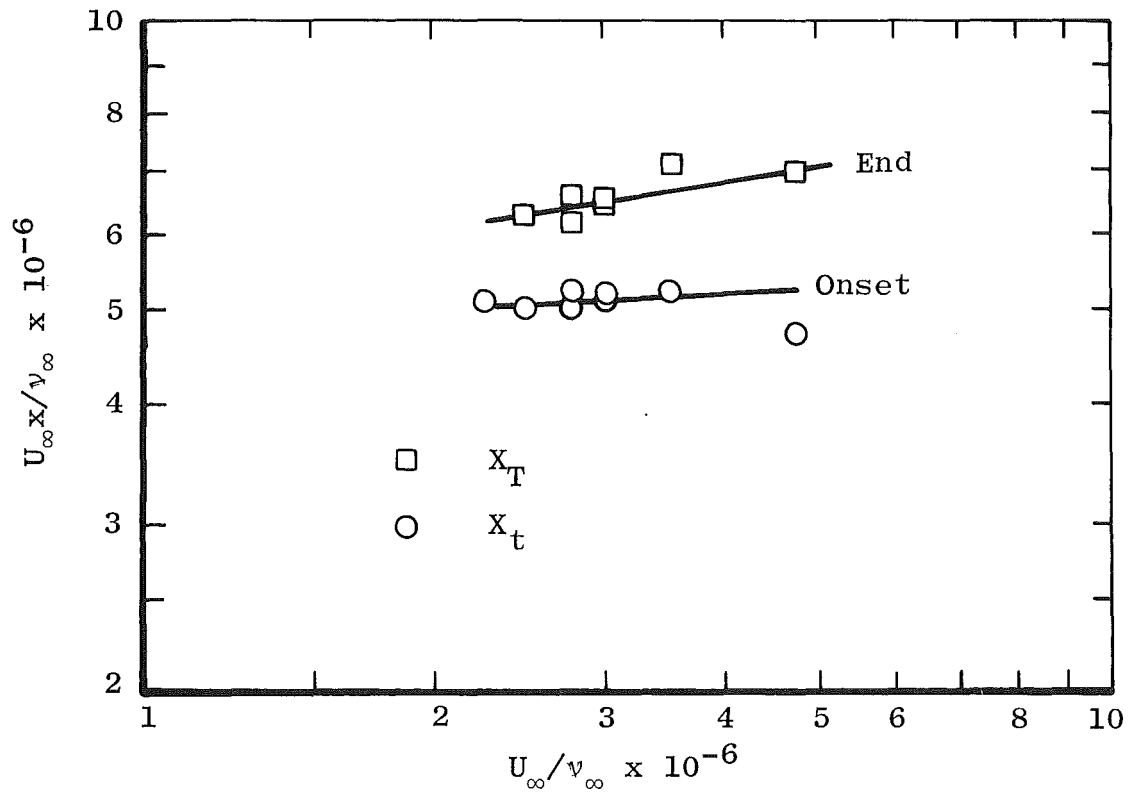


Figure 116. Transition Reynolds numbers at $M_\infty = 2.0$ in the NASA/Ames 9 x 7 SWT.

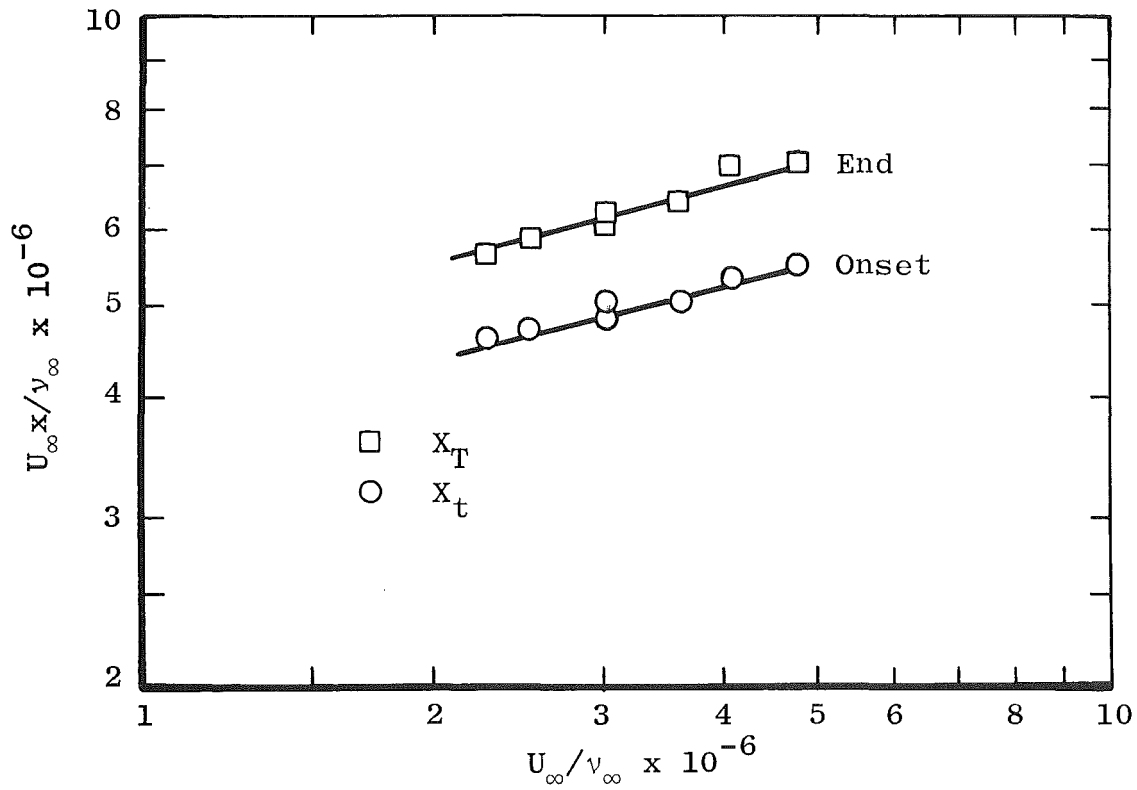


Figure 117. Transition Reynolds numbers at $M_\infty = 2.2$ in the NASA/Ames 9 x 7 SWT.

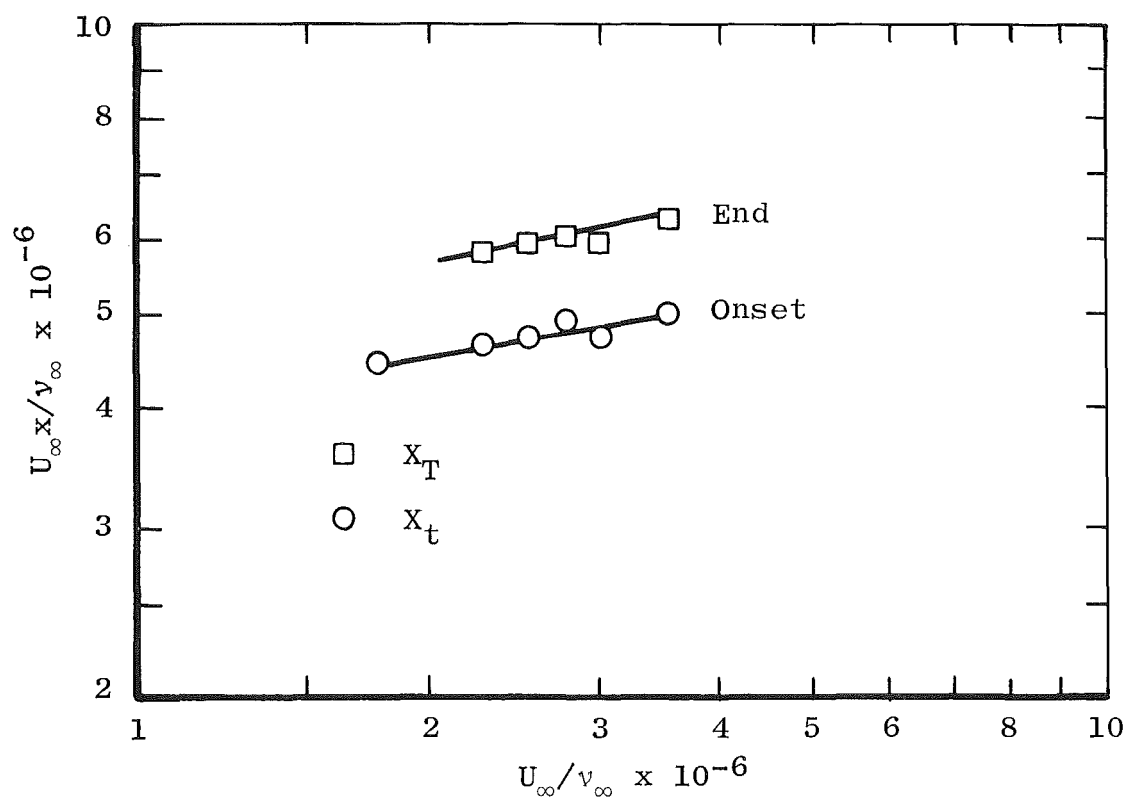


Figure 118. Transition Reynolds numbers at $M_\infty = 2.5$ in the NASA/Ames 9 x 7 SWT.

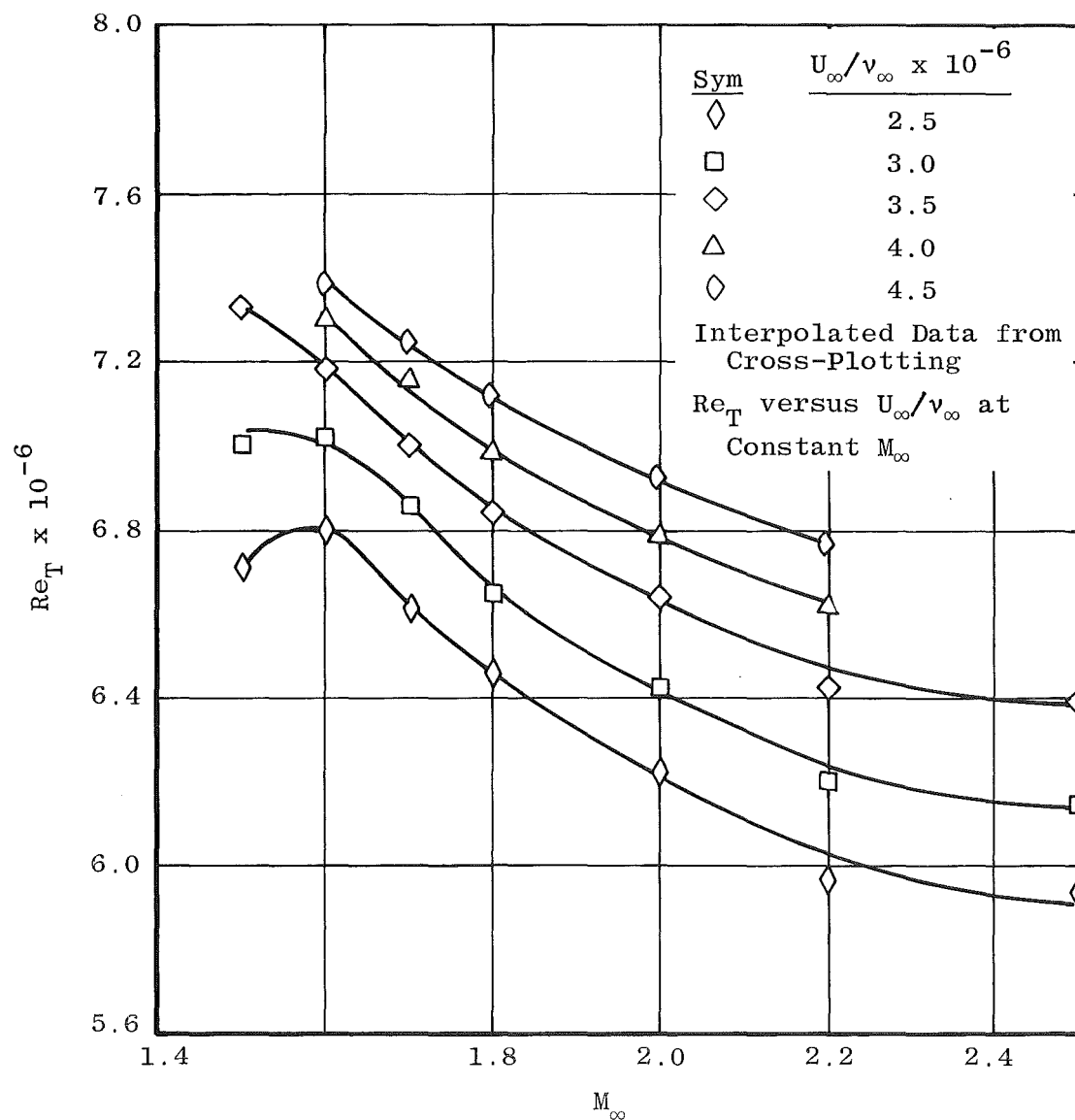
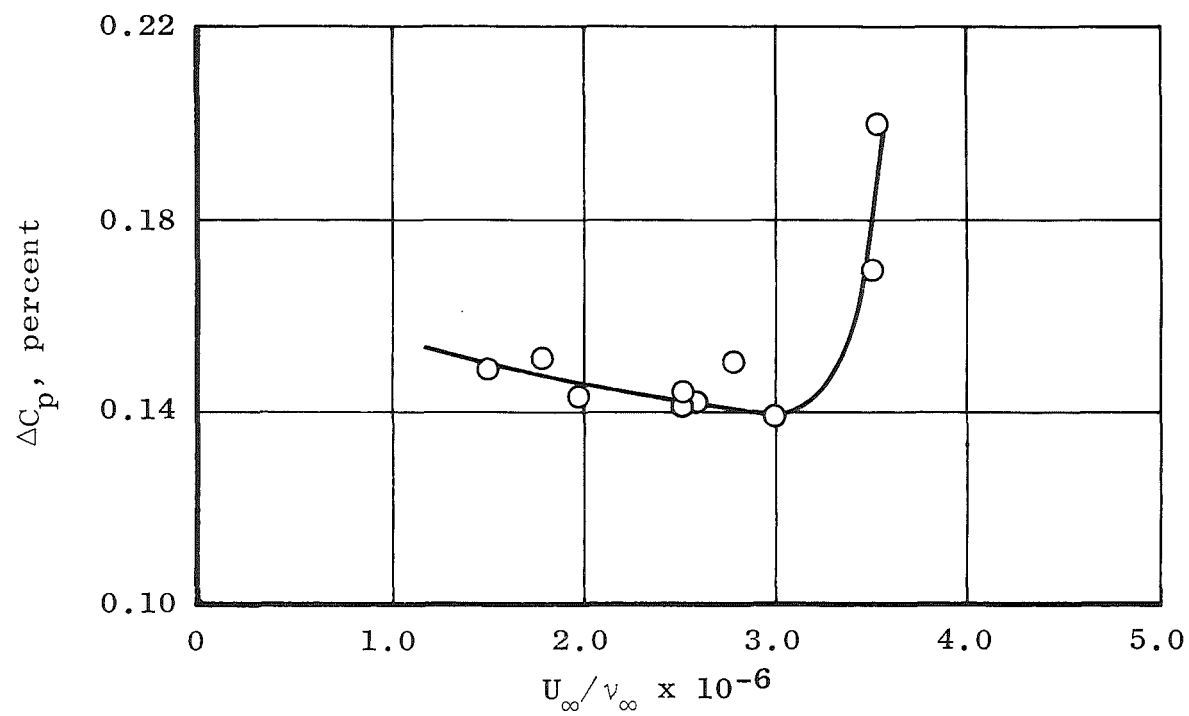
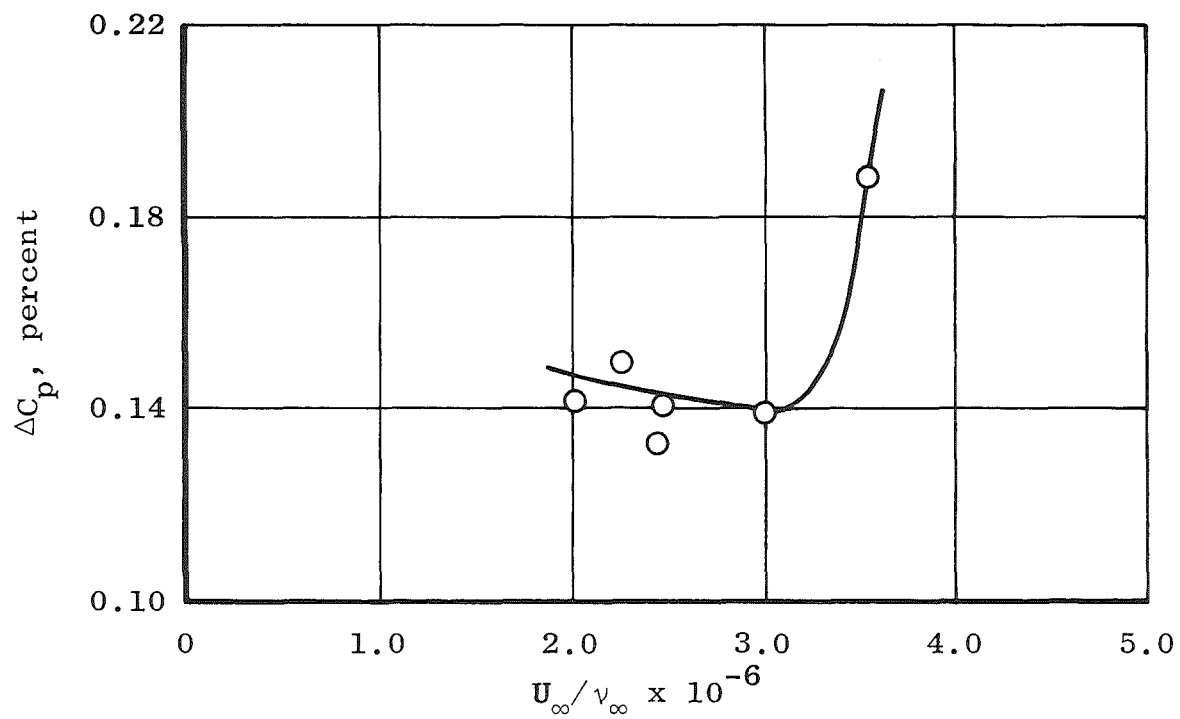


Figure 119. Composite envelope of end-of-transition Reynolds numbers in the NASA/Ames 9 x 7 SWT.



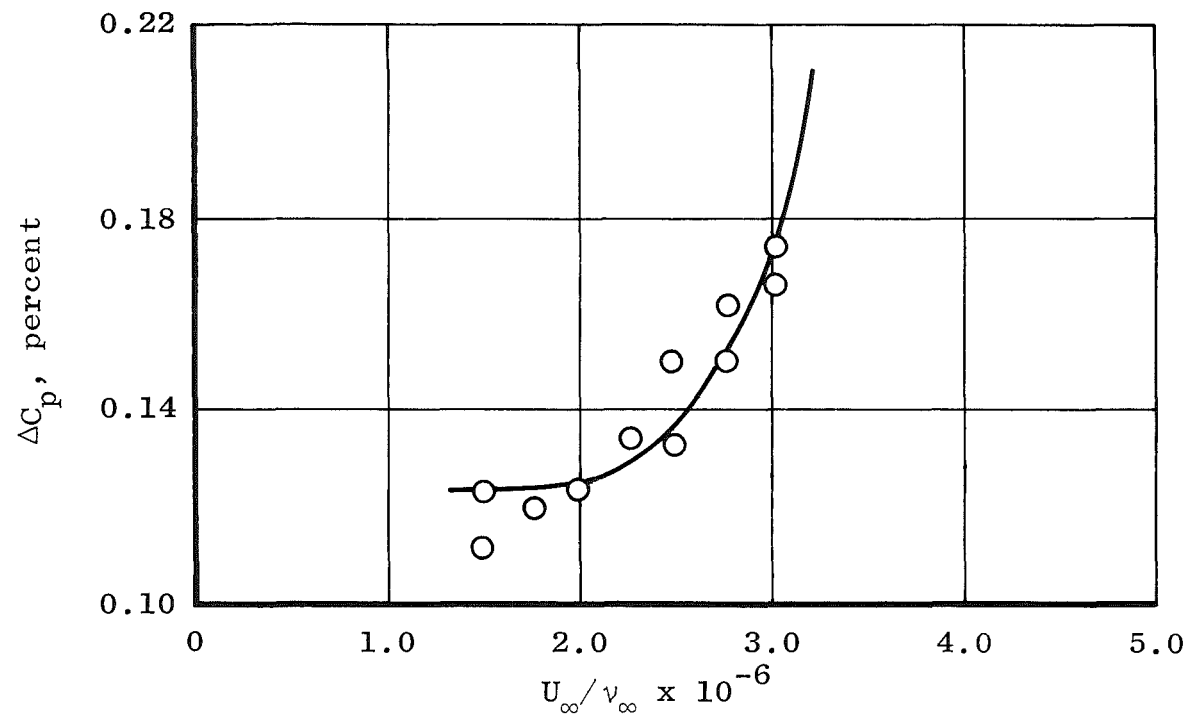
a. $M_\infty = 1.6$

Figure 120. Noise levels in the NASA/Ames 9 x 7 SWT.

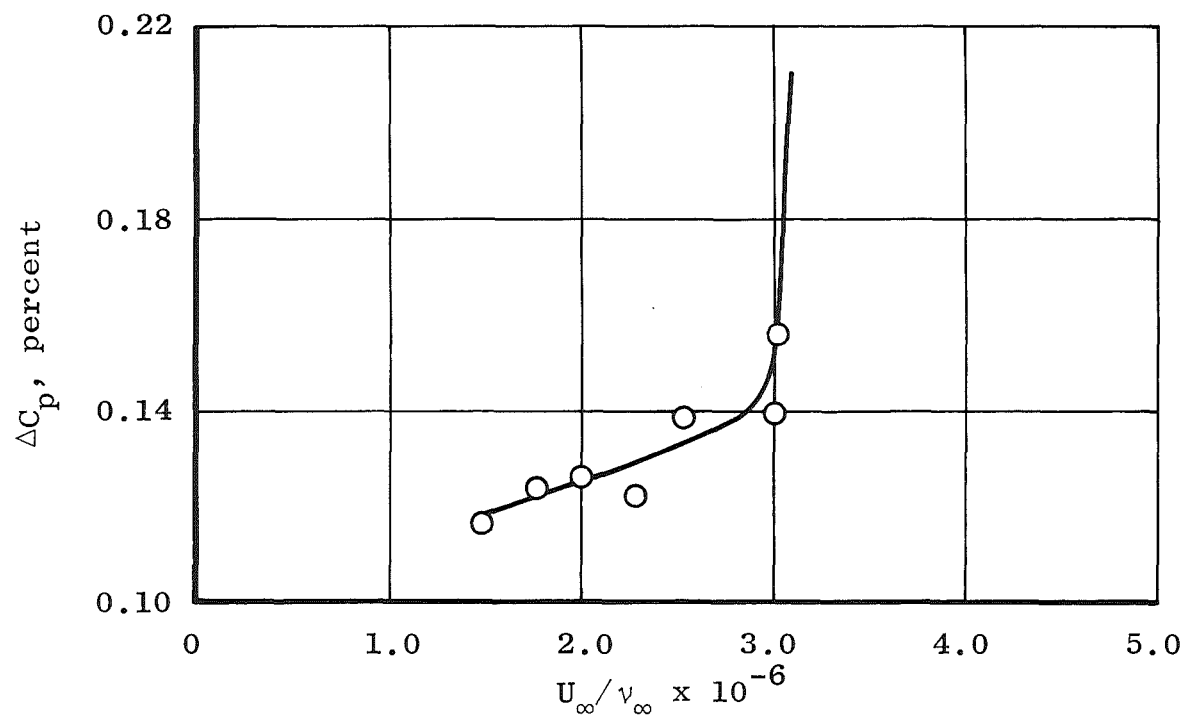


b. $M_\infty = 1.8$

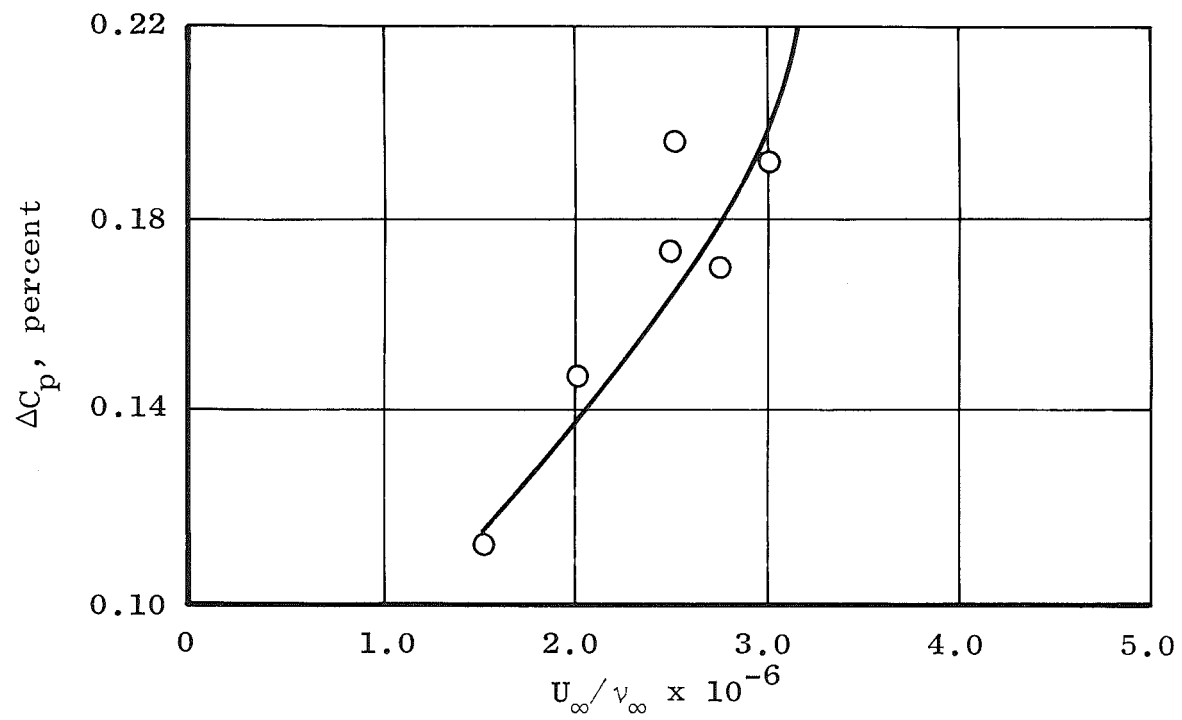
Figure 120. Continued.



c. $M_{\infty} = 2.0$
Figure 120. Continued.



d. $M_\infty = 2.2$
Figure 120. Continued.



e. $M_\infty = 2.50$

Figure 120. Concluded

Table 14. NASA/Ames 9 x 7 SWT Data

M_∞	U_∞ / v_∞ $\times 10^{-6}$	ΔC_p , percent	$Re_t \times$ 10^{-6}	$Re_T \times$ 10^{-6}
1.500	2.252	-	4.504	-
1.505	2.509	-	4.642	5.890
1.500	2.989	-	5.056	6.849
1.505	3.521	-	5.252	7.042
1.602	2.259	-	5.346	-
1.603	2.512	0.143	4.940	6.468
1.603	2.760	0.150	5.474	6.992
1.603	3.010	0.138	5.418	6.848
1.603	3.018	-	5.430	6.890
1.603	3.035	-	5.680	7.000
1.603	3.519	0.169	5.044	7.331
1.602	3.519	0.190	5.425	7.654
1.602	4.039	-	5.857	6.967
1.602	4.507	-	5.972	7.286
1.703	2.256	-	5.302	-
1.703	3.022	-	5.112	6.623
1.703	3.025	-	5.243	6.705
1.703	3.033	-	5.552	6.920
1.703	3.524	-	5.110	6.725
1.703	4.040	-	4.969	6.848
1.799	2.256	0.149	4.926	-
1.802	2.473	0.132	5.090	6.306
1.801	2.751	-	4.745	6.809
1.802	3.020	0.138	5.335	6.644
1.799	3.022	0.138	5.170	6.660
1.800	3.022	-	5.510	6.750
1.799	3.022	-	5.380	6.780
1.802	3.513	0.188	5.182	6.792
1.802	3.528	-	4.880	6.615
1.800	4.023	-	5.430	6.537
1.799	4.580	-	5.840	7.061
1.900	2.256	-	5.132	-
1.974	2.259	0.134	5.102	-
1.993	2.485	0.150	5.011	6.275
1.994	2.767	0.150	5.027	6.134
1.993	2.771	0.162	5.242	6.604
1.994	3.027	0.166	5.125	6.540
1.994	3.034	0.174	5.208	6.447
1.993	3.036	-	5.161	6.401
1.993	3.500	-	5.220	7.058
1.993	4.732	-	5.442	6.980

Table 14. Concluded

M_∞	U_∞ / v_∞ $\times 10^{-6}$	ΔC_p , percent	$Re_t \times$ 10^{-6}	$Re_T \times$ 10^{-6}
2.200	2.265	0.122	4.624	5.681
2.197	2.501	0.138	4.710	5.857
2.201	3.011	-	4.818	6.223
2.201	3.022	0.139	5.040	6.060
2.200	3.031	0.156	5.077	6.188
2.201	3.583	-	5.076	6.420
2.200	4.049	-	5.365	6.985
2.200	4.751	-	5.543	7.047
2.496	1.763	-	4.481	-
2.496	2.273	-	4.698	5.815
2.496	2.518	0.173	4.721	5.959
2.495	2.757	0.170	4.963	6.019
2.495	3.002	0.192	4.750	5.930
2.496	3.532	-	5.004	6.299

NASA/Langley 4 SUPWT (TS No. 1)

Data were acquired in the low Mach number test section of the NASA/Langley 4 SUPWT (TS No. 1) at $M_\infty = 1.6$, 2.0, and 2.86. A photograph of the cone installation is shown in Fig. 121. Both transition and noise measurements were made; however, the extent of the transition zone was so great at both $M_\infty = 1.6$ and 2.86 that the data at all U_∞/ν_∞ levels had either transitional or turbulent influences. Only at $M_\infty = 2.0$ were sufficient cone forward microphone data acquired to make any projection of estimated background noise level in the tunnel.

End, Re_T , and onset, Re_t , of transition Reynolds numbers are shown for $M_\infty = 1.6$, 2.0, and 2.86 in Figs. 122, 123, and 124, respectively. Noise levels in the form of ΔC_p versus U_∞/ν_∞ are presented for $M_\infty = 1.6$, 2.0, and 2.86 in Figs. 125, 126, and 127, respectively. The data are presented in Table 15.



Figure 121. Photograph of the cone installation in the NASA/Langley 4 SUPWT (TS No. 1).

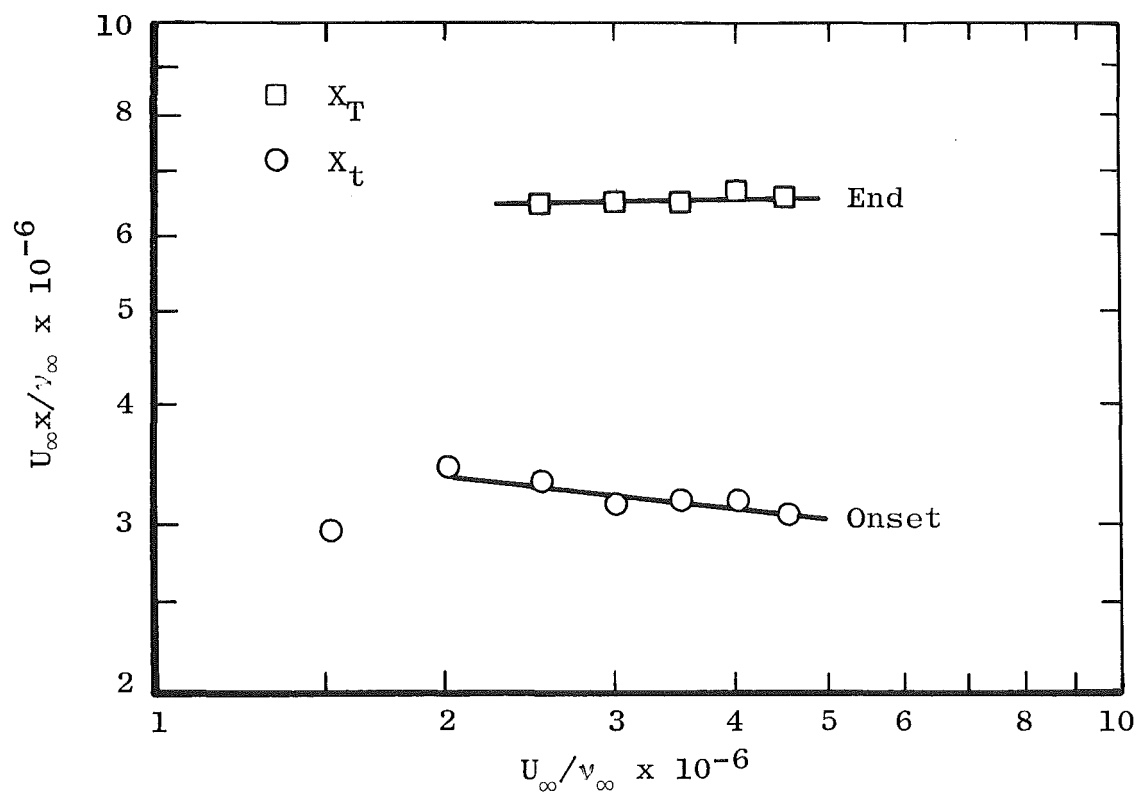


Figure 122. Transition Reynolds numbers at $M_\infty = 1.6$ in the NASA/Langley 4 SUPWT (TS No. 1).

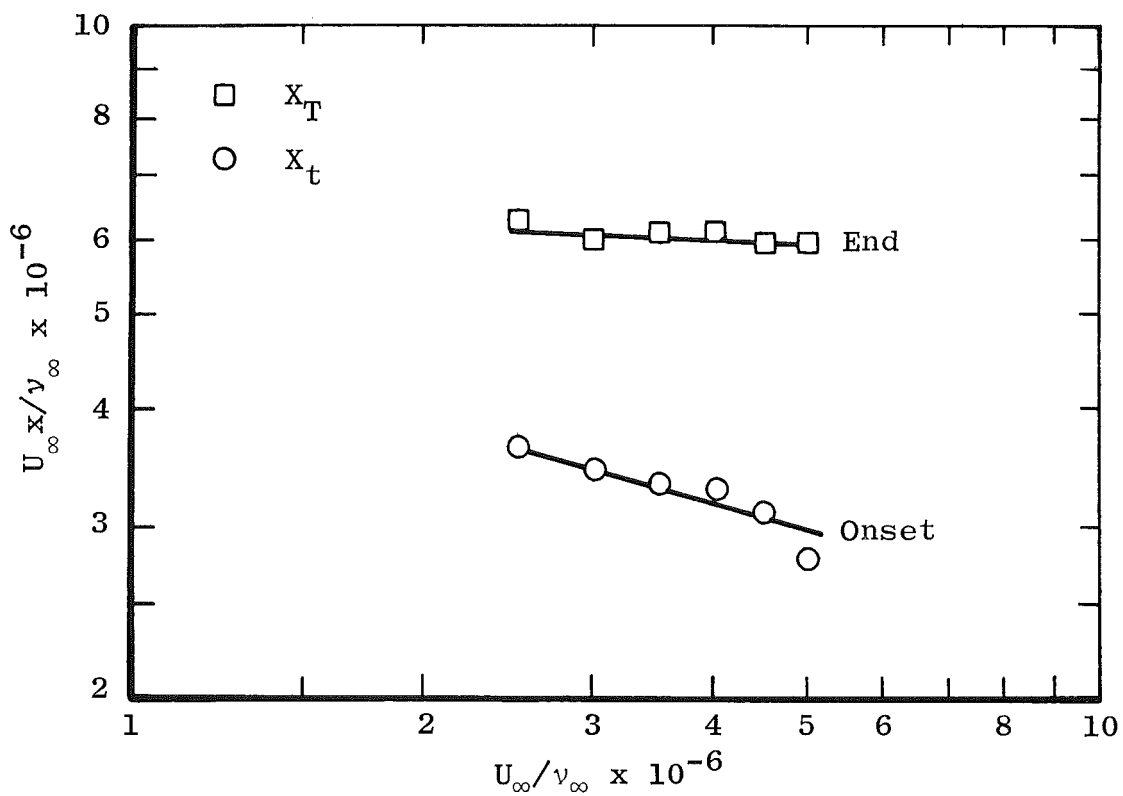


Figure 123. Transition Reynolds numbers at $M_\infty = 2.0$ in the NASA/Langley 4 SUPWT (TS No. 1).

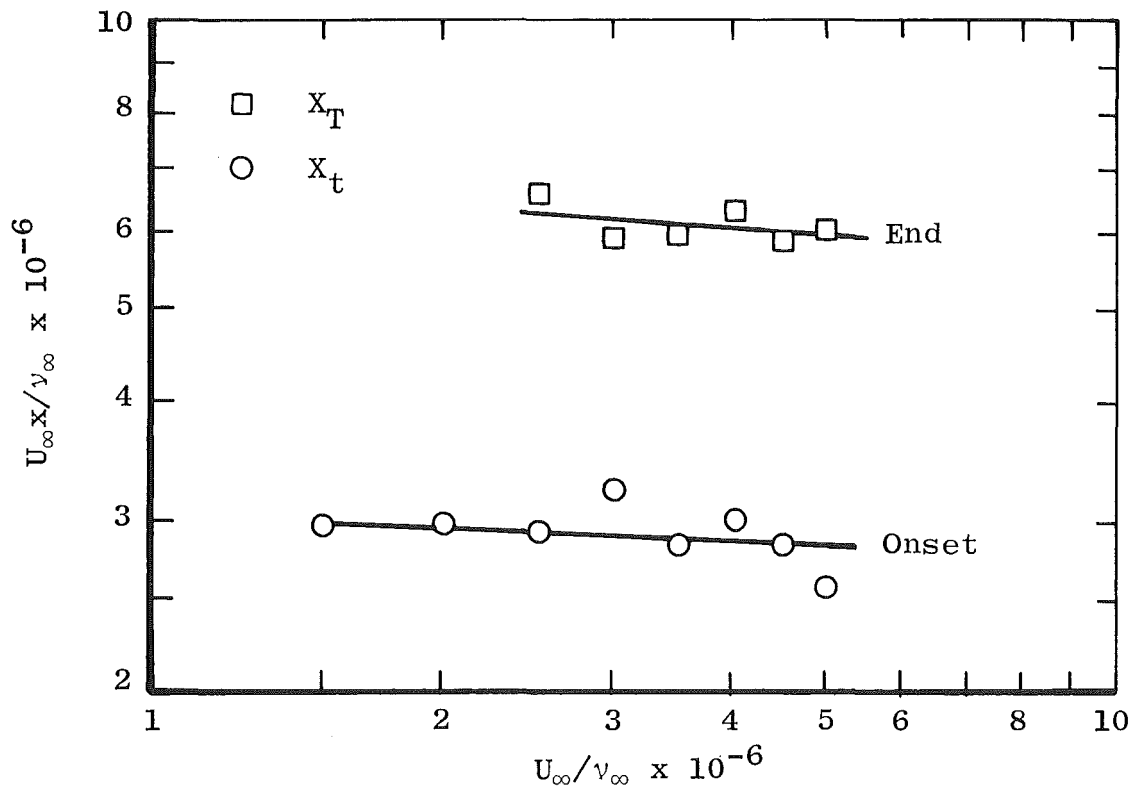


Figure 124. Transition Reynolds numbers at $M_\infty = 2.86$ in the NASA/Langley 4 SUPWT (TS No. 1).

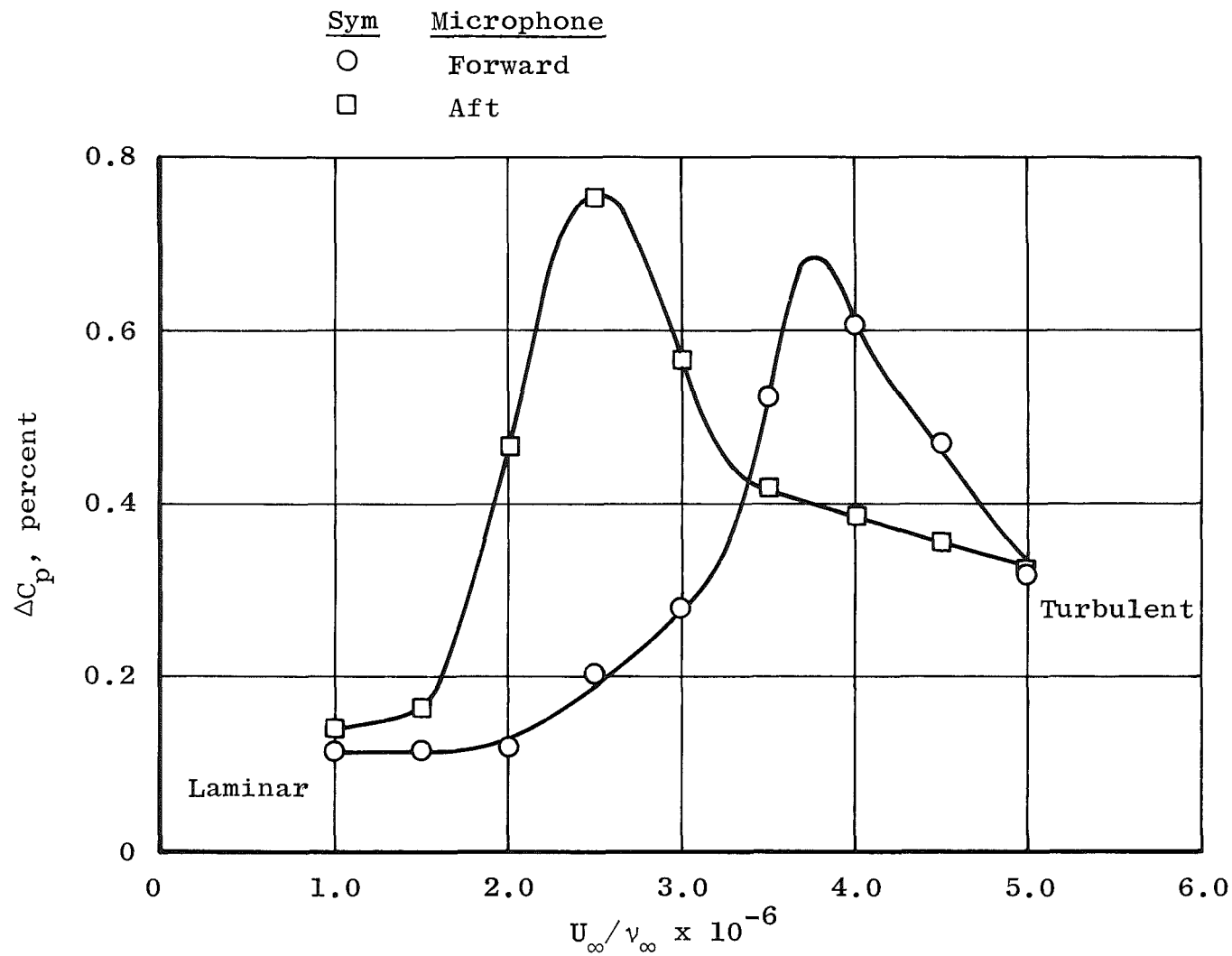


Figure 125. Noise Levels at $M_\infty = 1.6$ in the NASA/Langley 4 SUPWT (TS No. 1).

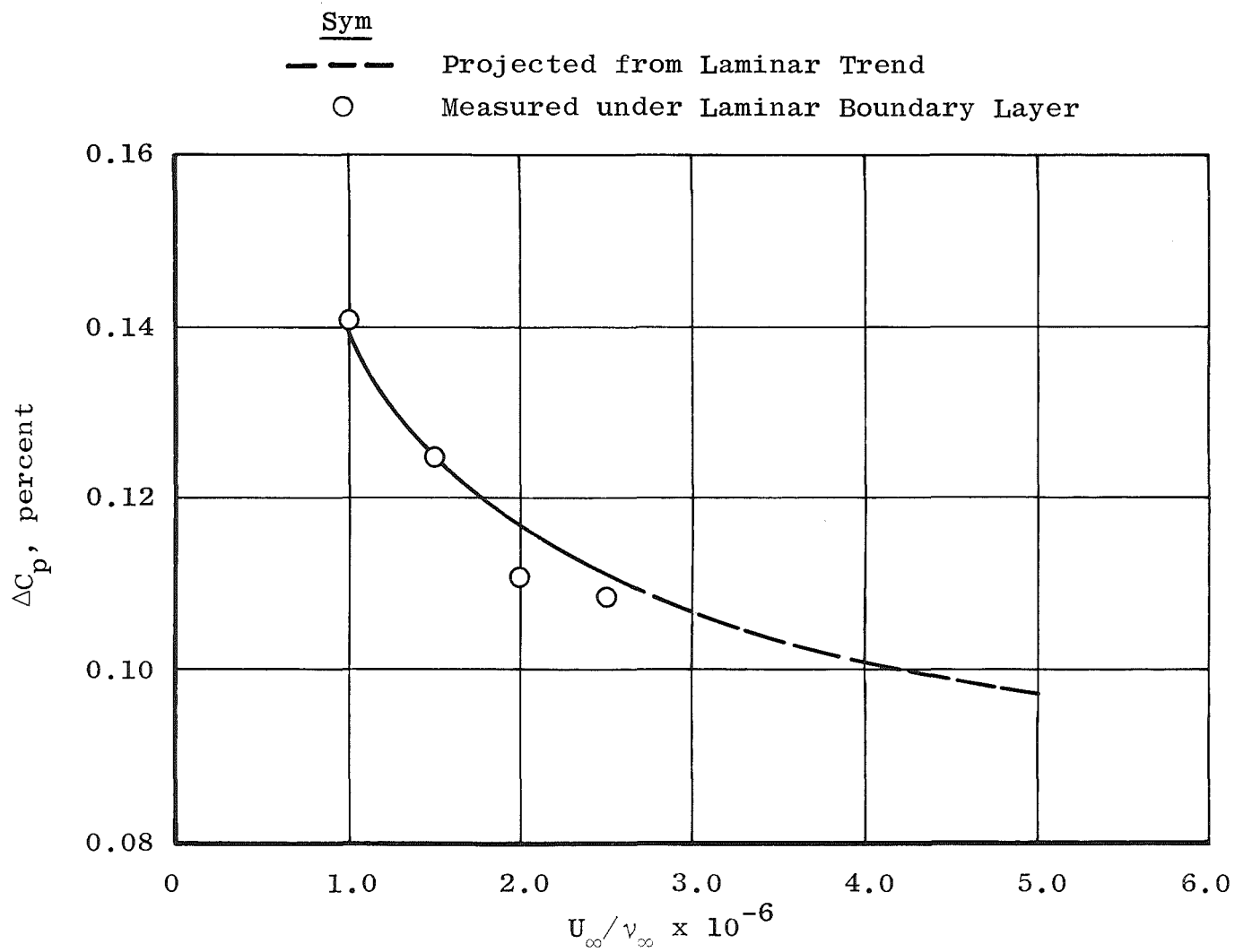


Figure 126. Noise levels at $M_\infty = 2.0$ in the NASA/Langley 4 SUPWT (TS No. 1).

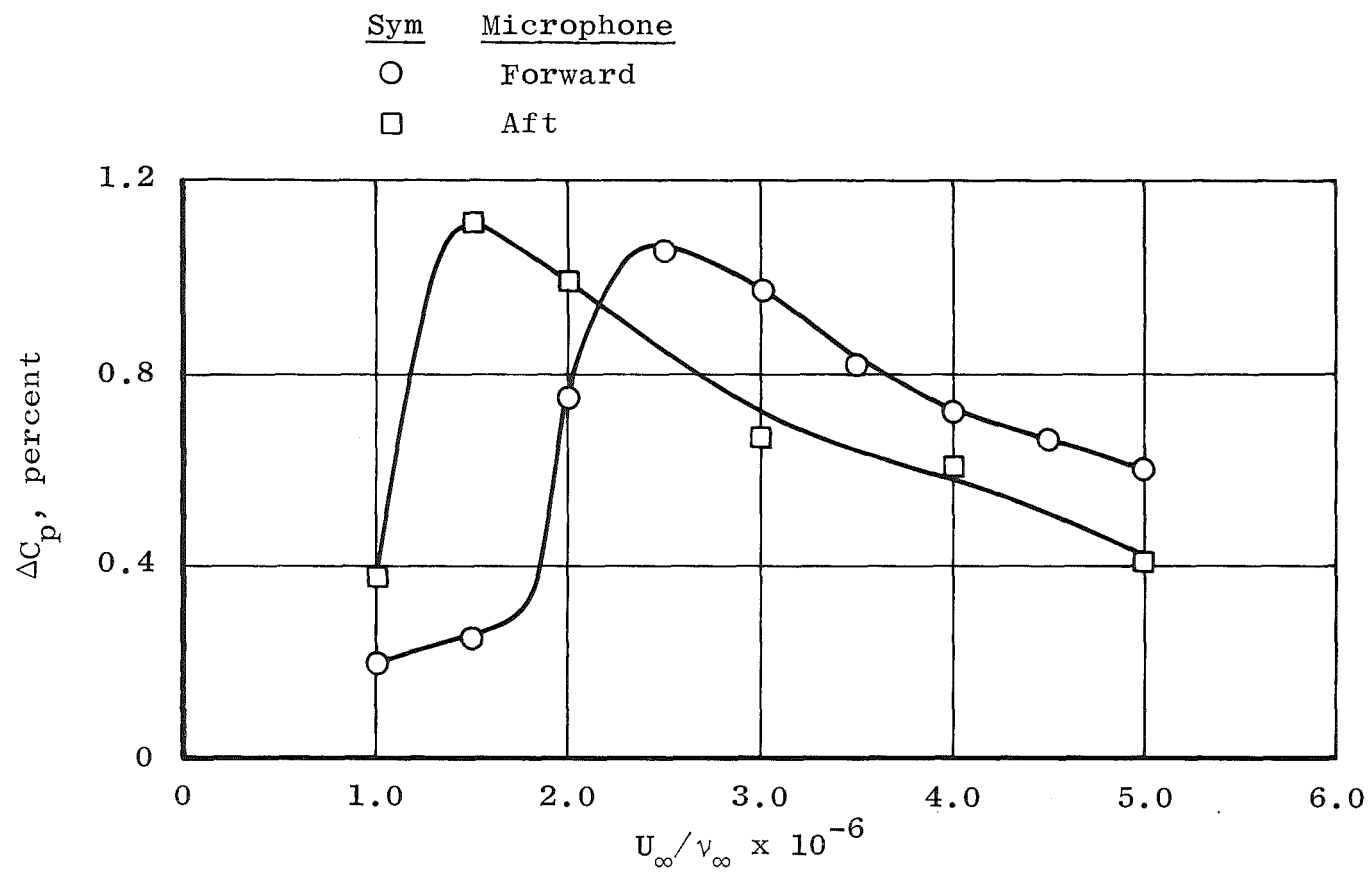


Figure 127. Noise levels at $M_\infty = 2.86$ in the NASA/Langley 4 SUPWT (TS No. 1).

Table 15. NASA/Langley 4 SUPWT (TS No. 1) Data

M_∞	U_∞ / ν_∞ $\times 10^{-6}$	ΔC_p , percent	$Re_t \times$ 10^{-6}	$Re_T \times$ 10^{-6}
1.60 ↓	1.501	0.11	2.97	-
	2.003	0.12	3.42	-
	2.504	-	3.34	6.47
	3.004	-	3.15	6.50
	3.503	-	3.18	6.50
	4.001	-	3.17	6.70
	4.503	-	3.07	6.60
2.00 ↓	1.003	0.140	3.71	-
	1.502	0.129	3.17	-
	2.001	0.111	3.67	-
	2.503	0.108	3.63	6.21
	3.003	-	3.45	6.00
	3.504	-	3.33	6.04
	4.005	-	3.30	6.13
	4.505	-	3.11	5.92
2.86 ↓	5.006	-	2.79	5.96
	1.504	-	2.97	-
	2.001	-	2.98	-
	2.509	-	2.93	6.63
	3.008	-	3.26	5.94
	3.511	-	2.84	6.00
	4.008	-	3.01	6.38
	4.510	-	2.86	5.90
	4.979	-	2.57	6.02

NASA/Langley 4 SUPWT (TS No. 2)

Data were taken in the NASA/Langley 4 SUPWT (TS No. 2) in the same manner as in TS No. 1. The extent of the transition zone appeared to be so large that virtually all of the noise measurements appeared to have either transitional or turbulent boundary-layer influence over the full range of U_∞/ν_∞ .

End, Re_T , and onset, Re_t , of transition Reynolds numbers are presented as a function of U_∞/ν_∞ for $M_\infty = 2.86$, 3.51, and 4.6 in Figs. 128, 129, and 130, respectively. The noise data in the form of ΔC_p versus U_∞/ν_∞ are presented for $M_\infty = 2.86$, 3.51, and 4.6 in Figs. 131, 132, and 133, respectively. The data are tabulated in Table 16.

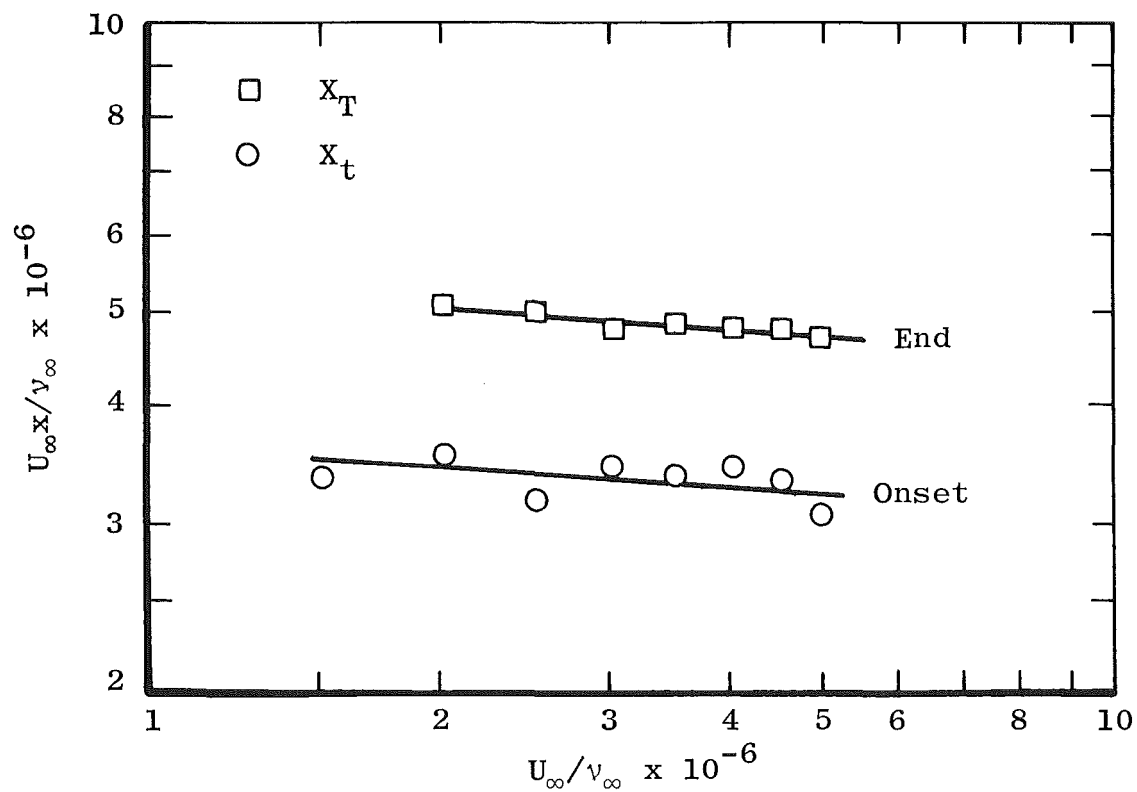


Figure 128. Transition Reynolds numbers at $M_\infty = 2.86$ in the NASA/Langley 4 SUPWT (TS No. 2).

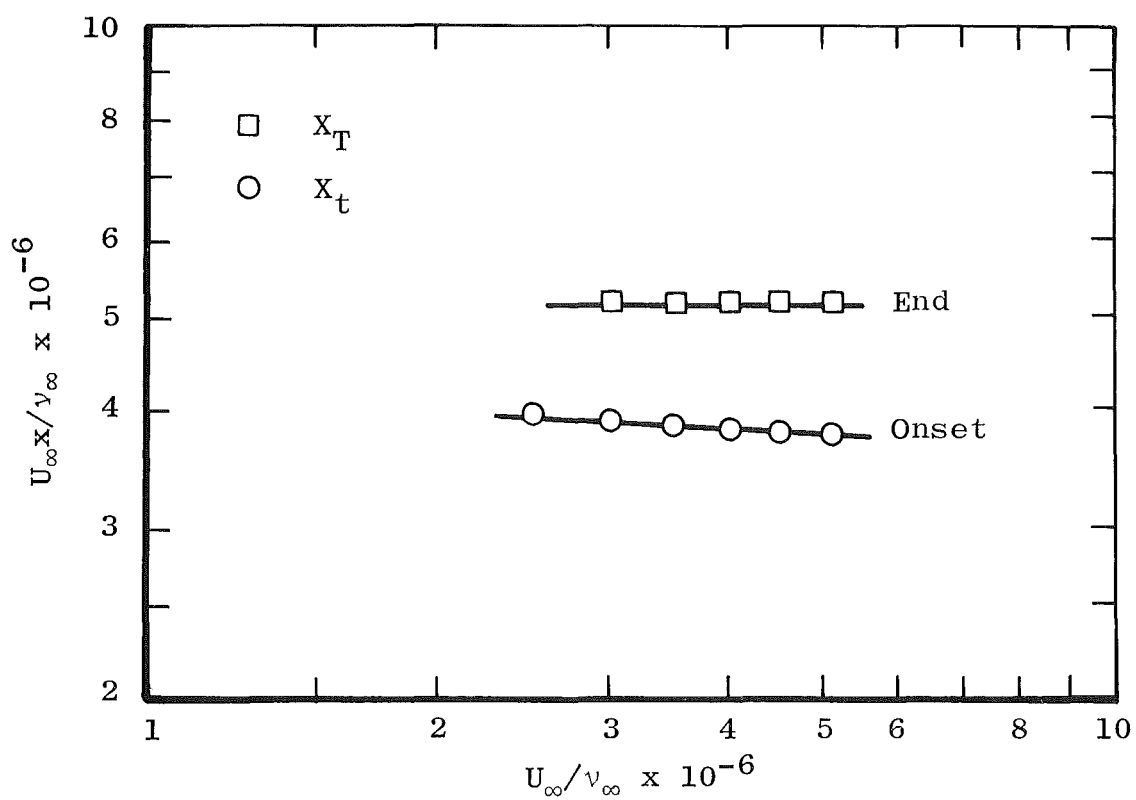


Figure 129. Transition Reynolds numbers at $M_\infty = 3.5$ in the NASA/Langley 4 SUPWT (TS No. 2).

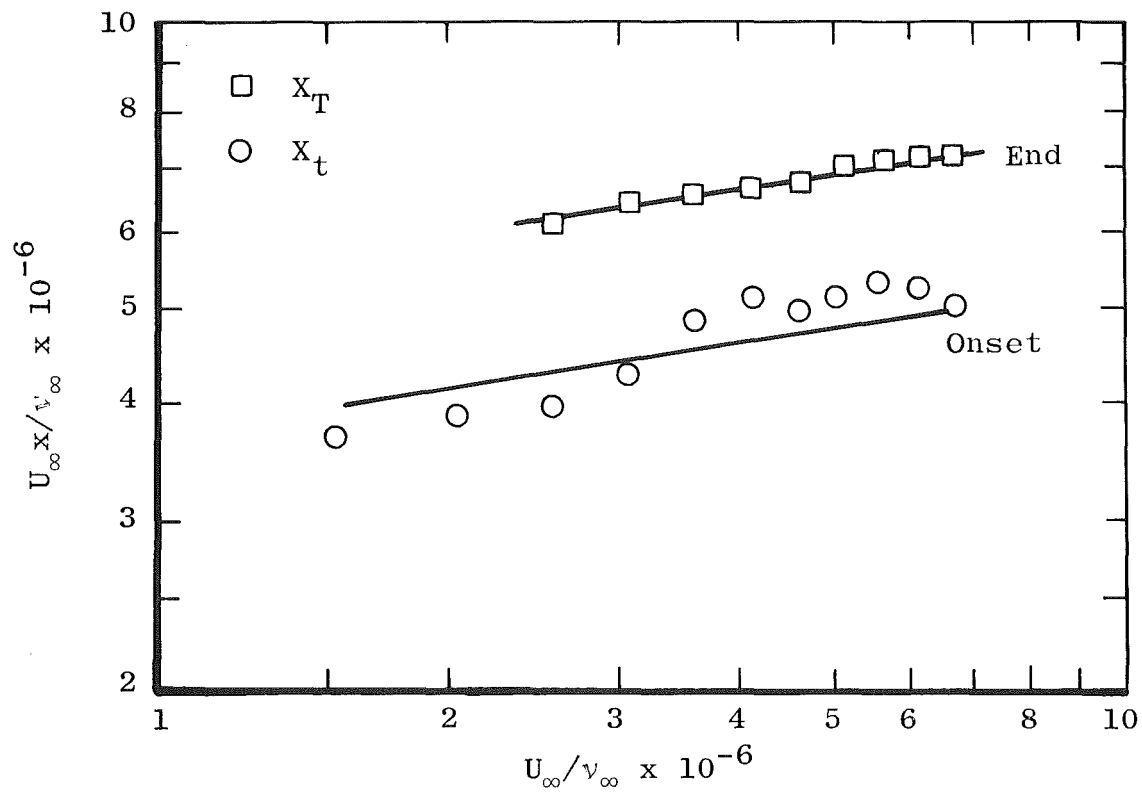


Figure 130. Transition Reynolds numbers at $M_{\infty} = 4.6$ in the NASA/Langley 4 SUPWT (TS No. 2).

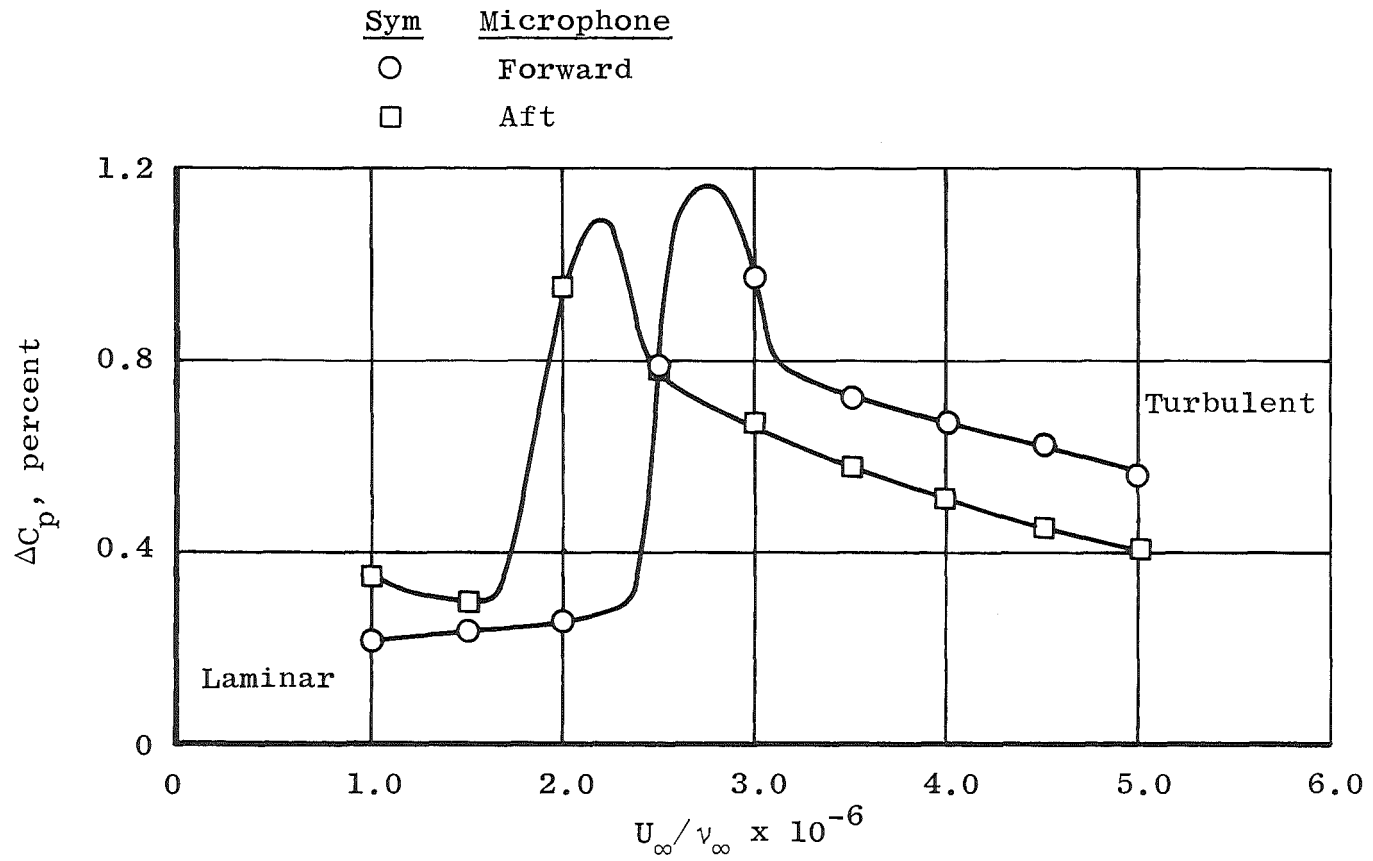


Figure 131. Noise levels at $M_{\infty} = 2.86$ in the NASA/Langley 4 SUPWT (TS No. 2).

240

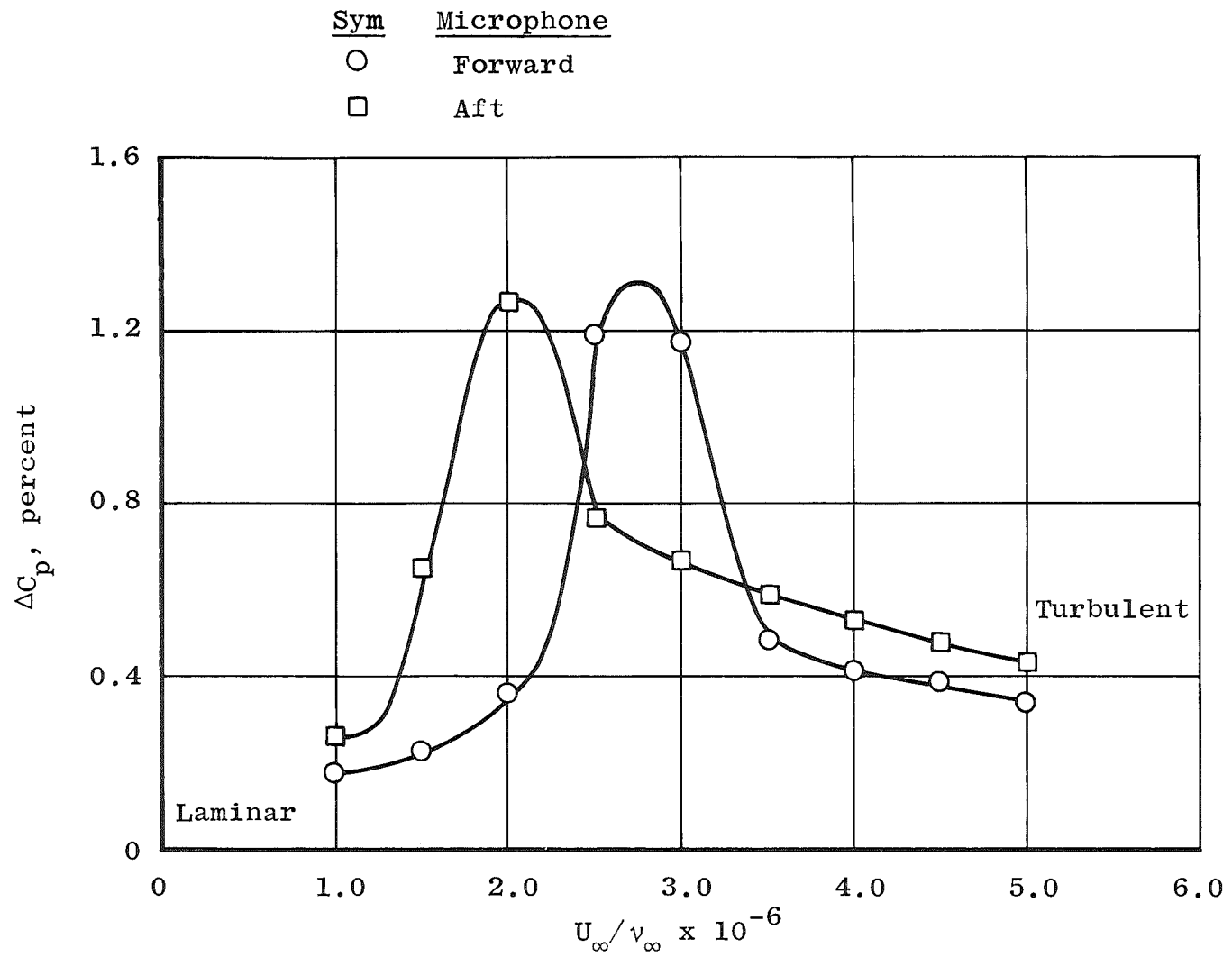


Figure 132. Noise levels at M_∞ = 3.5 in the NASA/Langley 4 SUPWT (TS No. 2).

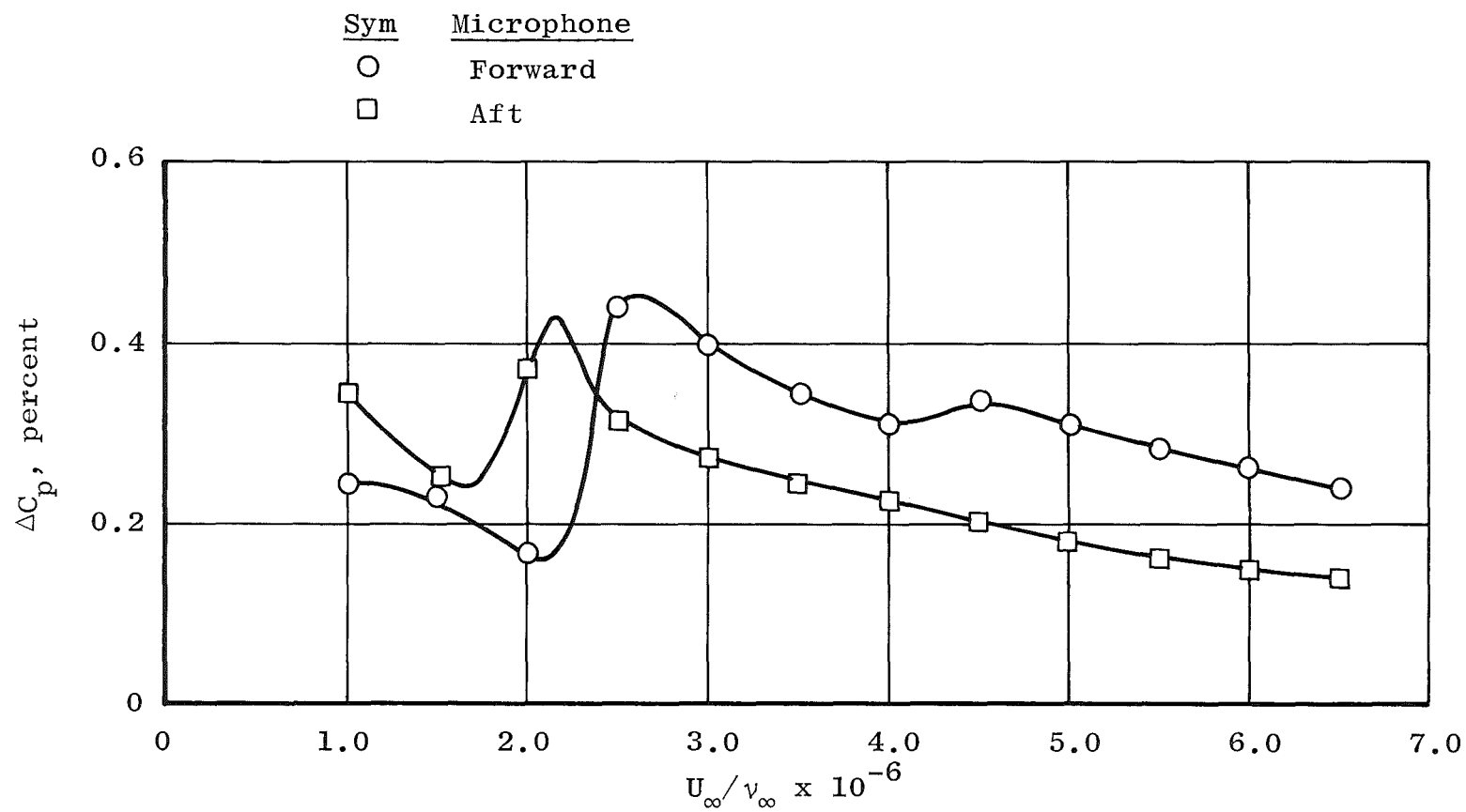


Figure 133. Noise levels at $M_\infty = 4.6$ in the NASA/Langley 4 SUPWT (TS No. 2).

Table 16. NASA/Langley 4 SUPWT (TS No. 2) Data

M_∞	U_∞ / v_∞ $\times 10^{-6}$	ΔC_p , percent	$Re_t \times$ 10^{-6}	$Re_T \times$ 10^{-6}
2.86 ↓	1.503	0.22	3.33	-
	2.004	0.25	3.52	5.06
	2.506	-	3.17	4.97
	3.004	-	3.43	4.78
	3.505	-	3.36	4.82
	4.007	-	3.44	4.78
	4.506	-	3.34	4.77
	4.975	-	3.07	4.68
3.51 ↓	1.501	0.22	-	-
	2.001	-	-	-
	2.503	-	3.94	-
	3.004	-	3.89	5.17
	3.507	-	3.85	5.16
	4.010	-	3.81	5.18
	4.504	-	3.78	5.18
	5.127	-	3.77	5.19
4.60 ↓	1.538	0.22	3.67	-
	2.052	0.16	3.88	-
	2.564	-	3.93	6.13
	3.078	-	4.28	6.46
	3.589	-	4.85	6.58
	4.101	-	5.16	6.73
	4.610	-	4.99	6.88
	5.127	-	5.13	7.01
	5.646	-	5.36	7.06
	6.138	-	5.77	7.11
	6.652	-	5.04	7.21

4.0 CONCLUDING REMARKS

An extensive experimental investigation was carried out in 23 wind tunnels, in several countries, to document effects of wind tunnel test section noise level on boundary-layer transition location on a 10-deg included-angle cone. Care was taken to maintain the cone in the same physical condition for each experiment and to make measurements using the same techniques each time. Additional precautions were taken to eliminate the unwanted influence of model incidence and heat transfer on the transition measurements. A summary of the data is compiled in Volume I, and complete sets of data from all tunnels are given in Volume II.

REFERENCES

1. Whitfield, J. D. and Dougherty, N. S., Jr. "A Survey of Transition Research at AEDC." AGARD Fluid Dynamics Panel Symposium on Laminar-Turbulent Transition, CP No. 224, Paper No. 25, Lyngby, Denmark, May 2-4, 1977; also AEDC-TR-77-52 (ADA041740), July 1977.
2. Pate, S. R. and Schueler, C. J. "Effects of Radiated Aerodynamic Noise on Model Boundary-Layer Transition in Supersonic and Hypersonic Wind Tunnels." AEDC-TR-67-236 (AD666644), March 1968.
3. Ross, R. and Rohne, P. B. "Noise Environment in the NLR Transonic Wind Tunnel HST." NLR TR 74128U, August 1973.
4. Dods, J. B. and Hanly, R. D. "Evaluation of Transonic and Supersonic Wind-Tunnel Background Noise and Effects on Surface Pressure Fluctuation Measurements." AIAA Paper No. 72-1004, AIAA 7th Aerodynamic Testing Conference, Palo Alto, California, September 1972.
5. Mabey, D. G. "Boundary Layer Transition Measurements on the AEDC 10° Cone in Three RAE Wind Tunnels and Their Implications." ARC R&M No. 3821, June 1976.
6. Dougherty, N. S., Jr. and Steinle, F. W., Jr. "Transition Reynolds Number Comparisons in Several Major Transonic Tunnels." AIAA Paper No. 74-627, AIAA 8th Aerodynamic Testing Conference, Bethesda, Maryland, July 8-10, 1974.
7. Schutzenhofer, L. A. and Howard, P. W. "Suppression of Background Noise in a Transonic Wind-Tunnel Test Section." Fall 1974 Research Technology Review, NASA/Marshall Space Flight Center, Huntsville, Alabama, October 1974; also AIAA Journal, Vol. 13, No. 11, November 1975, pp. 1467-1471.

8. Vaucheret, X. "Fluctuation Acoustiques Engendrees Par Les Paroid Permeables D'Une Soufflerie Transonique." AGARD Fluid Dynamics Panel Symposium on Wind Tunnel Design and Testing Techniques, AGARD CP No. 174, Paper No. 25, London, England, October 6-8, 1975; also ONERA CHATILLON TP No. 1324, 1974.
9. Lowson, M. V. "Prediction of Boundary Layer Pressure Fluctuations." AFFDL-TR-67-167, April 1968.
10. Dougherty, N. S., Jr., Anderson, C. F., and Parker, R. L., Jr. "An Experimental Investigation of Techniques to Suppress Edgetones from Perforated Wind Tunnel Walls." AEDC-TR-75-88 (ADA013728), August 1975; also AIAA Paper No. 76-50, AIAA 14th Aerospace Sciences Meeting, Washington, D. C., January 26-28, 1976.
11. Varner, M. O. "Noise Generation in Transonic Tunnels." AIAA Paper No. 74-633, AIAA 8th Aerodynamic Testing Conference, Bethesda, Maryland, July 8-10, 1974; also AEDC-TR-74-126 (ADA007688), April 1975.
12. Cooksey, J. M. and Arnold, J. W. "Transonic Flow Quality Improvements in a Blowdown Wind Tunnel." Journal of Aircraft, Vol. 10, No. 9, September 1973, pp. 554-560.
13. Jordan, R. "Tests with the AEDC 10-Deg Transition Cone in the 9x8-Ft Transonic Tunnel." ARA Model Test Note 2.32, 1973.
14. Dougherty, N. S., Jr. "A Study of Acoustic Disturbances and Means of Suppression in Ventilated Transonic Wind Tunnel Walls." AEDC-TR-77-67 (ADA045347), October 1977.
15. Laderman, A. J. "Review of Wind-Tunnel Freestream Pressure Fluctuations." AIAA Journal, Vol. 15, No. 4, April 1977, pp. 605-608.
16. Maestrello, L., et al. "Measured Response of a Complex Structure to Supersonic Turbulent Boundary Layers." AIAA Paper No. 76-83, AIAA 14th Aerospace Sciences Meeting, Washington, D. C., January 26-28, 1976.
17. Dougherty, N. S., Jr. "Correlation of Transition Reynolds Number with Aerodynamic Noise Levels in a Wind Tunnel at Mach Numbers 2.0 - 3.0." AIAA Journal, Vol. 13, No. 12, December 1975, pp. 1670-1671.

NOMENCLATURE

ΔC_p	rms pressure fluctuation normalized with q_∞ and expressed in percent, $\sqrt{\bar{p}'^2}/q_\infty$
f	Frequency, cycles/sec or Hz
$G(f)$	Power spectral density function, $\overline{p'^2}/\text{Hz}$
ℓ	Cone surface length, 36 in. without extension
ℓ_0	Reference length dimension, in.
M_∞	Free-stream Mach number
p'	Fluctuating static pressure, psf
p_t	Tunnel total pressure, psfa
p_∞	Free-stream static pressure, psfa
q_∞	Free-stream dynamic pressure, $(\gamma/2)p_\infty M_\infty^2$, psfa
Re_p	Transition Reynolds number based on X_p (see Fig. 4)
Re_T	Transition Reynolds number based on X_T (see Fig. 4)
Re_t	Transition Reynolds number based on X_t (see Fig. 4)
rms	Root-mean-square value of fluctuating static pressure, $\sqrt{\bar{p}'^2} = (\int_0^f G(f)df)^{1/2}$, psf
T_t	Tunnel total temperature, °R
T_w	Cone surface temperature, °R
T_∞	Free-stream static temperature, °R
t	Time, minutes
U_∞	Free-stream velocity computed from M_∞ and T_∞ , ft/sec
U_∞/ν_∞	Free-stream unit Reynolds number, ft^{-1}
X_p	Location of peak in rms fluctuating pressure in transition zone, ft

X_T	Location of peak in steady-state pitot pressure profile called end-of-transition location, ft
X_t	Location of minimum in steady-state pitot pressure profile called onset-of-transition location, ft
x	Surface distance from cone apex, ft
α	Cone model angle of attack, deg
β	Cone model angle of yaw, deg
μ_∞	Kinematic viscosity, lbm/ft ² -sec (computed from T_∞)
ν_∞	Dynamic viscosity, ft/sec (computed from T_∞ , ρ_∞)
ρ_∞	Free-stream density, lbm/ft ³
ϕ	Cone roll angle, deg
τ	Tunnel wall porosity, percent open